UNIVERSITY OF CALIFORNIA
RIVERSIDE

Incorporation of Vasculature and Fat in Human Skin Equivalents, Validated Through Volumetric Analysis to Improve Aging Models

A Dissertation submitted in partial satisfaction
of the requirements for the degree of

Doctor of Philosophy

in

Bioengineering

by

Martina M. Sanchez

December 2021

Dissertation Committee:

Dr. Joshua T. Morgan, Chairperson
Dr. Hyle Park
Dr. Cesunica Ivey

The Dissertation of Martina M. Sanchez is approved:

Committee Chairperson

University of California, Riverside

Acknowledgements

I thank the following individuals:

My advisor, Dr. Joshua T. Morgan for his mentorship, advice, and direction. My committee members, Dr. Cesunica Ivey and Dr. Hyle B. Park, for their guidance and support. My labmates for their encouragement and discussions: Shane Kennedy, Lisa Salmeron, Isabella Bagdesarian, Abby Barlow, Enrique Roman. Undergraduates who have helped me complete this work: Verena Tadros, Nicholas Higgins, Jordan Rolsma, William Darc, and Kristina Rodriguez. The Ronald E. McNair Scholar's Program at Wichita State University for their rigorous preparation program for support of underrepresented students to attain PhDs.

I am grateful to my family who has supported me in my ambition to reach this goal and lastly, to my husband for his un-conditional support and patience during my time at UCR.

Funding sources: Dissertation Research Grant from the Graduate Division at UCR. Graduate Research Mentorship Fellowship from the Graduate Division at UCR. American Heart Association (19IPLOI34760636).

The text of this dissertation, in full, is a reprint of the material as it appears in Journal of Video Experiments 2021 (Chapter 2); Other chapters are in preparation for submission to Aging Journal (Introduction) , Biotechniques (Chapter 3) , Biomaterials (Chapter 4), Molecular Biology of the Cell (Chapter 5).

ABSTRACT OF THE DISSERTATION

Incorporation of Vasculature and Fat in Human Skin Equivalents, Validated Through Volumetric Analysis to Improve Aging Models

by

Martina M. Sanchez

Doctor of Philosophy, Graduate Program in Bioengineering
University of California, Riverside, December 2021
Dr. Joshua T. Morgan, Chairperson

Aging Associated Diseases (AADs) represent a continuing and increasing burden on elderly patients and their families. AADs have many commonalities, such as inflammation and reduced healing, and are difficult to study with current animal and *in vitro* models. The overarching aim of this work was to develop *in vitro* tissue models that act as platforms for AAD research. Focus of these studies is on the development of tissue engineered human skin equivalents that more closely re-capitulate human systems. To this end, we have developed and validated culture methods for human skin equivalents that incorporate dermal vasculature and subdermal adipose. The developed protocols are highly customizable, and we have demonstrated success using multiple human cell lines. Further, we improve upon the gold standard of analysis, histological sectioning and staining, by utilizing volumetric analysis which aids in understanding

these complex three-dimensional tissues. Imaging through confocal microscopy and optical coherence tomography allow for quantification of several parameters including many that cannot be obtained through two-dimensional studies: vascular network diameter and diffusion length, volumetric fraction of specific cells/structures, thickness measurements of skin epidermis and adipose, and protein expression/intensity throughout a sample rather than on a single cross section. Further, automated algorithms have been developed to quantify and characterize the tissue engineered samples outlined. Similar techniques have also been applied to separate toxicity studies. Skin and fat cells were used as two-dimensional models to understand the toxic mechanisms of perfluoroalkyl substances (PFAS), commonly referred to as "forever chemicals" due to their environmental persistence. The underlying mechanisms of PFAS at the human cell level are not well understood. In these studies we show that PFAS dysregulate the cytoskeleton and enhance adipogenesis .

Table of Contents

List of Figures

List of Tables

Chapter 1
Introduction

This work, in part, is in preparation for submission to the journal: Aging Journal

Native skin aging

Skin is one of the largest organs of the body and has functional roles in immune response, physical protection, and thermal regulation [1]. As aging occurs, skin function and healing capacity is reduced. Skin aging is frequently divided into two related processes: intrinsic and extrinsic aging [2–5]. Intrinsic aging, also referred to as chronological aging, includes genetic and hormonal changes and the progression from cell maturity to cellular senescence [2,3]. Extrinsic aging, also referred to as environmental aging, represents the impact of the environment, including: photoaging associated with sun exposure [2,6,7], cigarette smoking, pollution, chemical exposure, trauma [3]. Due to the different underlying mechanisms, characteristics of each type of aged skin are different. Chronologically (intrinsically) aged skin presents as unblemished, smooth, pale, dry, lower elasticity, and has fine wrinkles while environmentally (extrinsically) aged skin has coarse wrinkling, rough textures, pigmentation changes, and lower elasticity [3,8].

Microstructural changes in intrinsically aged skin include decreased dermal vasculature [9]; changes in dermal elasticity and increased collagen disorganization [10,11]; build-up of advanced glycation end products (AGEs) and changes in glycosaminoglycan (GAG) and proteoglycan (PG) concentrations/organization contributing to stiffening of dermal structure and frailty, and decreased hydration [4,8,12–18]; imbalance of tissue inhibitors and matrix metalloproteinases (MMPs) resulting in imbalance between collagen deposition

and breakdown [3,19]; and flattening of the dermal epidermal junction/loss of rete ridges [3,7,20–22]. Aging also contributes to variations in epidermal and dermal thickness [21–24] and reduced subcutaneous fat volume [3]. There are also many changes related to cell population in all three main skin compartments (epidermal, dermal, sub-dermal) including reduced epidermal cell turnover [3,20], drop in number of active melanocytes [3]; decreases in dermal fibroblast concentrations [22], decreases in immune cells [21,22] and immune function. Abnormalities of skin barrier (a major function of the epidermis) occur during aging and often present as dryness or skin irritation. In aged skin, barrier function has been studied in the context of decreases of filaggrin [25], increases in pH (5 to ~5.6), altered lipid presence [26,27], and changes in cornified envelope arrangement [21,28–30]. These changes add to fragility of older skin and higher chances of infection [31], it remains unclear exactly how these changes take place and what mechanisms are controlling them.

On the molecular scale, expression levels of soluble factors, proteins, and vitamins are both effects and contributors to aging phenotypes. Examples include upregulation of stress regulatory proteins (hypoxia-inducible factors, nuclear factor kappa-light chain-enhancer) [21], increases in AP-1 (leading to increased collagen breakdown via MMP activity) [7,19], and declines in vitamin D production by the epidermis [21]. These changes are largely attributed to increases in reactive oxygen species (ROS) [7,21], DNA mutations (including mitochondrial DNA), telomere shortening[21], increased cell senescence, and hormonal changes [4,21]. Changes in skin aging have been associated with fluctuations in expression patterns of integrins including α6 and ß1 integrins [11,14,32–34].In healthy human skin, α6 and ß1 (and other α/ ß subunits) integrin expression are localized on the basal side of basal keratinocytes [14,34]. Defects in integrin expression are present in human blistering skin diseases with supporting evidence in knockout mice [34] and also in aged human skin [14,32],

although further work is necessary to understand how integrin expression changes in aging. Aging in the skin has sex-related differences as well, specifically, sex is linked to faster thinning of the dermis and collagen density decline in males as opposed to females [3,35]. Males undergo a decline in androgen levels while estradiol levels are constant, these changes result in a linear decline of skin thinning and collagen content in men [10]. Women experience both androgen and estrogen decline linearly and an additional post-menopausal estrogen decline which is linked to lower collagen content, lower skin moisture and capacity to hold water, lessened would healing response, thinner skin, and lower skin elasticity [3,8,10,36]. Detailed summary and discussion of sex-related changes in skin aging have been previously reviewed [10].

These intrinsic mechanisms are compounded by environmental skin aging (extrinsic aging) [4,7,21]. A key example is the effects of ultraviolet (UV) irradiation (an extrinsic aging mechanism), which accelerates telomere shortening and DNA damage present with intrinsic aging [3,37]. Other extrinsic aging and examples of compounding UV effects are discussed in previous literature[4,11,38–44]. Overall, skin aging at the molecular, cellular, and tissue levels continues to be a field of active research. While *in vivo* and traditional cell culture models remain important tools, there is increasing interest in more physiologically relevant culture models, and there is a growth in recent studies employing organotypic skin models (OSCs).

Organotypic Skin Models

Researchers have used organotypic models to study skin biology since the 1980s [45,46]. OSCs are also commonly referred to as human skin equivalents (HSEs) or full-thickness skin models; they typically have dermal and epidermal layers with proper stratification of the epidermis. These models have proven useful for studying skin development, evaluating cytotoxicity, studying wound healing, and more recently as disease and aging models. OSCs

are highly customizable and allow for control of organotypic cell populations, genotypes, and culture conditions to enable carefully controlled studies on tissue-level biology. OSCs have the capacity to be used for in depth aging studies without the dangers of human trials or expensive animal models; with long-term culture stability for chronic studies (typical culture lengths of 8-12 weeks) [47,48]. Most commonly, OSCs contain dermal fibroblasts and keratinocytes and are cultured at an air-liquid interface for epidermal differentiation and stratification. However, with the growth of interest in heterogeneous cell-cell communication, an increasing number of models have been demonstrated with additional cell populations [11,49,50]. These include vascular endothelial cells [48,51–56], immune cells [57–60], adipose derived stem cells and adipocytes from adipose derived stem cells [61–63], embryonic stem cells [11], melanocytes [64–66] and melanocytes derived from induced pluripotent stem cells [67]. With this customizability and a growing number of accessible protocols, OSCs represent a useful tool for studying skin aging; exemplar applications are discussed below, first for disease generally and then with aging specifically.

OSCs have been used in a number of disease studies, both directly and as "hybrid" studies where a humanized OSC is grafted onto immunodeficient mice. Additionally, models have been shown useful for testing potential therapeutic techniques for debilitating skin disorders or injuries [68]. OSC skin disorder models include: psoriasis [69,70] [71], recessive dystophic epidermolysis bullosa [72,73], xeroderma pigmentosum, vitiglio, Forlin syndrome, lamellar ichthyosis [74], Netherton syndrome [75], congenital pachyonychia [76], Junctional epidermolysis bullosa [11,77], and fibrosis [78–80]. Of these disease models, the fibrosis model by Varkey et al. is especially interesting for its potential to be adapted to use as an aging model. In this study, OSCs were generated using either deep dermal fibroblasts or superficial dermal fibroblasts in combination with normal human keratinocytes [78]. They found that the

antifibrotic properties of deep dermal fibroblasts and the fibrotic properties of superficial fibroblasts can influence OSC characteristics. Authors found that when compared to constructs with superficial or mixed fibroblast populations, OSCs with deep fibroblasts had higher levels of interleukin-6, reduced TGF-β1 production, higher PDGF expression, and epidermal formation was less defined and less continuous. This model is potentially interesting as a platform for aging research, as TGF-β is implicated in skin aging through regulation of matrix metalloprotease activity [81,82]. The work of Varkey et al. highlights the usefulness of OSCs to study signaling between specific cellular subpopulations in a controlled way; an approach that could be readily adapted to aging studies. While there is a great deal of room for OSCs to be used to study the processes of aging in isolation or in combination with disease, several researchers have applied OSCs to aging.

Organotypic Skin Models to study aging

As OSCs are stable for long culture periods (>17 weeks), using the extended culture time to study intrinsic aging is perhaps one of the most straightforward techniques and can be combined with other aging models and/or cell types [20]. With this model, authors demonstrated that extended culture (using a non-traditional matrix of collagen-glycosaminoglycan-chitosan porous polymer) exhibited several age-related aspects similar to those that occur with *in vivo* aging, including decreases in epidermal thickness, decreases in hyaluronin expression, increases of the aging biomarker $p16^{Ink4a}$, decreases in keratinocyte proliferation over time, loss of expression of healthy epidermal markers, and basement membrane alterations. Another straightforward application of OSCs in aging is studying the impact of senescent cells. A number of studies have incorporated senescent fibroblasts into OSCs to generate models that recapitulate many of the features of *in vivo* aged skin. [23,83,84]. Diekmann and colleagues induced senescence in human dermal fibroblasts

and keratinocytes using Mitomycin-C (MMC) treatment and incorporated the cells into OSCs [84]. When compared to mitotic OSCs, the senescent models demonstrated changes similar to aged *in vivo* skin, including a more compact stratum corneum of the epidermis, reduced dermal fibroblast population, decreased collagen type I and III fiber content, decreased elastin expression and looser elastin structures, increases in MMP1, and disordered epidermal differentiation. Authors also isolated fibroblasts after OSC cultures to re-validate their senescence through aging markers and showed senescent morphology, increased senescence associated β-galactosidase (SA-β-gal), lower proliferative activity determined by Ki67 expression, upregulated p53 activity, upregulated ROS, and increased concentrations of MMP1 as compared to mitotic fibroblasts [84]. A similar study involving senescent fibroblasts used healthy fibroblasts that were exposed to H_2O_2 to induce senescence and then cultured the senescent fibroblasts in skin equivalents with healthy keratinocytes [83]. Aging phenotypes were again characterized by changes in proliferation, differentiation of suprabasal epidermal layers, impairments of skin barrier function, and surface property modification. Further, authors found that fibroblasts exhibited senescence-associated secretory phenotype (SASP) markers including IL-6, GmCSF, and IL-1α, however, this response was blunted in the 3D culture with keratinocytes. Lower levels of IL-6 were also measured in OSCs generated with fibroblast that underwent doxorubicin induced senescence. Interestingly, Weinmueller et al. observed more Ki67 positive epidermal cells when senescent fibroblasts were present. More research is required to understand senescence in the dermis and how it may effect keratinocyte homeostasis [85]. Serial passaging of fibroblasts has also been employed to simulate aging in OSCs, showing that constructs generated with late passage fibroblasts were similar to *in vivo* aged skin [23]. OSCs were generated with 15-20% SA-β-gal positive fibroblasts cells in 2D culture prior to 3D

seeding. Authors observed few changes in the epidermal compartment while the dermal component of OSCs presented a thinner dermis and increased MMP1, similar to *in vivo* aged skin [23]. Defects in epidermal-dermal junction in these OSCs were not observed and keratinocytes exhibited a healthy phenotype. Although not shown, authors noted that when greater than 30% Beta-gal positive fibroblast cells in 2D were used to generate OSCs, the fibroblasts did not produce ECM and constructs were not viable likely due to ineffective support for keratinocytes [23]. As Janson et al. found, generating an OSC using senescent cells is technically challenging since the percentage of senescent cells used to generate an OSC can alter skin structure and long-term culture health [23].

Similar studies focused on the aging of the keratinocyte population have also been done. In OSCs generated from primary cells isolated from donors, cell donor age is an option for simulating intrinsic aging *in vitro* [11]. OSCs generated with either keratinocytes isolated from aged individuals or serially passaged keratinocyte cells have been used to examine the effects of replicative senescence [86]. Constructs generated with older keratinocytes (61 or 35-year-old donors) exhibited thinner epidermis compared to cells from 1-year old donors. Additionally, there were differences in epidermal organization, where constructs generated with young keratinocytes were well organized with better stratification, while older cells produced more disorganized and less complete stratification. This study also investigated amounts of epidermal stem cell markers. They found that when keratinocytes were passaged over six times (modeling *in vitro* cellular senescence), there was a loss of stemness, indicated by high expression of α6 integrin and low expression of CD71 (a proliferation-associated cell surface marker) [86]. Likewise, in constructs generated with young (infant) keratinocytes, α6 integrin expression was observed in basal cells of epidermis while in constructs generated with adult and elderly cells there was faint and

absent α6 integrin expression (respectively). These OSC findings demonstrated in both intrinsic aging (simulated from aged donor cells) and *in vitro* senescence induced by serial passaging results in depletion of stem cells in the epidermis of skin [86].

Epidermal changes associated with aging have also been shown in models generated through genetically altering expression of key components, for example $p16^{Ink4a}$ [87]. *In vivo* chronological human aging markers, $p16^{Ink4a}$ and its repressor BM1, are established markers of *in vitro* aging tissue [11,20,87,88]. $p16^{Ink4a}$ is an inhibitor of cyclin-dependent kinases that blocks the progression from G1 phase to S phase of the cell cycle and promotes senescence onset. *In vitro* aged skin models can be generated from young donor keratinocytes cells by $p16^{Ink4a}$ overexpression [87]. Conversely, aging phenotypes observed in old donor keratinocytes can be rescued through silencing $p16^{Ink4a}$. Aged models (either through older donors or $p16^{Ink4a}$ overexpression) resulted in thinner epidermis, loss of stratum corneum (the terminal epidermal layer), and atrophy [87].

OSCs also allow for studies of matrix and cell-matrix interactions in aging skin. Expression patterns of glycosaminoglycans (GAGs) and proteoglycans (PGs) are important in skin tissue mechanical integrity, and aging-related changes contribute to frailty in both intrinsically and extrinsically aged skin [8,12,89–93]. Glycation and the presence of advanced glycation end products (AGEs) increase in aging skin, and this has been leveraged in OSCs to create an aged skin model [14,32]. In this model, collagen was glycated *in vitro* prior to construction of the OSC. This simulated intrinsic aging of the construct, resulting in modified integrin patterns in the suprabasal epidermal layers, activation of the dermal fibroblasts to increase the production of metalloproteinase, type III procollagen, and type IV collagen [14,32]. Authors found that these morphological and molecular changes in the epidermis and dermis could be partially rescued by antiglycation agents such as

aminoguandine [14]. More investigation is necessary to understand exactly how GAGs and PGs are affected during skin aging. Open questions include how sex specific hormones may affect concentrations [8] and what downstream effects GAGs and PGs have on the expression of cytokines and growth factors [94]. Building off of the previous OSCs, multi-cellular skin models can help to elucidate aging mechanisms regarding GAGs and PGs and their effect on skin homeostasis.

OSCs can also be employed as a testing platform for aging therapeutics [91,94]. C-Xyloside is a xyloside derivative that has been investigated as therapeutic to improve dermal-epidermal junction morphology in aging skin [95,96]. Sok et al. exposed OSCs to C-Xyloside and investigated the resulting DEJ morphology. C-Xyloside exposure resulted in higher basement membrane protein concentrations, specifically collagen IV, laminin 5, and collagen VII, and a structure more similar to the microanatomy of healthy human skin. Further, C-Xyloside increased concentrations of dermal proteins such as pro-collagen I and fibrillin, which are key ECM proteins for the maintenance of skin elasticity. Since defects in the basement membrane, DEJ, or elasticity contribute to skin fragility in aging, this model has potential as a test bed for other aging therapeutics [91].

This body of work builds on the framework that previous organotypic skin models have developed and importantly demonstrates further customization through incorporation of different cell types and photoaging studies. We have generated protocols for establishing fully vascularized human skin equivalents alone, and additionally to establish adipose and vascularized human skin equivalents. These OSCs have been analyzed volumetrically and thus, protocols for volumetric imaging of this *in vitro* skin tissue were developed for optical coherence tomography and confocal microscopy. Although it is an improvement upon the classic histological analysis that OSCs traditionally undergo,

volumetric imaging introduces new challenges of analysis, which we have addressed through automated image analysis based on custom algorithms. These end-to-end processes are novel contributions to the tissue engineering field and they importantly enable aging studies because of the skin's stability over time.

Through the generation and analysis of *in vitro* skin models, multiple image analysis techniques were developed for three-dimensional structures. Specifically, through these algorithms, we were also able to analyze cell monolayers (two-dimension) which is demonstrated in chapter 4. PFAS chemicals, or perfluooalkyl substances are very abundant and stable molecules that tend to accumulate in biological systems, or bio-accumulate[97–101]. These chemicals are especially dangerous in fetal development and have been linked to decreased birthweight but increases in adiposity, and altered lipid profiles in youth and young adults[102–106]. Through the skills learned in adipose tissue development and automated image analysis, we were able to study the effects that PFAS has on epidermal cell monolayers, adipose derived stem cell monolayers, and the differentiation process of adipose derived stem cells to mature fat cells, adipocytes. This work presents a novel contribution in understanding PFAS mechanistic actions on human cells and how specifically PFAS acts on adipogenesis. Additionally, we have elucidated action of PFAS chemicals on human cells through cytoskeletal disruption.

Chapter 2

Generation of Self-assembled Vascularized Human Skin Equivalents

This work, in full, appears in the Journal of Visual Experiments

Sanchez, M. M.; Morgan, J. T. Generation of Self-Assembled Vascularized Human Skin Equivalents. *JoVE* **2021**, No. 168, e62125. https://doi.org/10.3791/62125.

Abstract

Human skin equivalents (HSEs) are tissue engineered constructs that model epidermal and dermal components of human skin. These models have been used to study skin development, wound healing, and grafting techniques. Many HSEs continue to lack vasculature and are additionally analyzed through post-culture histological sectioning which limits volumetric assessment of the structure. Presented here is a straightforward protocol utilizing accessible materials to generate vascularized human skin equivalents (VHSE); further described are volumetric imaging and quantification techniques of these constructs. Briefly, VHSEs are constructed in 12 well culture inserts in which dermal and epidermal cells are seeded into rat tail collagen type I gel. The dermal compartment is made up of fibroblast and endothelial cells dispersed throughout collagen gel. The epidermal compartment is made up of keratinocytes (skin epithelial cells) that differentiate at the air-liquid interface. Importantly, these methods are customizable based on needs of the researcher, with results demonstrating VHSE generation with two different fibroblast cell types: human dermal fibroblasts (hDF) and human lung fibroblasts (IMR90s). VHSEs were developed, imaged through confocal microscopy, and volumetrically analyzed using computational software at 4- and 8-week timepoints. An optimized process to fix, stain, image, and clear VHSEs for volumetric examination is described. This comprehensive

model, imaging, and analysis techniques are readily customizable to the specific research needs of individual labs with or without prior HSE experience.

Introduction

Human skin performs many essential biological functions including acting as an immune/mechanical barrier, regulating body temperature, participating in water retention and sensory roles[107–110]. Anatomically, skin is the largest organ in the human body and is made up of three main layers (epidermis, dermis, and hypodermis) and possesses a complex system of stromal, vascular, glandular, and immune/nervous system components in addition to epidermal cells. The epidermis itself is composed of four layers of cells that are continuously renewed to maintain barrier function and other structures of native skin (i.e., sweat and sebaceous glands, nails)[109]. Skin physiology is important in immune function, wound healing, cancer biology, and other fields, leading researchers to use a wide range of models, from in vitro monocultures to in vivo animal models. Animal models offer the ability to study the full complexity of skin physiology, however, commonly used animal models such as mice have significant physiological differences when compared to humans[111]. These limitations, and the increased cost of animal models, have led many researchers to focus on developing in vitro models that more closely reflect the physiology of human skin[107,112]. Of these, one of the simpler model types is the human epidermal equivalent (HEE; also referred to as half-thickness skin models) which are composed of only epidermal keratinocytes on an acellular dermal matrix, but capture epidermal differentiation and stratification seen in vivo. Building on this, models containing dermal and epidermal components (keratinocytes and fibroblasts) are often referred to as human skin equivalents (HSE), full-thickness skin models, or organotypic skin constructs (OSC).

Briefly, these models are generated by encapsulating dermal cells within gel matrices and seeding epidermal cells on top. Epidermal differentiation and stratification can then be achieved via specialized media and air exposure[113]. Skin equivalents have most often been generated through self-assembly techniques using dermal gels made of collagen type I (either of rat tail or bovine skin origin)[107,114], but similar models have incorporated other matrix components such as fibrin[115,116], fibroblast derived[47,117], cadaveric de-epidermized membranes[11,118–120], commercially available gels and others[107,117,118,121–123]. Currently, there are skin equivalents commercially available (as previously reviewed[107,108]). However, these are primarily developed for therapeutic purposes and cannot be readily customized to specific research questions.

HSEs have been applied in studies of wound healing, grafting, toxicology, and skin disease/developement[11,47,117,118,122,124–127]. Although 3D culture more comprehensively models functions of human tissue compared to 2D cultures[128], the inclusion of diverse cell types that more accurately reflect the in vivo population enables studies of cell-cell coordination in complex tissues[128–130]. Most HSEs only include dermal fibroblasts and epidermal keratinocytes[131], although the in vivo skin environment includes many other cell types. Recent studies have started including more cell populations; these include endothelial cells in vasculature[53,55,116,132–136], adipocytes in sub-cutaneous tissue[137,138], nerve components[123,125], stem cells[131,139,140], immune cells[70,116,141–143], and other disease/cancer specific models[11,69,70,77–79,85]. Particularly important among these is vasculature; while some HSEs include vascular cells, overall they still lack comprehensive capillary elements with connectivity across the entire dermis[53,116] , extended in vitro stability [132], and appropriate

vessel density. Further, HSE models are typically assessed through post-culture histological sectioning which limits analysis of the three-dimensional structure of HSEs. Three dimensional analysis allows for volumetric assessment of vascular density[144,145] as well as regional variation of epidermal thickness and differentiation.

Although HSEs are one of the most common organotypic models, there are many technical challenges in generating these constructs including identification of appropriate extracellular matrix and cell densities, media recipes, proper air liquid interface procedures, and post-culture analysis. Further, while HEE and HSE models have published protocols, a detailed protocol incorporating dermal vasculature and volumetric imaging rather than histological analysis does not exist. This work presents an accessible protocol for the culture of vascularized human skin equivalents (VHSE) from mainly commercial cell lines. This protocol is written to be readily customizable, allowing for straight-forward adaptation to different cell types and research needs. In the interest of accessibility, availability, and cost, the use of simple products and generation techniques was prioritized over the use of commercially available products. Further, straightforward volumetric imaging and quantification methods are described that allow for assessment of the three-dimensional structure of the VHSE. Translating this procedure into a robust and accessible protocol enables non-specialist researchers to apply these important models in personalized medicine, vascularized tissue engineering, graft development, and drug evaluation.

Protocol

1. Preparation for 3D culture

1.1. Prepare rat tail collagen stock at 8 mg/mL, using established protocols[146–148]. Alternatively, rat tail collagen can be purchased from vendors (see materials list) at appropriate concentrations.

NOTE: Collagen can be prepared or purchased at different concentrations in the range of 3-10 mg/mL, or higher[146–148]. The calculations in the protocol assume an 8 mg/mL concentration but can be adjusted based on the needs of the researcher.

1.2. Expand cell lines: Endothelial and fibroblast cells need to be ready for seeding at the start of 3D collagen dermal component generation (step 2). Keratinocytes need to be ready on day 7 of 3D culture. One complete VHSE construct requires 7.5 x 10^5 endothelial cells; 7.5 x 10^4 fibroblasts; and 1.7 x 10^5 keratinocytes for generation (**Table 2.1**).

NOTE: These densities are appropriate for 12-well size permeable tissue culture inserts or equivalent. Cell density and format can be scaled up or down based on the needs of the researcher. To clarify, this amount of endothelial and fibroblast cells will seed 1-3 dermal components, while each epidermal component requires 1.7 x 10^5 keratinocytes.

1.3. Perform all cell centrifugation in this protocol for 5 min at 300 x *g*, but this may be decreased for more fragile cell types.

2. Generation of 3D collagen dermal component

NOTE: Step 2 is a time sensitive procedure and must be completed in one setting. It is advised to complete a quality check of the collagen stock to ensure proper gelation and homogeneity before beginning dermal component seeding, see troubleshooting in discussion.

2.1. Acellular collagen layer preparation and seeding

2.1.1. Prepare two 1.7 mL capped microcentrifuge tubes, one for the acellular support and one for the cellular dermis. Amounts given in this step will prepare 1 mL of 3 mg/mL collagen (target collagen concentration), sufficient for (3) 12-well size VHSEs. Equations are listed if adjustment is necessary. Both volume and density can be scaled based on the needs of the researcher (common reference numbers are given in **Table 2.2**).

2.1.2. To each tube, add 100 µL of culture grade 10x Phosphate-buffered saline (PBS) (one tube will yield 3 VHSEs) and add 8.6 µL of 1 N NaOH. Place capped tubes on wet ice to chill for at least 10 min.

$C_s = Collagen\ Stock\ Concentration$

$V_f = Final\ Volume\ of\ Collagen\ Needed$

$C_t = Target\ Collagen\ Concentration$

$V_s = Volume\ of\ stock\ collagen\ necessary\ for\ desired\ amount\ (V_f)$

$V_{pbs} = Volume\ of\ 10X\ PBS\ needed\ for\ target\ collagen\ concentration\ (C_t)$

$V_{NaOH} = Volume\ of\ 1N\ NaOH\ needed\ for\ C_t$

$V_{media} = Volume\ of\ media, cell\ suspension, or\ ddH2O\ needed\ for\ C_t$

$$V_{pbs} = \frac{V_f}{10}$$

$V_{NaOH} = V_s * (0.023\ mL)$

$V_s = V_f * \frac{C_t}{C_s}$

$V_{media} = V_f - V_s - (V_{pbs}) - (V_{NaOH})$

2.1.3. Prepare 1000 and 250 µL positive displacement pipettes for use and set aside. As later steps are time sensitive, it is convenient to load pipette tips and set volumes (375 µL and 125 µL, respectively). Additionally, setup a normal 1000 µL pipette for 516 µL.

NOTE: Positive displacement pipettes can be substituted with normal pipettes if necessary, but because of the high viscosity of collagen and the time/temperature sensitivity of this procedure, positive displacement pipettes are recommended to help produce consistent seeding results. If using normal pipettes, use slow movements.

2.1.4. Prepare culture insert well plates: Use sterile forceps to place three 12-well size culture inserts into a sterile 12-well tissue culture plate, place into the center columns.

2.1.5. Set out cold media appropriate for fibroblast and endothelial cell types.

2.1.6. After cooling of capped tubes, place one tube (for the acellular support) on a rack with the contents visible. Leave the other tube (for the cellular dermis) on ice.

2.1.7. Remove 8 mg/mL collagen stock from refrigeration and place on wet ice.

NOTE: Do not use freezer ice or -20 °C benchtop coolers, as this will freeze the collagen.

2.1.8. To the cold capped tube, add 516 µL of media and immediately add 375 µL of cold collagen using the 1000 µL positive displacement pipette. Dispense collagen into the solution (not to side of the tube). Immediately remove the empty pipette tip and switch to the prepared 250 µL positive displacement pipette to mix.

2.1.8.1. Mix quickly but gently to prevent bubble formation, do not remove tip from the solution, if possible. Mix until the solution is of homogenous color, which typically takes about 5 pipette cycles or 10 s (if using media with phenol red, the color will become lighter and uniform). When mixing, be sure to draw from different positions of the tube (bottom and top) for uniform mixing.

NOTE: This can be performed with 516 µL of cell culture grade water or other cell culture grade liquid, however, phenol red of most media is a good indicator of the mixing. Use either fibroblast or endothelial media that was used for 2D expansions.

2.1.9. Immediately disperse 125 µL of acellular collagen onto the membrane of each of the three 12-well culture inserts. To ensure uniform coverage of the acellular collagen gel, rock the dish; if that does not create uniform membrane coverage then use the pipette tip to essentially paint the membrane by gently spreading collagen around; avoid applying pressure to the membrane. Gelation begins almost immediately; perform this step quickly to ensure even coverage.

NOTE: There will be excess acellular collagen. The volume can be reduced, however, preparing less than 1 mL of collagen suspension can result in difficulties mixing the solution and insufficient gelation.

2.1.10. Immediately move the 12-well plate to a 37 °C cell culture incubator to let it gel for at least 20 min (acellular collagen can gel for longer if needed; during this gelation time, proceed to step 2.2). Remove the collagen suspension from ice and place back into refrigeration (collagen is most stable at 4 °C).

2.2. Cell suspension & seeding preparation

NOTE: For the culture timeline of this protocol, this corresponds to Submersion Day 1 (SD1)

2.2.1. During gelation of the acellular collagen support, trypsinize and count the endothelial and fibroblast cell lines.

2.2.2. Suspend 7.5 x 10^5 endothelial cells and 7.5 x 10^4 fibroblasts in 258 µL of their respective medias and combine cell suspensions to create a 516 µL aliquot. Maintain the cell suspensions on wet ice until use.

2.2.3. Prepare 1000 and 250 µL positive displacement pipettes for use and set aside. As later steps are time sensitive, it is convenient to load pipette tips and set volumes (375 µL and 250 µL, respectively). Additionally, setup a normal 1000 µL pipette for 516 µL.

2.3. Cell laden collagen seeding of dermal compartment

2.3.1. After the gelation period, remove the 12 well plate of acellular collagen from the incubator.

NOTE: If this collagen is not gelled after 30 min, do not continue the procedure as there was likely a mistake during seeding or the collagen stock may have a problem (see troubleshooting in discussion).

2.3.2. Remove the 1.7 mL capped tube from wet ice (contains 10x PBS and NaOH). Place the tube in a rack so that the contents are visible. Loosen/open all caps (cell suspension, cold capped tube).

2.3.3. Remove the stock collagen (8 mg/mL) from 4 °C refrigeration and place it on wet ice. Leave the cap open.

2.3.4. Add the 516 µL of cooled cell suspension to the cold capped tube. Use the 1000 µL positive displacement pipette to immediately pipette 375 µL of cold collagen solution directly into the solution of the capped tube.

2.3.5. Expel all collagen from pipette into the tube and discard the positive displacement pipette tip. Immediately switch to the 250 µL positive displacement pipette and mix the collagen solution.

2.3.6. Mix the collagen solution as completed previously (quickly but gently to prevent bubble formation), do not remove tip from gel if possible. Mix until solution is homogenous (about 5 pipette cycles or 10 s). When mixing be sure to draw from different positions of the tube (bottom and top) for uniform mixing.

2.3.7. Once mixed, immediately transfer 250 µL of cellular collagen solution onto the acellular collagen supports in each of the three 12-well culture inserts. To ensure uniform coverage of the acellular collagen support, rock the dish and/or use the positive displacement pipette to gently move the freshly seeded cellular collagen around without disturbing the acellular layer.

2.3.8. Immediately move the 12-well plate to 37 °C cell culture incubator to let it gel for at least 30 min. Place collagen back into 4 °C refrigeration after use.

2.3.9. After the 30-minute gel time, gently tilt the plate to assess the gelation. Ensure the collagen is solidified.

2.3.10. Add 500 µL and 1000 µL of blend media (half endothelial and half fibroblast maintenance media) to the upper chamber and lower chamber of the insert, respectively (top first, then bottom to prevent hydrostatic pressure from pushing collagen up). Add media slowly to the side of the well, not directly onto collagen gel, to minimize disruption of the collagen.

2.3.10.1. Ensure that the collagen gel is submerged, add more media if necessary. Place the well plate in the cell incubator for overnight incubation. At this stage, media contains 10% FBS; the normal maintenance media for each cell line (timeline and schematic given in **Figure 2.1, A**).

NOTE: Media throughout VHSE culture can be adapted for custom cell types; some optimization may be necessary.

2.4. Submersion Day 2 (SD2) media change

2.4.1. Change 10% FBS media in VHSE wells to 5% FBS half fibroblast, half endothelial media supplemented with 100 µg/mL L-Ascorbic Acid. Add 500 µL to upper chamber of the culture insert at the side of the well (again, add carefully to the sidewall to minimize disruption of the collagen) and add 1000 µL to lower chamber.

2.4.2. Renew media every 2 days (SD4 and SD6) until Submersion Day 7 (SD7).

2.4.3. Use a manual pipette to remove media from the wells. Using an aspirator is possible but can result in damage or destruction of the construct.

NOTE: L-ascorbic acid must be made up fresh every 2-3 days (it oxidizes in solution to produce hydrogen peroxide thus, inducing oxidative stress and eventually cellular damage[149]). Thus, media must be changed every 2-3 days from SD2 until the end of the VHSE culture since L-ascorbic acid is present. It is easiest to make a stock of media and add a freshly prepared amount of L-ascorbic acid to a media aliquot every feeding day. Use culture grade water or media as a solvent and prepare fresh L-ascorbic acid at 100 mg/mL. L-ascorbic acid stimulates collagen synthesis by fibroblasts at an appropriate rate and promotes collagen stability[150–152]; it also decreases endothelial permeability and maintains vessel wall integrity[152,153] and additionally contributes to epidermal barrier formation[26,112].

3. **Seeding of epidermal component and stratification induction**

3.1. Submersion Day 7 (SD7): seed keratinocytes

NOTE: Seed keratinocytes to establish the epidermis on SD7. This time point can be shifted based on the needs of the researcher. Duration of submersion culture without keratinocytes should not exceed 9 days, as a longer submersion often leads to increased dermal contraction. If contraction occurs before SD7, it is recommended to shorten the submersion period to 5 days and seed epidermis on SD5. Optimize the submersion period as required for specific experiments (see troubleshooting in discussion).

3.1.1. Culture keratinocytes (N/TERT-1[124,154] or other appropriate cells) to their confluency limit before trypsinization and seeding onto VHSEs. For N/TERT-1 cells, confluency should not significantly exceed 30% to prevent un-wanted differentiation of keratinocytes in 2D culture[154]. For other appropriate cell lines, such as primary human epidermal keratinocytes, a confluency limit of 75-80% is generally used[155].

3.1.2. After trypsinization, count and suspend 510,000 cells in 600 µL of Human Skin Equivalent (HSE) Differentiation media supplemented with 5% FBS (**Table 2.1**).

NOTE: 510,000 cells in 600 µL allows 170,000 cells/construct when seeding 200 µL per construct (3 VHSEs).

3.1.3. Using a manual pipette, collect and discard media currently in the bottom and top chamber for each construct well. Be sure to collect as much media as possible. Collect media that may be stuck directly under the permeable membrane by gently placing the pipette tip under the culture insert membrane and knocking the insert out of place temporarily. Media may have been stuck due to surface tension. Be sure that the inserts sit flat in their wells before proceeding. Using an aspirator is possible but can result in damage or destruction of the construct.

3.1.4. Add 1 mL of HSE media supplemented with 5% FBS to the lower chamber of each well. Then add 200 µL of cell suspension to the top chamber of each well. Seed directly onto the dermal construct surface. Let keratinocytes settle for 2 h in the incubator.

3.1.5. Two h after seeding the keratinocytes, carefully add 300 µL of HSE media supplemented with 5% FBS to the top chamber of each construct well; slowly pipette media onto side of culture insert. Load media into the top chamber very carefully as to not disturb settled keratinocytes that may not have adhered tightly to the underlying collagen gel yet.

3.1.6. After loading the media, place construct back into the incubator.

3.2. Submersion Day 8/9 (SD8 or SD9)

3.2.1. Make up HSE media supplemented with 1% FBS and 100 µg/mL L-ascorbic acid.

3.2.2. Remove media from both the upper and the lower chambers with a manual pipettor.

3.2.3. Add 500 µL media into the top chamber first and then 1 mL into the bottom chamber. (This step can be done on SD8 or SD9)

3.3. Submersion Day 9/10 (SD9 or SD10, this should be the day after step 3.2)

3.3.1. Make up serum free HSE differentiation media with 100 µg/mL L-ascorbic acid.

3.3.2. Remove media from both the upper and the lower chambers with a manual pipettor.

3.3.3. Load 500 µL into the upper chamber and 1 mL in the lower chamber.

3.4. Air-Liquid Interface Day 1 (ALI1

NOTE: ALI is performed the day after step 3.3.

3.4.1. Lift each construct to air-liquid interface (ALI) by removing media waste from the upper chamber only. Use a manual pipette to get as close to the epidermal layer as possible without touching or damaging it.

3.4.2. Tilt the plate slightly at different angles to collect the media. Remove as much media as possible in this step. Add approximately 2 mL of sterile water to the surrounding wells in the plate to maintain consistent humidity; keep the wells filled with water throughout culture.

3.4.3. Check the plate a few h later to make sure the keratinocytes are still at the air-liquid interface. If there is media in the upper chamber remove it. Keep track of how much media is removed for each VHSE well, (The initial volume of upper and lower chambers (1500 µL) – media removed = a good starting point for ALI feeding).

NOTE: VHSEs do not necessarily require the same media level for air lift; usually if the VHSEs are seeded together then they need about the same level of media for air lift, but this is not always the case. Adjust the volumes as needed to maintain ALI but ensure that the media levels are not so low that the VHSEs dry out. It is safer to be cautious and remove small media amounts daily until a balance between air lift and hydration has been met.

3.5. ALI Day 2 (ALI2)

3.5.1. From this point on, only use serum free HSE media supplemented with 100 µg/mL L-ascorbic acid. Change media on ALI Day 2 (ALI2). If there is media in the top chamber, remove it and add it to the amount of removed media recorded previously. Calculate the volume of media needed using the equation in the previous step. For example: If 200 µL of media was removed from the upper chamber then add 1300 µL to establish ALI (as 1500 µL – 200 µL = 1300 µL)

3.5.2. Use the volume calculated to load into the bottom chamber of each well, then place the plate back into the cell incubator. Keep track of the volume used per day. When using the recommended collagen amounts in 12-well culture inserts, the usual range of ALI values falls between 750 µL and 1300 µL. Typically, the volume decreases over culture maturation and becomes consistent around week 2/3 of ALI. Depending on the culture specifics, this number may change and must be optimized (as described in 3.4.2 - 4.1).

4. Routine maintenance of vascular human skin equivalent

4.1. From ALI Day 3 (ALI3) through culture endpoint: Renew media of the lower chamber every 2-3 days using serum free HSE media with 100 µg/mL L-ascorbic acid. Continue to adjust and track the media level needed in the bottom chamber for ALI as described in Step 3.5.2.

4.2. As the epidermal surface must remain in contact with the air, check and adjust the media level daily until consistent ALI levels are established. The epidermal layer should look hydrated, not dry, but there should not be media pooled on top of the construct. Cultures with 8 weeks of ALI have provided the most consistent morphology and expression; however, depending on the application, cultures of 4 to 12 weeks may be appropriate. Culture duration for different cell and culture conditions may need to be optimized.

NOTE: Changing media Monday, Wednesday, Friday is a good practice. The VHSEs are healthy over the weekend, but media should be changed early on Monday and late on Friday. After entirely completing steps 1-4, the generation of a VHSE is complete. Steps 5-end of the protocol are optional processing and imaging techniques that have been optimized for this type of 3D construct.

5. Fixation and permeabilization of 3D constructs

NOTE: Step 5 has been optimized for imaging techniques specific to this 3D construct that are outlined in the remainder of the protocol. The following steps are not necessary for generating a VHSE.

5.1. Fixation/permeabilization

5.1.1. Carefully remove all media from upper and lower chambers of each well at the end point of the culture period.

NOTE: The epidermal layer is possibly fragile, handle with care and do not agitate the epidermis with aggressive pipetting.

5.1.2. Add 4% paraformaldehyde (PFA) in PBS (pH 6.9) to the upper chamber wall (not directly on the construct) and then to the lower chamber, to pre-fix each construct. Add 1 mL per chamber and expose for 5 min at room temperature.

CAUTION: PFA is dangerous and should be handled with care and appropriate personal protection equipment (PPE), including eye protection.

5.1.3. Remove 4% PFA solution after 5 min and add the 0.5% Triton X 100 in 4% PFA solution to the upper and lower chambers as described in the previous step. Expose for 1 hour at room temperature; VHSE construct does not require a sterile environment from now on.

5.1.4. After 1 hour, carefully remove the permeabilization/fixation solution from both the chambers and wash the sample 3 times with 1x PBS.

5.1.5. Store samples in PBS in 4 °C refrigeration or immediately stain. To store the samples, wrap the dish in a plastic wrap and then foil to minimize evaporation and light exposure

NOTE: Pause point - After fixation and permeabilization, this procedure can be paused since the samples are stable for several weeks if prepared as outlined in step 5.1.5. Alternatively, staining (as described in step 6) can be completed immediately following step 5.

6. Immunofluorescent staining of 3D constructs

6.1. Construct Preparation

NOTE: VHSEs stain well when separated from porous membrane of the culture insert; separation from the membrane is also necessary for un-obstructed imaging and enable reduced volumes for staining.

6.1.1. To prepare the construct for immunofluorescent staining, turn an insert upside down and place it over its well on the well plate (if the VHSE falls, it will fall into the well with PBS) (**Figure 2.5**).

6.1.2. Stabilize the insert with one hand over the well while using fine tip forceps and/or an precision knife to cut about half of the circumference of the insert membrane. Cut as close to the plastic housing as possible with a gentle hand to prevent damage of the VHSE construct.

6.1.3. Using the fine tip forceps, grab the edge of the cut membrane flap and gently peel the porous membrane off the insert as well as the VHSE construct. Do this very carefully and slowly to prevent damage to the VHSE construct structure. If the VHSE construct separates

easily then it should fall into the well below, if it gets stuck on the side of the chamber then use the fine tip forceps or a small scoopula to move it to the well. Be very mindful of the epidermal layer as it is usually fragile (**Figure 2.5**).

NOTE: Sometimes the membrane does not come off easily or comes off in pieces, if this happens use the tools to carefully pull the membrane and VHSE construct apart. Ensure the VHSEs do not dry out during this process by dipping in PBS, if necessary.

6.1.4. Once the VHSE is in the well, discard any remaining pieces of the insert membrane and keep the culture insert housing in each well to hold the VHSEs in a submerged position during staining.

6.2. Staining

NOTE: Staining and associated handling/manipulation and washes should be performed as gently as possible since VHSEs can be fragile. If portions of the epidermis lift off, the pieces can be stained separately; upper layers of the epidermis are fragile and go through natural desquamation[110], but for analysis it is important to maintain integrity as much as possible.

6.2.1. Prepare the chosen primary antibody stains in 700 µL of blocking buffer per construct well (typically, all primary antibodies can be in the same staining solution, but this should be confirmed for new antibodies). 700 µL works for 12-well size, but may be adjusted for other culture formats. Recommended concentrations of primary and secondary antibodies with blocking buffer recipe are given in **Table 2.3** (optimization may be required).

6.2.2. Remove any PBS from the well using a manual pipette, be careful to pipette away from VHSEs (as VHSEs are floating, vacuum aspiration is not recommended).

6.2.3. Add the primary stain solution to each well and place the culture insert housing into the well to keep the VHSE submerged in fluid (**Figure 2.5, supplementary**). Wrap the well plate with plastic wrap. Foil and stain for 48 h in 4 °C refrigeration without agitation or rocking (rocking may damage the VHSE construct).

6.2.4. After 48 h, prepare secondary antibodies and chemical stains in 700 µL of blocking buffer (per well).

6.2.5. Remove the culture insert housing and the primary stain solution and wash with 1x PBS, 3x for 5 min before adding the secondary stain solution. Place the culture insert housing back into the well to keep VHSE construct submerged (**Figure 2.5, supplementary**). Expose for 48 h in 4 °C refrigeration without agitation or rocking.

6.2.6. After 48 h exposure, remove the stain solution with a manual pipettor and gently wash 3x with PBS; do not pipette fluid straight onto the VHSEs as they may be fragile. Rehydrate with excess PBS and place the culture insert housing back into the well to keep the VHSE submerged and hydrated during storage (store by wrapping in plastic wrap and foil to minimize evaporation and light exposure)

6.3. Clearing (optional & terminal)

NOTE: Clearing is optional for imaging. If completed, it should be done after staining/imaging the sample completely since clearing prevents further staining, may alter fluorophore performance, and may damage VHSE structure. Multiple tissue clearing methods exist[145,156,157] and can be optimized for specific projects. Methyl salicylate clearing, described below, is both simple and effective for VHSE. The following clearing technique must be completed in glass containers and pipette tips must be glass or polypropylene (polystyrene will dissolve in contact with methyl salicylate). Complete all clearing procedure in a well-ventilated area or fume hood.

6.3.1. Add 100% methanol to a small shallow glass container (glass Petri dishes work well). Use the smallest possible container that will fit the construct (to minimize reagent waste).

6.3.2. Remove the construct from the well plate using forceps/scoopula (**Figure 2.5**) and place in the methanol filled container. Add more methanol if construct is not submerged.

6.3.3. Dehydrate the VHSE construct in methanol for 3 x 10 min immersions; fully replace methanol after each immersion and promptly remove methanol after the last bath. Over the course of this procedure, the construct may become more opaque and shrink slightly.

NOTE: These durations and repetitions have been optimized but methanol and the following methyl salicylate procedures may need to be customized, depending on the specific culture format and stains.

6.3.4. Immediately after removing methanol, add methyl salicylate and submerge the VHSE in 5 x 5 min immersions. Fully replace the reagent after each immersion and leave the VHSE in the 5th immersion solution for storage. Over the course of this procedure, the construct becomes transparent.

6.3.5. Image the construct or store at 4 °C. After clearing, complete all imaging as soon as possible, as the fluorophores may degrade in methyl salicylate within days. Clearing causes the constructs to become brittle and the extended storage, while not recommended, needs a regular check to ensure that there is a sufficient amount of methyl salicylate.

7. Confocal Imaging of 3D constructs

NOTE: Imaging through tissue culture plastic will not yield the same quality of image as imaging through coverslip glass, this method describes fabrication of a custom glass-bottom well to prevent drying during confocal imaging. Typically, this is sufficient for at least 3 h of imaging.

7.1. Two days before imaging: prepare polydimethylsiloxane (PDMS)

7.1.1. Prepare PDMS[144,158,159] at a suggested concentration of [9:1], base: crosslinker. Prepare 30 g of PDMS total: 27 g of base component and 3 g of crosslinker. Place any clean mixing vessel on a weighing balance and tare the scale. Add the base (27 g) and then add the crosslinker (3 g) to achieve a total of 30 g. Always add base prior to crosslinker.

7.1.2. Stir the solution vigorously for at least 4 min; this will create small bubbles. After sufficient mixing, pour the PDMS into a 100-mm Petri dish, or similar flat bottom heat resistant container.

7.1.3. De-gas the PDMS in a vacuum chamber until all bubbles from mixing disappear and PDMS is clear. Release the vacuum slowly and remove the PDMS (slowly). Place the dish into an oven to cure overnight (50-60 °C); ensure the dish is sitting flat for PDMS to cure evenly.

NOTE: After curing, PDMS should be clear and the surface should be smooth and not sticky (stickiness may indicate inadequate mixing).

7.2. One day before imaging: PDMS well preparation

7.2.1. Using a steel punch or handheld precision knife, punch or cut out a circular well from the PDMS sheet prepared in 7.1. The well should be around the same size as the VHSE

construct. Cut a square patch around the circular well to create a single PDMS well. The 30 g PDMS amount prepared should yield at least four custom wells.

NOTE: The PDMS well must be close to the size of the VHSE construct. It must constrict sample motion during imaging. Multiple wells can be fabricated at once and stored indefinitely in a clean container.

7.2.2. Using a glass coverslip of a similar size to the PDMS well, add cyanoacrylate glue (e.g., super glue) to the bottom surface of the PDMS (the smooth surface that was in contact with the Petri dish) and smear evenly with a disposable pipette tip. Center, and press the PDMS well onto the glass while leaving a clear glass window within the punched circle (ensure the glue is not smeared over the viewing window).

NOTE: If available, plasma bonding of the PDMS to the coverslip is an alternative[160–162].

7.2.3. Let the glue dry for several hours, or overnight, before using. These are reusable until they break from normal wear and tear.

NOTE: It is not recommended to stain the samples in the glued PDMS well used for imaging. These wells hold fluid for several hours but can leak during longer staining.

7.3. VHSE imaging

NOTE: If imaging uncleared samples, use PBS as imaging solution. If imaging with cleared samples, use methyl salicylate (or the chosen clearing solution) as the imaging solution.

7.3.1. Add a few drops of imaging solution into the PDMS well and check for leaks (if there is a leak, repair it with a dot/smear of cyanoacrylate super glue or use another well).

7.3.2. Keep the imaging solution in the PDMS well when adding the VHSE. Using scoopula or fine tip forceps (**Figure 2.5, supplementary**), remove construct from 12-well plate and place into the PDMS well onto the glass coverslip. Place construct with the orientation of interest facing toward the objective. For example, to image the epidermis using an inverted microscope, make sure the epidermis is facing down, toward the glass.

7.3.2.1. Alternatively, for an upright microscope, face the epidermis up. The below imaging procedures are described for an inverted microscope, but could be readily adapted for an upright.

NOTE: Be cautious when manipulating the VHSE to avoid damage. Transfer over the well plate in case the VHSE falls. A bent, flat tip scoopula is the easiest way to transfer the construct (**Figure 2.5, supplementary)**.

7.3.3. Make sure the sample is sitting flat in the well and that no portions of the epidermis or dermis are folded under the sample. If folding occurs, gently manipulate the sample with

forceps or a scoopula; adding extra imaging solution temporarily to float the VHSE may help it straighten out. Folding or wrinkling of the sample can be seen by eye or using the microscope.

7.3.4. Fill the well with imaging solution, using just enough fluid to keep sample hydrated; too much fluid will float the sample, resulting in motion during imaging. The construct should be sitting on the glass viewing window; test for movement by tilting the PDMS well. If there is movement, remove some fluid; add and remove fluid drop wise until the movement stops.

7.3.5. Place a glass slide over the well to minimize evaporation during imaging (**Figure 2.5**). For longer imaging sessions, check sample frequently to ensure proper fluid levels. If accessible, a humidified chamber during imaging can be used (although it is typically not necessary).

7.3.6. Place sample on the microscope stage and image through the glass coverslip window (**Figure 2.5**)This technique allows for at least 3 h of continuous confocal imaging, but the hydration of the sample should be checked regularly, with imaging solution added when needed.

NOTE: If sample is cleared, methyl salicylate will degrade the glue over time. The glue bonding the PDMS can be re-applied between imaging runs; or the sample can be transferred to new wells periodically. In wells with plasma bonding, this will not be an issue.

7.3.7. After imaging, float the sample with imaging fluid as much as possible in the well. Use a scoopula or fine tip forceps to transfer the sample into its storage well. Perform the transfer over a well plate in case the sample falls.

7.3.8. Each PDMS well and top glass coverslip can be re-used until they break. Clean bottom glass before imaging, both inside and outside the well. Before re-using, always check for leaks and repair with glue, as necessary.

Store samples as described in step 6.3.6 and add PBS every few months to maintain; if samples are cleared, store in glass using methyl salicylate and check the levels regularly. Cleared samples may degrade rapidly (within days) and should be imaged as soon as possible.

Representative Results

Here is presented a protocol for generation of in vitro vascularized human skin equivalents (VHSE) using telomerase reverse transcriptase (TERT) immortalized keratinocytes (N/TERT-1[124,154]), adult human dermal fibroblasts (hDF), and human microvascular endothelial cells (HMEC-1) (**Figure 2.1**). Additionally, the customizable nature of this protocol is highlighted by also demonstrating VHSE generation and stability when using commonly available lung fibroblasts (IMR90) instead of hDF. Generation of the VHSE is completed in steps 1-4, while steps 5-7 are optional end point processing and imaging techniques that were optimized for these VHSEs. It is important to note that the VHSEs can be processed according to specific research questions and steps 5-7 are not required to

generate the construct. Volumetric imaging, analysis, and 3D renderings were completed to demonstrate a volumetric analysis method. These volumetric construct preparation and imaging protocols preserve VHSE structure at both the microscopic and macroscopic levels, allowing for comprehensive 3D analysis.

Characterization of the epidermis and dermis show appropriate immunofluorescent markers for human skin in the VHSE constructs (**Figure 2.2 & 2.3**). Cytokeratin 10 (CK10) is an early differentiation keratinocyte marker which usually marks all suprabasal layers in skin equivalents[122,133,163] (**Figure 2.2**). Involucrin and filaggrin are late differentiation markers in keratinocytes and mark the uppermost suprabasal layers in skin equivalents[117,133,163,164] (**Figure 2.2**). A far-red fluorescent nuclear dye (see materials list) was used to mark nuclei in both the epidermis and dermis, with Col IV marking the vasculature of the dermis (**Figure 2.2-4**). Epidermal basement membrane (BM) components are not always properly expressed in HSE cultures[11,120]; and Col IV staining of the BM is not consistently observed using this protocol. Research focused BM components and structure would benefit from additional media, cell, and imaging optimization[119].

Though confocal imaging through the bulk of the VHSE cultures often yields high resolution images that are sufficient for computational analysis of the dermis and epidermis, the clearing method described allows for deeper tissue imaging. Clearing improves confocal laser penetration depth, and effective imaging in VHSEs can be achieved to over 1 mm for cleared samples (compared to ~250 μm for uncleared). The described clearing technique (methanol dehydration and methyl salicylate) sufficiently matches refractive index throughout VHSE sample tissue[156]. Clearing the VHSE allowed for straightforward imaging

through the entire construct without manipulation (e.g., reorienting the construct to image the dermis and epidermis separately), (**Figure 2.3**).

Volumetric images allow for generation of 3D rendering to map vasculature throughout each construct (**Figure 2.4**). Briefly, confocal image sets were taken in dermal to epidermal orientation of several sub-volumes of VHSEs to detect Collagen IV stain (marking vessel walls) and nuclei (marked by a far-red fluorescent nuclear dye). Image stacks are loaded into computational software (see materials list) and a custom algorithm (based on these sources [144,165–170]) is used for 3D rendering and quantification as described previously[144]. This algorithm automatically segments the vascular component based on the Col IV stain. The volumetric segmentation is passed to a skeletonization algorithm based on fast marching[170–172]. Skeletonization finds the definitive center of each Col IV marked vessel and the resulting data can be used to calculate vessel diameter as well as vascular fraction (**Figure 2.4**). Widefield fluorescent microscopy is an accessible option if laser scanning microscopy is not available; the vascular network and epidermis can be imaged with widefield fluorescent microscopy (**Figure 2.6, supplementary**). Three-dimensional quantification is possible using widefield imaging of VHSEs rather than laser scanning microscopy, although it may require more filtering and deconvolution of images due to out-of-plane light.

Discussion

This protocol has demonstrated a simple and repeatable method for the generation of VHSEs and their three-dimensional analysis. Importantly, this method relies on few

specialized techniques or equipment pieces, making it accessible for a range of labs. Further, cell types can be replaced with limited changes in the protocol, allowing researchers to adapt this protocol to their specific needs.

Proper collagen gelation is a challenging step in establishing skin culture. Especially when using crude preparations without purification, trace contaminants could influence the gelation process. To help ensure consistency, groups of experiments should be performed with the same collagen stock that will be used for VHSE generation. Further, the gelation should ideally occur at a pH of 7-7.4, and trace contaminants may shift the pH. Before using any collagen stock, a practice acellular gel should be made at the desired concentration and the pH should be measured prior to gelation. Completing this collagen quality check before beginning dermal component seeding will identify the problems with proper gelation and collagen homogeneity prior to setting up a complete experiment. Instead of seeding acellular collagen directly onto a culture insert, seed some collagen onto a pH strip that evaluates the whole pH scale and verify a pH of 7-7.4. Gelation can be evaluated by applying a droplet of the collagen gel solution onto a coverslip or tissue culture plastic well plate (a well plate is recommended to simulate the confined sides of a culture insert). After gelation time, the collagen should be solid, i.e., it should not flow when the plate is tilted. Under phase contrast microscopy, the collagen should look homogeneous and clear. Occasional bubbles from collagen seeding are normal but large amorphous blobs of opaque collagen within the clear gel indicates a problem-likely due to insufficient mixing, wrong pH, and/or failure to keep the collagen chilled during mixing.

The cell seeding amounts and media may be adjusted. In the protocol above, the encapsulated cell amounts have been optimized for a 12-well insert at 7.5 x 10^4 fibroblasts and 7.5 x 10^5 endothelial cells per mL of collagen with 1.7 x 10^5 keratinocytes seeded on top of the dermal construct. Cell densities have been optimized for this VHSE protocol based on the preliminary studies and the previous research investigating 3D vascular network generation in various collagen concentrations[144] and HSE generation[126,173,174]. In similar systems, the published endothelial cell densities are 1.0 x 10^6 cells/mL collagen[144]; the fibroblast concentrations often range from 0.4 x 10^5 cells/mL of collagen[126,132,175] to 1 x 10^5 cells/mL of collagen[26,114,176–178]; and the keratinocyte concentrations range from 0.5 x 10^5 [cells/cm^2][173] to 1 x 10^5 [cells/cm^2][114]. Cell densities can be optimized for specific cells and research question. Three-dimensional cultures with contractile cells, such as fibroblasts, can contract leading to viability reduction and culture loss[179,180]. Preliminary experiments should be completed to test contraction of the dermal compartment (which can occur with more dermal cells, more contractile dermal cells, longer submersion cultures, or softer matrices) and to test epidermal surface coverage. Additionally, the number of days in submersion and the rate of tapering the serum content can also be customized if excessive dermal contraction is occurring or a different rate of keratinocyte coverage is required. For example, if contraction is noticed during the period of dermal submersion or while keratinocytes are establishing a surface monolayer, moving more quickly through the serum tapering process and raising VHSEs to ALI can aid in preventing additional contraction. Similarly, if keratinocyte coverage is not ideal, changing the number of days that the VHSE is submerged without serum may help increase the epidermal monolayer

coverage and mitigate the contraction since serum is left out. Changes in cell densities or other suggestions above must be optimized for the specific cultures and research goals.

To establish a proper stratification of the epidermis during the air liquid interface (ALI) period, it is critical to regularly check and maintain fluid levels in each well so that ALI and appropriate hydration of each construct is kept throughout the culture length. Media levels should be checked and tracked daily until consistent ALI levels are established. The epidermal layer should look hydrated, not dry, but there should not be pools of media on the construct. During ALI, the construct will develop an opaque white/yellow color which is normal. The epidermal layer will likely develop unevenly. Commonly, the VHSEs are tilted due to the collagen seeding or dermal contraction. It is also normal to observe a higher epidermal portion in the middle of the construct in smaller constructs (24 well size) and a ridge formation around the perimeter of the VHSE in 12 well size. Contraction of the constructs[118] may change these topographical formations, and/or may not be observed at all.

Staining and imaging of VHSEs introduces mechanical manipulation to the VHSEs. It is very important to plan and limit manipulation of each culture. When manipulation is necessary, maintain gentle movements when removing VHSEs from the insert membranes, when adding staining or wash solutions to the construct surface, and when removing and replacing VHSEs in their storage/imaging wells during imaging preparation. Specifically, the apical layers of the epidermal component may be fragile and are at risk of sloughing off the basal epidermal layers. Apical layers of the epidermis are fragile and go through desquamation even in native tissue[110], but for accurate analysis of epidermal structure it is

important to minimize damage or loss. If epidermal layers lift off the construct, they can be imaged separately. The basal layers of the epidermis are most likely still attached to the dermis while portions of the apical layers may detach. For visualization of the epidermis, a nuclear stain is helpful in observing this since dense nuclei is a characteristic of lower and mid layers of the epidermis.

Confocal imaging of the VHSE post-fixation has been discussed in the protocol, but it is also possible to image the VHSEs throughout the culture via upright based optical coherence tomography (OCT)[181–186]. VHSE are stable enough to withstand imaging without incubation or humidification for at least two hours without noticeable effects. As OCT is label free and noninvasive, it is possible to track the epidermal thickness during maturation. Other noninvasive imaging modalities can likely be employed as well.

Volumetric imaging of the combined dermal and epidermal structures can be challenging due to laser attenuation deeper in the VHSE. This can be mitigated by imaging the construct in two orientations, from the epidermal side (**Figure 2.2**) and from the dermal side (**Figure 2.3**), allowing for good resolution of dermal vascular structures and the epidermis. Additionally, the sample can be cleared, allowing for volumetric images of the entire structure with minimal attenuation. Several clearing methods were attempted, however, the methanol/methyl salicylate method described yielded the best results. Researchers interested in optimizing other clearing methods are directed towards these reviews[145,156,157]. If clearing, it is suggested to fully image the sample prior to clearing, as the method can damage the fluorophores and/or the structure. Further, the imaging should be completed as soon as possible after clearing, as the fluorescence may fade within days.

For simplicity and accessibility, this protocol utilized the simplest media blends found in previous literature[47,173]. Although there are many advantages to using simple media blends, the limitations of this choice are also recognized. Other groups have studied the effects of specific media components on epidermal and dermal health and found that other media additives[187], such as external free fatty acids/lipids, enhance the stratum corneum of the epidermis and improve the skin barrier function. Although our immunofluorescent markers show appropriate differentiation and stratification in the epidermis, depending on the studies being conducted, additional media optimization may be needed. Further, an extensive analysis of the epidermal BM was not conducted when evaluating the VHSEs presented here. The integrity of the BM is an important indication of skin equivalents; various groups have done research on the culture duration and its effect on BM markings[20] as well as analysis of fibroblast presence and added growth factor effects on BM expression[119]. It is important to note that analysis of the BM component should be evaluated and optimized when using this protocol.

In this protocol is described a procedure for VHSE generation, demonstrating results after 8 weeks at ALI. VHSE cultures have been cultured up to 12 weeks at ALI without noticeable change or loss of viability, and it is possible that they may be viable longer. Importantly, this protocol is readily adaptable to commonly available cell types, as demonstrated by the replacement of dermal fibroblasts with IMR90 lung fibroblasts. Depending on the researcher's need and available resources, the cell types and media blends on the culture can be adjusted, although more dissimilar cell types may require media optimization. In summary, these procedures are meant to provide clarity on the culture of VHSEs for the

study of skin biology and disease. To maximize accessibility, the protocol was developed this simple and robust using common equipment, cell lines, and reagents as a minimal effective approach that can be further customized to the specific needs of research studies.

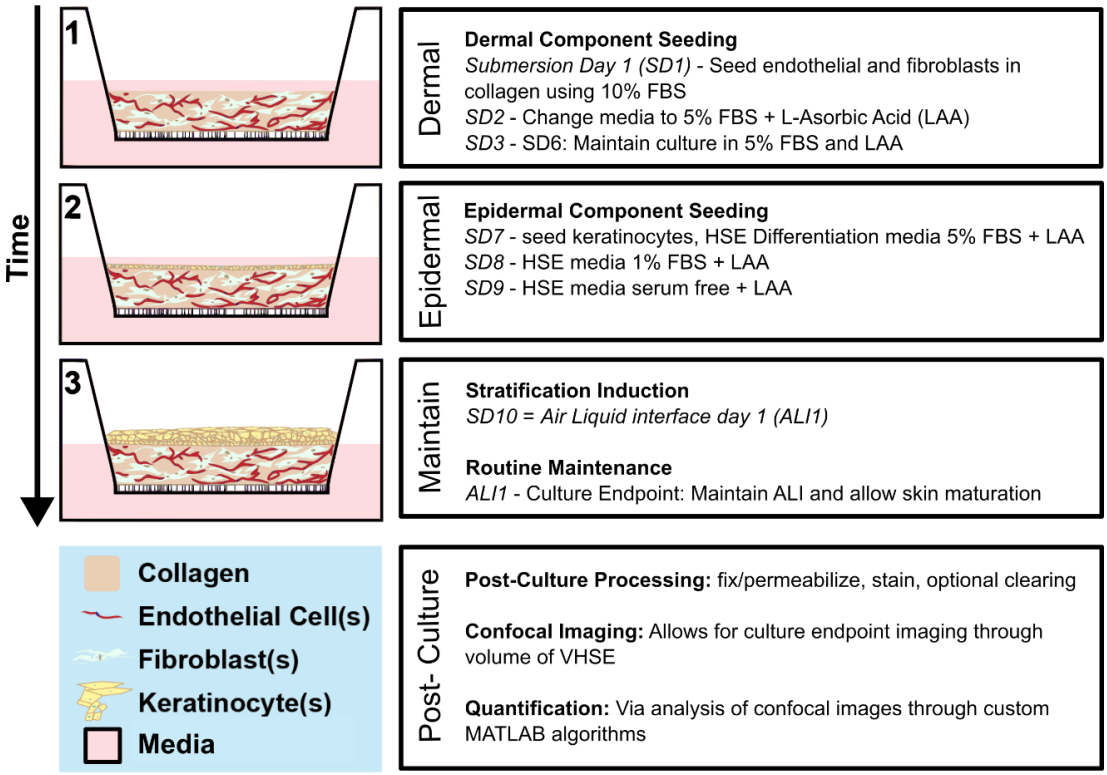

Figure 2.1. Schematic timeline of vascularized human skin equivalent generation. A) Shows progression of the VHSE model from 1) dermal component seeding, 2) keratinocyte seeding onto the dermal component, 3) epithelial stratification via air liquid interface and culture maintenance. Post-culture processing and volumetric imaging can be performed at culture endpoint. **B)** Camera images of hDF VHSE macrostructure in the culture inserts at their culture endpoint, 8 weeks. Various levels of contraction are normal for VHSEs; contraction can be reduced as protocol describes. (1 & 2) Less contracted samples. (3 & 4) More contracted samples still yield proper skin elements.

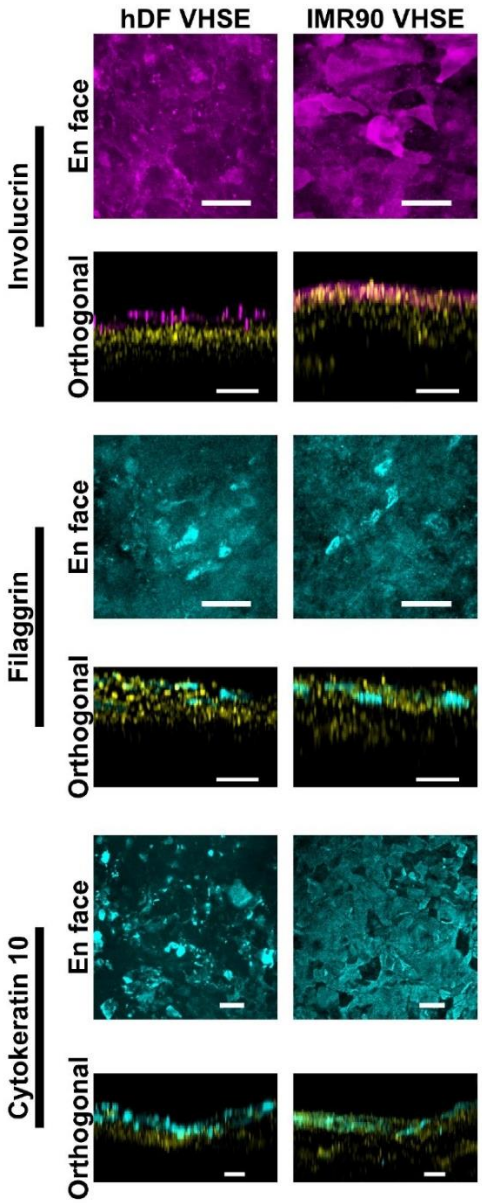

Figure 2.2 Epidermal characterization via immunofluorescent markers. All images were taken of VHSEs at 8wk culture timepoint via confocal microscopy. Corresponding staining methods are described in protocol step 6. Proper epithelial markers are present in both hDF VHSEs (left column) and IMR90 VHSEs (right column). Involucrin and Filaggrin are late differentiation markers of keratinocytes and demonstrate that the epidermis is fully stratified in both VHSE types. Cytokeratin 10 is an early differentiation marker which is identifying suprabasal layers in the VHSEs. Nuclei are shown in orthogonal views in yellow. En face and orthogonal max projection images were rendered via computational software; Images are individually scaled with background subtraction and median filtering for clarity. Scale bars are 100 μm. (Primary and secondary antibodies with in-house blocking buffer recipe are given in **Table 2.3**).

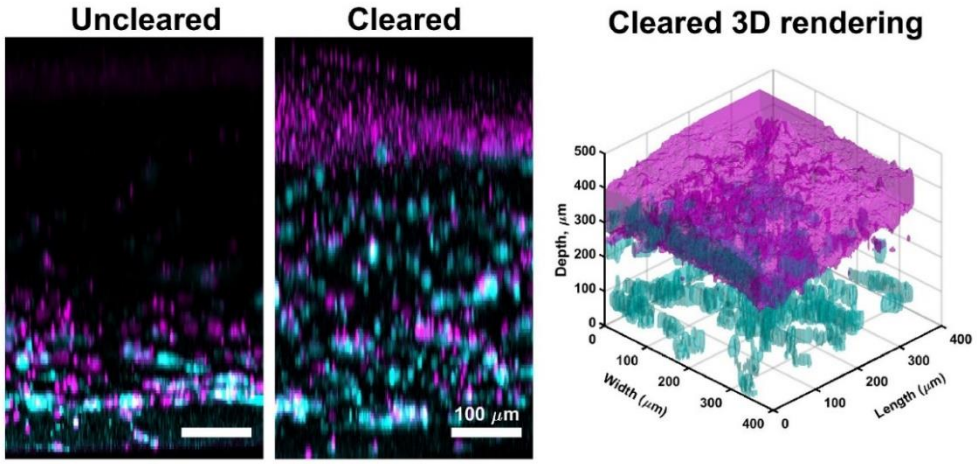

Figure 2.3. Comparison of uncleared vs. cleared VHSE. This VHSE was generated with IMR90s and images were taken at 4wk culture timepoint via confocal microscopy. Collagen IV is shown in cyan; Nuclei are shown in magenta; magenta in the cleared 3D rendering represents consolidation of nuclei in the epidermal layer of the VHSE. The uncleared VHSE image is an example of laser attenuation in thicker VHSE constructs, through clearing (methanol and methyl salicylate) the whole construct can be imaged with little/no laser attenuation from the dermal side of the construct. Imaging settings including laser line, gain, and pinhole were lowered for cleared VHSE to reduce oversaturation. Clearing and imaging were completed as described in steps 6 & 7 in the protocol. Orthogonal max projection images and 3D rendering were completed with computational software, 3D rendering was generated from cleared construct images. Images are individually scaled with background subtraction and median filtering for clarity. Scale bars are 100 μm.

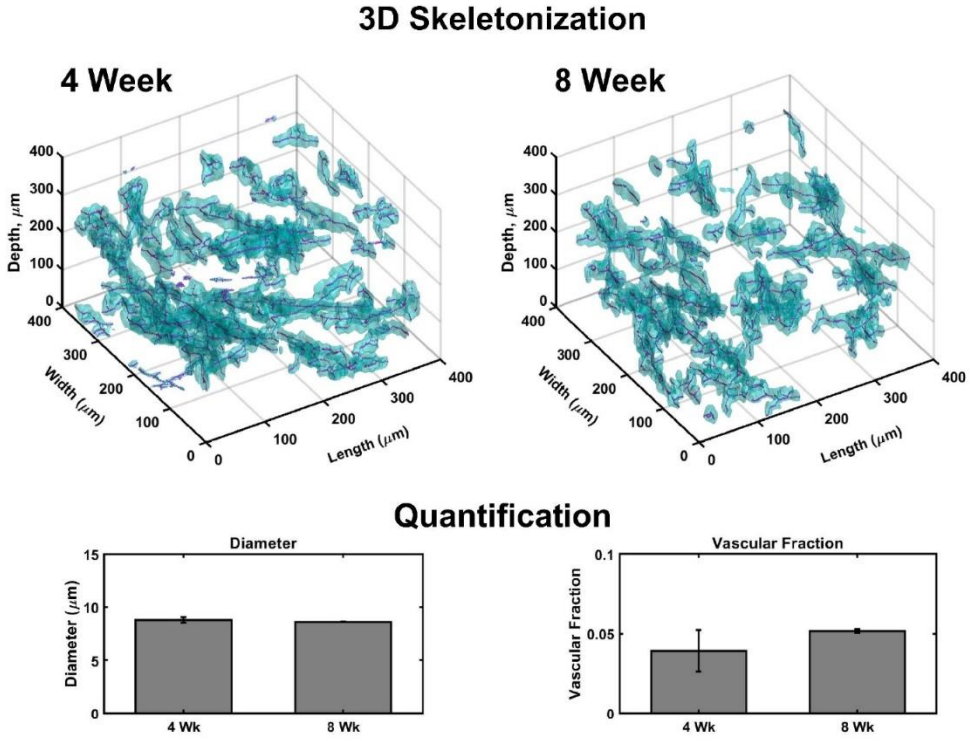

Figure 2.4. Three-Dimensional analysis of vasculature within VHSEs. Volumetric images taken via confocal microscopy enable vascular parameter quantification at the culture endpoints through computational image analysis. From VHSE sub-volumes, detection of Collagen IV stain (cyan) marks endothelial walls of vasculature and allows for segmentation of vascular based on collagen IV location; segmentation data is then skeletonized, and the center of each vessel is found (magenta). Examples of 3D skeletonization are shown for 4 week and 8 week IMR90 VHSE samples, un-cleared. Resulting data of an IMR90 VHSE experiment set was used to calculate the vessel diameters and the vascular fractions for four sub-volumes (each 250 μm in the z-direction) within each construct, data was averaged per VHSE and further averaged per culture timepoint. These data show the vascular network homeostasis spanning 4 and 8 week culture durations with diameters relevant to in vivo human skin[188], and the vascular fraction within the same order as in vivo human skin[189] (vascular fraction in collagen constructs has been shown to be customizable[144] and could be further optimized for increased values). Data is represented as means ± standard error mean (S.E.M); n = 3 for each timepoint.

Media	Components
Human Dermal Fibroblast cell line (hDF)	DMEM HG 5% Fetal Bovine Serum (FBS) 1% Penicillin/Streptomycin (P/S)
IMR90 Fibroblast cell line	DMEM/HAM'S F12 50:50 10% FBS 1% P/S
HMEC-1 Endothelial cell line	MCDB131 Base medium 10% FBS 1% P/S L-Glutamine [10 mM] Epidermal Growth Factor (EGF) [10 ng/mL] Hydrocortisone [10 µg/mL]
N/TERT-1 Keratinocyte cell line	K-SFM media base 1% P/S Bovine Pituitary Extract (BPE) [25 µg/mL], from K-SFM supplement kit Epidermal Growth Factor (EGF) [0.2 ng/mL], from K-SFM supplement kit $CaCl_2$ [0.3 mM]
Human Skin Equivalent (HSE) Differentiation	3:1 DMEM: Ham's F12 1% P/S 0.5 µM Hydrocortisone 0.5 µM Isoproterenol 0.5 µg/mL Insulin

Table 2.1. Media recipes**.** Media recipes for 2D culture of the human dermal fibroblasts, IMR90 fibroblasts, HMEC-1, and N/TERT-1 keratinocytes are given. These recipes were used to expand cell lines before generating VHSEs. Human skin equivalent (HSE) differentiation media is used to generate VHSEs; a base recipe is given, during portions of submersion culture and stratification induction, tapering amounts of FBS should be added as described in protocol step 3. HSE recipe based on these sources[47,173].

Collagen stock concentration (C_s) :	**8**	**mg/mL**
Desired Volume (V_f):	**1**	**mL**
Normalizing NaOH Adjustment*:	**1**	**X**

*Each lot of collagen needs to be tested to determine the amount of NaOH needed to set pH 7.4

	Desired Collagen Concentration (mg/mL)			
	2	**3**	**4**	**5**
10X PBS (V_{pbs})	0.1	0.1	0.1	0.1
Collagen stock (V_s)	0.25	0.375	0.5	0.625
1N NaOH (V_{NaOH})	0.00575	0.008625	0.0115	0.014375
Media (V_{media})	0.64425	0.516375	0.3885	0.260625

Table 2.2. Collagen calculation reference table. Reference table gives commonly desired collagen concentrations calculated assuming an 8 mg/mL collagen stock concentration and a desired final volume of 1 mL. The equations used to calculate these amounts are given in protocol step 2.2. It is important to check pH for each collagen stock; if necessary, NaOH amounts should be added to achieve pH 7.4 (after PBS, NaOH, collagen stock, media are added). The protocol has been optimized for VHSEs using a 3 mg/mL collagen concentration; changes in collagen concentration may be necessary for different cell lines/desired end results[144].

Primary Antibody	Source	Concentration	Use
Filaggrin (AKH1) mouse monoclonal IgG	Santa Cruz; sc-66192 (200 µg/mL)	[1:250]	Late differentiation marker(Roger et al. n.d.)
Involucrin rabbit polyclonal IgG	Proteintech; 55328-1-AP (30 µg/150 µL)	[1:250]	Late terminal differentiation marker(Roger et al. n.d.)
Cytokeratin 10 (DE-K10) mouse IgG, supernatant	Santa Cruz; sc-52318	[1:350]	Suprabasal epidermal marker(Mieremet et al. 2017; Kim et al. 2018; El Ghalbzouri, Lamme, and Ponec 2002)
Collagen IV rabbit polyclonal	Proteintech; 55131-1-AP	[1:500]	Endothelial vascular wall(Xu and Shi 2014)
DRAQ 7	Cell Signaling; 7406 (0.3 mM)	[1:250]	Nuclear marker
Secondary Antibody	**Source**	**Concentration**	**Use**
Goat Anti-Rabbit IgG DyLight™ 488 Conjugated	Invitrogen; 35552 (1 mg/mL)	[1:500]	Collagen IV secondary
Anti-Rabbit IgG (H&L) (GOAT) Antibody, DyLight™ 549 Conjugated	Rockland Immunochemicals; 611-142-002	[1:500]	Involucrin secondary
Goat Anti-Mouse IgG (H&L), DyLight™ 488	Thermo Scientific; 35502 (1 mg/mL)	[1:500]	Filaggrin or Cytokeratin 10 secondary

BLOCKING BUFFER (500 mL)	
Reagent	***Amount***
ddH_2O	450 mL
10 x PBS	50 mL
Bovine Serum Albumin (BSA)	5 g
Tween 20	0.5 mL
Cold water Fish Gelatin	1 g
Sodium Azide (10% Sodium Azide in diH_2O)	5 mL (0.1 % final concentration)

Table 2.3. Primary and secondary antibodies with blocking buffer recipe. The listed antibodies and chemical stains were used for staining shown in **Figures. 2.2-4**. The staining was completed as given in protocol step 6 using the blocking buffer recipe listed here. Some optimizations of the staining concentrations and the duration may be required depending on the chosen culture techniques and the cell lines.

Acknowledgements

The authors thank Dr. Jim Rheinwald[154] and Dr. Ellen H. van den Bogaard[124] for their generous gift of N/TERT cell lines. This work was supported by the American Heart Association (19IPLOI34760636).

Supplementary material

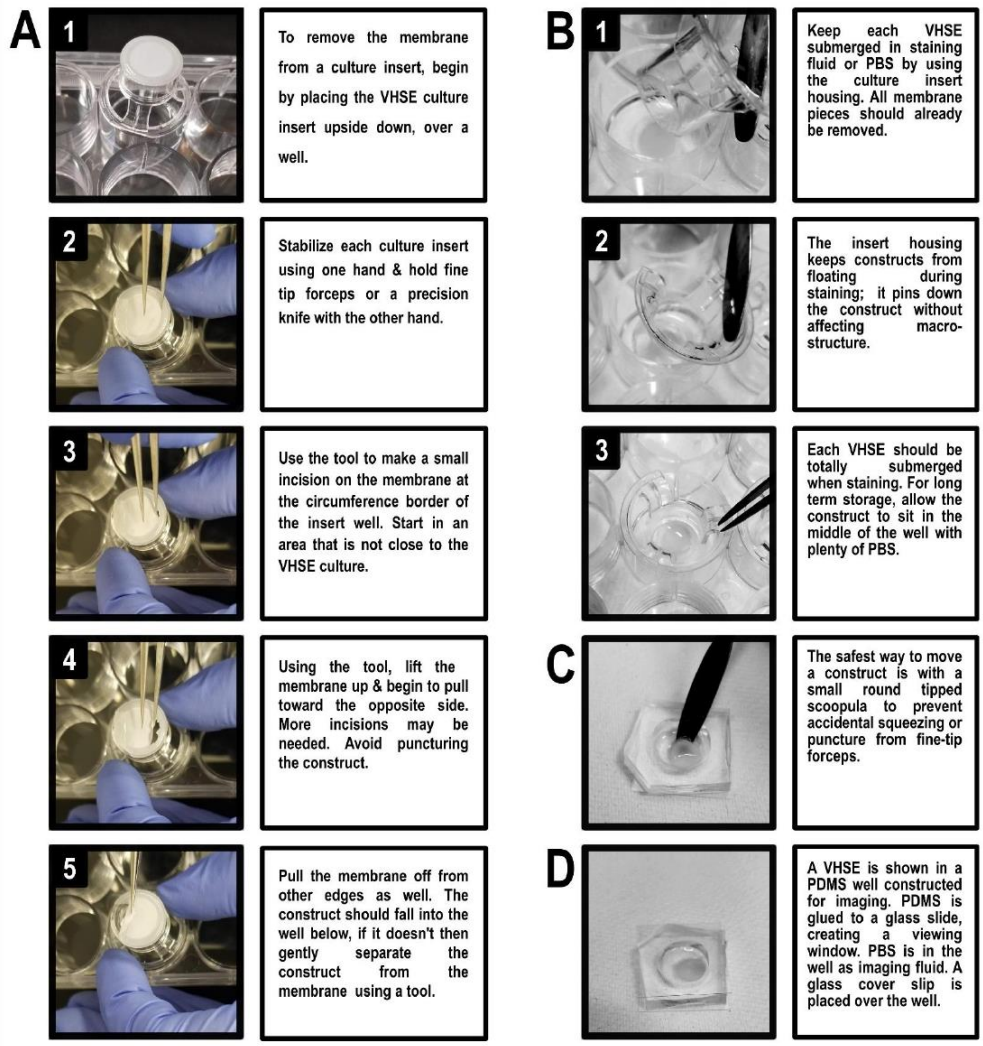

Figure 2.5. (Supplementary). **VHSE technical aid for handling.** Handling of VHSEs is challenging especially during fixation, processing, and staining. **A-D** corresponds to instructions in steps 5-7. **A** shows the technical handling of removing the porous membrane from a culture insert to ensure proper staining. **B** shows how to keep each VHSE submerged during staining and storage. **C** shows the safest and easiest way to move constructs to PDMS imaging wells. **D** shows a VHSE sitting in a PDMS imaging well: PDMS well is glued to a glass slide on the bottom, creating a window for imaging, a glass slide is placed on top to maintain the humidity through long imaging runs.

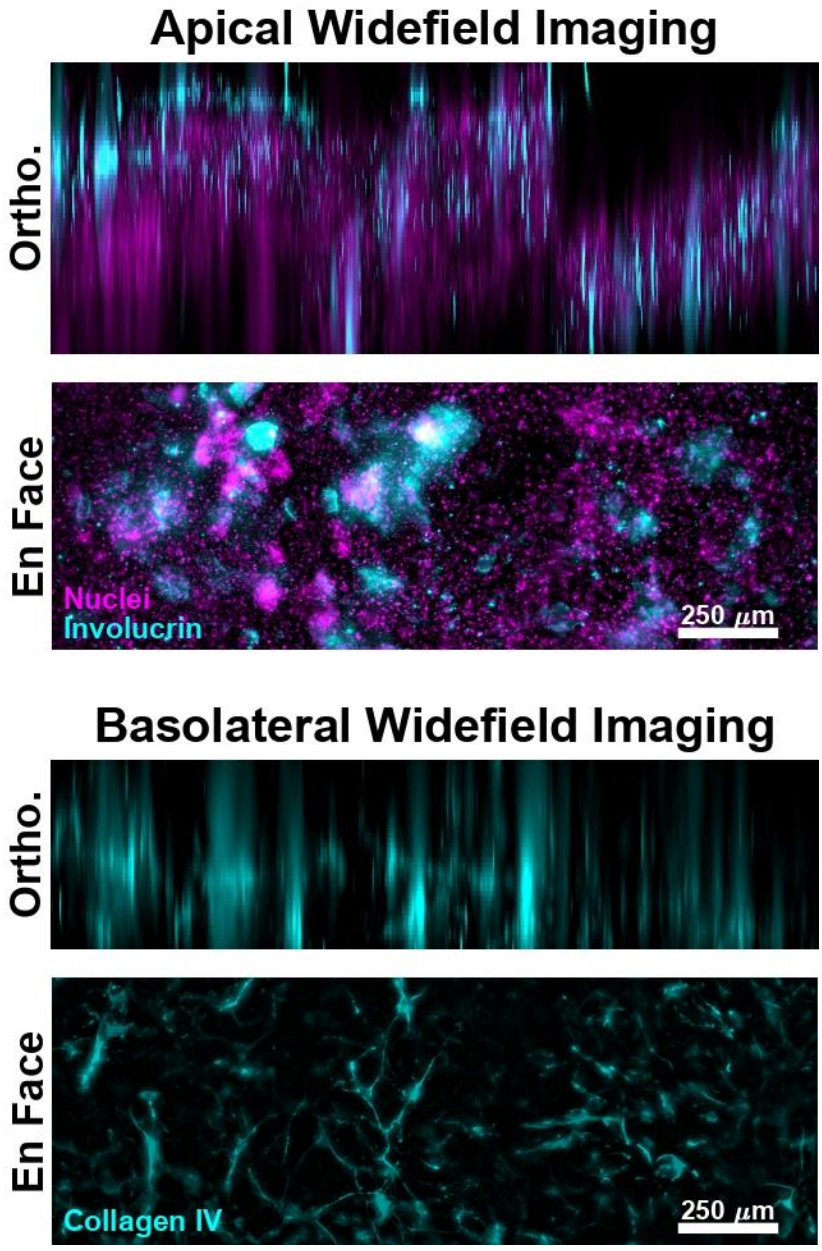

Figure 2.6. (Supplementary). **Standard widefield fluorescence microscopy can be used to assess VHSEs.** Widefield imaging can be used for volumetric imaging for routine assessment when laser scanning microscopy is not available. As an example, imaging of VHSEs from both the apical and basolateral aspects are shown as en face and orthogonal (Ortho.) maximum projections. (**Top**) The epidermis was imaged using involucrin and nuclei as markers. (**Bottom**) Dermal vasculature was imaged using collagen IV as a marker. Images are background subtracted for clarity. Out-of-plane light leads to the "streaking" or "flare" artifacts evident in the orthogonal views. Widefield imaging can be used for quantification but may require more image processing.

Chapter 3

Automated epidermal thickness quantification of tissue engineered human skin equivalents using optical coherence tomography

This work is in preparation for submission to the journal: Biotechniques

Martina M. Sanchez[1†] & Danielle Orneales[1†], B. Hyle Park[1], Joshua T. Morgan[1*]

Department of [1]Bioengineering

University of California, Riverside, CA 92521

([†]) Authors contributed equally to the work

Abbreviations:

HSE: Human skin equivalent; VHSE: vascularized human skin equivalent; OCT: Optical coherence tomography.

Abstract

Human skin equivalents (HSEs) are tissue engineered *in vitro* models of native human skin. They are used to study skin development, diseases, wound healing, and toxicity. The gold standard of analysis of human skin equivalents is histological staining and sectioning which both limits the understanding of three-dimensional components of the tissue and is an endpoint analysis technique. Optical coherence tomography (OCT) has been previously used to visualize *in vivo* human skin and *in vitro* models. OCT is a non-invasive imaging technique and enables real-time volumetric analysis of HSEs. The techniques presented here demonstrate the use of OCT imaging to track HSE epidermal thickness over 8 weeks of culture and improve upon previous processing of OCT images by presenting algorithms that automatically quantify volumetric thickness of the epidermis rather than taking manual measurements of a few representative images. Through this volumetric automated analysis of OCT images, HSE stability and development can be accurately tracked in real-time.

Method Summary

A method for automatic quantification of epidermal thickness of tissue engineered human skin equivalents using optical coherence tomography. Using this technique, epidermal thickness can be quantified throughout live culture in a non-invasive manner.

Keywords (5): human skin equivalent, vascularized human skin equivalent, optical coherence tomography, tissue engineering

Introduction

Tissue engineered human skin equivalents (HSE), also referred to as organotypic skin cultures (OSC) or full-thickness models, have been used to study skin development, cytotoxicity, healing, and disease[11,113,121,190]. Typically, they are analyzed post-culture through sectioning and histology. These methods of analysis conceal the three-dimensionality of the *in vitro* constructs and do not allow for real-time assessment of epidermal thickness during the long culture periods that HSE require (3-10 weeks). Increased availability of volumetric imaging provides an opportunity for HSE research; however, the three-dimensional analysis can be laborious. As an example, optical coherence tomography (OCT) has been used before to analyze native human skin[182,183,191,192] and a few *in vitro* skin models non-invasively[181,184,193–195]. OCT and other non-invasive live imaging techniques[183,191,195] allow for time-tracking of culture health and progression which is especially important when using HSEs for wounding, development, and aging studies[194]. Further, as a non-invasive technique, OCT avoids disruption of sample morphology, which can occur during histology[181,194].

Typically, when prior OCT studies that have investigated epidermal thickness in humans and in HSE models, the common thickness calculation is acquired by manually measuring then averaging a few (3-5) pre-defined OCT line scans (A-lines), and it is unclear how many OCT images (B-frames) are taken into account[193,194]. Further, due to this manual selection, there is potential for bias introduction from the investigator(s). Here we present a technique for automated analysis of epidermal thickness in tissue engineered HSE using live, non-invasive OCT imaging, including optimized OCT imaging procedures and

automated image analysis algorithms. These results were further validated against post-culture fluorescent confocal imaging and epidermal thickness quantification.

Materials & Methods

Skin Equivalent Generation

IMR90s (human lung myofibroblast; passage 18; ATCC), human microvascular endothelial cells (HMEC1; passage 7; ATCC), and N/TERT-1 human keratinocytes (passage 7; a gift from Dr. Jim Rheinwald[154] and Dr. Ellen H. van den Bogaard[124]) were routinely maintained at 5% CO_2 and 37 °C. Culture media was as follows: IMR90 fibroblasts: DMEM/F12 50:50, 10% fetal bovine serum (FBS), 1% penicillin/streptomycin (P/S); HMEC1: MCDB131 base medium, 10% FBS, 1% P/S, 10 mM L-Glutamine, 10 ng/mL Epidermal Growth Factor (EGF), 10 μg/mL Hydrocortisone, N/TERT-1: K-SFM media base, 1% P/S, 25 μg/mL Bovine Pituitary Extract , 0.2 ng/mL EGF, and 0.3 mM $CaCl_2$. Vascularized human skin equivalents (VHSEs) were generated in culture inserts (12 well size; 0.4 micrometer pore; PET membrane; Corning, Corning, NY) as previously described[48]. Briefly, to generate the dermal portion of the VHSE, 120 μL of acellular Type I collagen (3 mg/mL) was seeded onto the insert membrane and allowed to gel for 30 minutes. IMR90s and HMEC1 cells were suspended in a Type I collagen matrix (3 mg/mL) at 75,000 and 750,000 cells/mL, respectively. 250 μL of cellular collagen was seeded onto the acellular component and allowed to gel for 30 minutes, then submerged in growth media (1:1 complete HMEC1 media and complete IMR90 media, at 10% FBS total). 24 h after collagen seeding, media was changed to 5% FBS complete IMR90 media and supplemented with 100 μg/ml L-ascorbic acid (L-AA). The dermal component was cultured for 7 days with the 5% FBS media blend. To establish the epidermis, on day 7 of dermal culture, N/TERT-1s (170,000

cells/construct) were seeded onto the dermal surface and cultured to confluence for 3 days. On day 8 of culture media was changed to 1% FBS HSE differentiation media[48] (3:1 DMEM/F12, 1% P/S, 0.5 μM Hydrocortisone, 0.5 μM Isoproterenol, 0.5 μg/mL Insulin) with a supplement of100 μg/mL L-AA. On day 9 of culture, media was changed to serum free HSE media with 100 μg/mL L-AA, this media blend was used until culture endpoint as maintenance media. Surrounding wells were filled with PBS to promote controlled humidity throughout culture and during OCT imaging. At day 10 of culture, VHSEs were brought to air-liquid interface (ALI) and cultured with routine media supplemented with L-AA at 100 μg/mL and maintained for 8 weeks (for every media change, fresh L-AA supplement was used)[48]. All media and timepoints for media changes are as previously described[48].

Imaging

Imaging occurred at weeks 2, 3, 4, 5, 7, 8 of the air-liquid interface culture period. To ensure sterility during OCT imaging and prevent optical artifacts caused by the plastic well plate lid, residual media at the air-liquid interface, and condensation, specific procedures were followed. Culture plates were equilibrated at room temperature with the lid off in a sterile biosafety cabinet for 20 minutes after being removed from the incubator, reducing condensation. Immediately prior to imaging, the constructs were checked for any residual media at the air interface of the VHSE, and it was removed with aspiration if necessary while maintaining media below the culture insert. Even with the removal of visible media from the epidermal surface, the sample remained moist and reflective. To minimize reflective effect of the epidermal surface and well plate lid, the sample arm of the OCT system was tilted at 15°, reducing reflection while maintaining an adequate sample

illumination for structural imaging. During OCT imaging, constructs were at room temperature for a maximum of two hours; no loss of sample viability was observed.

OCT imaging was conducted with a FC/APC fiber optics based spectral domain optical coherence tomography (SD-OCT) system centered at 1310 nm. Through SD-OCT, the reference arm remains stationary, and the interference pattern is detected in a spectrally resolved manner on a line scan camera. Light is sent into a circulator and then to an optical splitter that splits the light between the reference and sample arms. The reflected light from each arm travels back through the splitter where it interferes and is redirected by the circulator to the detection arm. Here, the light is collimated, dispersed by a grating, and focused onto a line scan camera. A galvo mirror system in the sample arm is controlled by the image acquisition program and performs raster scanning of the optical beam for 2D and 3D imaging. Technical settings for data acquisition were as follows: scanning area 4 mm x 4 mm (-1 V x 1 V); 4096 A-lines per B-frame, 400 B-frames per volume, 10 volumes averaged per construct. Resulting image size was 4096 x 512 x 512 voxel

Fixation, staining, and confocal imaging

After 8 weeks of ALI, VHSEs were processed as previously described[48]. Briefly, samples were fixed and permeabilized at culture endpoint: 5 minute pre-fix with 4% paraformaldehyde in PBS then 1 h fix with 0.5% Triton X-100 and 4% paraformaldehyde in PBS at room temperature. For staining, primary antibodies used were Filaggrin (AKH1) mouse monoclonal IgG (sc-66192, 1:250 dilution, Santa Cruz Biotechnology, Santa Cruz, CA), Involucrin rabbit polyclonal IgG (55328-1-AP, 1:250 dilution, Proteintech Group, Rosemont, IL), Cytokeratin 10 (DE-K10) mouse IgG supernatant (sc-52318, 1:350 dilution, Santa Cruz Biotechnology), then DRAQ7 was used as a nuclear counterstain (7406, 12 μM

final concentration, Cell Signaling, Danvers, MA). All sample staining was completed in blocking buffer[48] at 4 °C for 48 h. Following staining, samples were imaged via confocal microscopy (TCS SPEII, Leica Microsystems, Buffalo Grove, IL).

Image processing and quantification

Confocal and OCT volumes were automatically segmented, and epidermal thickness was quantified using a custom algorithm implemented in MATLAB 2020b (MathWorks, Natick, MA). Example MATLAB code is included in the appendix. Briefly, the OCT algorithm was as follows. First, areas of high reflectance were removed by performing an initial intensity calculation, identifying pixels of outlier intensity, then updating the reference spectrum before recalculating the final intensity. To reduce speckle noise, a single volume of each HSE was obtained by averaging 10 volume scans, resulting in a single 16-bit 4096 x 512 x 512 voxel (3.9 x 2 x 3.9 mm) volume. From the single volume per sample, custom algorithms were used to detect the skin epidermis by identifying regions of high intensity. To smooth small gaps in the image, a morphological closing with a two-dimensional disk (40 voxel radius) followed by a Gaussian filter (standard deviation 1.5 x 8 x 1.5 voxels) was applied to the image volume. To segment the epidermis, hysteresis thresholding was applied with a high threshold of 16000 and a low threshold of 8000 or 4200 (thresholds empirically determined for this 16-bit dataset). The resulting binary volume was cleaned via area opening to remove small artifacts and a morphological closing with a (40 voxel radius disk). The bottom and top surfaces of the binary object were detected. Streaking artifacts, common in OCT imaging, presented as sharp peaks on the surfaces, and were removed via automatic detection of high gradients and local averaging. Volumetric thickness was calculated from the voxel difference between the top and bottom surfaces

scaled by the acquisition size (4 x 2 x 4 mm). For each volume, 30 A-lines were removed from left and right sides (1.4%) for each frame due to edge effects. Thickness average was calculated from imaging volumes of 3.9 x 2 x 3.9 mm.

For confocal, epidermal thickness was calculated from imaging volumes of ~3.3 mm x 370 μm x 250-400 μm (imaging depths were adjusted per sample but a consistent voxel size of 0.7 x 0.7 x 3 μm was used). A similar custom algorithm was applied to calculate epidermal thickness from confocal volumes. Briefly, noise was removed via a median filter (5x5 pixel kernel for epidermal specific markers and 3x3 kernel for nuclear markers) was applied to each XY-plane and intensities were scaled by linear image adjustment. Background auto-fluorescence was removed using a 20 voxel radius rolling ball filter on each XY-plane and the epidermis was segmented using hysteresis thresholding with values empirically determined for each fluorescent channel (for epidermal markers 3000 and 65000 were used while nuclei thresholds were set at 1150 and 64000; all images were 16-bit). Small artifacts and gaps in the epidermal binary volume were removed through morphological closing and opening with a disk structuring element (pixel radius 10) for epidermal stains and a sphere structuring element (pixel radius 8) for nuclear stain. Epidermal thickness was calculated from the binary epidermal volume scaled by the voxel size (0.7 x 0.7 x 3 μm).

Data Analysis

OCT imaging was performed at ALI week 2, 3, 4, 5, 7, and 8 (n = 4 technical replicates for every timepoint). Confocal imaging was completed on three of the same samples that were OCT imaged, after fixation and staining (n = 3). ANOVA followed by Tukey's HSD post-hoc test was used to test for statistically significant differences between

timepoints; and pairwise comparisons of 8 week confocal and OCT data were completed through two-tailed t-test. Significant differences ($p < 0.05$) are represented by a single asterisk.

Results & Discussion

The epidermis of both native and *in vitro* skin is highly reflective, producing a strong signal in OCT[183]. This allows for effective automatic segmentation of the epidermis, as demonstrated with our algorithm (**Figure 3.1 A**). Here, the higher threshold (8000 in this 16-bit dataset) limits the automated segmentation to the highly reflective epidermis. As validation, after culture the HSEs were fixed, stained, and confocal imaged for epidermal markers (Error! Reference source not found. **B**). Median thickness values for OCT from w eeks 2-8 and post-fixation confocal are shown in **Figure 3.1 C**. No statistically significant difference between the OCT timepoints and confocal thickness quantifications was found using the high threshold value, indicating stable culture morphology and agreement between the OCT and confocal modalities. The values obtained using the high threshold value (**Figure 3.1**) are similar to *in vivo* epidermal thickness determined by OCT found in young and aged humans at the forearm (young 71.8 ± 10 μm and aged 60.8 ± 7.4 μm, mean ± standard deviation)[194]. The confocal thickness values at week 8 are slightly low compared to the human epidermal thickness values found in literature[193,194] as well as the OCT measurements. This may be due to shrinkage of the epidermis during fixation, as formaldehyde-based fixations have been shown to reduce cell and tissue size[196]. Further, it is important to note that the *in vivo* thickness values were obtained manually, for example via measurement of five pre-defined positions in the OCT image and then the average of 5 measurements was calculated by a single user while the amount of volumes acquired is

unknown[194]. The automated method presented here eliminates the necessity of an investigator to manually determine thickness and enables automatic detection of every XY position in a volume.

Additionally, we observed a prominent reflective region immediately basal to the strongly reflective epidermis (**Figure 3.2 A**). This region can be efficiently segmented from the bulk of the dermis using a lower threshold value (4200 in this 16-bit dataset) and quantified (**Figure 3.2 B**). Using the lower threshold value, a significant difference in thickness was found between the 8-week timepoints of OCT and confocal measurements ($p < 0.05$). No significant variation was found among OCT measurements. The thickness values obtained using the lower threshold are similar to prior OCT studies in half-thickness skin equivalents at 22 days (100-200 μm, as reported by the authors)[181] These higher thicknesses may represent inclusion of the basement membrane and reticular dermis[192], differences in epidermal morphology, or differences in quantitation methodology.

All data presented here was obtained for whole sample volumes. To demonstrate the increased dimensionality of the dataset, representative thickness heat maps of single samples analyzed with high and low thresholds are shown in **Figure 3.3 A**. To determine the volumetric stability of samples over time, interquartile range (IQR) of each sample is presented for both thresholds (**Figure 3.3 B**). IQR for all samples were similar from week 2-8 with no significant changes ($p < 0.05$), again demonstrating stability of the culture model. The small spread of IQRs show the spatial uniformity of the HSE epidermal volumes. These data combined with thickness values demonstrate both volumetric and temporal stability of the HSE epidermis. Importantly, tracking coverage and stability of the epidermis could be used to optimize HSE protocol steps including epidermal seeding and timepoints of air

liquid interface establishment, which can be technically challenging[48] . It can additionally be used to investigate developmental, disease, and aging models over time, and for wound tracking *in vitro*, as previously shown[184,193].

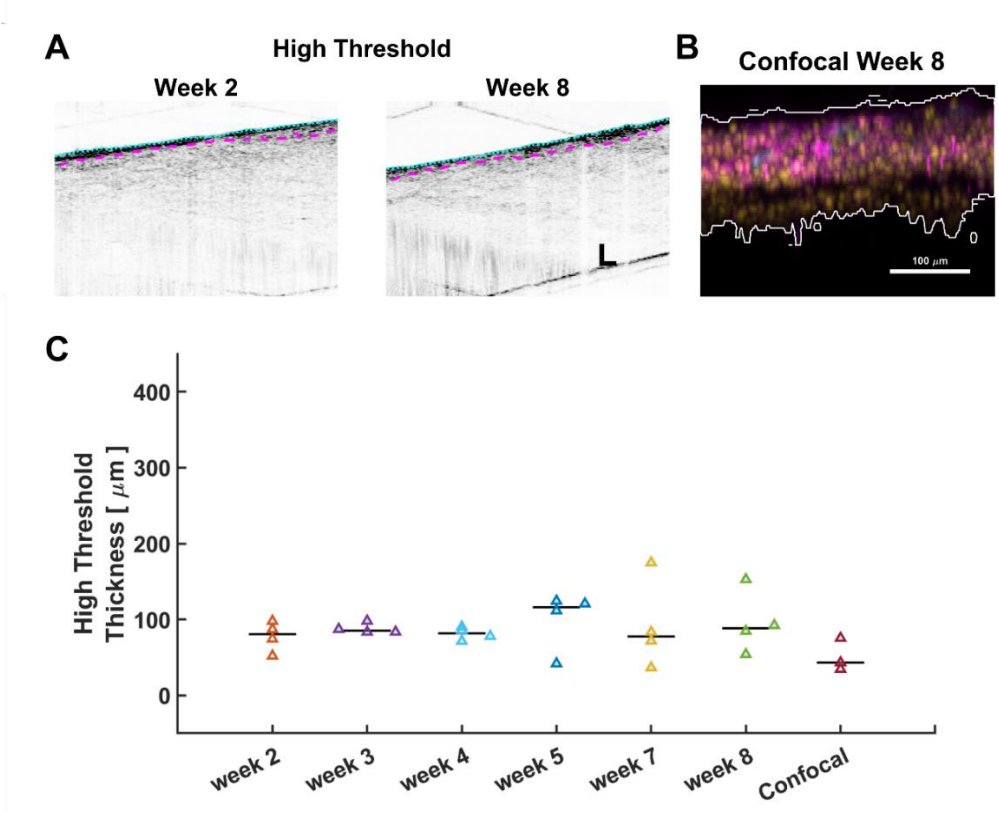

Figure 3.1. A) Representative OCT cross-sectional image at week 2 and week 8 with example of high threshold used for detecting the lower epidermal boarder. Upper boarder detection is marked with a cyan dotted line, lower boarder marked with a magenta dashed line. Scalebar is 200 μm. **B)** Representative confocal cross-sectional image from a HSE culture fixed and stained after 8 weeks of culture. **C)** Epidermal thickness comparison of HSEs gathered from OCT imaging and automatically analyzed with high threshold to detect the lower epidermal boarder. Culture weeks 2, 3, 4, 5, 7, 8 shown with thickness determined from OCT images. The right most data point shows the thickness calculated from confocal images from week 8 after post-culture fixation and staining for comparison. Confocal thickness is similar to thickness calculated from OCT, but the formaldehyde fixation necessary for post-culture processing may have shrunken epidermal features. No statistically significant differences ($p < 0.05$) were found between OCT time points but by pairwise comparison, OCT wk8 and confocal wk8 thickness values are different ($p<0.05$). Data shown as median (black bar) and individual data points (triangles). Data points are the thickness average of whole epidermal volume per sample.

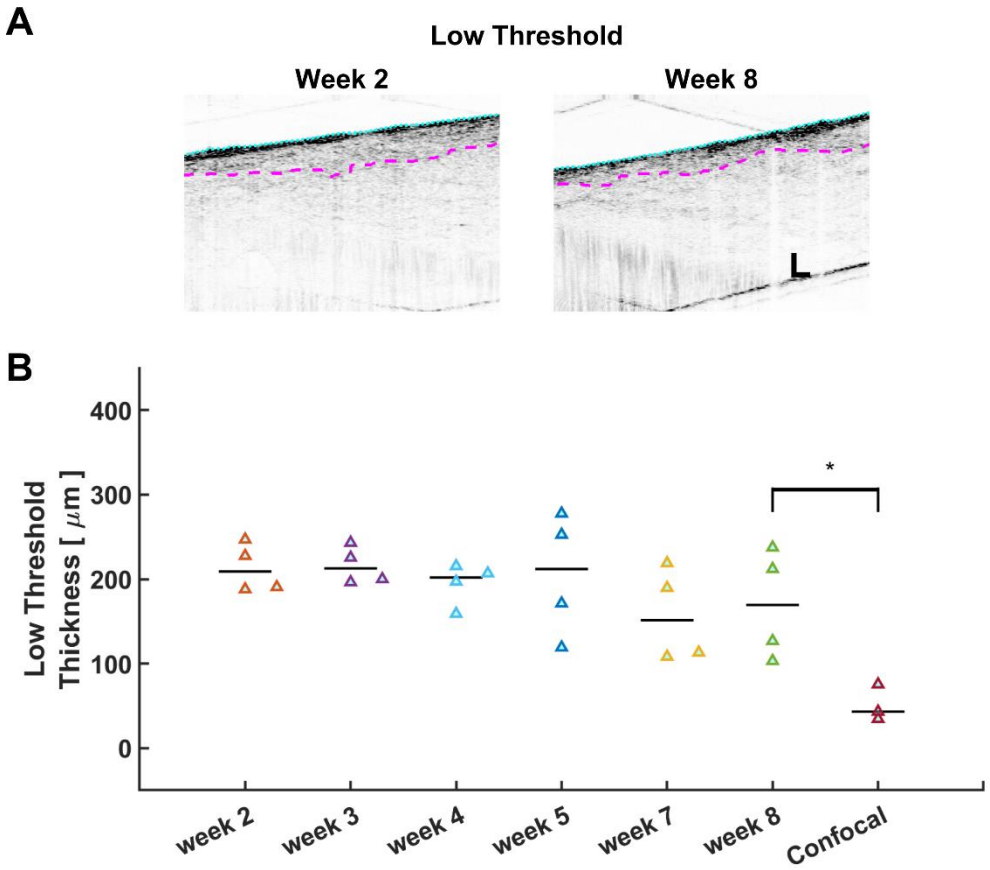

Figure 3.2. A) Representative OCT cross-sectional image at week 2 and week 8 with example of low threshold used for detecting the lower epidermal boarder. Thresholds are adjustable depending on strictness of detection desired. Upper boarder detection is marked with a cyan dotted line, lower boarder marked with a magenta dashed line. Scalebar is 200 μm. B) Epidermal thickness comparison of HSEs gathered from OCT imaging and automatically analyzed with low threshold. Culture weeks 2, 3, 4, 5, 7, 8 shown with thickness determined from OCT images. The right most data point shows the thickness calculated from confocal images from week 8 after post-culture fixation and staining for comparison. Confocal thickness quantification is lower than the OCT thickness quantified at wk8 with the low threshold ($p < 0.05$). Data shown as median (black bar) and individual data points (triangles).

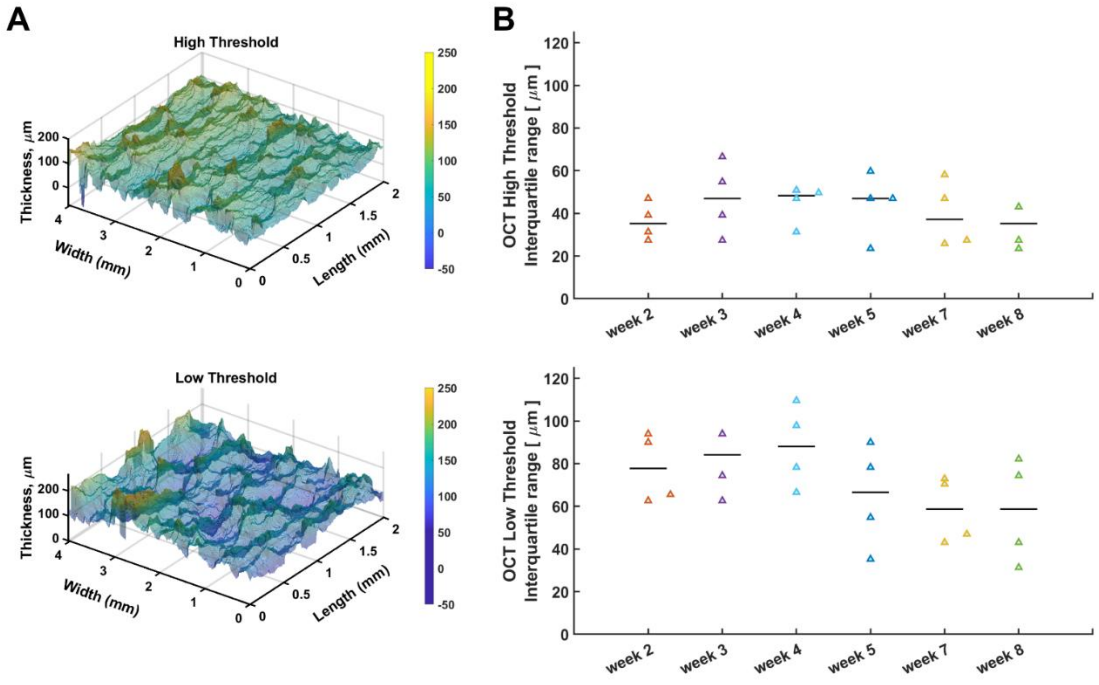

Figure 3.3. A) Representative heat maps of epidermal thickness values across whole OCT volumes for both threshold values. B) Interquartile range of thickness values per OCT imaging volume for each sample over time. No significant changes were detected ($p < 0.05$). Data shown as median (black bar) and individual data points (triangles).

Conclusion

This work establishes an automated epidermal thickness tracking technique for tissue engineered skin constructs using image analysis of OCT images. Detailed OCT scanning parameters and analysis algorithms are provided. To demonstrate the method, HSEs were generated and their epidermal thickness was tracked throughout the air-liquid interface culture period of 8 weeks. Quantification of epidermal thickness was completed through custom MATLAB algorithms using two different threshold values (high and low). Thickness values (**Figure 3.1 C** and **Figure 3.2 B**) were similar to those found from epidermal thickness calculated from *in vivo* human skin OCT studies and prior manual OCT studies of half-thickness skin models[193,194]. Values obtained with the high threshold analysis were similar

to our validation with post-fixation confocal imaging (**Figure 3.1 C**). We conclude that the method of automated epidermal thickness detection using the non-invasive OCT system is a simple and straightforward indication of HSE development throughout culture.

Future perspective

The preservation of volume in engineered tissue is necessary for analysis of their three-dimensional morphology, and automated analysis is needed to reduce bias and enable collection of larger data sets. The non-invasive nature of OCT is a powerful tool for assessing engineered cultures over time, especially important in HSEs given the long culture times relative to conventional culture models.

Author contributions

MM Sanchez generated skin constructs, imaged via confocal microscopy, prepared the manuscript, and portions of the analysis code. DN Ornelas performed all OCT imaging and wrote processing code with supervision from BH Park. MM Sanchez, DN Ornelas, and JT Morgan developed thickness detection algorithms.

Financial & competing interest disclosure

This work was supported in part by the American Heart Association (19IPLOI34760636). The authors have nothing to disclose.

Acknowledgements

The authors thank Dr. Jim Rheinwald and Dr. Ellen H. van den Bogaard for their generous gift of N/TERT cell lines.

Chapter 4

Development of a vascularized human skin equivalent with hypodermis for aging studies

This work is in preparation for submission to the journal: Biomaterials

Martina M. Sanchez[1], Joshua T. Morgan[1*]

Department of [1]Bioengineering

University of California, Riverside, CA 92521

Keywords: HSE, VHSE, AVHSE, human skin equivalent, adipose and vascularized human skin equivalent, tissue engineering, tri-layer skin equivalent, self-assembly, full thickness skin models, wound healing, chronic wounds, plexus, scaffold, aging

Abbreviations: HSE: Human skin equivalent; VHSE: vascularized human skin equivalent; PDMS: polydimethylsiloxane; AVHSE: Adipose and vascular human skin equivalent

Introduction

Human skin provides essential physical protection, immune barrier function, and thermal regulation[121]. As humans age, there is a decline of skin function, including loss of barrier function and healing capacity[2]. This correlates with structural changes including decreased vasculature, decreased dermal elasticity and collagen organization, stiffening, lower hydration, reduced dermal and hypodermal (or subcutaneous fat) volumes[3,4,8–11,13,15–18,22–24,197]. These detrimental effects of natural aging are compounded by extrinsic aging factors such as Ultraviolet A (UVA; 320-400 nm)[198] photoaging that occurs with sun exposure[2,6,199,200]. With normal aging, the skin has fine wrinkles, is smooth and pale, and has lower elasticity but with photoaging skin is course, rough, even lower elasticity, and has changes in pigmentation[3,8]. Particularly, UVA sun exposure mainly damages by generation of reactive oxygen species[198,201] and effects the dermis and hypodermis but can also interact with epidermal keratinocytes to induce mRNA and protein expression of inflammatory cytokines, including IL-6[201]. Further, UVA exposure to human skin has demonstrated decreased expression of subcutaneous adipokines such as adiponectin[202–204]. These effects are harmful since adipokines have been found to benefit wound healing and anti-inflammatory skin properties and the hypodermis as a whole contributes to thermal regulation, skin elasticity and regeneration[39,205]. UVA exposure additionally degrades the dermal matrix through decreases in procollagen synthesis and increases in MMP-1, -3, and -9 expression[202–204]. Photoaged skin has also displayed reduced dermal vasculature and dermal connective tissue breakdown and disorganization in human explant cultures[9,198,204,206–208].

Human Skin Equivalents (HSEs) are *in vitro* tissue models that have been previously used for studies on photoaging, wound healing, skin development, alopecia, disease, stem cell renewal, and toxicology screening research[47,53,116,117,119,122,124–126,132,136,163,174,175,187,209–213]. The models rely on self-assembly of skin components within an appropriate matrix. Traditionally-used animal models such as rabbits, pigs, mice, and rats have different anatomies than humans, and so do not accurately model human healing/recovery rates[111,124]. In contrast, the self-assembly development of HSEs has similar development pace to normal human skin[47,119,122,126,163].

Although HSE research has been well developed to recreate the dermal and epidermal layers using fibroblasts and keratinocytes, more complex co-culture systems are needed to recapitulate human anatomy more closely[214] and mimic trophic factor exchange of different cell populations *in vivo*[128–130,136,214]. Building on our previously published protocol generating vascularized human skin equivalents[48], here we demonstrate inclusion of a hypodermis, which we term adipose and vascular human skin equivalent (AVHSE), and demonstrate suitability for UVA photoaging studies. Multi-cellular skin models similar to this AVHSE have been previously explored but with fewer cell types, much shorter culture lengths, and little to no volumetric characterization[137,215–217]. UV photoaging has been previously investigated with *in vitro* skin models of the epidermis[213], keratinocytes in 2D[218], dermal fibroblasts in 2D[62,219], adipose components in 2D[39,203]. This work combines photoaging studies with comprehensive *in vitro* skin models and allows for volumetric quantification of epidermal, dermal, and hypodermal components through volumetric imaging (confocal). Further, the effects of photoaging on adipokine and inflammatory cytokines have been quantified using ELISA.

Materials and Methods

Cell Culture

AVHSE cultures were created using N/TERT1 human keratinocytes (hTERT immortalized; gift of Dr. Jim Rheinwald and Dr. Ellen H. van den Bogaard[124,154]), HMEC1 human microvascular endothelial cells (SV40 immortalized; ATCC, Manassas, VA; #CRL-3243)[220] primary adult human dermal fibroblasts (HDFa; ATCC #PCS-201-012), and ASC52telo adipose derived mesenchymal stem cells (hTERT immortalized; ATCC #SCRC-4000)[221]. All cell lines were routinely cultured at 37 °C and 5% CO2; all media blends given in supplemental **Table 4.1**. N/TERT1 cells have been shown to maintain normal epidermal behavior in previous organotypic skin cultures[124,126,154]. N/TERT1 cells (passages: 8,10,16,19) were grown up in a modified K-SFM media blend including K-SFM base, 0.2 ng/mL endocrine growth factor (EGF), 25 μg/mL bovine pituitary extract, 0.3 mM $CaCl_2$, and 1% penicillin/streptomycin (PCN/STREP). N/TERT1 were routinely passaged once 30% confluence was met to prevent undesired differentiation in 2D cultures[154]. HMEC1 cells were grown up in MCDB1 base media with 10 mM L-glutamine, 1 μg/mL hydrocortisone, 10 ng/mL EGF, 10% FBS, and 1% PCN/STREP. HMEC1 cells at passages 9 and 11 were used. HDFa were originally expanded in fibroblast basal media supplemented with fibroblast growth kit as outlined by manufacturer. For short term expansion upon pull up for AVHSE cultures, HDFa cells (all passage 4) were grown up in DMEM (4.5 g/L glucose) supplemented with 5% FBS and 1% FBS. ASC52telo was used to generate the adipose component of the skin construct. Cells were originally expanded in mesenchymal stem cell basal media (ATCC #PCS-500-030) with added supplements from a mesenchymal stem cell growth kit (ATCC #PCS-500-040) and G418 at 0.2 mg/mL; this was used as the 2D culture

media until adipogenesis induction. Adipogenesis media[222,223] (recipe given in **Table 4.1**) was administered once ASC52telo plates were ~90% confluent (ASC52telo passages: 6, 8, 10 were used for AVHSEs).

Collagen Isolation: Rat-tail collagen

Collagen Type I was isolated from rat tail tendons as described previously [144,146–148]. In summary, tendons were extracted from rat tails (Pel-Freez Biologics, Rogers, AR), washed in 1 x DPBS and soaked in acetone for 5 minutes, 70% isopropanol for 5 minutes, and then dissolved in 0.1% glacial acetic acid for at least 72 hours rocking at 4 °C. After dissolving, collagen was centrifuged at ~20,000 x *g* for 1 hour and the supernatant was frozen at -80 °C and lyophilized for long term storage at -80 °C. When ready to use, collagen was dissolved in 0.1% glacial acetic acid to 8 mg/mL and stored at 4 °C.

Construct Fabrication Overview

Generation of AVHSE cultures includes four main steps, shown graphically in **Figure 4.1**Error! Reference source not found.: 1) adipogenesis, 2) dermal seeding and maturation, 3) epidermal seeding, and 4) air liquid interface; total duration is approximately twelve weeks: adipose differentiation (3 weeks), dermal maturation (< 1 week), epidermal seeding (2-3 days), air liquid interface exposure (8-9 weeks). Collagen gel was used to create the hypodermis and dermal layer of the AVHSE constructs in 12-well culture inserts (translucent PET, 3 μm pore; Greiner Bio-One, Monroe, NC; ThinCerts #665631), similar to previously used[119,122,124,126,163,174,175]. In all cases, final collagen concentration was 3 mg/mL[48].

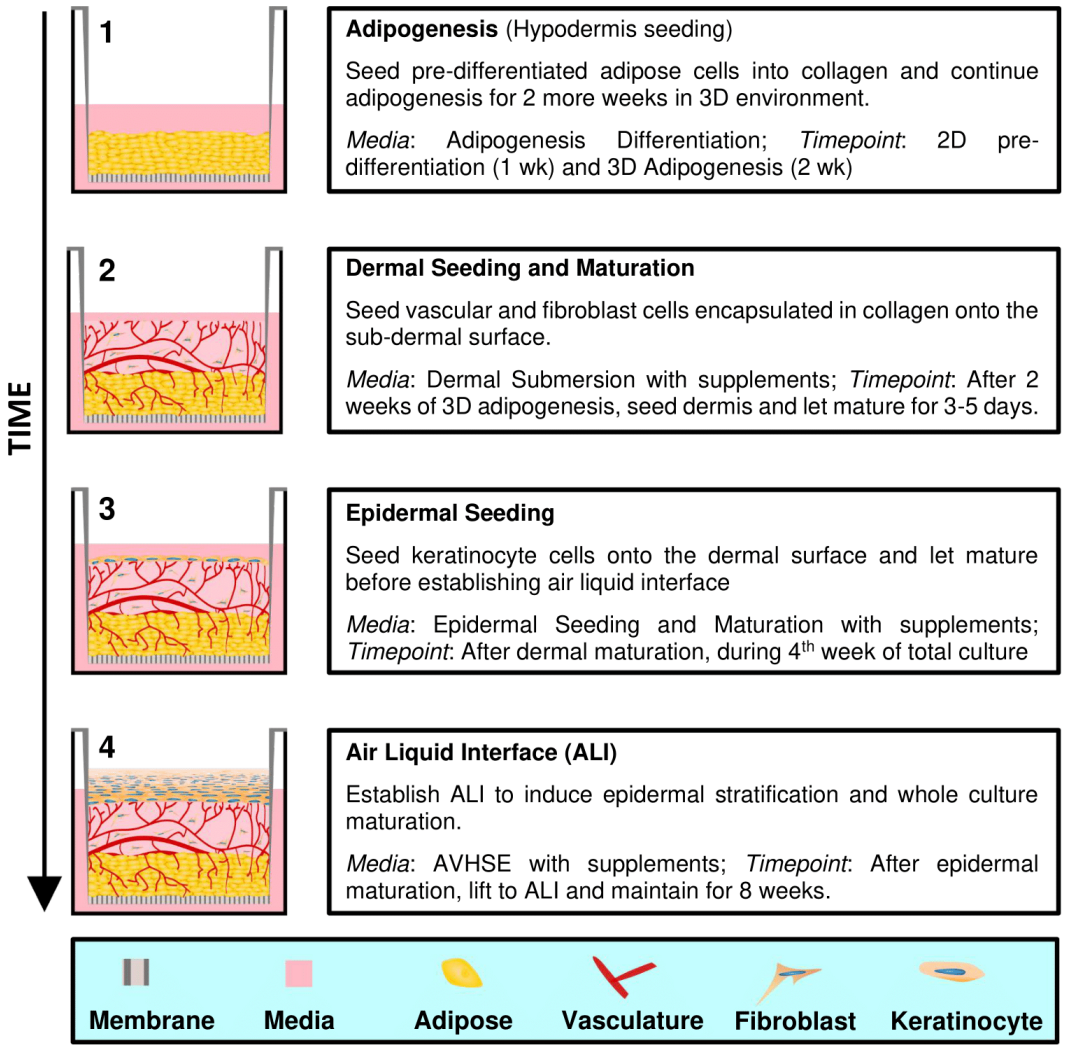

Figure 4.1 AVHSE generation. There are four main steps in creating an AVHSE: 1) Adipogenesis, 2) Dermal seeding and maturation, 3) Epidermal seeding, 4) Air liquid interface. Cartoons on the left show cross-sectional representations of AVHSE during each step.

Adipogenesis and hypodermal seeding

ASC52telo cells were grown to >90% confluent and adipogenesis was induced for 3 weeks (media blend given in **Table 4.1**), split between 1 week in 2D culture and 2 weeks in 3D culture. For 3D culture, ASC52telo cells (750,000 cells/mL of collagen) were encapsulated in 125 µL of 3 mg/mL collagen and seeded into the culture insert. After

gelation, constructs were submerged with adipogenesis media (~0.5 mL and ~1 mL of media in the culture insert and well, respectively). Media was added to the insert chamber first to prevent detachment of the collagen from the membrane). Media was changed every 2-3 days until dermal seeding.

Dermal/Epidermal Seeding & Air Liquid Interface

Media was aspirated from each well and 250 µL of 3 mg/mL collagen with HMEC1 and HDFa cells (750,000 and 75,000 cells/mL of collagen, respectively) was seeded onto the hypodermis then moved to 37 ℃ for gelation, done quickly to ensure cells remained suspended during gelation. After gelation, constructs were submerged with dermal submersion (DS) media (**Table 4.1**) supplemented with 3% FBS, 2 ng/mL vascular endothelial growth factor (VEGF-A; Peprotech, Cranbury, NJ; #100-20) and 100 µg/mL L-ascorbic acid (L-AA; Thermo Fisher Scientific, Waltham, MA). Media was changed every 2-3 days with fresh L-AA[48,144,149]. After 3-5 days of growth in submersion, DS media was aspirated and epidermal seeding and maturation media (ESM) supplemented with 1% FBS and 100 µg/mL L-AA (1.5 mL added to each well). N/TERT1 keratinocyte cells were immediately seeded dropwise at 170,000 cells per insert (~1.13 cm^2 growth area) using 200 µL of their maintenance media, K-SFM. One/two days after epidermal seeding, media was changed to AVHSE media and the cultures were lifted to Air Liquid Interface (ALI) within 8-24 h, with longer times leading to increased contraction[48]. The process to establish ALI was outlined previously[48]; typical ALI was established with ~1 mL of media. Following ALI establishment, media was changed every 2-3 days with AVHSE media and supplemented with 100 µg/mL L-AA and 30 nM selenium (sodium selenite; Fisher; CAS #10102-18-8).

Cell Line or Culture period	Recipe	Notes	Corresponding timepoint
N/TERT 1	K-SFM base media 1% P/S Bovine Pituitary Extract (BPE) [25 µg/mL] Epidermal Growth Factor (EGF) [0.2 ng/mL] $CaCl_2$ [0.3 mM]	Media recipe based off of these references[124,154]. BPE and EGF are from the K-SFM supplement kit.	Maintenance culture
HMEC1	MCDB131 base media 10% FBS 1% P/S L-Glutamine [10 mM] Epidermal Growth Factor (EGF) [10 ng/mL] Hydrocortisone [10 ug/mL]	Media recipe as recommended by manufacturer.	Maintenance culture
Human Dermal Fibroblasts	DMEM HG base 5% FBS 1% P/S	Media used for short term expansion in 2D. For longer expansion, use the manufacturer recommendation.	Maintenance culture
ASC52telo	Mesenchymal Stem Cell Basal Medium 2% MSC supplement L-Alanyl-L-Glutamine [2.4 mM] G418 [0.2 mg/mL]	MSC Basal Medium is from ATCC (ATCC PCS-500-030); To make the complete medium the MSC growth kit (ATCC PCS-500-040) is added. MSC supplement from the growth kit contains: 2% FBS, 5 ng/mL rhFGF basic, 5 ng/mL rhFGF acidic, 5 ng/mL rhEGF.	Maintenance culture

Adipogenesis Differentiation media	DMEM/HAM's F12 base media 3% FBS 3-isobutyl-1-methyl-xanthane (IBMX) [250 µM] Indomethacin [10 µg/mL; 28 µM] Insulin [5 µg/mL] Dexamethasone [1 µM] D-pantothenate [34 µM] Biotin [66 µM]	Media recipe is based on prior work[222,223]. IBMX, Insulin, and Dexamethasone stocks stored at -20 °C. Indomethacin, D-pantothenate, and Biotin stocks stored at 4 °C.	3 weeks prior to dermal seeding. 1 week for 2D culture and 2 weeks for 3D culture.
Adipocyte Maintenance Media **(serum free)**	DMEM/HAM's F12 base media Insulin [5 µg/mL] Dexamethasone [1 µM] D-pantothenate [34 µM] Biotin [66 uM]	This media blend is not used by itself for AVHSE culture, but it is used to make dermal submersion media. Adipocyte maintenance media is adipogenesis differentiation media without IBMX or Indomethacin (a PPARγ agonist)[223]	Used indirectly for Dermal Submersion media.
Dermal Submersion (DS)	1:1 Serum Free Adipocyte Maintenance media and serum free HMEC1 media *Aliquot supplement:* 3% FBS *Daily supplements:* L-Ascorbic Acid [100 µg/mL], VEGF [2 ng/mL]	Dermal submersion media is half adipocyte maintenance media and half HMEC1 media with supplement changes. Media prepared serum-free and used as base for ESM and AVHSE media.	During week 4 of culture: dermal cells are seeded and dermis is maturing.

Epidermal Seeding and maturation media (ESM)	Dermal submersion media with $CaCl_2$ [1.44 mM] *Aliquot supplement:* 1% FBS *Daily supplements:* L-Ascorbic Acid [100 µg/mL]	Media used for addition of N/TERT1s, shares base with DS and AVHSE media.	During week 4 of culture: epidermal cells are seeded and maturing.
AVHSE media	Dermal submersion media with $CaCl_2$ [1.44 mM] *Daily supplements:* L-Ascorbic Acid [100 µg/mL], Selenium (sodium selenite) [30 nM]	AVHSE media is serum free. L-ascorbic acid is important for collagen synthesis by fibroblasts, collagen stability, vessel wall integrity and barrier function.[26,112,150–153]	~4 weeks into whole culture and through culture endpoint. Media is used for ALI.

Table 4.1 Media used for 2D and 3D culture.

Photoaging of AVHSE's

After completing 7 weeks at ALI, AVHSEs were exposed to UVA to model photoaging (PA). A UVA LED array was established by drilling a 5 mm through-hole at center of each well in the plate lid, and inserting a 385nm/80mcd LED (VAOL-5GUV8T4; VCC, Carlsbad, CA); 1 LED directly illuminated each insert (**Figure 4.7**, supplemental**Error! Reference source not found.**). Four LEDs were powered in series with 14.2 V, providing a 0.45±0.15 mW/cm^2 dose as measured by a UV sensor (UVAB Digital Light Meter, #UV513AB, General Tools & Instruments, Secaucus, NJ). LEDs were measured and replaced every 3-4 days. AVHSEs were exposed to UVA for 2 hours daily for one week using an automated timer. UV dose and exposure was determined within values of prior work on human skin equivalents, cell monolayers, and mouse models[38–40,198,202,203,213].

ELISA (Adiponectin, IL-6, MMP-1)

AVHSE culture supernatant was collected at the end of ALI week 8 from controls and photoaged samples. Samples were centrifuged and frozen at -80 °C until use. ELISAs were performed for human Adiponectin, Interleukin-6 (IL-6), and total matrix metalloproteinase (MMP-1) according to the manufacturer's protocol (Proteintech Group, Rosemont, IL). Each sample was assayed in duplicate with standards completed for each run. For color development, tetramethylbenzidine (TMB)-substrate exposure was 20 minutes for Adiponectin and IL-6 and 15 minutes for MMP-1 at 37 °C in the dark. After stop solution was administered, color development was immediately measured at 450 nm with a correction wavelength of 630 nm using a SpectraMax M2 Multi-mode microplate (Molecular Devices, San Jose, CA) and corrected against a run zero standard. Four parametric logistic curves (4PLC) fits were used and values below detection limit were set to zero. Sample

sizes varied for each assay due to sample availability and are as follows: Adiponectin: for each condition n = 10, r^2 = 0.9975; IL-6: control n=6 and photoaged n = 8, r^2 = 0.9993; MMP1: control n = 7 and photoaged n = 10, r^2 = 0.9954 (9 values) and 0.91 (7 values)). Values that were not within range of the curve fit or standards were included in analysis.

Post-culture immunostaining and confocal microscopy

After culture, samples were pre-fixed in 4% paraformaldehyde for 5 minutes then fixed for 1 hour in 4% paraformaldehyde and 0.5% Triton X100 at room temperature. Samples were washed three times in PBS then stored at 4 °C until staining. For staining, culture insert membranes were removed using forceps, as described previously[48]. The staining and imaging processes were completed in four phases: epidermal, dermal vasculature, adipose, and post-clearing (**Table 4.2**). The nuclear marker DRAQ7 was administered during the epidermal staining phase and was used until imaging was completed. Imaging orientation of the AVHSEs were dependent on stain phase (**Table 4.2**). For staining, primary and secondary antibody stain solutions were made up in blocking buffer (**Table 4.2**). All samples were stored at 4 °C in PBS until imaging.

To image each fixed sample, custom polydimethylsiloxane (PDMS; Dow Corning, Midland, MI)-molds were punched specific to each sample size and adhered to glass slides[48]. Samples were placed in the well with PBS and covered with another glass slide to preserve humidity while imaging. As AVHSE are too thick for direct confocal imaging throughout the structure, each sample was imaged in both apical and basal orientations. Stains were multiplexed to laser excitations in cases of minimal overlap (e.g. epidermal and subdermal stains), and this was confirmed through the sequential staining process.

Staining Sequence			
Stain/Imaging phase	**Staining/Processing Used**	**Imaging Orientation**	
1. Epidermal	Cytokeratin 10, Involucrin, DRAQ7	Apical (epidermal)	
2. Dermal Vasculature	Collagen IV	Basal (hypodermis)	
3. Adipose	BODIPY	Basal (hypodermis)	
4. Post-clearing	(Methanol dehydration, methyl salicylate clearing)	Basal (hypodermis)	
Epidermal Staining			
Antibody/Stain	**Information & Source**	**Concentration**	**Notes**
DRAQ 7	Cell Signaling;	[1:250]	Nuclear marker
Cytokeratin 10			Suprabasal epidermal marker
Primary	Cytokeratin 10 (DE-K10) mouse IgG, supernatant. Santa Cruz; sc-52318		
Secondary	Goat Anti-Mouse IgG (H&L), DyLight™ 488. Thermo Scientific; 35502 (1 mg/mL)	[1:500]	
Involucrin			Stratum Corneum, terminal differentiation marker[117]
Primary	Involucrin rabbit polyclonal IgG. Proteintech; 55328-1-AP (30 µg/150 µL)		
Secondary	Anti-Rabbit IgG (H&L) (GOAT) Antibody, DyLight™ 549 Conjugated. Rockland Immunochemicals; 611-142-002	[1:500]	
Dermal Vasculature Staining			
Collagen IV			Vascular basement membrane
Primary	Collagen IV rabbit polyclonal Proteintech; 55131-1-AP	[1:500]	

Secondary	Anti-Rabbit IgG (H&L) (GOAT) Antibody, DyLight™ 549 Conjugated. Rockland Immunochemicals; 611-142-002	[1:500]	
Adipose Staining			
BODIPY	Difluoro{2-[1-(3,5-dimethyl-2H-pyrrol-2-ylidene-N)ethyl]-3,5-dimethyl-1H-pyrrolato-N}boron; dissolved in 200 proof EtOH, CAS: 121207-31-6; Aldrich; 790389	[2 μM]	Mature adipocyte marker
Clearing			
Methanol	CAS: 67-56-1	4 baths, 10 min. each	For sample dehydration.
Methyl Salicylate	CAS: 119-36-8	4 baths, 5 min. each	For sample clearing
Blocking Buffer Recipe			
Reagent		***Amount***	
ddH_2O		450 mL	
10 x PBS		50 mL	
Bovine Serum Albumin (BSA)		5 g	
Tween 20		0.5 mL	
Cold water Fish Gelatin		1 g	
Sodium Azide (10% Sodium Azide in diH_2O)		5 mL (0.1 % final concentration)	
All exposure for stains and antibodies: 48 hours, stationary, 4 °C			

Table 4.2. Staining sequence, antibodies, and blocking buffer used.

Tissue Clearing

After completing staining and imaging phases 1-3, constructs were cleared via methyl salicylate with methanol dehydration. Constructs were dehydrated in methanol with 4x 10 min baths then cleared in methyl salicylate with 4x 5 min baths. Constructs were stored in methyl salicylate and imaged via confocal microscopy on the same day, as detailed previously[48].

Quantitative epidermal analysis

Thickness of epidermal layers were automatically detected from confocal images via thresholding differences using a custom analysis algorithm designed in MATLAB (MATLAB 2018b; Mathworks, Natick, MA). For each sample, five confocal sub-volumes in the center of the AVHSE were used to detect thickness (total volume of 1.85 X 0.37 X 0.25-0.4 mm; imaging depths were adjusted per sample but a consistent voxel size of 0.7 X 0.7 X 3 μm was used). An average thickness was found for each XY position to obtain a volumetric thickness indication rather than from a single cross-sectional position or from max projection. Briefly, epidermis was localized using DRAQ7, cytokeratin 10, and involucrin stains. Noise was removed using median filters applied to each XY-plate and intensities were scaled by linear image adjustment. Background auto-fluorescence was removed using rolling ball filters on each XY plane and the epidermis was segmented using hysteresis thresholding. Gaps in the epidermal binary volume were removed via morphological closing and opening with a disk structuring element. The resulting binary volume created a computational plane from which the top and bottom difference could be calculated and metrically scaled by appropriate voxel size. Intensity comparison of the suprabasal markers, Cytokeratin 10 and Involucrin was completed across all samples using confocal images. A maximum projection image of

ten positions per sample was generated and average intensity values were calculated. For all epidermal quantification, three biological replicates with one/two technical replicates each were used for analysis, $n = 5$ for each group.

Quantitative dermal/hypodermal analysis

Adipose thickness, volume fraction (VF), and integrated intensity quantification was completed from 10 confocal sub-volumes per each sample (a total volume of 3.7 X 0.37 X whole Z-axis or 0.35 mm). VF is an estimate of the volume that adipose takes up within the hypodermis and dermal space together. Volumetric thickness was calculated using localization of the BODIPY mature adipose marker, as described for epidermal thickness quantification. Integrated intensity of BODIPY was quantified via custom algorithms. Briefly, image sub-volumes were segmented and the resulting binary masks were used to isolate BODIPY stain from background noise and autofluorescence. The sum of raw intensity along the z-axis was calculated for each sub-volume within its binary map, then all sub-volume values were averaged as a metric of the whole sample volume. These data were gathered from images taken in the 3rd imaging phase (**Table 4.2**). Three biological replicates with two technical replicates each were used for analysis, $n = 6$ for each group.

Vascular quantification parameters of diameter, VF, and diffusion length (Rk) were determined from the average of 6 confocal sub-volumes per each sample (total volume of 2.22 X 0.37 X whole Z-axis or 0.35 mm). Using the Collagen IV marker from cleared AVHSE structures (4th imaging phase, **Table 4.2**), vessels were located through segmentation (using MATLABs built in image toolbox and custom and published functions[224,225]) and ultimately edge detection via an enhanced hessian based frangi filter written for vessel detection[166,226,227]. VF was determined using the resulting volume segmentation. After

locating vessel location, segmentation data was skeletonized through a fast marching algorithm[48,144,170–172] and the center of each vessel was found which allows for calculations of diameter and Rk (as completed previously[144]). Briefly, diameter was quantified by calculating the difference in pixel location of the vascular segmentation orthogonal to the vessel skeleton and Rk was obtained by determining the Euclidean distance between each point in the collagen volume and the nearest point on the network (values indicating the distance that encompasses 90% of the volume)[144] . The vascular processing algorithm is given in supplementary appendix chapter 4. Two biological replicates with two technical replicates each were used for analysis, $n = 4$ for each group.

Statistics

Biological and technical replicates are noted for each quantification. Pairwise comparisons of control v. photoaged samples were completed through two-tailed t-test. ANOVA followed by Tukey's HSD post-hoc test was used to test for statistically significant differences when applicable. Un-normalized data points are shown for comparison to tissue scale morphology. For statistical comparison, data were normalized to each biological control for epidermal, vascular, and adipose quantification. Significant differences of normalized data are plotted with $p < 0.05$ represented by a single asterisk; $p < 0.01$ represented by a double asterisk. Differences between ELISA values were run on raw data due to uneven biological/technical replicates; the same p-value representation is indicated.

Results

AVHSE enables tissue-scale studies of skin biology

AVHSEs and the analysis techniques presented here enable study of skin volumetrically and at the tissue scale. We have shown that AVHSEs recapitulate epidermal, dermal, and hypodermal morphologies (**Figure 4.2**) through co-localization of epidermal markers, vascular markers throughout the dermis, and co-localization of vascular and adipose markers in the hypodermis (**Figure 4.2**). The automated image analysis of the three skin compartments was completed on biologically large volumetric areas with minimum volumes of 1.85 x 0.37 x 0.25 mm to analyze the epidermis and up to 3.6 x 0.37 x 0.35 mm to analyze the hypodermis. Importantly, tissue analysis at this scale provides a higher degree of precision over histological analysis in understanding skin as a whole.

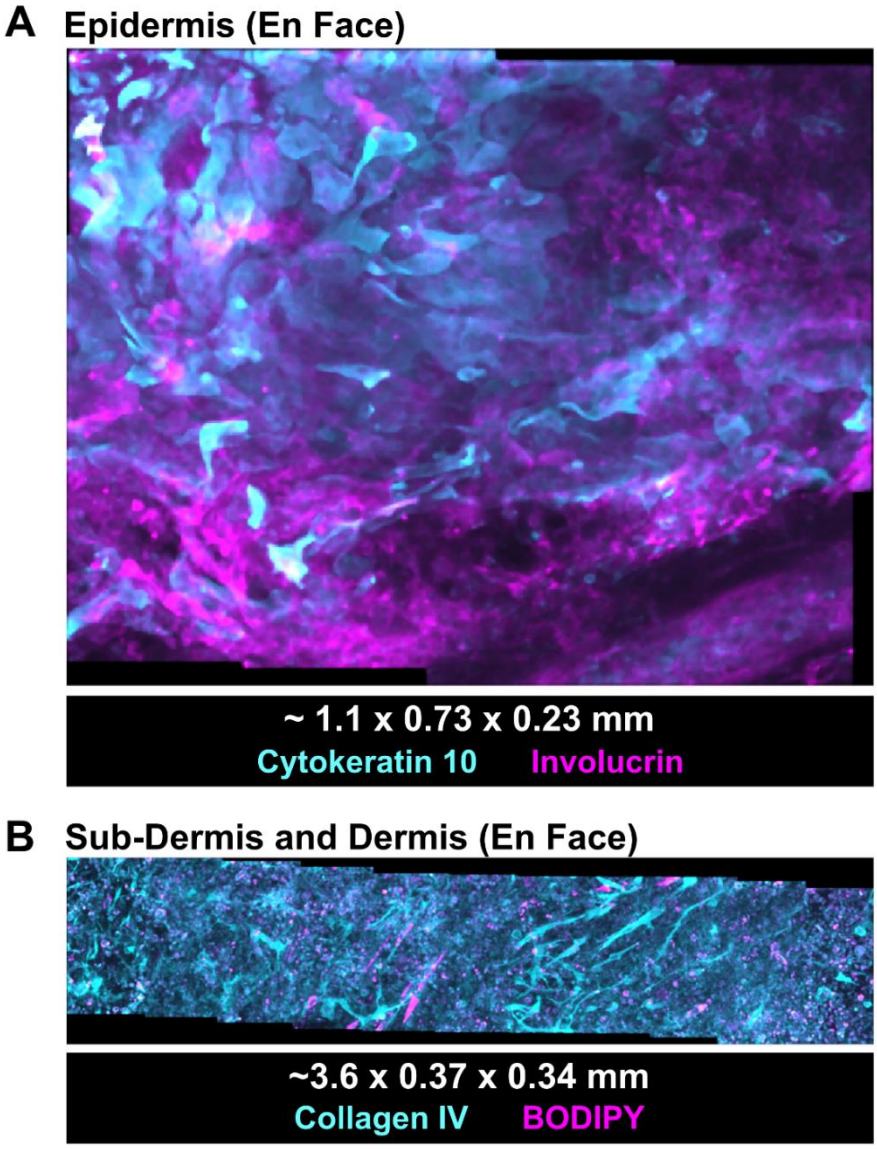

Figure 4.2 Large format, stitched max projections. A) Image details the epidermal layer and was acquired using a short working distance objective with a 0.7 x 0.7 x 0.5 µm voxel size. Cytokeratin 10 is a suprabasal epidermal marker shown in cyan. Involucrin is a stratum corneal marker shown in magenta. Images were taken in staining phase 1. B) Image details the sub-dermis and dermis. Importantly there is co-localization of adipose and vasculature stains that spans a length of 3.6 mm (approximately half of this representative AVHSE). Collagen IV marks vasculature in cyan. BODIPY marks lipid droplets secreted from mature fat cells (magenta). Images were taken in staining phase 3.

UVA photoaging alters adiponectin expression

Prior studies have demonstrated decreased adipokine production during photoaging, and adipokines are mediators of the dermal photoaging mechanism[203,228]. To test if the AVHSE cultures were similarly responsive to UVA, we measured production of adiponectin using ELISA. AVHSE cultures were prepared and maintained through ALI as described in the methods. After 7 weeks of ALI, AVHSE were exposed to 7 days of UVA (2 h/day, 385 nm, 0.45 ± 0.15 mW/cm^2), or left as controls. Media supernatant was collected from both photoaged and control samples after UVA exposure. Adiponectin expression was significantly reduced, in agreement with prior *in vivo* studies[203] (**Figure 4.3 A**). This was not accompanied by a general inflammatory response or increased matrix metalloproteinase-1 (MMP-1) presence, as indicated by stable IL-6 and MMP-1 expression (**Figure 4.3 B**).

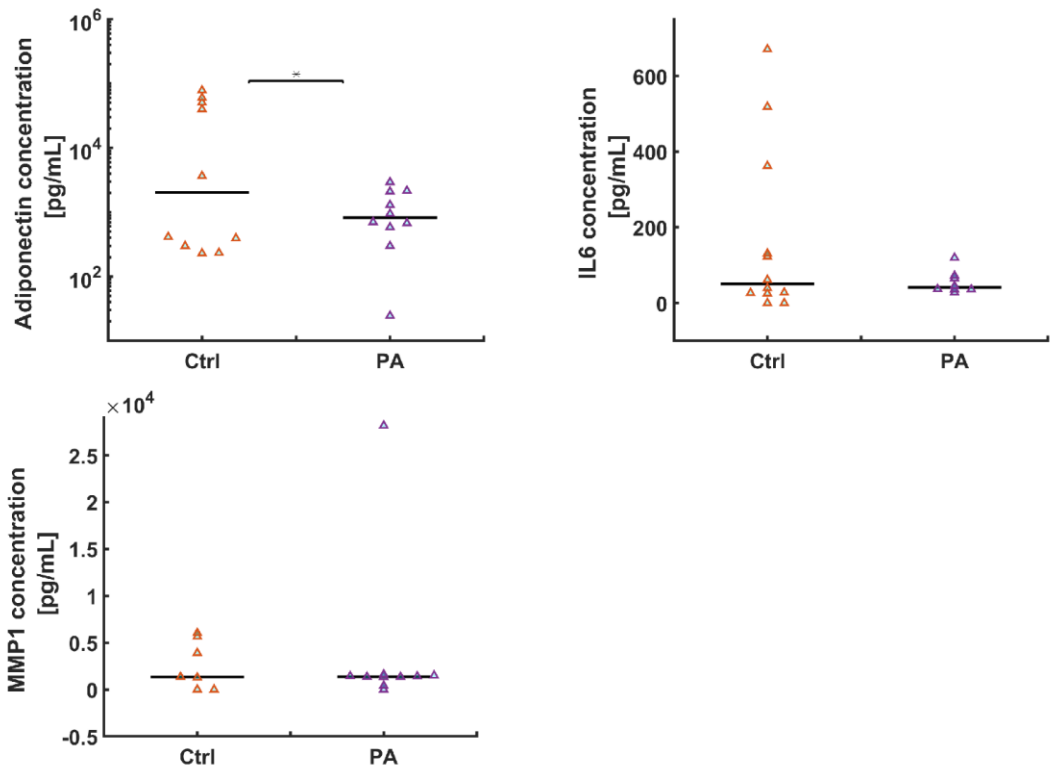

Figure 4.3. Cytokine evaluation from cell media was completed via sandwich ELISA. Cell media was collected after week 8 of culture. All values were corrected by a zero standard and values below detection limit were set to zero. All values were determined from four-parametric logistic curve fits. Sample sizes varied for each assay due to sample availability. (Adiponectin: for each condition n = 10; r^2 = 0.9975. IL-6: control n=6 and photoaged n = 8; r^2 = 0.9993; MMP1: control n = 7 and photoaged n = 10; r^2 = 0.9954 (9 values) and 0.91 (7 values)). Values that were not within range of the curve fit or standards were included here to maintain un-skewed results. A two-tailed t-test revealed a significant decline in the adiponectin secreted into media after photoaging AVHSEs. Median bars are indicated by black bar and data points are triangles.

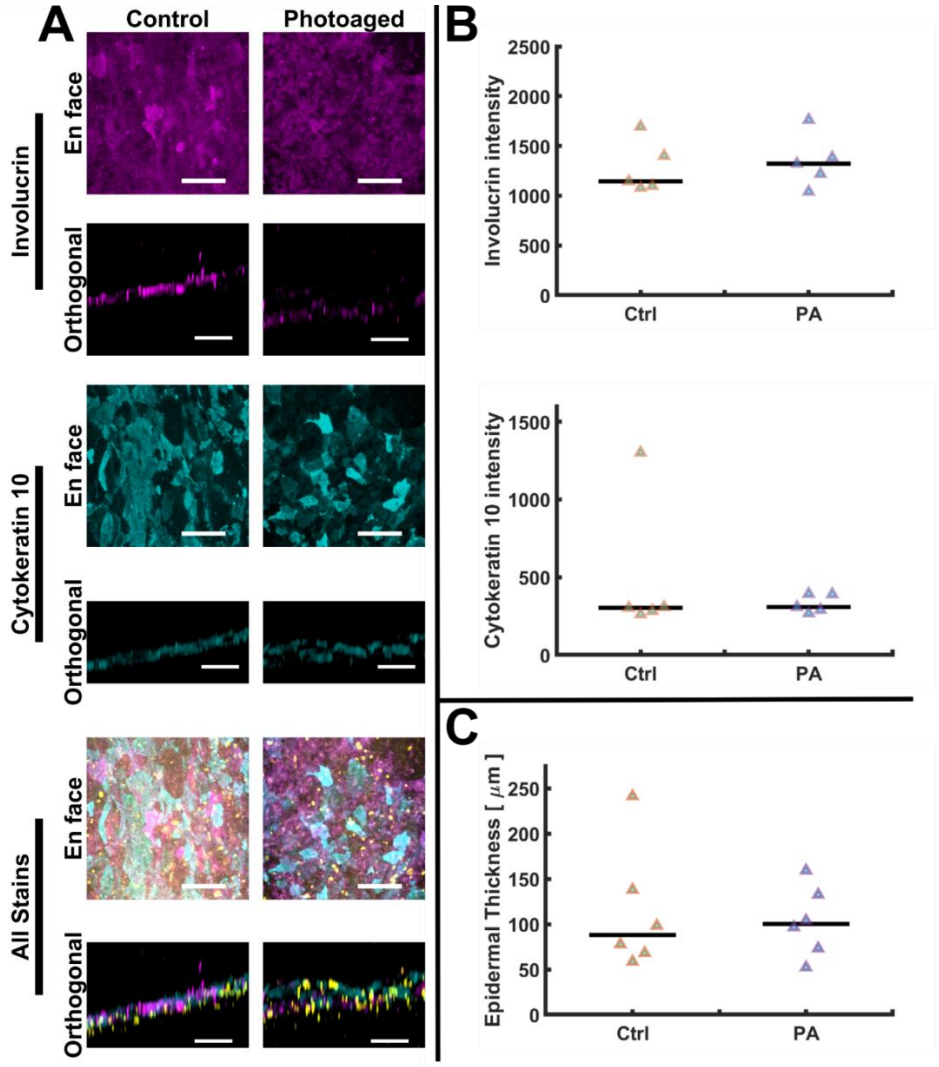

Figure 4.4. Epidermal characterization and quantification. A) The epidermal early differentiation marker, Cytokeratin 10 is localized in the appropriate epidermal region (suprabasal). The late differentiation marker, Involucrin is localized in the appropriate epidermal region (stratum corneum). Nuclei are marked with a DRAQ7 counterstain and shown in yellow. Nuclei are localized in the lower regions of the epidermis as shown in these orthogonal images. No apparent changes in the experimental groups are present in the epidermal stained samples as shown in these representative images. Scalebars are 100 μm. B) Quantification of epidermal intensities was completed from z-axis maximum projections; no indication of intensity changes were found in either epidermal stain when comparing control (Ctrl) to photoaged (PA) samples. (n = 5 for both control and photoaged groups, three biological replicates with one/two technical replicates each). C) Epidermal thickness was volumetrically quantified and no differences were indicated (n = 6 for both control and photoaged groups, three biological replicates with two technical replicates each). Median bars are indicated.

Epidermis is stable during UVA photoaging

Photoaging by UVA largely acts on the dermal and hypodermal portions of the skin rather than the epidermis, in contrast to UVB which shows epidermal toxicity[201]. To assess any changes in epidermal morphology, we stained suprabasal markers (involucrin and cytokeratin 10) along with the nuclear stain DRAQ7 to assess epidermal thickness. No statistically significant differences were observed in the staining intensity of involucrin and cytokeratin 10 (**Figure 4.4 A-B**), or in the overall thickness of the epidermis (**Figure 4.4 C**), when comparing the control and the photoaged AVHSEs. These data are consistent with the minimal *in vivo* effects of UVA on the epidermis[201].

Dermal vasculature is stable during UVA photoaging

Prior studies have shown dermal vascular damage is associated with chronic UVA exposure, as determined from sun-exposed skin biopsies from young v. aged individuals (20-80 years)[229]. As a proxy for vascular damage, we quantified overall morphology in the AVHSE. Vascular structures were identified through localization of collagen IV (**Figure 4.5 A**). Formation of well-developed vascular networks was observed throughout the dermal layer and hypodermis as shown in both the en face and orthogonal projections. Imaging for vascular quantification was performed after tissue clearing, to minimize the loss of signal deeper in the confocal volume. The 3D rendering shown is representative of the vascular network segmentation and skeletonization that was made possible with cleared tissues (**Figure 4.5 B**). Importantly, these techniques are possible with uncleared images as well[48] but clearing increases the volume of tissue that can be quantified. Vascular network diameters are representative of the inner vessel diameter and were quantified as 6.45±0.14 μm for control and 6.34±0.12 μm for photoaged (median ± S.D.). Volume fraction (VF) of

vasculature had median values of 0.037±0.01 and 0.032±0.007 (control and photoaged, respectively; median ± S.D.). No statistical difference was determined in comparison of diameter or vascular VF. Diffusion length (Rk)[144] was calculated with median values of 73.16±23.75 and 83±29.36 microns (control and photoaged, respectively; median ± S.D.). A significant increase in diffusion length of photoaged AVHSEs was detected ($p < 0.01$; normalized to biological replicate controls) which corresponds to a slight non-significant decrease in VF of photoaged samples. Increased VF and decreased Rk is preferable in metabolic tissues[144] and data here reflects that preference in control samples v. photoaged.

Hypodermal adiposity is reduced with photoaging

Prior *in vivo* studies have shown reduced lipid synthesis and lower amounts of fat in hypodermal adipose associated with UVA photoaging[228]. To test if this was mimicked in the AVHSE model, we used confocal imaging of the lipid stain BODIPY in both controls and photoaged AVHSE. Representative images shown in **Figure 4.6 A** show decreased staining intensity and representative volume renderings are shown in **Figure 4.6 B**. To quantify adiposity, we utilized two morphological measures (lipid volume fraction and adipose thickness) as well as the integrated intensity. Both morphological measures exhibit subtle declines, but the results are non-significant (**Figure 4.6 C-D**). However, the overall stain intensity was significantly decreased (**Figure 4.6 E**), indicating an overall loss of lipid content in the photo-aged AVHSE.

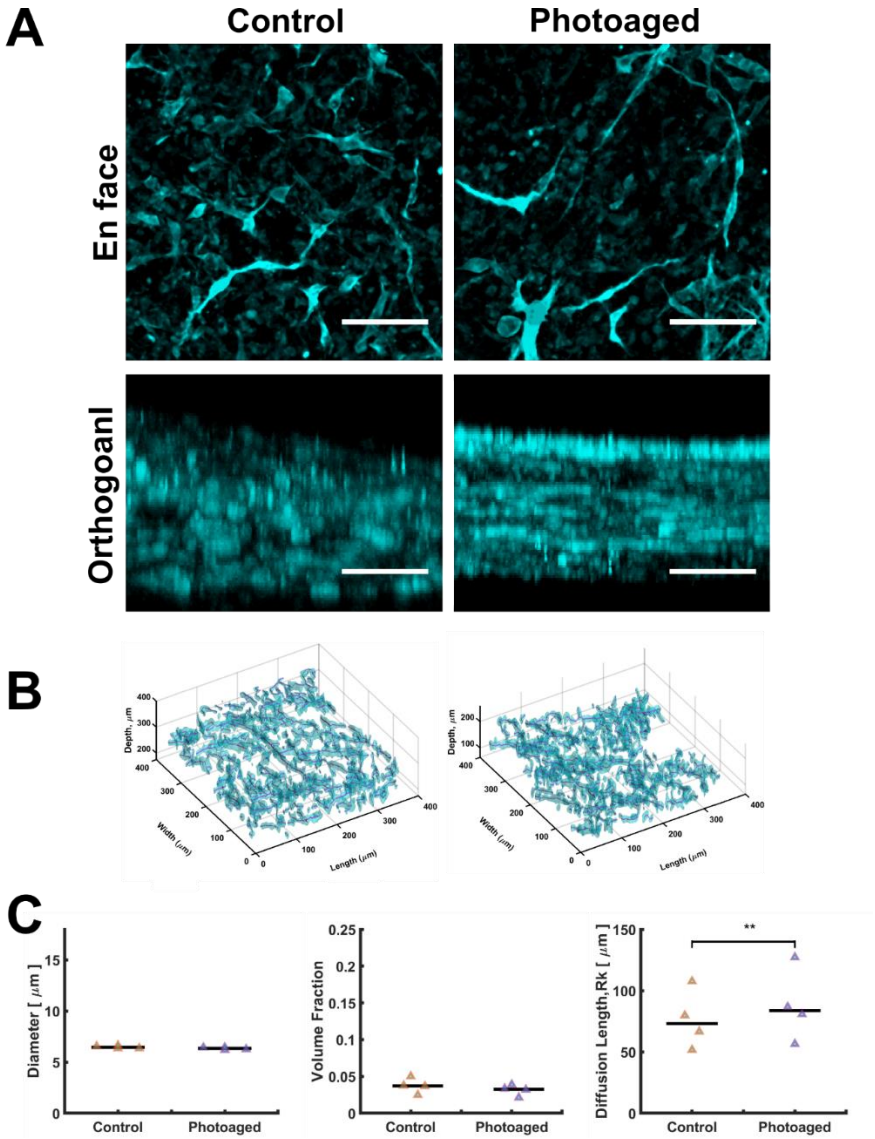

Figure 4.5. Vascular staining and quantification. A) A comparison of confocal images of control v. photoaged AVHSE sub-dermis and dermis; Collagen IV marks vasculature in cyan. En face images are from staining phase 3; orthogonal images are from cleared samples with the top surface also marking Involucrin. Scalebars are 100 μm. B) Vessel location was found through image segmentation of 6 cleared sub-volumes per sample. Skeletonization was completed using segmentation data and the definitive center of each vessel detected was determined (magenta line). This is a representative 3D rendering of one confocal sub-volume. C) Skeletonization of vascular networks makes possible the calculation of vessel diameter and diffusion of vascular network (n = 4 for each condition, two biological replicates with two technical replicates each). Quantification indicates that vessel diameter and volume fractions remain stable when AVHSEs are photoaged and there is an increase in diffusion length for photoaged ($p < 0.01$).

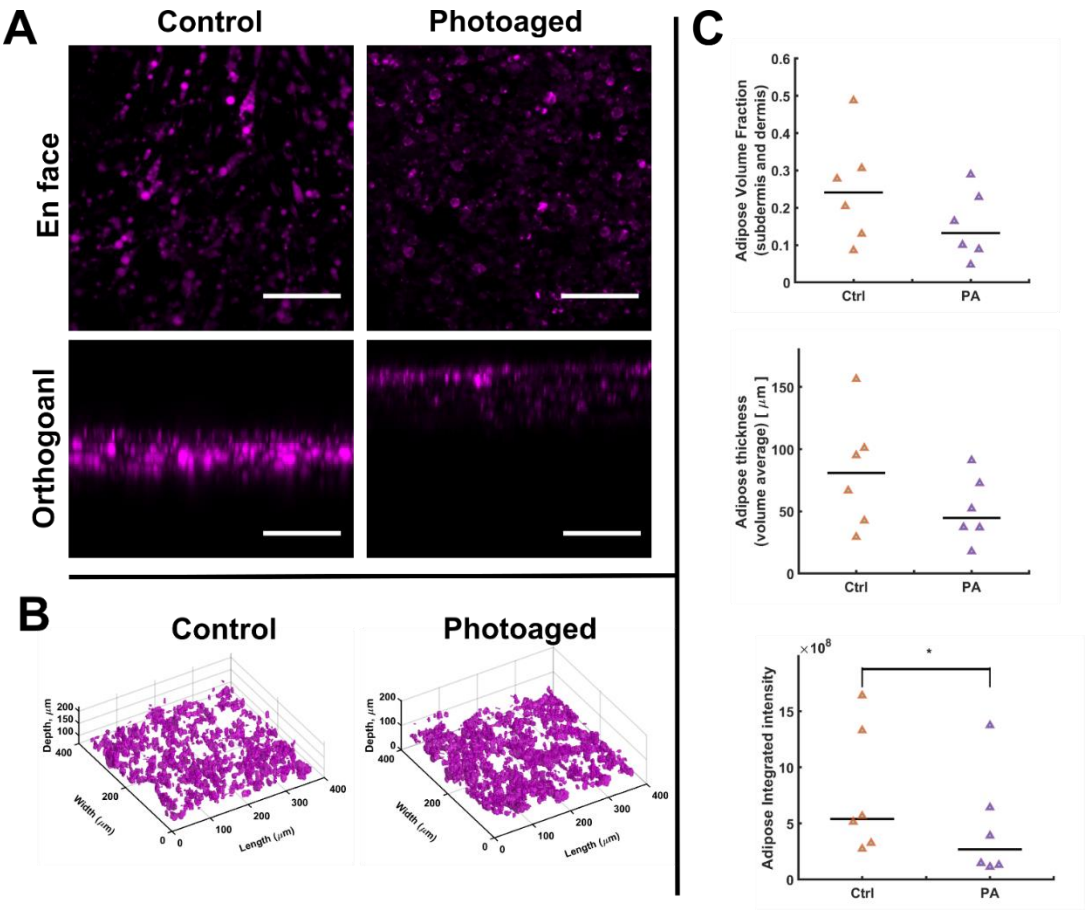

Figure 4.6. Adipose staining and quantification. A) A comparison of confocal images of control v. photoaged AVHSE sub-dermis; BODIPY marks lipid accumulation at mature adipocytes in magenta. Scalebars are 100 μm. B) Representative 3D rendering of adipose volume fraction for control and photoaged samples. C) Top-Volume Fraction was calculated based on segmentation of the BODIPY stain as seen in B. Middle-Thickness quantification based on morphological closing of BODIPY segmentation. Bottom- Integrated Intensity of BODIPY across the volume shows a significant ($p < 0.05$) drop in photoaged samples (statistics run on normalized data to each biological control: $n = 6$ for each condition, three biological replicates with two technical replicates each). Black bars are medians, triangles are data points.

Discussion

Skin provides critical barrier, insulation, and homeostatic functions in human physiology; these are known to be disrupted in aging[2,3,230]. Despite the importance, research is limited by the accessibility of physiologically relevant models, with conventional culture methods lacking the structure and organization of the overall tissue[11] and conventional animal models presenting key differences from human aging physiology[111,124]. To address this, human skin equivalents (HSE) have been previously established as valuable models in the study of skin and aging[11,13,14,16,20,23,84–88,91,95,96]; however limitations remain. Of special relevance, loss and dysregulation of hypodermal adipose is implicated in physiological aging[230–232] and aging-associated diseases including lipoatrophy[233] associated with insulin-resistant diabetes mellitus[234]. This dysregulation is poorly captured in current HSE. To address this, we have developed a robust and reproducible HSE that includes adipose and vascular components (AVHSE). This methodology builds off of previous studies[216,235–238] and provides a model to study crosstalk between adipose, vascular, stromal, and epithelial components of skin in the context of aging. Further, this model is tissue-scale, stable for long culture durations, and suitable for aging studies. Other researchers have reported that when skin models are cultured with adipose tissue, after 2 weeks of culture, there was epidermal disintegration and that 7 days is enough time at ALI to produce a fully functional skin equivalent[137]. Although we did not directly compare skin equivalents without adipose to AVHSEs here or directly compare culture timepoints, we have not observed any obvious changes in epidermal coverage compared to our previous work in vascularized human skin equivalents that do not contain a subcutaneous adipose compartment[48]. While the model is customizable to study the effects of intrinsic and extrinsic aging factors, as a test case we

have demonstrated suitability for studies in UVA photoaging due to the strong literature base of both *in vitro* and *in vivo* studies available for comparison. Finally, we demonstrated the accessibility of the model for both molecular (e.g. ELISA) and morphological studies (e.g. volumetric analysis of cell organization).

A key aspect of any HSE model is a differentiated and stratified epidermis. Here, N/TERT-1 keratinocytes[154] were used to generate skin epidermis as previously completed[48,124,126]. Importantly, N/TERTs are a suitable and robust substitute to primary keratinocytes which have disadvantages including limited supply, limited *in vitro* passage capabilities, and donor variability[126]. HSEs generated with N/TERT keratinocytes demonstrate comparable tissue morphology, appropriate epidermal protein expression, and similar stratum corneum permeability when compared to HSEs generated with primary keratinocytes[124,126]. Similar to prior models, we demonstrate AVHSEs appropriately model the skin epidermis with correct localization of involucrin (a stratum corneum marker), and cytokeratin 10 (suprabasal early differentiation marker)[121,122], and nuclei localized in the lower stratified layers (**Figure 4.4**). Further, volumetric imaging and automated analysis allows for epidermal thickness to be robustly calculated. AVHSE present with median epidermal thicknesses within 90-100 μm, similar to values in both prior *in vitro* studies 100-200 μm[181] and *in vivo* optical coherence tomography imaging of adult skin 59±6.4 to 77.5±10 μm (mean ± S.D.)[194]. Consistent with prior *in vitro* and *in vivo* results showing UVA wavelengths predominantly impact dermal rather that epidermal layers[239,240], UVA photoaging resulted in no observable changes in epidermal thickness or expression of differentiation markers in AVHSE (**Figure 4.4**).

In the dermis and hypodermis, skin is highly vascularized with cutaneous microcirculation playing important roles in thermal regulation and immune function[188,230]. Many prior HSE models have not included a vascular component[47,124,126,175,217]; however, there is increasing recognition of its importance[11,53,121,132,133,136,241]. In the present work, we used collagen IV as a marker of the vascular basement membrane, enabling the automated segmentation and mapping of a vascular network within AVHSEs. The vascular VF of AVHSEs is lower than *in vivo* dermis (~3% compared to 20.0±5.0 to 40.3±2.4 % measured by OCT at four positions in the arm, mean ± S.D[189]), but prior work has shown this is tunable by using different cell seeding conditions [144]. Optimizing the VF may be more involved in the AVHSE, since the ratio of adipose and vascular cells has been shown to be important in regulating tissue morphology[235]. Thus, ratio of adipose and vascular cells would need to be optimized again for new cell and collagen densities. Adipose tissue is densely vascularized[235,242,243] and the ability of adipocytes to generate lipid droplets and adipokines in the presence of endothelial cells is important to replicate the *in vivo* environment[236]. Previous work has shown that in co-culture of endothelial cells (ECs) and mature adipocytes can lead to dedifferentiation of mature adipocytes[243], but in homeostatic cultures ECs and adipocyte crosstalk is important. Through soluble factor release, ECs regulate lipolysis and lipogenesis and adipocytes regulate vasodilation and contraction[137,243]. Secretion of adipokines by adipocytes aids vascular formation and adipose tissue stability[236,243]. In prior work, Hammel & Bellas demonstrated that 1:1 is the optimal ratio for vessel network within 3D adipose[235], and we matched the 1:1 cell ratio in the present work.

Quantification of vessel diameter in the Hammel & Bellas study shows that a 1:1 ratio of adipocytes to endothelial cells gives an average vessel diameter of ~10 μm[235], our work

supports this finding with a median inner vessel diameter of ~6 μm. Importantly, these data are within the range of human cutaneous microvascular of the papillary dermis (4 to 15 μm[188]). We did not observe morphological changes of VF and diameter within the vasculature due to photoaging. This is not entirely unexpected, as UVA exposure and its effects on vasculature are still poorly understood. While it is established that chronic UVA exposure can contribute to vascular breakdown[229,244], the duration of our studies may be too short to see this effect in diameter and VF (1 week vs lifetime UV exposure in people over 80[9,229]). However, photoaging did induce an increase in diffusion length (Rk). Rk is a measure of the 90th percentile of distance from the vascular network and so a higher value corresponds to less coverage; values presented here match previous studies of vascularized collagen[144]. Rk of the vascular network for both control and photoaged samples was within the range of 51 - 128 μm which is importantly below the 200 μm diffusion limit[245]. Upon photoaging, AVHSEs did demonstrate a significant increase in Rk compared to controls. Rk is inversely related to volume fraction which showed a non-significant decrease in photoaged samples. In vascularized tissue, a high VF and low Rk is preferable[144] and the Rk increase demonstrated indicates a loss in vascular coverage in photoaged AVHSEs. These findings conflict with studies of acute UV exposure in skin, which show stimulation of angiogenesis[9,246]. It has been proposed that UV light exposure may improve psoriasis by normalizing disrupted capillary loops through upregulation of VEGF by keratinocytes[188]. The AVHSE model could be used to more thoroughly test the effects of UV light and other molecular mechanisms it induces in future studies.

The vascular networks extend from adipose to the epidermal-dermal junction (**Figure 4.5**), consistent with previous literature[53,144] and to normal human skin

histology/stereography[247]. Further, we observed vasculature colocalized with the lipid droplet BODIPY staining (**Figure 4.2**), indicating recruitment of the vascular cells to the hypodermis. Importantly, the vascular networks in prior studies and the present AVHSE are self-assembled. While there are advantages to self-assembly, especially the simplicity of the method, it is important to note the limitations. Cutaneous microcirculation *in vivo* has a particular anatomical arrangement with two horizontal plexus planes, one deep into the tissue in the subcutaneous fat region and one just under the dermal-epidermal junction[188,248]. Between these two planes are connecting vessels running along the apicobasal axis that both supply dermal tissues with nutrients and are an important part of thermoregulation[188,248]. Although the AVHSEs presented here are fully vascularized up to the epidermal junction they do not recapitulate this organization. While not covered in this work, future studies could incorporate layers of patterned or semi-patterned vasculature[245] to more closely match the dermal organization, depending on the needs of the researcher.

In contrast to the epidermal and some vascular components, photoaging impacted the hypodermis. Volumetric imaging of BODIPY, which stains lipid droplets[235], was used to identify the adipose. While small reductions in the morphological parameters (adipose thickness and lipid VF) were observed, they were not significant, suggesting there was not large-scale necrosis or loss of fat mass. However, there was a significant decrease in the intensity of BODIPY staining, indicating decreased lipid levels. This is consistent with photoaging of excised human skin showing that UV exposure decreases lipid synthesis in subcutaneous fat tissue[228]. We further collected culture supernatant and tested for the presence of adiponectin, IL6, and MMP-1. The data collected through ELISA (**Figure 4.3**) show that this AVHSE model secretes both adiponectin and IL6, which are also present in

native skin and both considered important adipokines[216,243,249,250]. Elevated serum adiponectin levels are linked to anti-inflammatory effects in humans[249,250] and centenarians (who are a good model of healthy aging) have elevated levels of adiponectin[249] Decreased adiponectin has previously been associated with photoaging in both excised human skin that was sun-exposed compared to protected skin and in protected skin that was exposed to acute UV irradiation[203]. Conversely, IL6 is a key factor in acute inflammation in skin, and has been shown to regulate subcutaneous fat function[228,251]. In prior studies of photoaging, IL6 has demonstrated an increase after UVA irradiation in monolayer fibroblast cultures[252] and excised human skin[228,251]. IL-6 is released after UV irradiation and has been linked to decreased expression of adipokine receptors and mRNA associated with lipid synthesis[203], decreases in lipid droplet accumulation[228], and enhanced biosynthesis of MMP1[252,253]. However, after one week of photoaging we did not observe an increase in IL-6 or MMP-1 via ELISA(**Figure 4.3**).

The absence of changes in IL-6 and MMP-1 expression but decreases in lipid accumulation and adiponectin are not expected results but they could be due to methodology differences in UVA exposure. We determined our UVA dose and exposure based on literature values[38–40,198,202,203,213]. The dose used here was 0.45 ± 0.15 mW/cm^2 with exposure for 2 hours daily for 7 d which roughly converts to 3.24 J/cm^2 per day and a total of 22.68 J/cm^2. Many studies do not report exposure time and/or present ambiguous timepoints. This, compounded with the practice of using doses based on sample pigmentation threshold and broad definition of UVA wavelengths is likely contributing to the discrepancy in IL-6 and MMP-1 expressions. Previous work has shown that neutralizing anti-IL-6 antibody prevents UV induced decrease of important fat associated mRNA (acetyl

CoA carboxylase, fatty acid synthase, sterol regulatory element binding protein-1) and that IL-6 secreted from keratinocytes and fibroblasts following UV irradiation inhibits lipid synthesis[228]. From previous work, it is clear that IL-6 secretion is upregulated by UVA and presence contributes to negative adipose function but more investigation is necessary to understand what UVA doses and exposures induce IL-6 and further at what timepoints after photoaging are these expressions quantifiable. In this model, it is possible that there were increases in IL-6 that contributed to adiponectin decreases in photoaged samples, these trends may have been caught with different media collection timepoints. Alternatively, other analysis of inflammatory responses and adipokines may show generalized inflammatory responses identified in literature and further, changes in dose/exposure or continued photoaging may mimic the previously shown effects.

There are notable limitations of the AVHSE model presented. Although we have presented a skin model that is closer to both anatomy and biology of human skin in comparison to past HSEs, we have not modeled skin fully through inclusion of other features of *in vivo* skin such as immune and nerve components. Including a functional immune system is important in understanding autoimmune diseases, cancer, wound healing, and decline of immune function in aged skin[11,230]. Additionally, neuronal cell inclusion will allow for modeling of sensory processes necessary for grafting and modeling of skin disorders associated with nerve dysregulation[230]. Further, while the cell lines used in this study were chosen for their low cost and accessibility, primary cells or populations differentiated from induced pluripotent stem cells (iPSCs) would more closely match the physiology *in vivo*. While changing cell populations would likely require some adjustment to the culture system, we have previously demonstrated that cell types can be replaced with

minimal changes[48]. We model epidermis, dermis, and hypodermis here, but we do not model the depth that is present in thick skin tissue; to mimic thicker skin the model would need to be taller. As nutrient and waste diffusion in tissues is limited to ~200 μm[245], thick tissues will likely require perfusion to maintain throughout culture. Vasculature in thicker skin has higher diameters, especially in the lower dermis and hypodermis, these can be up to 50 μm[188]. Finally, for ease of use, initial collagen density in the AVHSE model is 3 mg/mL, much lower than *in vivo* densities[35,254]. Decline of collagen density is an important aspect of skin aging, correlating with skin elasticity and wound healing[3,10,11,15,17–19]. Varying collagen density influences vascular self-assembly[144], but higher collagen densities are possible through a variety of techniques, including dense collagen extractions[146], and compression of the collagen culture[210]. By incorporating these tools, AVHSE could be modified to more closely represent the *in vivo* dermal matrix. Further, the AVHSE method was demonstrated with low serum requirements; but serum was used for initial growth and the cultures are maintained for weeks without serum. Serum replacements during the growth phase could potentially provide a chemically defined xeno-free culture condition in beginning culture stages for greater reproducibility and biocompatibility.

The presented AVHSE model provides unique capabilities compared to cell culture, *ex vivo*, and animal models. Excised human skin appropriately models penetration of dermatological products but there is limited supply and high donor variability[255]; replacing excised human skin with animal models or commercially available skin equivalents is not the best course of action because of the differences such as varying penetration rates, lipid composition, lipid content, morphological appearance, healing rates, and costs[255,256]; and limitations of customization. AVHSE can be cultured using routinely available cell

populations, are cost effective, and are customizable for specific research questions. Further, the model is accessible for live imaging, volumetric imaging, and molecular studies, enabling a wide range of quantitative studies. The current work focused on AVHSE as a research tool, but similar techniques could be further developed for the development of grafts. Grafting would require addressing many of the structural and biological limitations noted above, as well as modifications to address host immunity issues. Overall, we have demonstrated AVHSEs as a research platform with regards to photoaging effects, but expansions of this model could be utilized for clinical skin substitutes[112], personalized medicine, screening of chemicals/cosmetics, drug discovery, wound healing studies[112,256], and therapeutic studies[216].

Acknowledgements

This work was supported in part by the American Heart Association (19IPLOI34760636). We thank Dr. Jim Rheinwald and Dr. Ellen H. van den Bogaard for their generous gift of N/TERT cell lines.

Supplemental

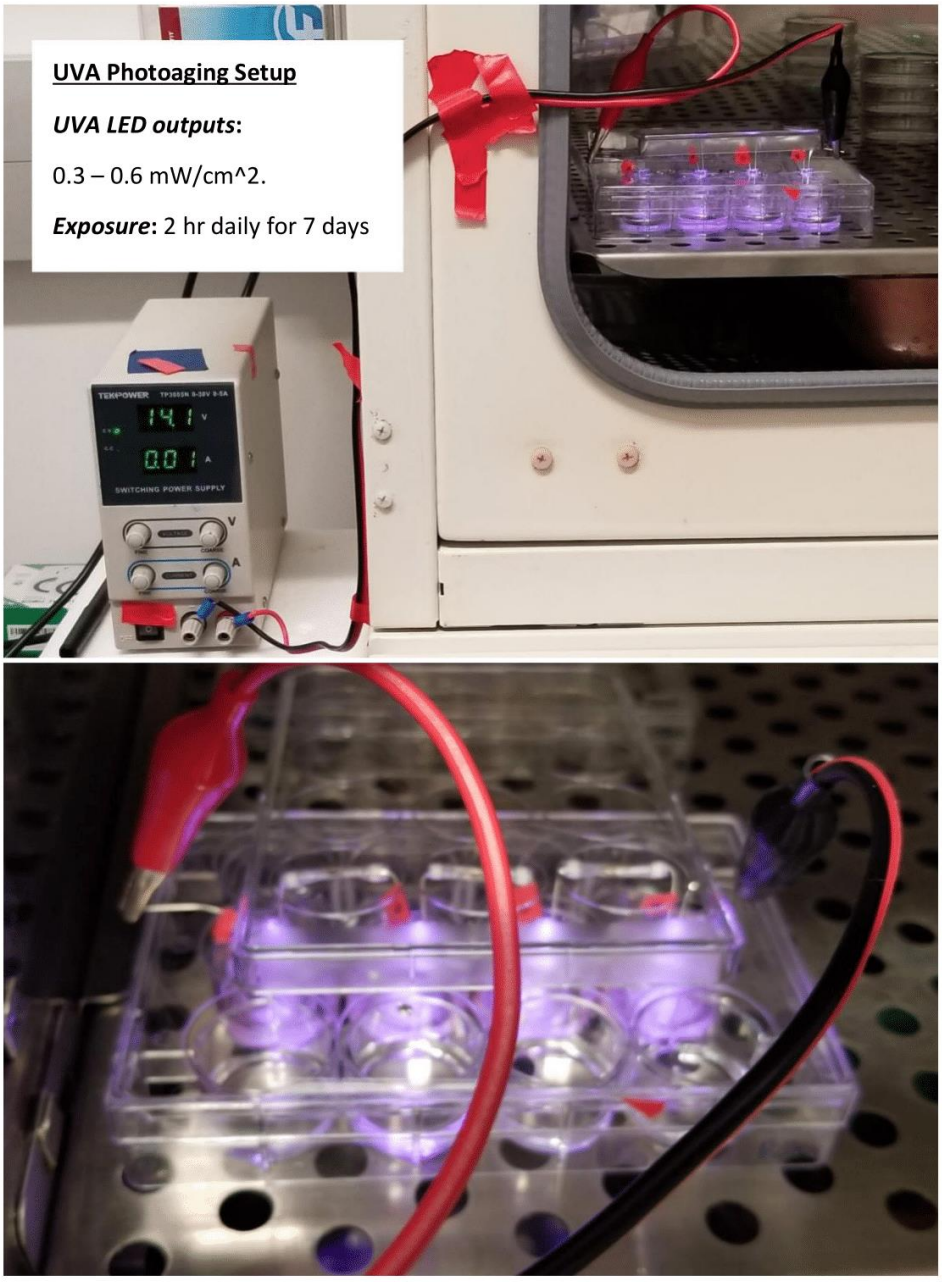

Figure 4.7 (Supplemental). UVA Photoaging Setup. UVA exposure was completed by drilling out a well plate lid and inserting UVA LEDs. Each LED had an output of 0.3-0.6 mW/cm^2. AVHSEs were exposed daily for 2 hours, for 7 days.

Chapter 5

Perfluoroalkyl substances dysregulate the human cell cytoskeleton and upregulate adipogenesis

This work is in preparation for submission to an academic journal

Martina M. Sanchez[1†], Verena Tadros[1†], Jordan Rolsma[1], Cesunica Ivey[2], Joshua T. Morgan[1*]

Department of [1]Bioengineering

University of California, Riverside, CA 92521

Department of [2]Civil and Environmental Engineering

University of California, Berkeley, CA 94720

([†]) Authors contributed equally to the work

(*) Address correspondence to:

Joshua Morgan

900 University Ave
Riverside, CA 92521

Tel: 951-827-6253

E-mail: jmorgan@engr.ucr.edu

Keywords: PFAS, PFOA, PFOS, adipogenesis, cytoskeletal disruption

Abbreviations:

PFAS: Perfluoroalkyl substances; PFOS: Perfluorooctanesulfonic acid tetraethylammonium salt; PFOA: Perfluorooctanoic acid

Introduction

Perfluoroalkyl substances (PFAS) are stable, water-soluble compounds that persist in the environment and are of major concern for the public[98]. These substances are widely used in surfactants, lubricants, paints, polishes, paper/textile coatings, food packaging, and fire-retardant[97,99,100]. The most widely studied PFAS chemicals are PFOS and PFOA. These are organic compounds in which all hydrogens on all non-functional group associated carbons have been replaced by fluorine; thus, PFOS and PFOA are extremely stable due to their numerous strong carbon-fluorine bonds[100]. Due to their stability and bioaccumulative properties, PFAS are ubiquitous and are found in food and water[99,101,257,258]. PFASs have come under recent scrutiny as bioaccumulating toxins; once they reach a certain concentration in the body, their hydrophobic long chain structures penetrate cellular lipid bilayers and displace and disrupt membrane structures[259–261]. Concerningly, in people aged 12 or older, PFAS chemicals including PFOS, PFOA, PFNA, and PFHxS have been detected in more than 95% participants of a ~7800 sample study in the U.S.[262]. These chemicals have also been found to environmentally bioaccumulate with detection in several animals including mammals and aquatic species[263].

The primary route of PFAS exposure in adults is through food and water ingestion. There are also a few studies demonstrating toxicity of PFAS through skin exposure in human tissue engineered skin and in animals[263–265]. In US children (~age 2), the exposure from dust ingestion and dietary ingestion is nearly equal[258]. Bioaccumulation of PFAS results in multiple health detriments with exposure ranging from pre-natal timepoints into adulthood. Toxicity mechanisms of PFAS within the cell and on tissue development are poorly understood but implications have been made regarding disruption of viability and proliferative capacity[263], immune response [263],

pro-estrogenic endocrine processes[266], lipid profile and fat development [267,268], cell membrane [259,261,269], endothelial barrier[270], gap junctions[269,271,272], and cytoskeleton[273 271].

Epidemiological studies

Higher PFAS concentrations in adults (especially women) are associated with greater weight regain[105]. Evidence for non-favorable lipid profiles linked to PFAS plasma concentrations has also been found including greater total cholesterol low-density-lipid (LDL), higher triglycerides, increased very low-density lipoprotein (VLDL), and increased gamma glutamyl aminotransferase (a liver enzyme)[267,268]. Further, hormonal effects have been linked to PFAS compounds in adult subjects. Reproductive hormones such as sex-hormone binding globulin, follicle stimulating hormone, and testosterone concentrations have been found to be inversely related to PFOA and PFOS in people aged 12-30 years[274]. Thyroid stimulating hormones and total T4 have been positively associated with PFAS while negative associations have been found with kidney function[275].

Children have a higher burden of PFAS partially due to mouthing behaviors, their lower body size to area ratio, and possible exposure via breastfeeding[257]. Studies with concerning outcomes concluded associations of increased PFAS exposure in utero and during childhood with adolescent/adult obesity[105,276,277], cholesterol[257], and increased beta cell dysfunction (a main factor for hyperglycemia which characterizes type 2 diabetes)[276,278]. Childhood obesity and overweight risk is in turn associated with higher adult risk of obesity and multiple chronic diseases including cardiovascular disease and diabetes[277]. Several PFAS compounds are able to penetrate the placental barrier in pregnant women and reach fetal circulation[279–282]. Although the mechanism of accumulation is not yet understood, multiple studies have shown that this transfer

is preferential, that is, fetal concentration is higher than maternal concentration-possibly due to differences in fetal v. maternal blood[281,282]. Studies have associated higher maternal serum concentrations/exposure with decreased birthweight[283,284] but increased infant adiposity[284]. A growing number of studies have also linked high maternal serum concentrations of PFAS to increased pediatric/young adult adiposity[102,104,106,285,286] and changes in lipid profiles[287].

Hypothesized mechanisms of PFAS association with low birthweight and increased infant/childhood adiposity include lipid metabolism changes, reduced food/water intake by the mother, direct fetotoxic effect, endocrine disrupting effects, and other altered hormone levels[279,288]. Much evidence points toward hormonal effects and their downstream interference of tissue development and function including body weight and adipose regulation. One direct example of hormone sensitive development effects include changes in anogenital distance which have been observed in female infants[284,289]. Negative PFAS effects have also been explored with mechanisms acting on constitutive andostane receptor, pregnane-X receptor, estrogen receptor beta, and the phosphatidylinositol 3-kinase-serine/threonine protein kinase pathway[284].

Hypothesized mechanisms for greater weight regain in adulthood include PFASs possible involvement in changing energy metabolism and homeostasis of thyroid hormones[105,290–292] through transcriptional factor activation like peroxisome proliferator-activated receptors (PPARs)[284]. PPARα and PPARγ are key regulators in fatty acid oxidation, differentiation, adipocyte proliferation and function, glucose breakdown, and lipid and lipoprotein metabolism [105,293–297]. In mice, PFOA was shown to affect leptin and adiponectin release during differentiation of fat cells (adipocytes); leptin is a regulator of energy homeostasis while adiponectin is secreted by mature adipocytes and effects insulin responsiveness[296]. Low leptin levels at birth may increase risks of insulin resistance and obesity in later life[296,298,299].

Conflicting evidence of PFAS effect on health

At this time, the high PFOA/PFOS exposure association with decreased birthweight is based on multiple conflicting literature[280]. However, to shed light on conflicting conclusions, a case study that systematically reviewed 18 epidemiological and 21 animal studies regarding PFOA toxicity concluded that exposure to PFOA is in fact toxic to human reproduction and development[300]. Conflicting evidence of the associations between PFAS maternal concentrations and childhood adiposity is also present, although a recent mass analysis of cohort studies has concluded an association with early life exposure to PFOA and increased risk for childhood obesity[286]. Speculation upon the conflicting evidence of associations between PFAS maternal concentrations and childhood adiposity have been made regarding the differences in concentrations of PFAS evaluated in study populations[104] and differences in method of subject weight measurement[284]. In many studies PFAS associations with negative health effects were only observed in the highest fraction of serum concentration studied while in lower concentrations associations were not present[267]. More evidence is required to fully understand PFAS associations and how they may vary with concentrations. It has been suggested that low maternal serum concentrations show positive associations with childhood adiposity and higher serum concentrations show positive, negative, or non-monotonic dose responses (NMDR) with childhood obesity[104]; this evidence is supported by the fact that PFAS are endocrine disrupting chemicals (EDCs)[106], since EDCs have been shown to induce NMDR[104,106,301,302]. Much of this association has been investigated due to concrete developmental effects PFASs have on rodent birthweight when exposed in utero[303]. Importantly, animals have differences in PFAS metabolization and gestational duration when compared to humans and many animal effects were observed with very high levels of PFAS[105,280,304].

Lipid profiles are associated with adult weight and prevalence of obesity[250,267]. There is much conflicting evidence on whether PFAS plasma concentrations are associated with less favorable or beneficial outcomes on lipid profiles. Several studies have linked PFAS with higher total cholesterol, higher triglyceride levels, and higher low-density lipoprotein[267,268,305–315] while other studies have linked higher PFAS plasma concentrations with beneficial lipid profile effects[267,287,293,316,317]. Drawing conclusions based on adiposity effects of PFAS in animals should be carefully considered as well. Notably, mice have differences in adipocyte derived hormones; for example, resistin is secreted by adipocytes in the mouse but in humans is not expressed in adipocytes and is primarily present in monocytes and macrophages[296].

Hypothesized PFAS effects on Hippo signaling and the cytoskeleton

Conflicting literature of PFAS and associations with health elucidate a need for further understanding at the cell and biological signaling level of PFAS effect on humans. These contradictions are exacerbated due to the poor understanding of the toxic mechanisms PFAS elicits. Several of these mechanisms share common modulators, the Hippo signaling pathway and the cell cytoskeleton.

Hippo signaling is a crucial cellular pathway involved in organ development, growth, homeostasis, stem cell maintenance, and regeneration[318–326]. Briefly, the classic Hippo cascade involves kinase regulators mammalian Ste20-like kinases 1/2 (Mst1/2) and large tumor suppressor 1/2 (Lats1/2) which act to regulate phosphorylation and degradation of Yes-associated protein (YAP) and transcriptional co-activator with PDZ-binding motif (TAZ)[321,326–328]. As downstream effectors of the Hippo pathway, YAP and its paralog TAZ target genes involved in cell growth, proliferation, differentiation and development[319–321]. When Hippo is active, YAP/TAZ are phosphorylated leading to YAP/TAZ degradation and cytoplasmic retention[326]. In

the inactive state, YAP/TAZ accumulate in the nucleus and target proteins of TEA-domain containing family (TEAD1-4), runt-related transcription factor (RUNX), and others.[318,321,326]. Several factors can mediate activation of the Hippo pathway including the classic cascade involving Mst1/2 and Lats1/2, mechanical cues, cell polarity and adhesion mechanisms, metabolic pathways, ligand-dependent activation, and hormone/growth factor control[321,329]. Further, YAP/TAZ are involved in pathway crosstalk as well[321,329]. YAP and its core upstream regulators Mst1/2 and Lats1/2 have been investigated in several organs and their developmental dysregulation which may be linked to changes in body weight.

Many organ systems have been studied to identify developmental problems after knockout of Mst1/2, Lats1/2, or YAP. Through these investigations, it has been shown that changes in the main regulators and effector YAP have caused lung epithelial defects[318], faults in kidney structure development[318,330], bone to fat ratio disruptions[331], over proliferation during intestinal development[318,319,324,330,332], improper regulation of liver development including epithelial and hepatocyte maturation changes[318,319,324,326,328,333], and pancreas mass/size changes[324,325]. It is still unclear how PFAS may disrupt YAP regulation and how these mechanisms tie into body weight and organ development/size control. PFAS may regulate the Hippo pathway via mechanosensing extracellular matrix changes through focal adhesions and the actin cytoskeleton, a known Hippo pathway propagation[334]. YAP/TAZ regulation through Rho/ROCK activation acts as a control mechanism for transcriptional control of cytoskeleton stability[334], PFAS is likely effecting cell function and viability through this Hippo pathway cascade as well.

Adipogenic versus osteogenic polarization of mesenchymal stem cells is dependent on YAP/TAZ localization in the Hippo signaling pathway, a relationship linked through mechanical

cues and cytoskeletal tension[331,335,336]. An increase in nuclear YAP/TAZ localization corresponds to increased osteogenic stem cell differentiation while increases in cytosolic YAP/TAZ correspond to higher adipogenic differentiation[319]. Mechanical regulation of adipogenesis upon nuclear localization has been suggested to work through transcription factor ß-catenin or SMAD proteins rather than TEAD[336]. Due to the cytoskeletal involvement in adipose tissue, it is plausible that PFAS may dysregulate adipose through perturbation of cell cytoskeleton. PFAS chemicals have been found to act on the cell cytoskeleton through disruption of f-actin, microtubules, and gap junctions[269–273,337,338]. PFAS has been shown to disrupt and fragment actin cytoskeleton and tight junctions in mice Sertoli cells and human microvascular endothelial cells (respectively)[271,338]. It is likely that PFAS effects cytoskeleton integrity and could change balance of osteogenic/adipogenic polarization of mesenchymal stem cells and/or adipose tissue homeostasis.

During adipogenesis, cytoskeleton remodeling is a preliminary process and it has been found that the cytoskeletal components actin, tubulin, vimentin, and septin (a novel cytoskeletal component in adipocytes[339]) undergo localization and expression changes [340]. Specifically, actin forms filament bundles in the cytoplasm of pre-adipocytes and short filaments in mature adipocytes with similar organization in the microtubules, and vimentin regulates lipid droplet accumulation by forming cage structures that surround lipid droplets [340]. Septin has been found to form filaments or rings depending on timepoint within adipocyte differentiation. These findings support the cytoskeleton's role in regulation of adipogenesis and lipid accumulation.

In a study completed with rat cardiomyocytes, it was found that the adipokine, adiponectin acts on Rho/ROCK and increases RHO GTPase activity and induces cytoskeletal remodeling to further regulate glucose uptake and metabolism[341]. Adiponectin effects were

demonstrated by its ability to increase membrane microvillar like protrustions, and increasing actin polymerization to form filamentous actin/actin stress fibers[341]. Potentially PFAS chemicals may be directly disrupting the cytoskeleton or disrupting it indirectly through changes in the adipokine profiles that adipose tissue secretes. On the other hand, PFAS may regulate the Hippo pathway via mechanosensing extracellular matrix changes through focal adhesions and the actin cytoskeleton, a known Hippo pathway propagation[334]. YAP/TAZ regulation through Rho/ROCK activation acts as a control mechanism for transcriptional control of cytoskeleton stability[334], PFAS could be effecting cell function and viability through this Hippo pathway cascade as well. The mechanical control of adipogenic differentiation of MSCs relies on both the integrity of the actin cytoskeleton itself and tension feedback from myosin II motor which directly acts on the Hippo signaling pathway[336]. It is possible that PFAS effects YAP/TAZ localization via cytoskeleton integrity.

These connections between adipose tissue maturation and cytoskeletal remodeling are a potential avenue for PFAS perturbation and how it effects lipid profiles and fat development. In obesity, adipocytes are hypertrophic and the expression of the adipokine leptin increases and inflammatory cytokines (TNF-alpha and IL-6) are increased while adiponectin and lipoprotein lipase are decreased[249,341–343]. There are also increases in angiogenesis, immune cell infiltration, and adipose inflammation. These changes are characteristics of insulin resistance, hyperglycemia, dyslipidemia, hypertension, and obesity/adiposity [249,250] and could be common ground for PFAS associations with obesity in humans.

Based on these observations, we hypothesize that PFAS may be mechanistically perturbing the cell cytoskeleton and working through the Hippo pathway resulting in abnormal developmental outcomes in children. In the current study, we have evaluated PFAS' effects on

skin epithelial and adipose derived stem cell lines. We performed in vitro experiments to determine if the cytoskeleton is modulated by PFAS in two types of cells and investigated dysregulation of f-actin and acetylated tubulin. Functional effects on cell survival of both cell types and differentiation of adipose was evaluated in response to PFAS exposure. To investigate if the Hippo signaling effector, YAP, is modulated by PFAS, we quantified YAP expression and localization. Further, we have shown that damaged phenotypes due to PFAS effect the wound healing processes of keratinocyte skin cells and adipose derived mesenchymal stem cells and that some doses of PFAS chemicals induce higher amounts of adipogenesis as determined by lipid droplet staining and qPCR.

Materials and Methods

Routine Cell Culture

All cell types were routinely cultured at 37 °C and 5% CO_2. The human immortalized keratinocyte cell-line N/TERT-1, expressing hTERT and loss of $p16^{INK4a}$ function[124,344] was a generous gift from Smits and Rheinwald[124,154]. N/TERT-1s were grown up in modified K-SFM media blend including K-SFM base, endocrine growth factor (EGF) [0.2 ng/mL], bovine pituitary extract [25 μg/mL], and 5% penicillin/streptomycin. Cells were routinely passaged at 30-50% confluence[154] (passages 5-7 were used for experiments). Adipose derived mesenchymal stem cells, hTERT immortalized (ASC52telo; ATCC SCRC-4000, Manassas, VA), were also used for experiments at passages 3-7. ASC52telos were grown up as recommended by the manufacturer in Mesenchymal Stem Cell Basal Medium (ATCC PCS-500-030) and supplemented with Mesenchymal Stem Cell Growth Kit for adipose and umbilical derived MSCs- low serum components (ATCC PCS-500-040: Fetal bovine serum 2%, rh FGF basic [5 ng/mL], rh FGF acidic [5 ng/mL], rh EGF [5 ng/mL]), L-Alanyl-L-

Glutamine [2.4 mM], and G417 [0.2 mg/mL]. ASC52telos were regularly passaged at ~80% confluence.

Experimental Cell Culture

All PFAS exposure experiments were completed in 24 well plates on 10/12 mm glass coverslips. N/TERT-1s and ASC52telos were seeded at 50,000 cells/well for 24 and 72 hour exposure timepoints. Prior to PFAS treatments, cells settled for 24 hours and then chemical exposure was begun via administration in media. No media changes were completed after chemical administration. PFAS chemicals of interest include Perfluorooctanoic acid (PFOA, 95%; Sigma Aldrich CAS #: 335-67-1) and Perfluorooctanesulfonic acid tetraethylammonium salt (PFOS, 98%; Sigma Aldrich CAS #56773-42-3). For PFAS treatment experiments, N/TERT-1 cells were evaluated in the previously mentioned K-SFM media blend while ASC52telo cells were evaluated in DMEM High Glucose base, 5% FBS, 1% P/S. Working stock of PFOA [10 mM] was made by adding 41.407 mg of PFOA to 10 mL of warm (37 °C) cell specific media. Working stock of PFOS [400 μM] was made by adding 10.069 mg of PFOS to 40 mL of warm (37 °C) cell specific media. PFOA and PFOS stocks were vortexed then warmed for an additional hour at (37 °C) before being used for dilutions. Each well contained 1 mL of media with chemical dose during treatments.

PFOS effects were studied in N/TERT-1s at [0 μM, 30 μM, 40 μM] and in ASC52telo at [0 μM , 30 μM, 40 μM]. PFOA effects were studied in N/TERT-1s at [0 μM , 100 μM, 125 μM] and in ASC52telo at [0 μM , 100 μM, 125 μM]. All doses were determined empirically.

Adipogenesis Assays

PFAS effect on the differentiation process of adipose derived mesenchymal stem cells into adipogenic phenotype was also investigated. Adipogenic differentiation was induced via media, as completed previously[222]. Adipogenic induction media was DMEM (high glucose) supplemented with 10% FBS and 1% P/S, 500 µM 3-isobutyl-1-methyl-xanthine (Sigma), 1 µM Dexamethasone (Sigma), 10 µg/mL Insulin (Sigma), and 10 µg/mL indomethacin (Sigma). To examine how PFAS effected these processes, ASC52telo cells were plated at a density of 25,000 cells/coverslip in 24 well plates on 12 mm glass slides and cultured in adipogenic conditions. After initial seeding in routine culture media, at 48 hours PFOA [100 and 125 µM] and PFOS [20, 30, 40 µM] were added to well plates. Control media was Adipogenic Induction media. Cultures were carried out for 19 days, at endpoint, all wells were fixed with 4% PFA for 15 minutes then washed x 3 with PBS (-,-). Plates were either stored at 4 °C or were immediately exposed to oil-red-o staining for adipogenesis assessment.

To assess adipogenesis, lipid content was assayed using Oil Red O (ORO) staining which marks lipids secreted by adipocytes. ORO staining was completed similar to previous studies[222,345]. Briefly, a 0.5% lab stock was made up by dissolving 0.2 g Oil Red O in 40 mL Isopropanol . After dissolving overnight, a working stock was made up by diluting the lab stock 2:3 with culture grade water to yield a 0.2% solution in 40% Isopropanol. The 0.2% solution was made up immediately before exposure then filtered before use with a 0.2 µm sterile syringe filter. Each 24 well was filled with 0.5 mL ORO and incubated for 30 minutes at room temperature. After exposure, coverslips were washed 5x with autoclaved distilled water. Phase Contrast imaging at 10x was performed to evaluate adipogenesis and oil-red-o

accumulation. For oil-red-o analysis, 3 images were taken per coverslip for each replicate set.

Isolation of mRNA and quantitative polymerase chain reaction

For RNA isolations, ASC52telo cells were plated at a density of 500,000 cells/60 mm tissue culture plate then grown up for 48 hours in their routine culture media. At 48 hours, adipogenesis was induced via media and cells were cultured in adipogenic conditions for 19 days with experimental chemical doses. At day 19, mRNA was isolated using the Thermo GeneJet RNA Purification Kit (Thermo Scientific, Ref #K0732). All RNA isolations were carried out as outlined by the manufacturer. Assays were completed to assess for adiponectin, leptin, PPARγ, CEBP, and CTGF, using the housekeeping gene GAPdh. Primer sequences given in supplementary data **Table 5.1** Primer Sequences used for qPCR.

. Quantitative polymerase chain reaction (qPCR) was performed via SensiFAST™ SYBR No-ROX One-Step mastermix from Bioline. All reactions were performed in triplicate. qPCR reactions were completed using a Mic Real Time PCR Cycler (Version 2.10.1, bio molecular systems) at 10 minutes at 45 °C then 2 minutes at 95 °C then 40 3-step cycles of 95 °C for 5 seconds, 60 °C for 20 seconds, and 72 °C for 10 seconds and a melt from 72 °C to 95 °C at 0.3 °C/s. For quantification of mRNA, *n = 4.*

Fixing, Staining, and Imaging

Following culture, coverslips were fixed and permeabilized in place for 20 minutes via 4% paraformaldehyde and 0.25% triton x 100. After fixation, coverslips were washed with PBS x 3 and either stored at 4 °C in PBS or blocked and stained immediately. Samples were first blocked for one hour then stain solution of primary antibodies was added (blocking

buffer recipe given in supplemental data). All stain solutions were made up in blocking buffer except DAPI which was made up in 1 x PBS. Primary antibodies and chemical stains used include: YAP-1, Acetylated Tubulin, Ki67, Phalloidin, DAPI (1 x); antibody specifications given in supplemental data **Table 5.2**. Coverslips were exposed overnight at 4 °C to primary stain solution then removed, washed x3 with 1x PBS, then exposed overnight to the secondary solution (**Table 5.2**). DAPI was used to mark nuclei and coverslips were exposed for 20-30 minutes at room temperature in 1x PBS, after initial staining was complete. All coverslips were mounted to glass slides using gelvitol (made in house) allowed to dry, then cleaned with 70% ethanol prior to imaging. Confocal imaging was performed using a Leica TCS SPEII confocal, sCMOS camera attachment. Imaging parameters remained the same for each coverslip in order to compare intensities; each coverslip was imaged using a 20-25 position tilescan (~1mm^2 area) and a 1 micron voxel size.

Quantitative Analysis

Confocal volumes were assessed via custom algorithms designed in MATLAB (MathWorks, Natick, MA). Briefly, maximum projections of each tile-position per sample was filtered and segmented which enabled antibody intensity quantification and cell colony health evaluations. YAP intensity at nuclei and cytosol was quantified in N/TERT-1 and ASC52telo and the number of nuclei per sample was also quantified as an indication of cell-colony health after PFAS exposure. For ASC52telo cells, Ki67 was quantified at nuclei as an indication of proliferation. To evaluate dysregulation of the cytoskeleton of N/TERT-1 cells, expression of phalloidin (f-actin stain) and acetylated tubulin were quantified using concentric annular rings. Cells were identified using the phalloidin stain then two regions

were indicated. A peri-nuclear region (encompassing the nuclei) and a peripheral nuclear region was identified for each cell and the intensities of phalloidin and acetylated tubulin were quantified within the segments. For all analysis, each experimental condition quantification was based on at least 20 positions per coverslip, intensities were averaged per position per coverslip. For all analysis of confocal images, *n = 3* for N/TERT-1 cells for each timepoint and *n = 4* for all ASC52telo cells for each timepoint.

For quantification of adipogenesis, custom MATLAB algorithms were written to assess pixel area of ORO present in each control and dosed coverslips. Three phase contrast images were taken per well; cell coverage and ORO content was determined via image segmentation and averaged for each sample then ORO content was normalized to both the cell coverage of the sample and to the control of each experiment group (*n = 6*).

Statistics

Pairwise comparisons were performed using two tailed t-test, and variance analysis completed through one-way anova. Significance of $p < 0.05$ is denoted with one asterisk, while significance of $p < 0.01$ is denoted with a double asterisk. Results are indicated with medians.

Results

PFAS regulates cytoskeletal disruption

After exposing N/TERT1s to PFAS, localization of f-actin and acetylated tubulin expression within the cytosolic regions shifted. To quantify these expression differences, phalloidin staining established cell location through automated image segmentation. Stains of interest were found within the cell location and nuclei were found through segmentation

of the DAPI marker. Two annular regions were identified within cells, the first region encompassed the nuclei and the second region was on the edge of the cell boarder (**Figure 5.1 A).** Representative images of N/TERT-1 cells after 72 h of PFAS exposure demonstrate the shifts of acetylated tubulin and f-actin expression from control to experimental groups (**Figure 5.1B).** The ratio of the outer region to the inner region (R2:R1) was calculated (**Figure 5.1C**). At 24 hours after chemical exposure, there were not significant changes in acetylated tubulin or f-actin expression. At 72 hours after chemical exposure, there were significant drops in intensities of each stain from outer region (R2) to the inner region (R1) for some doses. Significant shifts in intensity of Acetylated tubulin were demonstrated for all doses: PFOA 100 μM ($p<0.05$), PFOA 125 uM ($p<0.05$), PFOS 30 μM ($p<0.01$), and PFOS 40 μM ($p<0.05$). Significant shifts in intensity of f-actin expression (phalloidin) were demonstrated with exposure to PFOA 125 μM ($p<0.05$), PFOS 30 μM ($p<0.01$), and PFOS 40 μM ($p<0.01$).

PFAS regulates YAP localization in epidermal cells

To investigate wheter PFAS acts on the Hippo Signaling pathway through YAP, we quantified YAP intensity at the nuclei and in the cytosol for each experimental dose at all timepoints using image segmentation (as described in the methods). Ratio of nuclear:cytosolic YAP are presented (**Figure 5.3).** Representative images show YAP expression in N/TERT-1 and ASC52telo cell lines at 72h and 48h exposures, respectively (**Figure 5.3 A**). Quantification of YAP intensities are given in **Figure 5.3 B**. YAP intensity in N/TERT1 cells under both doses of PFOA and PFOS at 72 h did exhibit significant shifts. In all cases, YAP intensity at the nuclei was greater than cytosolic YAP. At 24 h, N/TERT-1 cells did not demonstrate significant changes in YAP localization under PFOS or PFOA exposure

(**Figure 5.8**). At 48 h, ASC52telo cells showed no signficant shifts in distribution of YAP for either PFOA or PFOS.

PFAS effects cell viability in epidermal cells

Cell counts were measured as an indication of colony viability for both N/TERT-1 and ASC52telo. Nuclei were counted via automated image segmentation of DAPI expression (**Figure 5.4**). At 24 h, 40 μM PFOS induced a significant drop in nuclei counts (cell death) of N/TERT-1 ($p < 0.01$). Both doses of PFOA tested induced significant cell death at 72 hours ($p<0.01$ each) and both doses of PFOS induce significant cell death as well ($p<0.01$, each). From these data, we conclude that the tested doses of PFOA and PFOS are more toxic to the epidermal cell line at 72 h and PFOS is more toxic than PFOA. At 48 h, ASC52telo cell counts were stable with no significant changes for any dose of PFAS exposure. Because of the ASC stability under PFAS exposure, we also investigated whether PFAS may be affecting the proliferation of this cell line (**Figure 5.5**). Nuclei were segmented, as described in the methods, and Ki67 intensities at the nuclei were quantified. Neither PFOA or PFOS induced significant changes in proliferation of the ASC52telo cells, although there was more variability at high PFOS doses.

PFAS regulates adipogenesis

To understand the effect that PFAS chemicals have on adipogenic differentiation of the adipose derived stem cell line (ASC52telo), ASCs were exposed to PFAS chemicals over the course of a 19 day differentiation induced via adipogenic media. In this experiment, PFAS was dissolved in cell culture media and so for every media change, another dose of the PFAS chemical was given. To evaluate adipogenesis, fat cells were stained with Oil Red O to

mark lipid accumulation. Through automated image analysis, ORO pixel area was quantified then normalized to cell coverage and to the control. Data gathered show a significant increase in lipid droplets (ORO) in cells exposed to PFOA 100 μM ($p<0.05$), PFOS 30 μM ($p<0.05$), and PFOS 40 μM ($p<0.01$); statistical significance was determined by paired two-tailed t-tests.

Leptin and Adiponectin are two important adipokines secreted by mature adipose tissue [ref]. We evaluated amplification of leptin and adiponectin mRNA after 19 days of PFAS chemical exposure during adipogenesis (**Figure 5.7**). qPCR results indicate significant ($p < 0.01$) drops in amplification of Leptin mRNA under PFOS doses of 30 and 40 μM as compared to their control (respective medians of 0.208, 0.2046, and 1.009). No other significant changes were detected. We also investigated expression of Adiponectin mRNA, and results indicated no significant changes in expression.

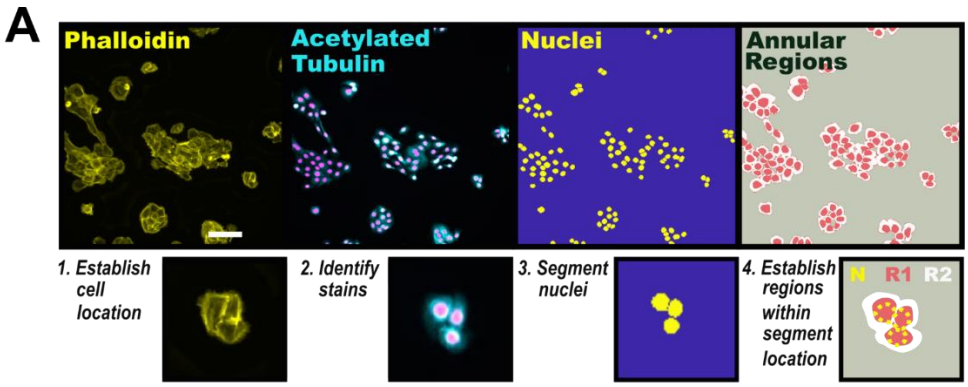
A
Phalloidin
Acetylated Tubulin
Nuclei
Annular Regions
1. Establish cell location
2. Identify stains
3. Segment nuclei
4. Establish regions within segment location
N
R1
R2

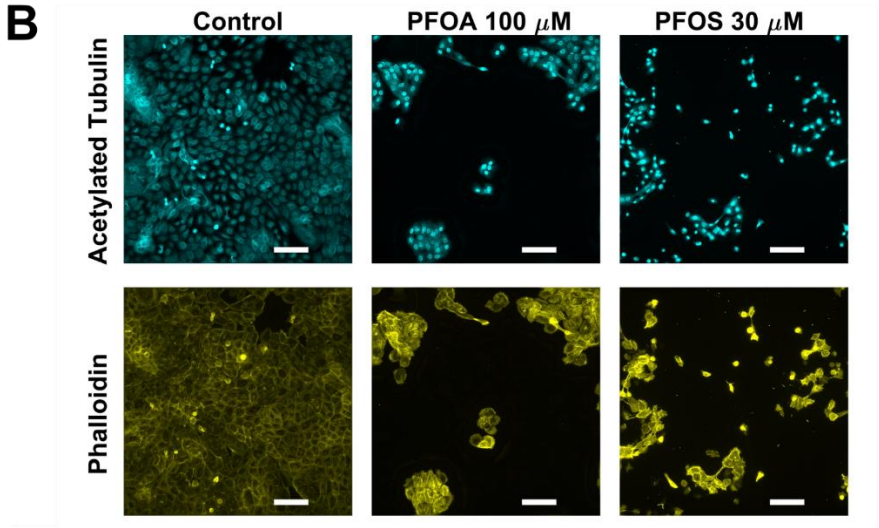
B
Control
PFOA 100 μM
PFOS 30 μM
Acetylated Tubulin
Phalloidin

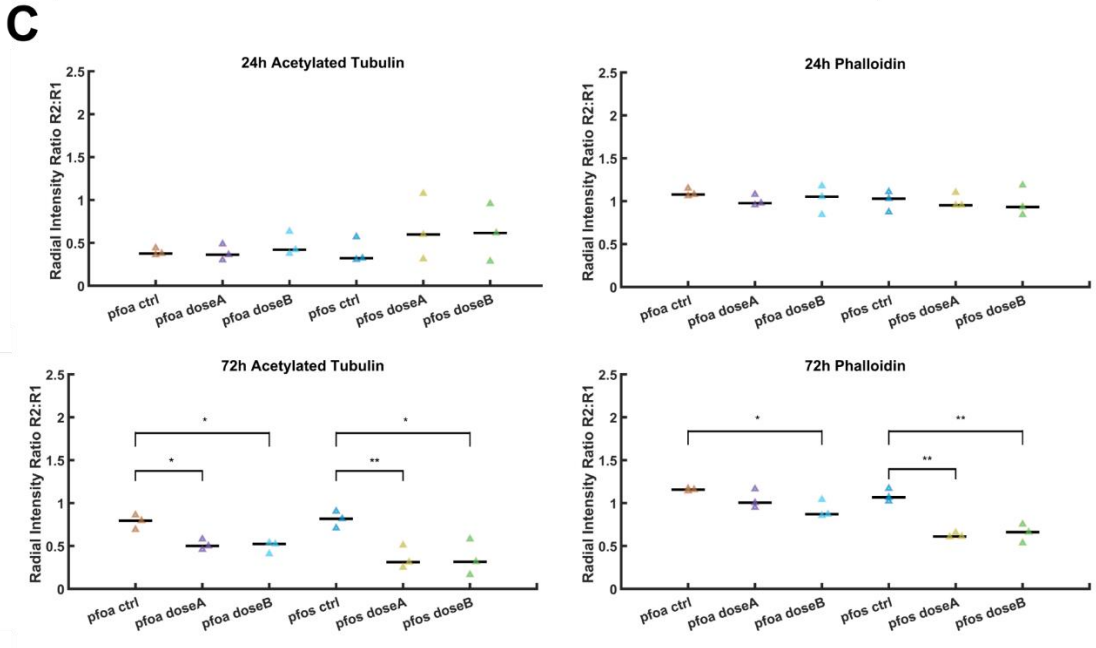
C
24h Acetylated Tubulin
24h Phalloidin
72h Acetylated Tubulin
72h Phalloidin
Radial Intensity Ratio R2:R1
pfoa ctrl
pfoa doseA
pfoa doseB
pfos ctrl
pfos doseA
pfos doseB

Figure 5.1 Radial Nuclear Intensity Quantification. A) Schematic of basic automated image segmentation process to isolate regions within cell. 1. Phalloidin (f-actin marker, yellow) is used to establish cell location mask and then 2) stains of interest are identified within those areas (Acetylated Tubulin-cyan, DAPI-magenta). 3)Nuclei are segmented based off of DAPI stain. 4. Two annular regions within the cell area are defined off of nuclei centroids. B) Representative images of the cytoskeletal markers Acetylated Tubulin and Phalloidin (marks f-actin) in N\TERT-1 cells after 72h PFAS treatment. C) Quantification of intensity is displayed as ratio of intensity (Region2:Region1). PFOA doses are A: 100 μM, B: 125 μM. PFOS doses are A: 30μM, and B: 40 μM. *n = 3.* At 24 h there are no significant changes in distribution of acetylated tubulin or f-actin for all experimental groups. At 72 h, all PFAS doses tested induce a shift in Acetylated tubulin staining toward region 1 ($p<0.05$ for all doses except for PFOS 30 μM ($p<0.01$)). Expression of f-actin intensities are also shifted toward region 1 for PFOA 125 μM ($p<0.05$) and PFOS 30 and 40 μM ($p<0.01$,each). Data shown as median (black bar) and individual data points (triangles). Scalebars are 100 μm.

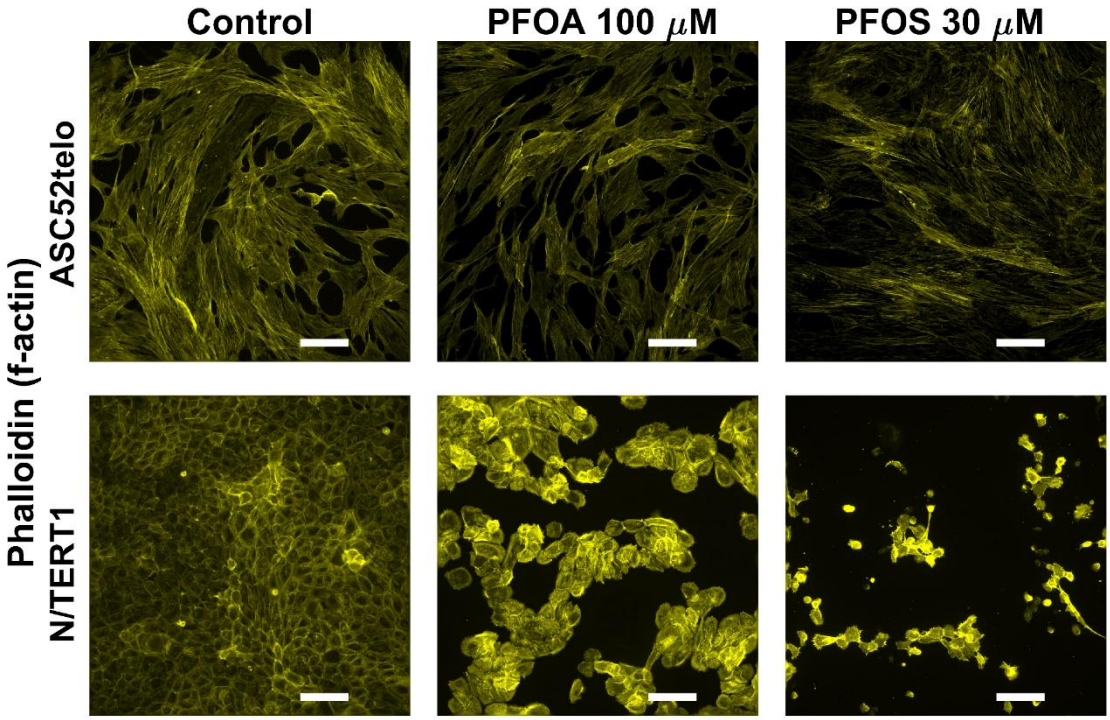

Figure 5.2. Cytoskeletal disruption. Phalloidin was used as an anti f-actin marker. Representative images of ASC52telos at 48 h and N/TERT-1 at 72 h are shown. Actin fiber dysregulation is demonstrated by the changes in bundling, fiber length, and alignment in ASCs. N/TERT-1 fiber dysregulation is demonstrated here general shifts in intensity and fiber localization and particularly noticeable are the prominent filopodia at cell edges. Scalebars are 100 μm.

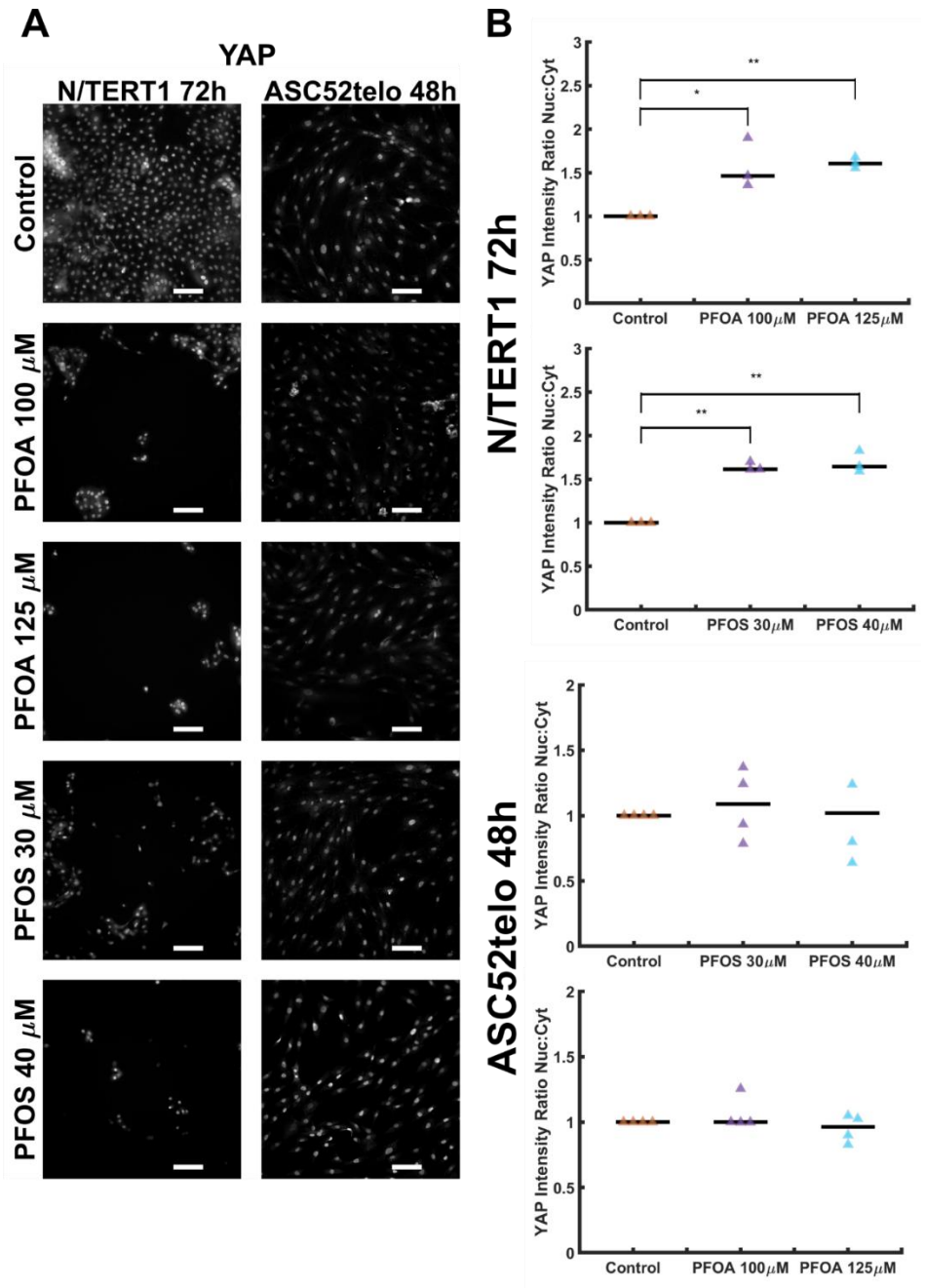

Figure 5.3. YAP localization. YAP intensities were quantified at the cytosol and nuclei for all experimental groups. Generally, there were not significant changes in localization of YAP with the exception of N/TERT-1s after 72 h of exposure of PFOS (30 and 40 μM; $p < 0.05$). In ASC52telos, after 48 h of exposure to PFOS 40 μM, there was a significant increase in nuclear and cytosolic YAP ($p<0.05$ at nuclei and $p<0.01$ at cytosol). For N/TERT-1 experiments, *n = 3;* for ASC52telo experiments, *n = 4.* Data shown as median (black bar) and individual data points (triangles). Scalebars are 100 μm.

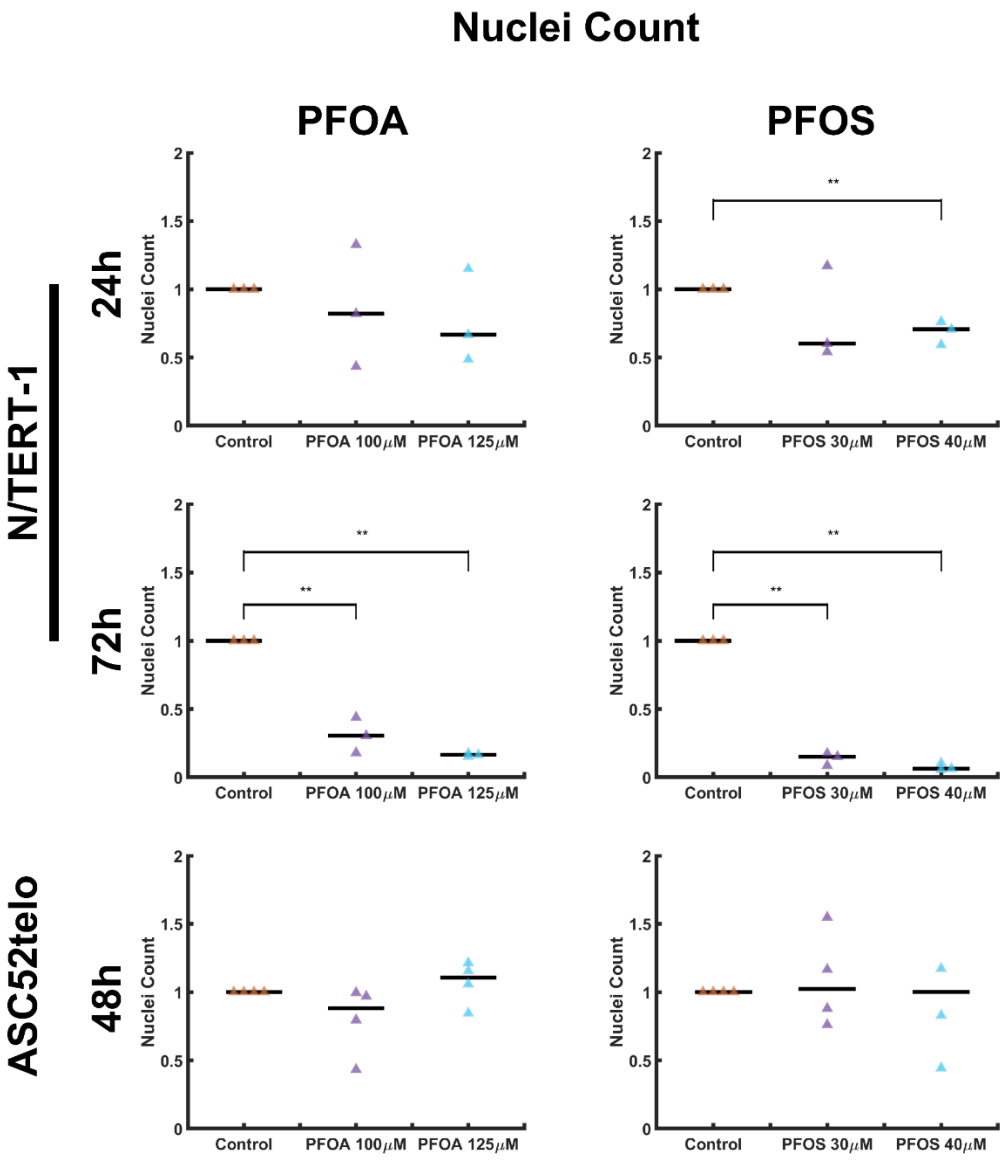

Figure 5.4. Nuclei Counts. Nuclei were identified through DAPI segmentation then automated counting was used to determine nuclei number per experimental group. At 24 h, PFOA induced no cell count changes while PFOS 40 μM induced a drop in counts, indicating high toxicity. At 72 h, All tested doses were detrimental to cell health as indicated with significant nuclei count changes (for all doses $p<0.01$). ASC52telo cells were stable after 48 h or PFAS exposure and exhibited no significant changes in nuclei counts. For N/TERT-1, *n = 3.* For ASC52telo, *n = 4.* Data shown as median (black bar) and individual data points (triangles).

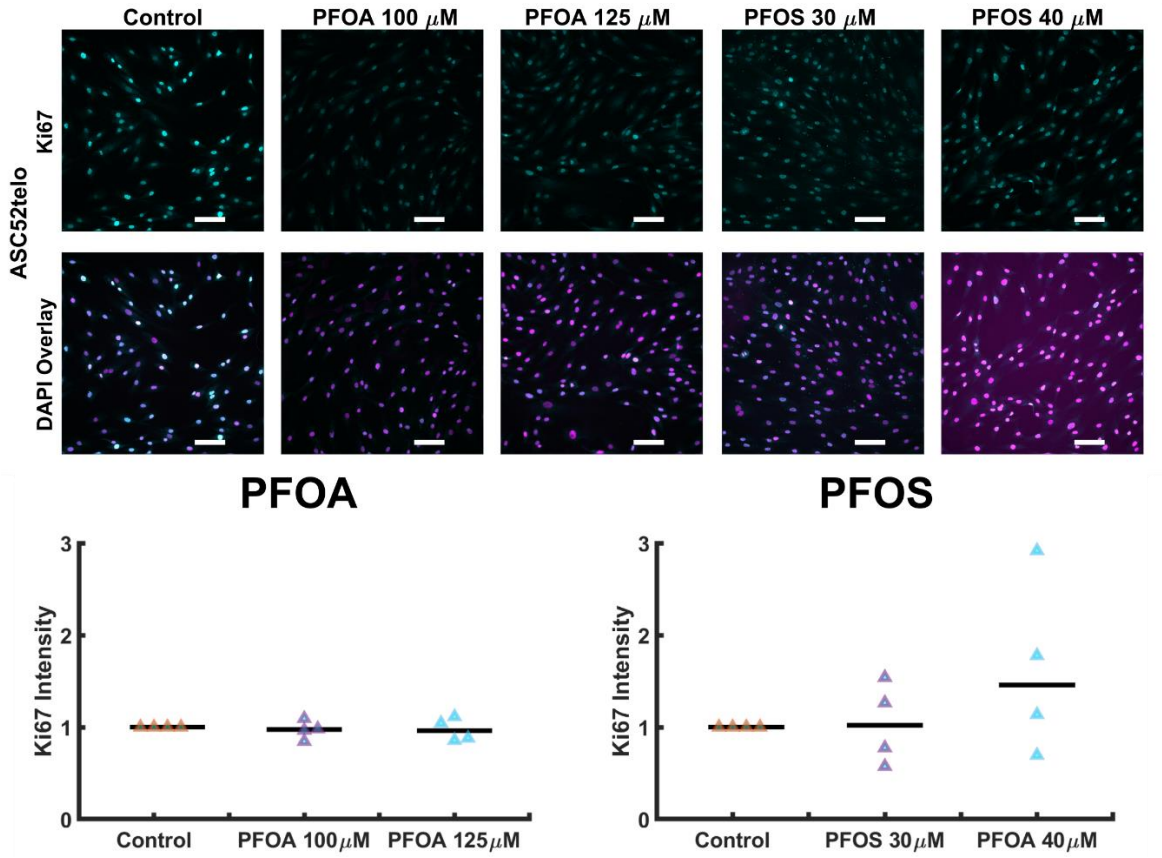

Figure 5.5. Proliferation of ASC52telo cells. Ki67 expression was used to determine proliferative capabilities of ASC52telos under PFAS chemical dosing. Nuclei were segmented via DAPI and Ki67 expression at cell nucleis were quantified. For both chemicals, there were no significant changes in proliferation ($p<0.05$). Data shown as median (black bar) and individual data points (triangles). Scalebars are 100 μm.

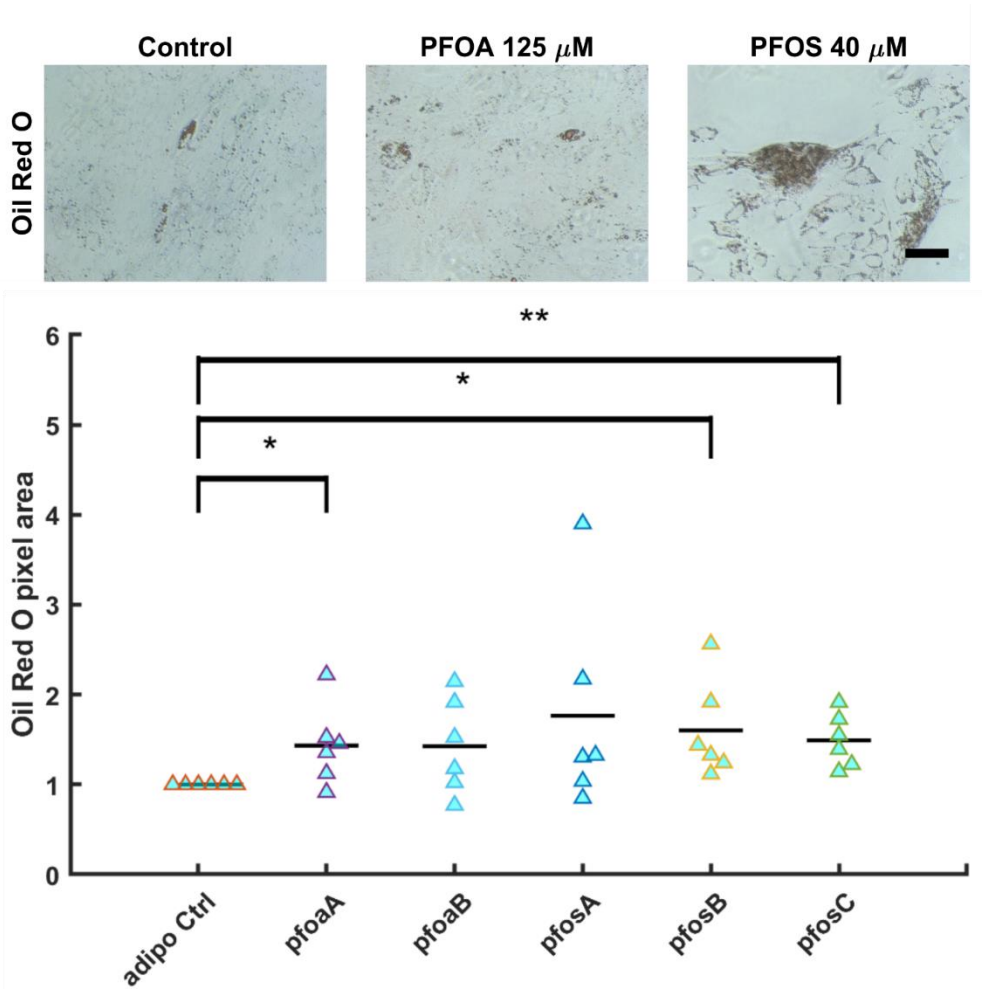

Figure 5.6. Oil Red O quantification. Representative images show Oil Red O staining of lipid droplets secreted by mature fat cells. Area of ORO was quantified via automated image analysis All data points were normalized to adipogenesis control and cell coverage. PFOA doses are A: 100 μM, B: 125 μM. PFOS doses are A: 20 μM, B: 30μM, and C: 40 μM. The PFAS doses PFOA 100 μM and PFOS 30 μM significantly increased lipid droplet presence ($p<0.05$). The high PFOS dose, 40 μM, also induced a difference ($p<0.01$). Scalebar is 250 microns. Data shown as median (black bar) and individual data points (triangles).

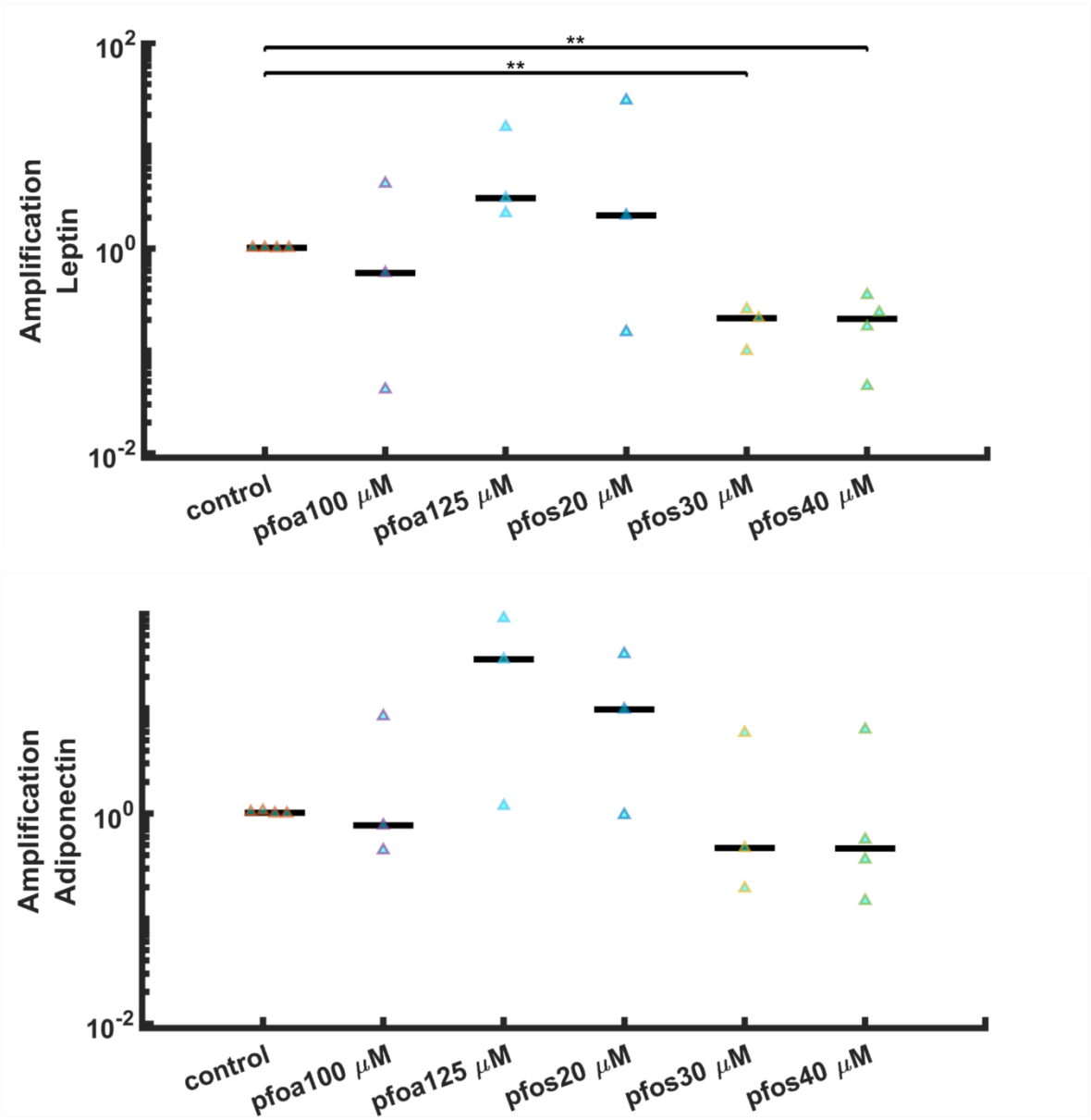

Figure 5.7. Gene amplification via qPCR. Adiponectin and Leptin are adipokines secreted by mature fat cells. Significant differences were found when comparing leptin mRNA expressions of high PFOS doses to control samples. No significant changes were found in mRNA expression of Adiponectin. Data shown on log scales as median (black bar) and individual data points (triangles).

Discussion

PFAS chemicals have stable and bioaccumulative properties which makes them particularly dangerous to biological membrane structures and to the environment in general[98,100,259–261]. Previous work has shown that higher maternal serum concentration of PFAS are associated with decreased birthweight but increased adiposity in infants and in pediatric/young adults, but the mechanism of these changes and toxicity of PFAS chemicals are still largely unknown [102,104,106,284,285,316]. Work in animal models has shown that PFAS chemicals have toxic effects and that in some cases these follow nonmonotonic responses[293,346,347]. Generally, there is a discrepancy in research doses of PFAS and environmental exposure and detection of PFAS. The U.S Environmental Protection Agency (EPA) set federal drinking water guideline limits for PFAS at 70 ng/L (for both PFOA and/or PFOS, individually or combined) but, as of 2019 only seven states developed guidelines varying from 13-1000 ng/L[348]. Several states do not have any guidelines at all or only have guidelines for one of many PFAS chemicals. Although the PFAS doses administered in this work are higher than the limitations set (1000 ng/L of PFOS is ~2 μM and of PFOA is ~ 2.4 μM), the bioaccumulative properties of PFAS are an important consideration. Guidelines set by the EPA cannot account for bioaccumulation and only apply to drinking water even though humans are exposed to PFAS through many avenues including high amounts from contaminated aquatic species[263,349]. Thus, there is a mismatch between what guidelines say are safe to consume and what humans are actually consuming or being exposed to. Further, bioaccumulative properties of PFAS chemicals are difficult to model *in vitro* and hard to discern *in vivo* because of environmental and body variability. In the experiments completed here, samples were given the same doses for each timepoint and were only dosed a single time. For example, the 72 h

timepoint experiments did not get exposed to more PFAS toxicant than the 24 hr timepoint, but the cells were exposed longer. For the adipogenesis assays, cells were exposed to PFAS at every media feeding, and therefore may have modeled bioaccumulation in a different way than the N/TERT-1s and undifferentiated ASC52telos.

To help understand underlying mechanisms of PFAS toxicity in human cells, we studied PFAS effects on cell monolayers. The data presented here show that PFAS effects cell and colony health, as determined by nuclear counts (**Figure 5.4**). Interestingly, ASC52telo cell monolayers that were exposed to PFAS remained stable 48 h after exposure and there was not a significant difference in cell number. To understand if PFAS had detrimental effects on proliferation of ASC52telos, we quantified the proliferative marker, Ki67 but concluded that these doses of PFOS and PFOA do not have significant effects on proliferative capacity of ASCs either. However, in agreement with past literature[346] that investigated PFAS effects in the African clawed frog, we show that PFOS and PFOA treatments induce significant declines in cell number of N/TERT-1 cells, and that these declines are greater at longer timepoints (72 h). Additionally, we similarly show that higher PFOS doses produce the greatest cell decreases but our results from PFOA exposure do not follow nonmonotonic relationships (with the low dose producing a greater cell decrease when compared to high dose) as previously shown in the African clawed frog cell monolayers [346]. Importantly, the high dose of PFOS used here (40 μM) is similar to the frog study where the high PFOA and PFOS dose was 10 μM. However, the low dose used for both chemicals from the frog study (1 nM) is not similar to our PFOA doses (100 and 125 μM). More investigation is required to understand if low doses of PFOA produce nonmonotonic effects in human cells.

PFAS chemicals have been found to disrupt f-actin, microtubules, and gap junctions of the cell cytoskeleton[269–273,337,338]. We have demonstrated that PFOA and PFOS disrupt the cytoskeletal components, acetylated tubulin and f-actin, in two human cell lines. Increased intensities and shifts in expression of acetylated tubulin and f-actin support cytoskeletal disruption by PFAS that has been reported in other studies[271]. As seen through f-actin fibers (**Figure 5.2**) , there were also differences in N/TERT-1 cell edges with increased presence of filipodia and prominent protrusions. It could be argued that these cytoskeletal changes are largely due to cell death and colony disruption due to PFAS toxicity, but we have demonstrated that there are cytoskeletal disruptions in ASC52telo cell lines as well. ASC cell lines were resistant to the cytotoxic effects of PFAS exposure and the number of cells and their proliferative capacities did not change after 48 h of exposure. Additionally, the cell death at 24 h seen with the high dose of PFOS (40 μM) did not correspond with radial distribution changes of cytoskeletal components. It is likely that cell death does play a part in the cytoskeletal disruption since colonies themselves are disrupted, but it does not seem to be the only mechanism here. PFAS likely perturbs the cytoskeleton independently of cell death, but this mechanism of action still requires more investigation.

A few groups have investigated cytoskeletal changes attributed to PFAS toxicity. Disruption has been demonstrated through actin filament remodeling, central actin stress fiber formation, microtubule and gap junction disorganization, and formation of lamellipodia and filipodia structures at cell periphery[271–273,337,338]. PFOS has been explicitly linked to disruption of blood testi barriers established by Sertoli cells in human[337] and animal studies[281,338,350] and thus, accumulation of testicular PFOS[350]. Barrier disruptions were attributed to the toxic effects of PFOS on f-actin, microtubule, and gap junction

organization. Specifically, dose dependent PFOS exposure disassembled tight and gap junctions responsible for barrier function of blood-testis barrier, increased blood-testis barrier permeability, and disrupted spermatogenesis[350]. PFAS chemicals have also demonstrated tight junction opening in brain endothelial cells, a main component of the blood-brain barrier, [272] and increases in reactive oxygen species that increases endothelial permeability[273]. PFOS was found to induce the remodeling of actin filaments through ROS production in human endothelial cells and increased gaps/breaks between endothelial cells in monolayers which resulted in increased permeability[273]. Authors observed formation of central cell actin stress fibers and the formation of lamellipodia and filopodia structures at cell periphery[273].

In alignment with the previous findings summarized, we observed the shift in f-actin expression toward the center of N/TERT-1 cells which could indicate formation of central stress fibers. The representative images shown display increased fiber formation near the center of the cells (**Error! Reference source not found.**, **Figure 5.2**). We also observed the formation of filopodia structures at cell edges which were observed due to ROS production by PFOS by Qian et al. Although we did not measure ROS production, is likely that these cell models are being affected in the same way; PFOS may increase ROS production by the host cell and in turn dysregulate the cytoskeleton. Importantly, previous literature showed that the disruptions caused to the cytoskeleton by PFAS increase permeability of crucial barriers such as the blood-brain barrier and the blood-testis barrier. Skin keratinocytes are responsible for formation of the skin barrier, but instead of working in a monolayer, keratinocytes differentiate into 4 different epidermal layers with the top corneal layer acting as the barrier[121]. N/TERT-1 cells are skin keratinocytes[124,154] and are what were used

for epidermal monolayer cultures in this work. We used these cells as a general model to study PFAS effects, but the implications of PFAS toxicity on epidermal skin cells are important in understanding PFAS absorption through the skin and the dangers it might cause to human health. The study of PFAS effects on skin tissue and cells is lacking with only a few investigations completed thus far using human tissue engineered skin and animal models[263–265]. PFAS was previously deemed to be not well absorbed through the skin by the US Environmental Protection Agency (EPA) in 2002[263], but since then, it has been demonstrated that after topical exposure, PFOA permeates human tissue engineered skin (epidermis and dermis containing fibroblasts only)[263,264], human and rat skin explants[265], and mouse skin (*in vivo*)[263]. In the mouse studies completed by Franko et al., it was demonstrated that there were dose-responsive increases in serum PFOA after dermal exposure and concluded that PFOA is dermally absorbed[263]. Han et al. showed that after 6 days of dermal exposure to PFOA (2.5 mM), there was decreased skin thickness and portions of degeneration in the epidermal layers and necrotic fibroblasts in human tissue engineered skin but did not observe decreases in cellular viability. They also demonstrated that after 2 weeks of dermal exposure in rats with another type of PFAS, short-chain perfluoroalkyl carboxylic acids (SC PFCA) rather than long, there were adverse effects on kidney, liver, testes, and skin that resulted in death via ulcerative dermatitis at application sites with high doses (1000 mg/kg)[264]. Our findings of PFAS toxicity and cytoskeletal dysregulation on N/TERT1 cells support the need for more research on dermal absorption of PFAS.

Previous investigations have concluded that tubulin acetylation plays a role in cell migration[351] and cell development and it has been concluded that alpha tubulin acetylation

helps to protect microtubules against mechanical stress and enhance microtubule flexibility[352]. Acetylation of alpha tubulin is a common post-translational modification of alpha tubulin that happens on stable microtubules [351,353]. Disrupted acetylation process can contribute to negative effects in cell polarization, cell division, adhesion, motility and have been linked to neurodegenerative disorders and tumor metastasis[352]. To our knowledge, no studies have investigated tubulin acetylation specifically in regards to PFAS toxicity. The work presented here demonstrates dysregulation of acetylated tubulin by differences in localization (signal collapse to perinuclear region) within N/TERT1 cells(**Error! Reference s ource not found.**) and further implicates PFAS as a cytoskeletal disrupter. These underlying roles of tubulin acetylation and f-actin and the consequences of dysregulation may be involved in the developmental changes of children and metabolic/reproductive toxicity changes in adults

Many studies have focused on YAP localization and Hippo signaling regarding organ size and development[318–323]. YAP and its upstream regulators have been investigated in liver, pancreas, intestine, kidney, lung, and bone but regulation through the Hippo pathway is different in each system. Disruption of YAP localization can cause several developmental problems in many organs. Notably, deletion of YAP in the lung epithelium of mice and humans was shown to cause defective lung development [318,354]; correct YAP localization in the cytoplasm is required for proximal airway maturation while nuclear YAP is required for progenitor specification. In the mouse kidney, deletion of YAP led to hypoplastic kidneys, fewer glomeruli, and defect formations in distal tubules and loop of Henle[318,330]. YAP is essential for nephron development and establishing kidney morphology and function[319,330,355,356]. YAP knockout has also been found to decrease bone formation and increases bone marrow fat[331]. The pancreas and liver have

been a focus of Hippo signaling pathway and organ development research. Rather than YAP knockout and upregulation, the Hippo pathway was altered via deletion/knockout of Mst1/2 in the pancreas[324] and deletion of Mst1/2 and Lats1/2 in the liver[318,324,326,328,333]. Changes in the levels of Hippo pathway regulators MST and LATS (upstream of YAP) and their effect on organ size poses other mechanisms of organ development dysregulation; in which Hippo is inactivated and nuclear YAP is upregulated. These too could be causes of changes in organ mass and body weight decrease during infancy and in mice have been shown to be a cause of decrease in pancreatic mass resulting in body weight differences[324]. Although the current study did not investigate knockout of YAP and PFAS effects, these summarized studies suggest that perturbation of YAP localization and Hippo signaling pathway activity by PFAS can lead to organ developmental changes and possible decreased body weight due to changes in organ size/mass tied to developmental issues.

To investigate the possibility that PFAS acts directly on the Hippo pathway effector, YAP, we studied localization of YAP in the cytosol and nuclei under PFAS exposure in the N/TERT-1 and ASC52telo cell lines. Through this work, data show that in N/TERT1 cells at the 72 h timepoint, expression of nuclear YAP increased for PFOS doses of 30 and 40 μM and PFOA doses of 100 and 125 μM. These data indicate that these PFAS chemicals regulate the Hippo pathway in N/TERTs through YAP/TAZ regulation. Because of the crosstalk between Hippo pathway and Rho/ROCK cytoskeletal perturbation, it is plausible that PFAS regulates Hippo through mechanosensing and extracellular matrix/focal adhesion changes that propagate through the Hippo mediator YAP/TAZ[331,334,335]. At the 24 h timepoint in N/TERT-1 cells and at 48 h in ASC52telo cells, there were no differences in YAP localization.

General mesenchymal stem cell polarization toward adipogenesis and osteogenesis is dependent on Hippo signaling and particularly related to YAP localization[331] . Reduced expression of upstream regulators of YAP such as Lats1/2 inhibit Hippo signaling and promote *in vitro* adipogenic and osteogenic differentiation, proliferation, and migration of bone marrow derived mesenchymal stem cells[357]. With increased nuclear localization of YAP, there is increased osteogenic differentiation. Conversely, with decreased nuclear localization of YAP (thus, increased cytosolic localization) there is increased adipogenic differentiation[319]. Though we did not directly quantify YAP in mature adipocyte cells under PFAS exposure, to aid in the understanding of adiposity changes, we explored PFAS' impact on mesenchymal stem cell differentiation toward adipogenesis. We found that some doses of PFOA and PFOS upregulated adipogenesis as measured by lipid droplet presence (**Figure 5.6**). qPCR results further support the finding that PFAS disrupts fat homeostasis, but instead of showing upregulation of fat markers, data shows downregulation of mRNA expressions of the adipokine leptin and no changes in Adiponectin (**Figure 5.7**). PFOA and PFOS upregulated adipogenesis indicated by lipid droplet analysis but the mechanism of action still requires more investigation especially in understanding the non-supporting mRNA expression results. One avenue that may elucidate changes in the adipogenic process is specifically investigating cytoskeleton changes that may occur when PFAS is present during adipogenesis. Here, we investigated cytoskeleton in pre-adipogenic ASC52telo cells under PFAS, but not changes during or after exposure through 19 days of differentiation. Cytoskeletal components are involved in the maturation and homeostasis of fat cells[336]. Our findings that PFAS chemicals disrupt cytoskeletal stability in skin and pre-adipose cells lend support to previous literature and suggest that the upregulation of adipogenesis could be due to the cytoskeletal perturbations. Palanivel et al. found, in rat cardiomyocytes, that an

increase in adiponectin induces cytoskeletal remodeling and increases membrane microvillar like protrustions and actin polymerization[341]. It is clear that PFAS is effecting pre-adipose and adipose cells, but it is unclear whether or not PFAS upregulates adipokines in mature fat cells which then disrupt the cytoskeleton through rho/rock and/or if PFAS acts directly on the cytoskeleton or not at all. In their undifferentiated state, ASC52telos did exhibit cytoskeletal changes including increase of protrustions at the cell boarder, shifts in cytoskeletal component intensities and location, and dysregulation of fibers (**Error! R eference source not found.** and **Figure 5.2**). Our findings show that PFAS exposure dysregulates adipogenesis. This dysregulation may be contributing to the PFAS associated increased adolescent obesity. Further investigation on lipid profiles and hormonal changes due to increased adipogenesis should be explored to help in understanding prior observations regarding increased childhood adiposity and higher PFAS serum concentrations.

The goal of this work was to better understand the mechanistic actions of PFAS on human cells specifically of their effect in altering the cell cytoskeleton and the Hippo signaling pathway. We investigated PFAS chemicals, PFOA and PFOS, for their effects on an adipose derived mesenchymal stem cell line (ASC52telo) and a keratinocyte skin cell line (N/TERT-1).-In conclusion, these data support previous findings that PFAS chemicals affect cytoskeletal integrity of the f-actin and microtubules and have demonstrated this in the human skin keratinocyte cell line, N/TERT-1 and the adipose derived mesenchymal stem cell line, ASC52telo. We also investigated if PFOA and PFOS directly effect the Hippo signaling pathway modulator, YAP. Our results support a direct modification of YAP localization by PFOA and PFOS chemicals. Finally, to gain an understanding into the

negative effects of PFAS chemicals on infant and adolescent bodyweight, we examined the adipogenic process under PFAS dosing. PFAS indeed upregulates the adipogenic process as quantified by presence of lipid droplets through ORO assays and qPCR. Key adipokines (leptin and adiponectin) were dysregulated in dose-dependent exposure to PFOA and PFOS. Although more investigation is required in understanding how PFAS specifically acts to upregulate adipogenesis, we speculate that the cytoskeleton changes involved in adipogenesis are being dysregulated and aiding in dysregulation of fat maturation. These findings reinforce the need for more in depth detection and more stringent limitations of PFAS exposure to the public, particularly pregnant mothers and children.

Acknowledgements

The authors would like to acknowledge Isabella Bagdesarian for her work in developing the nuclei/cytosolic localization algorithms used to quantify YAP. We also thank Dr. Jim Rheinwald and Dr. Ellen H. van den Bogaard for their generous gift of N/TERT cell lines.

Supplemental

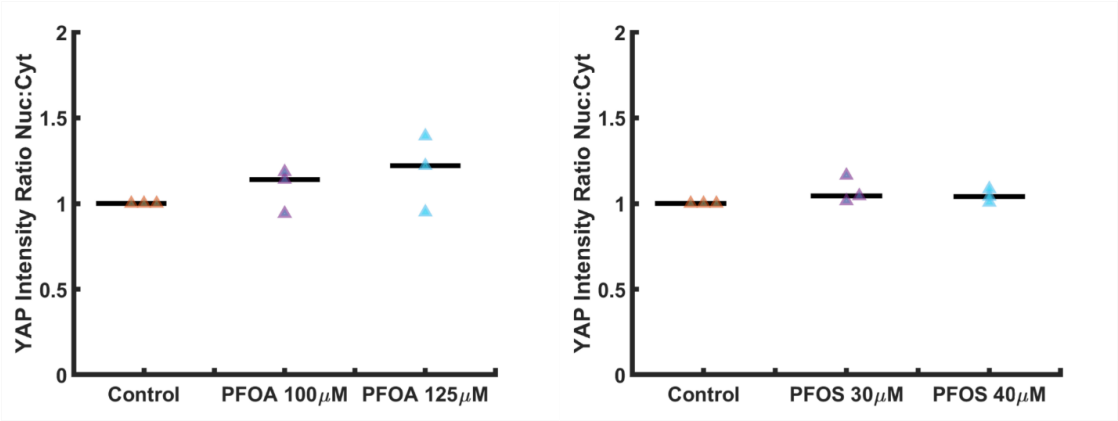

Figure 5.8 YAP localization in N/TERT-1 after 24 h timepoint. No significant changes were found. Medians are indicated by black bars and data points are triangles. (n = 3 biological controls).

Primers (human)			
Target	**Forward**	**Reverse**	**Notes**
Adiponectin	GGCTTTCCGGGAATCCAAGG	TGGGGATAGTAACGTAAGTCTCC	source (Hammel & Bellas, 2020).
Leptin	TGCCTTCCAGAAACGTGATCC	CTCTGTGGAGTAGCCTGAAGC	source (Hammel & Bellas, 2020)
Gapdh-1	ACA GTC AGC CGC ATC TTC TT	ACG ACC AAA TCC GTT GAC TC	

Table 5.1 Primer Sequences used for qPCR.

Antibodies/Stains Used			
Antibody/Stain	**Information & Source**	**Concentration**	**Notes**
DAPI	1X, diluted from a 100 x stock.	1X, made up in 1X PBS	Nuclear marker
Phalloidin	Phalloidin, Dylight™ 488, Cell Signaling	[1:500]	f-actin marker
Ki67			Proliferation marker. Used for ASC52telo staining
Primary			
Secondary			
YAP			Used for ASC52telo and N/TERT-1 staining.
Primary	YAP 1, rabbit, Proteintech, 13584-1-AP	[1:500]	
Secondary	Goat Anti-Rabbit IgG (H&L), DyLight™ 633 conjugated. Invitrogen	[1:500]	
Acetylated Tubulin			Used for N/TERT-1 staining.
Primary	Acetylated Tubulin, mouse, Santa Cruz, sc-23950	[1:500]	
Secondary	Goat Anti-mouse IgG, Dylight™ 550, at 1 mg/mL, Thermo Sci, #84540	[1:500]	
Blocking Buffer Recipe			
Reagent		***Amount***	

ddH_2O	450 mL
10 x PBS	50 mL
Bovine Serum Albumin (BSA)	5 g
Tween 20	0.5 mL
Cold water Fish Gelatin	1 g
Sodium Azide (10% Sodium Azide in diH_2O)	5 mL (0.1 % final concentration)
All exposure for stains and antibodies: 24 hours, rocking, 125 µL/well, 4 °C	

Table 5.2. Antibodies and stains used for evaluation.

Chapter 6
Conclusions

Three-dimensional organotypic models have been generated in the context of investigating aging and it is clear that this type of model has the potential to overcome several limitations of current aging models. In summary, organotypic models improve upon animal model organisms because they are not as costly to establish or maintain and specifically model human biology. This allows for re-capitulation of human disease and aging phenotypes that animals may not experience naturally or may experience differently [57,358]. Organotypic models improve upon two dimensional models because they incorporate structural-cell and cell-cell interactions which have shown to be complex in a 3D environment[11]. These models improve specifically upon organoid and microchips because of their size and volume. The scale of organotypic models is closer to human tissue and presents spatial challenges that human tissue presents, such nutrient deficiency in over 200 micron settings. Appropriately scaled models are especially important when investigating aging because in many cases, aging contributes to breakdown of 3D matrices and shape changes which often drives cell communication and homeostasis in tissues. In addition to these improvements on current models, the customizability that organotypic models offer is boundless.

Building upon and combining techniques used in previous work to incorporate them into organotypic constructs will generate comprehensive aging models that can readily be patient specific if necessary. Importantly, organotypic models are straightforward to customize and, with some optimization, can be a reliable and powerful tool to study biological and structural changes that occur with aging and aging associated diseases. This work in HSEs and AVHSEs, two types of organotypic skin models, demonstrates an

advancement in OSCs by adding vasculature and fat and developing three-dimensional analysis tools. We have validated our skin models through customization by including several cell types and modeling an aging study to demonstrate their use in understanding aging/aging associated diseases.

Additionally, PFAS chemicals are a threat to cell health and biological systems. The work shown here on two-dimensional investigation of how PFAS effects human epidermal cells and stem cells contributes to the understanding of PFAS actions. Specifically, PFAS action has been studied in human systems rather than animal and on the fat development process which has been linked to dysregulation with high PFAS serum concentrations in humans. Our results show that the PFAS chemicals PFOA and PFOS do not seem to regulate YAP/TAZ, but they do disrupt cytoskeletal health and upregulate adipokine markers and adipogenesis.

Chapter 7

Appendix

Chapter 2: Materials Table

Name of Material/ Equipment	Company	Catalog Number	Description/Comments
1 N NaOH	Fisher Chemical	S318-100	(Dilute from Lab stock)
4% Paraformaldehyde	ACROS Organics	#41678-5000, Lot # B0143461	Made up using solid Paraformaldehyde in PBS, pH adjusted to 6.9
Autoclaved forceps	Fine Science Tools	#11295-00	Dumont #5 forceps
CaCl2	Fisher bioreagents	Cat # BP510-250, Lot # 190231	Rnase, Dnase, Protease-Free
Cell line, Endothelial: Microvascular Endothelial Cell (HMEC1)	ATCC	CRL-3243	SV40 Immortalized microvascular endothelial cell. Note that 750,000 cells/mL of collagen were used.
Cell line, Fibroblasts: dermal Human fibroblast, adult	ATCC	PCS-201-012	Primary dermal cells. Note that 75,000 cells/mL of collagen were used.
Cell line, Fibroblasts: human lung firbroblast (IMR90)	ATCC	CCL-186	Primary embryonic cells. Note that 75,000 cells/mL of collagen were used.
Cell line, Keratinocyte: N/TERT-1			Immortalized via hTERT expression. N/TERT-1 was made using a retroviral vector conferring hygromycin resistance. Cell line established by Dickson et al. 2000. Can be replaced with ATCC PCS-200-010 or PCS-200-011. Note that 170,000 cells were used per construct; N/TERT1 cells must be used from plates that are 30% confluent- two 30% confluent 90 mm tissue culture dishes give more than enough cells.The authors thank Dr. Jim Rheinwald and Dr. Ellen H. van den Bogaard for their generous gift of N/TERT cell lines.
Centrifuge	Thermo Scientific; Sorvall Legend X1R		(standard lab equipment)
Computational Software	MATLAB	MATLAB 2020a	MathWorks, Natick, MA.
Confocal Microscope	Leica TCS SPEII confocal		Laser scanning confocal. Can be replaced with other confocals or deconvolution microscopy.
Cover Glass (22 x 22)	Fisher Scientific	12-545F	0.13-0.17 mm No.1 Thickness
Cyanoacrylate super glue or silicone grease	Glue Masters	#THI0102	Glue Masters, THICK, Instant Glue, Cyanoacrylate; super glue is preferred
DMEM media base	Corning; Mediatech, Inc	REF # 10-013-CM; Lot # 26119007	DMEM, 1X (Dulbecco's Modification of Eagle's Medium) with 4.5 g/L glucose, L-glutamine & sodium pyruvate
DMEM/F-12 50/50	Corning; Mediatech, Inc	REF # 10-090-CV; Lot # 21119006	DMEM/F-12 50/50, 1X (Dulbecco's Mod. Of Eagle's Medium/Ham's F12 50/50 Mix) with L-glutamine
Ethanol	Decon Labs	#V1101	(standard lab reagent)
Fetal Bovine Serum	Fisher Scientific	Cat # FB12999102, Lot # AE29451050	Research Grade Fetal Bovine Serum, Triple 0.1 um sterile filtered
Fine tip forceps	Fine Science Tools	#11295-00	Dumont #5 forceps
Human Epidermal Growth Factor (EGF)	Peprotech	Cat # AF-100-15-1MG, Lot # 0318AFC05 D0218	Made up in 0.1% BSA in PBS
Hydrocortisone	Alpha Easar	Lot # 5002F2A	made up in DMSO

Insulin (human)	Peprotech	Lot # 9352621	
Inverted Light/Phase Contrast Microscope	VWR	76317-470	(standard lab equipment)
Isoproterenol	Alfa Aesar	#AAJ6178806	DL-Isoproterenol hydrochloride, 98%
Keratinocyte-SFM (1x) media base	Gibco; Life Technologies Corporation	REF #: 10724-011; Lot # 2085518	Keratinocyte-SFM (1X); serum free medium
L-Ascorbic Acid	Fisher Chemical	Cat # A61-100, Lot # 181977, CAS # 50-81-7	Crystalline. L-Ascorbic acid can also be purchased as a salt
L-glutamine (solid)	Fisher Bioreagents	CAT # BP379-100, LOT # 172183, CAS # 56-85-9	L-Glutamine, white crystals or Crystalline powder
MCDB 131 media base	Gen Depot	CM034-050, Lot # 03062021	MCDB 131 Medium Base, No L-Glutamine, sterile filtered
Metal punches	Sona Enterprises (SE)	791LP, 12PC	Hollow Leather Punch Set, High Carbon Steel, Hardness: 48HRC; (various sizes including): 1/8", 5/32", 3/16", 7/32", 1/4", 9/32", 5/16", 3/4", 7/16", 1/2", 5/8:, 3/4". This punch set is helpful, but x-acto knife can work as well. Size of metal punch that works well for 12 well transwell VHSE is 3/8" or 1/2".
Methanol	Fisher Chemical	CAS # 67-56-1	(optional). For clearing dehydration step.
Methyl Salicylate	Fisher Chemical	O3695-500; Lot # 164535; CAS # 119-36-8	(optional). For clearing.
Microtubes, 1.7 mL	Genesee Scientific Corporation; Olympus Plastics	Cat # 24-282; Lot # 19467	1.7 ml Microtubes, Clear; Boilproof, Polypropulene, Certified Rnase, Dnase, DNA, PCR inhibitor and endotoxin-Free
PBS, 10x Culture grade or autoclaved	APEX Bioresearch Products	Cat # 20-134, Lot # 202237	PBS Buffer, 10x Dry Pack; add contents of pack into container and add water to 1 liter to produce 10x concentrated.
PBS, 1x Culture grade, (-) Calcium, (-) magnesium	Genesee Scientific Corporation	Ref # 25-508; Lot # 07171015	
PBS, 1x non-Culture grade	APEX Bioresearch Products	Cat # 20-134, Lot # 202237	PBS Buffer, 10x Dry Pack; add contents of pack into container and add water to 1 liter to produce 10x concentrated. Dilute to 1x with water.
Penicillin/Streptomycin	Gibco; Life Technologies Corporation	Ref # 15140-122, Lot # 2199839	Pen Strep (10,000 Units/mL Penicillin; 10,000 ug/mL Streptomycin)
Petri Dish, glass, small	Corning	PYREX 316060	(optional). To be used as a clearing container
Petri Dishes, 100 mm	Fisher Scientific	FB0875713	Use for making up PDMS.
Polydimethylsiloxane (PDMS)	Dow Corning	GMID 02065622, Batch # H04719H035	Sylgard 184 Silicone Elastomer Base, Dow Corning, Midland, MI)
	Dow Corning	GMID 02065622, Batch # H047JC4003	DOWSIL 184, Silicone Elastomer Curing Agent
			note: PDMS is usually sold as a kit that includes both the base and curing agent components.
Positive Displacement Pipettes (1000 & 250 uL)	Gilson	1000 uL: HM05136, M1000. 250 uL: T12269L	M1000 pipette capacity (100-1000 uL); M250 pipette capacity to 250 uL
Positive Displacement Tips/Pistons (1000 & 250 uL)	Gilson	1000 uL: CAT # F148180, BATCH # B01292902S; 250 uL: CAT # F148114, BATCH # B05549718S	Sterilized capillaries and pistons
Round tipped scoopula			(optional; standard lab equipment) For manipulation of VHSEs prior to imaging

Supplements for Keratinocyte-SFM media	Gibco; Life Technologies Corporation	Ref # 37000-015, Lot # 2154180	Contains EGF Human Recombinant (Cat # 10450-013), Bovine Pituitary Extract (Cat # 13028-014)
Tissue Culture Plate Inserts, 12 well size, 3 µm pore size	Corning; Costar	REF # 3462 - Clear; Lot # 14919057	Transwell; 12 mm Diameter Inserts, 3.0 um pore size, tissue culture treated, polyester membrane, polystyrene plates,
Tissue Culture Plates, 12 well size	Greiner Bio-one; CellStar	Cat # 665 180; Lot # E18103QT	12 well cell culture plate; sterile, with lid; products are sterile, free of detectable Dnase, Rnase, human DNA and pyrogens. Contents non-cytotoxic
Tissue Culture Plates, 60.8cm^2 growth area	Genesee Scientific Corporation	Cat # 25-202; Lot No: 191218-177B	Tissue culture dishes; treated, growth area 60.8 cm^2; sterile, Dnase, Rnase, Pyrogen Free; virgin polystyrene
Triton x 100	Ricca Chemical Company	Cat # 8698.5-16, Lot # 4708R34	Wetting agent
Trypsin 0.25%	Corning; Mediatech, Inc	Ref # 25-053-CI	0.25% Trypsin, 2.21 mM EDTA, 1x [-] sodium bicarbonate
Type 1 Collagen isolated from Rat tail	Pel-Freez Biologicals	56054-1	Sprauge-Dawley rat tails can be purchased frozen from Pel-Freez or other suppliers. Collagen can be isolated from the tail tendons. Isolation Protocol references [Cross et al.,2010; Rajan et al.,2007; Bornstein, 1958] .Alternatively, high concentration rat-tail collagen can be purchased from suppliers including Corning (Catalog Number: 354249)
Vaccum chamber, benchtop	Bel-Art	F42010-0000	(standard lab equipment)
Handheld Precision knife	X-Acto	X3311	(X-Acto knife optional if purchased steel punches)

Chapter 3: Thickness quantification of OCT and confocal data

OCT Thickness detection Shell Script

```
%shell for thickness detection
% (core script: OCTFrame_Test_JTM_MMS_publication)

%%
%Authors: Martina M. Sanchez, Joshua T. Morgan
%Lab: TIME lab, PI:Dr. Joshua Morgan, Bioengineering Department
%Institution: Univerisity of California, Riverside
%last edited 09/22/2021 MMS


% description: shell script-calls pre-processed OCT images
```

```
%% wk2
clearvars;clc;close all;
% 2wk (20200102)
% 20191204_1-4
AllFiles = ["D:\Martina\Temporary Data
Files\20200102_sample20191204\20200102_Skin_20191204_1\ProcessedData\1\AveragedFrames\*.m
at";...
    "D:\Martina\Temporary Data
Files\20200102_sample20191204\20200102_Skin_20191204_2\ProcessedData\1\AveragedFrames\*.m
at";...
    "D:\Martina\Temporary Data
Files\20200102_sample20191204\20200102_Skin_20191204_3\ProcessedData\1\AvgeragedFrames\*.
mat";...
    "D:\Martina\Temporary Data
Files\20200102_sample20191204\20200102_Skin_20191204_4\ProcessedData\1\AveragedFrames\*.m
at"];
FileName = ["sample 20191204_1 wk2";"sample 20191204_2 wk2";"sample 20191204_3
wk2";"sample 20191204_4 wk2"];
datey = [date ' wk2'];
OCTFrame_Test_JTM_MMS_publication
%% week 3
clearvars;clc;close all;
% 3wk (20200109)
% 20191204_1-4
AllFiles = ["D:\Martina\Temporary Data
Files\20200109_sample20191204\20200109_Skin_20191204_1\ProcessedData\1\AveragedFrames\*.m
at";...
    "D:\Martina\Temporary Data
Files\20200109_sample20191204\20200109_Skin_20191204_2\ProcessedData\1\AveragedFrames\*.m
at";...
    "D:\Martina\Temporary Data
Files\20200109_sample20191204\20200109_Skin_20191204_3\ProcessedData\1\AveragedFrames\*.m
at";...
    "D:\Martina\Temporary Data
Files\20200109_sample20191204\20200109_Skin_20191204_4\ProcessedData\1\AveragedFrames\*.m
at"];
FileName = ["sample 20191204_1 wk3";"sample 20191204_2 wk3";"sample 20191204_3
wk3";"sample 20191204_4 wk3"];
datey = [date ' wk3'];
OCTFrame_Test_JTM_MMS_publication
%% week 4
clearvars;clc;close all;
% 4wk (20200116)
% 20191204_1-4
AllFiles = ["D:\Martina\Temporary Data
Files\20200116_sample20191204_1\ProcessedData\1\AveragedFrames\*.mat";...
    "D:\Martina\Temporary Data
Files\20200116_sample20191204_2\ProcessedData\1\AveragedFrames\*.mat";...
    "D:\Martina\Temporary Data
Files\20200116_sample20191204_3\ProcessedData\1\AveragedFrames\*.mat";...
    "D:\Martina\Temporary Data
Files\20200116_sample20191204_4\ProcessedData\1\AveragedFrames\*.mat"];
FileName = ["sample 20191204_1 wk4";"sample 20191204_2 wk4";"sample 20191204_3
wk4";"sample 20191204_4 wk4"];
datey = [date ' wk4'];
OCTFrame_Test_JTM_MMS_publication
%% week 5

clearvars;clc;close all;
% 5wk (20200123)
% 20191204_1-4
AllFiles = ["D:\Martina\Temporary Data
Files\20200123_sample20191204_1\ProcessedData\1\AvgeragedFrames\*.mat";...
    "D:\Martina\Temporary Data
Files\20200123_sample20191204_2\ProcessedData\1\AveragedFrames\*.mat";...
    "D:\Martina\Temporary Data
Files\20200123_sample20191204_3\ProcessedData\1\AveragedFrames\*.mat";...
```

```
    "D:\Martina\Temporary Data
Files\20200123_sample20191204_4\ProcessedData\1\AveragedFrames\*.mat"];
FileName = ["sample 20191204_1 wk5";"sample 20191204_2 wk5";"sample 20191204_3
wk5";"sample 20191204_4 wk5"];
datey = [date 'wk5'];
OCTFrame_Test_JTM_MMS_publication

%% week 7
clearvars;clc;close all;

% 7wk (20200207)
% 20191204_1-4
AllFiles = ["D:\Martina\Temporary Data
Files\20200207_sample20191204_1\ProcessedData\1\AveragedFrames\*.mat";...
    "D:\Martina\Temporary Data
Files\20200207_sample20191204_2\ProcessedData\1\AveragedFrames\*.mat";...
    "D:\Martina\Temporary Data
Files\20200207_sample20191204_3\ProcessedData\1\AveragedFrames\*.mat";...
    "D:\Martina\Temporary Data
Files\20200207_sample20191204_4\ProcessedData\1\AveragedFrames\*.mat"];
FileName = ["sample 20191204_1 wk7";"sample 20191204_2 wk7";"sample 20191204_3
wk7";"sample 20191204_4 wk7"];
datey = [date ' wk7'];
OCTFrame_Test_JTM_MMS_publication

%% week 8
clearvars;clc;close all;
% 8wk (20200213)
% 20191204_1-4
AllFiles = ["D:\Martina\Temporary Data
Files\20200213_sample20191204_1\ProcessedData\1\AveragedFrames\*.mat";...
    "D:\Martina\Temporary Data
Files\20200213_sample20191204_2\ProcessedData\1\AveragedFrames\*.mat";...
    "D:\Martina\Temporary Data
Files\20200213_sample20191204_3\ProcessedData\1\AveragedFrames\*.mat";...
    "D:\Martina\Temporary Data
Files\20200213_sample20191204_4\ProcessedData\1\AveragedFrames\*.mat"];
FileName = ["sample 20191204_1 wk8";"sample 20191204_2 wk8";"sample 20191204_3
wk8";"sample 20191204_4 wk8"];
datey = [date ' wk8'];
OCTFrame_Test_JTM_MMS_publication
```

OCT Thickness detection Core Script & functions

```
%%% use with shell script (OCTFrame_ThicknessDetect_SHELL_publication)
%%
%Authors: Martina M. Sanchez, Joshua T. Morgan
%Lab: TIME lab, PI:Dr. Joshua Morgan, Bioengineering Department
%Institution: Univerisity of California, Riverside
%last edited 09/22/2021 MMS

% description: core script-uses pre-processed OCT images and detects thickness based on
% use inputted thresholds. functions needed are at the end
%%
close all
clc
clearvars -except AllFiles FileName datey
%% find code dependencies
[fList,pList] =
matlab.codetools.requiredFilesAndProducts('OCTFrame_Test_JTM_MMS_publication.m');
fList = fList';
%%
%use this script as a core and call the allfiles, filename, datey in shell
%% Set thresholds to detect upper and lower epidermal boarders
lowThreshy = [4200 8000];%set thresholds to detect lower boundary, can 1 or more
highThresh = 16000; %set thresholds to detect upper boundary. set 1 threshold
```

```
%% run

tic
for q = 1: length(lowThreshy);

    lowThresh = lowThreshy(q);
    fprintf('\n lowThresh%d begun \n',lowThresh)

for k = 1: length(AllFiles)
clearvars -except k lowThresh q datey FileName AllFiles lowThreshy highThresh
%% set locations
strData = AllFiles(k);
strGen = (['D:\Martina\OCT\AllThickness\' datey '\lowThresh' sprintf('%d', lowThresh)]);
%general location

%general location of thickness
if ~isdir(sprintf('%s',strGen))
    mkdir(sprintf('%s',strGen))
end

strDFP = 'D:\Martina\OCT\Processed\';; %Folder location to store data
sampleNum = [FileName(k)];

fprintf('\n running %s \n',sampleNum)


strProcessedData = ([ strDFP 'Gen' datey '\Thickness\lowThresh' sprintf('%d',
lowThresh)]);
strFigure = ([ strDFP 'Gen' datey '\Figures\lowThresh' sprintf('%d', lowThresh)]);

%Thickness Folder
    if ~isdir(strProcessedData)
        mkdir(strProcessedData)
    end

%Figure folder
    if ~isdir(strFigure)
        mkdir(strFigure)
    end

strDataPrefix = sprintf('%s Thickness Data',sampleNum); % prefix of saved data

%% load frames
FL = dir(AllFiles(k));
frames = 400;
IM = zeros(511,4096,frames,'uint16');

%load all frames
tic
for i = 1: frames
    fname = [FL(i).folder '\' FL(i).name];
    load(fname)

    IM(:,:,i) = uint16(pdFrame);
end
toc

%% filtering
fprintf('\n filtering begun \n')
se = strel('disk',40);
nhood = se.Neighborhood([12 40 12],:);
se = strel(nhood);

T = false(size(IM));
I2 = zeros(size(IM),'uint16');
```

```
I2 = imclose(IM,se);
I3 = imgaussfilt3(I2,[1.5 8 1.5]);

[~,T] = hysteresis3draw(I3,lowThresh,highThresh); %potentially rescale I3 based on local
surface intensity

%find the largest object, which should be the surface
%save as T2
CC = bwconncomp(T);
s = regionprops3(CC,'Volume');
[~,ind] = max([s.Volume]);
T2 = false(size(T));
T2(CC.PixelIdxList{ind}) = true;

%close to fill in gaps
se2 = strel('disk',40);
nhood = se2.Neighborhood([4:9:79],:);
se2 = strel(nhood);

T3 = imclose(T2,se2);

%find and fill in gaps in the top surface
[~,TopSurf] = max(T3,[],1); %identify the top surface using a quirk of max()
TopSurf = squeeze(TopSurf)+1;
TopSurf2 = regionfill(TopSurf,TopSurf==1);

%find "pits" that represent apical artifacts
[x,y] = derivative5(TopSurf2,'x','y');
G = sqrt(x.^2+y.^2); %find gradient magnitudes
G([1:2 end-1:end],:) = 0; %trim edges
G(:,[1:2 end-1:end]) = 0; %trim edges

ses = strel('disk',100);
nhood = ses.Neighborhood(:,1:3:end);
ses = strel(nhood);

Gb = imbothat(G,ses);
Sb = imbothat(TopSurf2,ses);

Ts = hysthresh(Gb+Sb,15,5);

TopSurf3 = regionfill(TopSurf2,Ts); %fill in pits

%Find bottom surface
[~,BotSurf] = max(flipud(T3),[],1); %identify the bottom surface using a quirk of max()
BotSurf = squeeze(BotSurf);
BotSurf2 = regionfill(BotSurf,BotSurf==1);
BotSurf2 = size(IM,1)-BotSurf2+1; %readjust to account for flipping.

%find "peaks" that represent basal artifacts
ses = strel('disk',40);
nhood = ses.Neighborhood(:,1:4:end);
ses = strel(nhood);

Sb = imtophat(BotSurf2,ses);
Ts = hysthresh(Sb,10,9);
BotSurf3 = regionfill(BotSurf2,Ts); %flatten the peaks

%find "plataeus" that represent basal artifacts
ses = strel('disk',100);
nhood = ses.Neighborhood(:,1:4:end);
ses = strel(nhood);

BotSurf4 = imclose(BotSurf3,ses);
disp('end filtering')
%% set scale and scalebar positions
XstartSB=3000; %scale bar start position, xaxis
```

```
YposSB=425; %scale bar start position, yaxis
xPixel=4/4096; %pixel to  mm conversion in x direction (4mm/4096 pixels)
nPixel = 2/511; %pixel to mm conversion in z direction (2mm/pixxels)
close all
%%  generate figure gif (takes a long time)
figure(1);
PS = [6 4];
  set(gcf,'units','inches','position',[2 2 PS],'Color','w',...
    'PaperUnits','inches','PaperSize',PS,'PaperPosition',[0 0 PS]) ;

for i = 1:size(IM,3)

    tline = TopSurf3(:,i);
    bline = BotSurf4(:,i);

    axes('units','inches','position',[0 0 PS]);
    imagesc(imadjust(imcomplement(IM(:,:,i))),'CDataMapping', 'scaled');

    set(gca,'visible','off');

    hold on
    colormap('gray')
    plot(tline,'c','LineWidth',2)
    plot(bline,'m','LineWidth',2)

%     x = [XstartSB XstartSB+500/(xPixel*1000) XstartSB XstartSB];
%     y = [YposSB YposSB YposSB YposSB-500/(nPixel*1000)];
%
%     %create a 100 um scalebar by plotting a line. Because MATLAB scales images to
%     %pixels, the values you see are in pixels
%     plot(XstartSB, y),'w','linewidth', 6,'Rotation',90);
% line([XstartSB, XstartSB],y);
    %         plot(XstartSB,y,'w','lineWidth',7,'miter')

% %DISPLAY 500um IN TEXT ABOVE THE SCALEBAR
%     text((XstartSB+250/(xPixel*1000)),YposSB-3 ,'500
\mum','horizontalalignment','center',...
%
'verticalalignment','bottom','fontweight','bold','color','w','fontsize',14,'Rotation',90)
;


hi = figure(1);
frame = getframe(hi);
im = frame2im(frame);

[im,map] = rgb2ind(frame.cdata,colorcube(256),'nodither'); %define a colormap to be used
for the GIF


%assign indexed data to an image plane
    im(:,:,1,i) = rgb2ind(frame.cdata,map,'nodither');

    % Write to the GIF File
    name = sprintf('%s\\ThicknessVis_%s.gif',strFigure,sampleNum);
    if i == 1
        imwrite(im,map,name,'gif', 'Loopcount',inf);
    else
        imwrite(im,map,name,'gif','WriteMode','append');
    end
end
    % Write to the GIF File
    name = sprintf('%s\\ThicknessVis_%s.gif',strFigure,sampleNum);
    if i == 1
        imwrite(im,map,name,'gif', 'Loopcount',inf);
    else
        imwrite(im,map,name,'gif','WriteMode','append');
```

```
        imwrite(im,map,name, 'DelayTime',0.002,'LoopCount',inf)
    end
%% output variables

%pixel thickness
for i = 1:size(TopSurf3,1)
for    j = 1:size(TopSurf3,2)
    fPixelThickness(i,j) = BotSurf4(i,j)-TopSurf3(i,j);
end
end

fMetricThickness(:,:) = (fPixelThickness.* nPixel).*1e3;
fAvgMetricThick = mean(fMetricThickness,'all');
trimMetricThick(:,:) = fMetricThickness(30:4066,:);%trim sides of image
trimAvgMetricThick = mean(trimMetricThick,'all');
fSdMetricThick = std(trimMetricThick(:));
IQRMetricThick = iqr(trimMetricThick(:));
%% save data
disp('saving data')
SaveVar1 = ([strProcessedData '\' strDataPrefix '.mat']);
save(SaveVar1,'fPixelThickness','nPixel','xPixel' ,'fMetricThickness',...
    'fAvgMetricThick', 'trimMetricThick','trimAvgMetricThick',...
    'fSdMetricThick','IQRMetricThick');

%save a metric average and std for each sample number but append it to existing mass
sample thickness file
SaveThickness = ([strGen '\' strDataPrefix '.mat']);
save(SaveThickness,'fPixelThickness','nPixel','xPixel' ,'fMetricThickness',...
    'fAvgMetricThick', 'trimMetricThick','trimAvgMetricThick',...
    'fSdMetricThick','IQRMetricThick');

end
%%
end
toc
return


%% functions ************************************************
%% hysteresis3draw
function [tri,hys]=hysteresis3draw(img,t1,t2,conn)
% function [tri,hys]=HYSTERESIS3D(img,t1,t2,conn)
%
% Hysteresis3d is a simple function that performs trinarisation and
% hysteresis for 2D and 3D images. Hysteresis3d was inspired by Peter
% Kovesi's 2D hysteresis function
% (http://www.csse.uwa.edu.au/~pk/research/matlabfns/). This 3D function
% takes advantage of the 3D connectivities of imfill instead of the 2D
% connectivities of bwselect.
%
% Usage:        [tri,hys]=HYSTERESIS3D(img,t1,t2,conn)
%
% Arguments:    img - image for hysteresis (assumed to be non-negative)
%               t1 - lower threshold value (fraction b/w 0-1, e.g.: 0.1)
%               t2 - upper threshold value (fraction b/w 0-1, e.g.: 0.9)
%                   (t1/t2 can be entered in any order, larger one will be
%                   set as the upper threshold)
%               conn - number of connectivities (4 or 8 for 2D)
%                                               (6, 18, or 26 for 3D)
% Returns:
%               tri - the trinarisation image (values are 0, 1, or 2)
%               hys - the hysteresis image (logical mask image)
%
% Examples:     [tri,hys]=HYSTERESIS3D(img,0.25,0.8,26)
%
% 2012/07/10: written by Luke Xie
% 2013/12/09: defaults added
```

```
%
% To see an example of hysteresis used to segment a kidney region, please
% refer to supplement in QSM of Kidney, NMR Biomed, 2013 Dec;26(12):1853-63
% (http://onlinelibrary.wiley.com/doi/10.1002/nbm.3039/abstract).
% Supplemental material is also available on our CIVMspace:
% http://www.civm.duhs.duke.edu/lx201204/

%% arguments
if nargin<3
    disp('function needs at least 3 inputs')
    return;
elseif nargin==3
    disp('inputs=3')
    if numel(size(img))==2;
        disp('img=2D')
        disp('conn set at 4 connectivies (number of neighbors)')
        conn=4;
    end
    if numel(size(img))==3;
        disp('img=3D')
        disp('conn set at 6 connectivies (number of neighbors)')
        conn=6;
    end
end

%% DO NOT scale t1 & t2 based on image intensity range
if t1>t2    % swap values if t1>t2
    tmp=t1;
    t1=t2;
    t2=tmp;
end
t1v=t1;
t2v=t2;

%% trinarisation
tri=zeros(size(img));
tri(img>=t1v)=1;
tri(img>=t2v)=2;

%% hysteresis
abovet1=img>t1v;                                        % points above lower threshold
seed_indices=sub2ind(size(abovet1),find(img>t2v));   % indices of points above upper
threshold
hys=imfill(~abovet1,seed_indices,conn);              % obtain all connected regions in
abovet1 that include points with values above t2
hys=hys & abovet1;

%% functions ************************************************
%% HYSTHRESH - Hysteresis thresholding
%
% Usage: bw = hysthresh(im, T1, T2)
%
% Arguments:
%             im  - image to be thresholded (assumed to be non-negative)
%             T1  - upper threshold value
%             T2  - lower threshold value
%                   (T1 and T2 can be entered in any order, the larger of the
%                   two values is used as the upper threshold)
% Returns:
%             bw  - the thresholded image (containing values 0 or 1)
%
% Function performs hysteresis thresholding of an image.
% All pixels with values above threshold T1 are marked as edges
% All pixels that are connected to points that have been marked as edges
% and with values above threshold T2 are also marked as edges. Eight
% connectivity is used.
```

```
% Copyright (c) 1996-2005 Peter Kovesi
% www.peterkovesi.com/matlabfns/
%
% Permission is hereby granted, free of charge, to any person obtaining a copy
% of this software and associated documentation files (the "Software"), to deal
% in the Software without restriction, subject to the following conditions:
%
% The above copyright notice and this permission notice shall be included in all
% copies or substantial portions of the Software.
%
% The Software is provided "as is", without warranty of any kind.

% December 1996  - Original version
% March    2001  - Speed improvements made (~4x)
% April    2005  - Modified to cope with MATLAB 7's uint8 behaviour
% July     2005  - Enormous simplification and great speedup by realizing
%                  that you can use bwselect to do all the work

function bw = hysthresh(im, T1, T2)

    if T1 < T2    % T1 and T2 reversed - swap values
    tmp = T1;
    T1 = T2;
    T2 = tmp;
    end

    aboveT2 = im > T2;                      % Edge points above lower
                                            % threshold.
    [aboveT1r, aboveT1c] = find(im > T1);   % Row and colum coords of points
                                            % above upper threshold.

    % Obtain all connected regions in aboveT2 that include a point that has a
    % value above T1
    bw = bwselect(aboveT2, aboveT1c, aboveT1r, 8);


%% functions ************************************************
%% derivative5
% DERIVATIVE5 - 5-Tap 1st and 2nd discrete derivatives
%
% This function computes 1st and 2nd derivatives of an image using the 5-tap
% coefficients given by Farid and Simoncelli.  The results are significantly
% more accurate than MATLAB's GRADIENT function on edges that are at angles
% other than vertical or horizontal. This in turn improves gradient orientation
% estimation enormously.  If you are after extreme accuracy try using DERIVATIVE7.
%
% Usage:  [gx, gy, gxx, gyy, gxy] = derivative5(im, derivative specifiers)
%
% Arguments:
%                       im - Image to compute derivatives from.
%    derivative specifiers - A comma separated list of character strings
%                            that can be any of 'x', 'y', 'xx', 'yy' or 'xy'
%                            These can be in any order, the order of the
%                            computed output arguments will match the order
%                            of the derivative specifier strings.
% Returns:
%  Function returns requested derivatives which can be:
%     gx, gy   - 1st derivative in x and y
%     gxx, gyy - 2nd derivative in x and y
%     gxy      - 1st derivative in y of 1st derivative in x
%
%  Examples:
%    Just compute 1st derivatives in x and y
%    [gx, gy] = derivative5(im, 'x', 'y');
%
%    Compute 2nd derivative in x, 1st derivative in y and 2nd derivative in y
%    [gxx, gy, gyy] = derivative5(im, 'xx', 'y', 'yy')
```

```
%
% See also: DERIVATIVE7

% Reference: Hany Farid and Eero Simoncelli "Differentiation of Discrete
% Multi-Dimensional Signals" IEEE Trans. Image Processing. 13(4): 496-508 (2004)

% Copyright (c) 2010 Peter Kovesi
% www.peterkovesi.com/matlabfns/
%
% Permission is hereby granted, free of charge, to any person obtaining a copy
% of this software and associated documentation files (the "Software"), to deal
% in the Software without restriction, subject to the following conditions:
%
% The above copyright notice and this permission notice shall be included in
% all copies or substantial portions of the Software.
%
% The Software is provided "as is", without warranty of any kind.
%
% April 2010
% May   2019 - Correction to calculation of dxy. Thanks to Sebastian Gesemann.

function varargout = derivative5(im, varargin)

    varargin = varargin(:);
    varargout = cell(size(varargin));

    % Check if we are just computing 1st derivatives.  If so use the
    % interpolant and derivative filters optimized for 1st derivatives, else
    % use 2nd derivative filters and interpolant coefficients.
    % Detection is done by seeing if any of the derivative specifier
    % arguments is longer than 1 char, this implies 2nd derivative needed.
    secondDeriv = false;
    for n = 1:length(varargin)
        if length(varargin{n}) > 1
            secondDeriv = true;
            break
        end
    end

    if ~secondDeriv
        % 5 tap 1st derivative cofficients.  These are optimal if you are just
        % seeking the 1st deriavtives
        p = [0.037659  0.249153  0.426375  0.249153  0.037659];
        d1 =[0.109604  0.276691  0.000000 -0.276691 -0.109604];
    else
        % 5-tap 2nd derivative coefficients. The associated 1st derivative
        % coefficients are not quite as optimal as the ones above but are
        % consistent with the 2nd derivative interpolator p and thus are
        % appropriate to use if you are after both 1st and 2nd derivatives.
        p  = [0.030320  0.249724  0.439911  0.249724  0.030320];
        d1 = [0.104550  0.292315  0.000000 -0.292315 -0.104550];
        d2 = [0.232905  0.002668 -0.471147  0.002668  0.232905];
    end

    % Compute derivatives.  Note that in the 1st call below MATLAB's conv2
    % function performs a 1D convolution down the columns using p then a 1D
    % convolution along the rows using d1. etc etc.

    for n = 1:length(varargin)
      if strcmpi('x', varargin{n})
          varargout{n} = conv2(p, d1, im, 'same');
      elseif strcmpi('y', varargin{n})
          varargout{n} = conv2(d1, p, im, 'same');
      elseif strcmpi('xx', varargin{n})
          varargout{n} = conv2(p, d2, im, 'same');
      elseif strcmpi('yy', varargin{n})
          varargout{n} = conv2(d2, p, im, 'same');
```

```
      elseif strcmpi('xy', varargin{n}) || strcmpi('yx', varargin{n})
          varargout{n} = conv2(d1, d1, im, 'same');
      else
          error('''%s'' is an unrecognized derivative option',varargin{n});
      end
    end
```

Confocal Thickness detection Shell Script

```
%% epidermal Thickness quant
%Authors: Martina M. Sanchez, Joshua T. Morgan
%Lab: TIME lab, PI:Dr. Joshua Morgan, Bioengineering Department
%Institution: Univerisity of California, Riverside

% Most Recent Edit: 202110801

% requires bioformats toolbox
    % https://docs.openmicroscopy.org/bio-formats/6.1.0/index.html

%description: shell script to quantify thickness of confocal images

%%
clearvars
close all
clc
%% set file feeder location
strData = 'D:\Martina\3D HSE_HEE_VHSE analysis\VHSE epidermal analysis\';
FileList = dir([strData, '*.lif']);
%% general save directory
outdir1 = 'D:\Martina\3D HSE_HEE_VHSE analysis\VHSE epidermal
analysis\EpidermalIntensityQuant\';
% cd('D:\Martina\3D HSE_HEE_VHSE analysis\VHSE epidermal analysis')
dataLoc = [outdir1 'QuantData\generated_' date '\'];%where to store all of the
mean intensities in one lcation
if ~isdir(sprintf('%s\\',dataLoc))
    mkdir(sprintf('%s\\',dataLoc))
end
%% all variable mass cell
varCell = cell(size(FileList,1),1);
volThickness = cell(size(FileList,1),1);
%% Select File to open
%Filename you want to open % change this location to where your image file
%is located
for h = 1: length(FileList)
clearvars -except keepVariables allFiles h strData FileList outdir1 varCell...
    varNum dataLoc volThickness
close all
clc
IM_FILE = FileList(h).name;
%%%%%%%%%%%%%%%%%%%%%%%%%%%%%%%%%%%%%%%%%%%%%%%%%%%%%%%%%%%%%%%%%%%%%%%%%%%%
%% Open File (takes time)
%Using the Bioformats Toolbox, we can extract most life sciences formats
%into a consistant structure
 tic;A = bfopen(IM_FILE);toc; %prompts to choose file in computer window
 fprintf('finished opening file');
%%%%%%%%%%%%%%%%%%%%%%%%%%%%%%%%%%%%%%%%%%%%%%%%%%%%%%%%%%%%%%%%%%%%%%%%%%%%
%% Save Directory
% change location based on where you want your images to be saved
BaseFileName = sprintf('M%s', IM_FILE(1:end-4));
varCell{h,1} = BaseFileName;
volThickness{h,1} = BaseFileName;
```

```
%% Define file names appropriate for File
fprintf('\n file name is'); IM_FILE

%% prep output folder for file
outdir2 = sprintf('Output %s\\%s\\',date,BaseFileName);

folderLoc = [outdir1 outdir2];
if ~isdir(sprintf('%s',folderLoc))
    mkdir(sprintf('%s',folderLoc))
end

outdir3 = 'thickness';
folderLocA = [outdir1 outdir2 outdir3];
if ~isdir(sprintf('%s',folderLocA))
    mkdir(sprintf('%s',folderLocA))
end
%% use this section to generate all images for every series
%%%use bioformats toolbox functions
lengthA = length(A(:,1));

%Open the OME metadata to access information about the image, such as
%number of slices, channels, and pixel size
reader = bfGetReader(IM_FILE); %the reader variable is a pointer to the file
omeMeta = reader.getMetadataStore(); %pull OME metadata
nS = reader.getSeriesCount(); %number of series
Sname = cell(nS,1);
%% use image prop 2 files for each loaded lif file.
%check epidermal lif file key to know series numbers
%-define series needed as sery
%-define channels per file

T1 = contains(IM_FILE,['20191204_1']);
if T1
    sery = 10:18; %imgprop2

FirstCh = 'Fil'%sprintf ('%s',p2);
SecndCh = 'Inv';%sprintf ('%s',p3);
ThirdCh = 'D7'%sprintf ('%s',p4);
FourthCh = 'Ref';%sprintf ('%s',p5);

end
% _____________________________
T2 = contains(IM_FILE,['20191204_2']);
if T2
    sery = 10:18; %imgprop2
FirstCh = 'Fil'%sprintf ('%s',p2);
SecndCh = 'Inv';%sprintf ('%s',p3);
ThirdCh = 'D7'%sprintf ('%s',p4);
FourthCh = 'Ref';%sprintf ('%s',p5);
%     sery = 11:20; %imagprop1
%     idCP = 0; %control sample
end
% _____________________________
T3 = contains(IM_FILE,['20191204_3']);
if T3
    sery = 10:18; %imgprop2
FirstCh = 'CK10'%sprintf ('%s',p2);
SecndCh = 'CK10';%sprintf ('%s',p3);
ThirdCh = 'D7'%sprintf ('%s',p4);
```

```
FourthCh = 'Ref';%sprintf ('%s',p5);
%     sery = 1:10; %imagprop1
%     idCP = 0; %control sample
end

sCorrect = 1;
for n = sery
   series=n-1
   series_1=n

    %% OME metadata opening (need bioformats toolbox files)

%Note: the below format looks a little odd because the OME metadata is a JAVA
%object, and the syntax reflects that
%the zero index refers to what is known as a "series" and this particular
%image has 2 series. Since JAVA is zero-indexed (0...m) rather than
%one-indexed (1...n) as MATLAB is, we refer to Series #1 as 0 and Series #2
%as 1
SX = omeMeta.getPixelsSizeX(series).getValue(); % image width, pixels
SY = omeMeta.getPixelsSizeY(series).getValue(); % image height, pixels
SZ = omeMeta.getPixelsSizeZ(series).getValue(); % number of Z slices
nC = omeMeta.getChannelCount(series); %number of channels
nP = omeMeta.getPlaneCount(series); %number of planes
PX = omeMeta.getPixelsPhysicalSizeX(series).value().doubleValue(); %physical
pixel X dim, um
PY = omeMeta.getPixelsPhysicalSizeY(series).value().doubleValue();%physical
pixel Y dim, um
PZ = omeMeta.getPixelsPhysicalSizeZ(series).value().doubleValue(); %physical
pixel Z dim, um
imgClass=class(A{series_1,1}{1,1});
Sname{sCorrect} = char(omeMeta.getImageName(n-1)); %image name


Ob = 20; %objective

%% quantify average intensity of each epidermal stain
idCP = 0;

%% quantify thickness of epidermis
epidermal_ThicknessDetect_CORE_MMS_publication

%%
if sCorrect == 1
save([sprintf('%sMetaData_%s_s%d.mat',dataLoc,BaseFileName,sCorrect)],...
    'PX','PY','PZ','SX','SY','SZ','imgClass','nC','nP');
end
%%
sCorrect = sCorrect +1; %counts what number within the imgProp2 images we are
on (1:10)

end

end

save([sprintf('%sThicknessVolValues.mat',dataLoc)],...
    'volThickness');

close all
disp('OPERATION Completed'); beep
```

Confocal Thickness detection CORE Script and functions

```
%% thickness of epidermis VOLUME and max projection
% (CORE script)
%Authors: Martina M. Sanchez, Joshua T. Morgan
%Lab: TIME lab, PI:Dr. Joshua Morgan, Bioengineering Department
%Institution: Univerisity of California, Riverside

% last edit date: 20210801

%description: uses confocal lif files to detect thickness over volume
%must optimize image adjustment and thresholds for data sets
%% find code dependencies
[fList,pList] =
matlab.codetools.requiredFilesAndProducts('epidermal_ThicknessDetect_CORE_MMS_p
ublication.m');
fList = fList';

%% clear variables
clear K P D R disky j Km1 Pm1 Dm1 Km2 Pm2 Dm2 Dm2a Km3 Pm3 Dm3 KBW PBW DBW...
    disky1 obj KBWc PBWc DBWc KBWcO PBWcO DBWcO BWsum FiltSum FiltSq
FiltOriented...
    SumSq SumOriented SumOL vertSum vertSumAvg_Pix vertSumAvg_mum PS2
nameStr...
    VolAvg_mum VolAvg_pix BWsumVol sphD

%% Filter plane by plane to preserve thickness edges
disp('thickness calcs started')
close all
tic
if nC ==4 %if there are 4 channels
%use Original images
   K = cat(3,A{series_1,1}{1:nC:end-3,1}); %CK10; channel 1
   P = cat(3,A{series_1,1}{2:nC:end-2,1}); %Inv
   D = cat(3,A{series_1,1}{3:nC:end-1,1}); %D7
   R = cat(3,A{series_1,1}{4:nC:end,1}); %ref; channel 4
elseif nC ==3
%use original images
   K = cat(3,A{series_1,1}{1:nC:end-2,1}); %CK10
   P = cat(3,A{series_1,1}{2:nC:end-1,1}); %Inv
   D = cat(3,A{series_1,1}{3:nC:end,1}); %D7
end

disky = strel('disk',20); %set structuring element

%median filter plane by plane to avoid changing thickness
   for j = 1: size(K,3)
   Km1 (:,:,j) = medfilt2(K(:,:,j),[5 5]);
   Pm1 (:,:,j) = medfilt2(P(:,:,j),[5 5]);
   Dm1 (:,:,j) = medfilt2(D(:,:,j),[3 3]);
   end

%adjust images
imgC = contains(imgClass,['uint8']); %this would have been accidental. should
be uint16
```

```
if ~imgC %uint16 images (this is what they should be)
%adjust the whole volume at once
   Km2 = imadjustn(Km1,[150/65535; 4000/65535]);
   Pm2 = imadjustn(Pm1,[180/65535; 4500/65535]);
   Dm2 = imadjustn(Dm1,[150/65535; 4000/65535]);
else %in case the images are uint8
   Km2 = imadjustn(Km1,[5/255; 60/255]);
   Pm2 = imadjustn(Pm1,[10/255; 255/255]);
   Dm2 = imadjustn(Dm1,[30/255; 200/255]);

end

%smooth or use rolling ball filter
   for j = 1: size(K,3)
   Dm2a(:,:,j) = imgaussfilt(Dm2(:,:,j),3);
   Km3(:,:,j) = imtophat(Km2(:,:,j),disky);
   Pm3(:,:,j) = imtophat(Pm2(:,:,j),disky);
   Dm3(:,:,j) = imtophat(Dm2a(:,:,j),disky);
   end

       if ~imgC %imgglass is uint16
   KBW = hysteresis3draw(Km3,3000,65000,18); %2000,6000,18
   PBW = hysteresis3draw(Pm3,3000,62000,26); %6000,20000,26
   DBW = hysteresis3draw(Dm3,1150,64000,26); %35000,80000,26
       else
           % just in case imgclass is uint8
           KBW = hysteresis3draw(Km3,5,254,26); %2000,6000,18
           PBW = hysteresis3draw(Pm3,7,254,26); %6000,20000,26
           DBW = hysteresis3draw(Dm3,10,255,26); %35000,80000,26

       end

%set structuring elements
   disky1 = strel('disk',10);% for morphological closing
   sphD = strel('sphere',8); %for morphological closing
   obj = 35; %define object size for morphological opening

   for j = 1: size(K,3)
   %swell features a little bit, plane by plane
   KBWc(:,:,j) = imclose(KBW(:,:,j),disky1);
   PBWc(:,:,j) = imclose(PBW(:,:,j),disky1);
   end

   DBWc = imclose(DBW,sphD);

    for j = 1: size(K,3)
   %remove small objects
   KBWcO(:,:,j) = bwareaopen(KBWc(:,:,j),obj);
   PBWcO(:,:,j) = bwareaopen(PBWc(:,:,j),obj);
   DBWcO(:,:,j) = bwareaopen(DBWc(:,:,j),obj);
   end

%specific to our data set:
%remove artifact that comes with confocal 633 laser line
DBWcO(245:305,235:295,:) = 0;

%% sum binaries
for j = 1: size(K,3)
BWsum(:,:,j) = KBWcO(:,:,j) + PBWcO(:,:,j) + DBWcO(:,:,j);
FiltSum(:,:,j) = Km3(:,:,j) + Pm3(:,:,j) + Dm3(:,:,j);
```

```
end

%% sum all volumetrically
for j = 1:size(BWsum,1);
    for q = 1:size(BWsum,2);
    BWsumVol(j,q) = sum(BWsum(j,q,:),'all');
    end
end

VolAvg_pix = mean(BWsumVol,'all');
VolAvg_mum = VolAvg_pix*PZ;
%% orthogonal max projection and thickness calc
%show orthogonals just as an indication. thickness calculations are
%volumetric
FiltSq = squeeze(max(FiltSum(:,:,:),[],1));
FiltOriented = flipud(permute(FiltSq  ,[2 1 3]));

SumSq = squeeze(max(BWsum(:,:,:),[],1));
SumOriented = flipud(permute(SumSq  ,[2 1 3]));
SumOL = logical(SumOriented);

for j = 1: size(SumOL,2)
vertSum(j) = sum(SumOL(:,j),'all');
end
vertSumAvg_Pix = mean(vertSum);
vertSumAvg_mum = vertSumAvg_Pix*PZ;
%% save thickness variables
save([sprintf('%s\\ThicknessValues_iprop2series%d.mat',folderLocA,sCorrect)],..
.

'vertSumAvg_Pix','vertSumAvg_mum','VolAvg_pix','VolAvg_mum','idCP','BaseFileNam
e');

save([sprintf('%s\\%s__iprop2series%d.mat',dataLoc,BaseFileName,sCorrect)],...

'vertSumAvg_Pix','vertSumAvg_mum','VolAvg_pix','VolAvg_mum','idCP','BaseFileNam
e'); %idCP is identifier for control (0) or photoaged(1)
%% put saving variables into a cell
varCell{h,2}{sCorrect,6} = vertSumAvg_Pix;
varCell{h,2}{sCorrect,7} = vertSumAvg_mum;

volThickness{h,2}{sCorrect,1} = VolAvg_mum;
volThickness{h,2}{sCorrect,2} = VolAvg_pix;


%% Output figures of thickness
close all
PS2 = (150/SY)*(PZ/PY);
PS2=[6 PS2*5];
nameStr = replace(BaseFileName,'_',' ');
figure; set(gcf,'units','inches','position',[1 1 PS2],'Color','w',...
    'PaperUnits','inches','PaperSize',PS2,'PaperPosition',[0 0 PS2])

%display the image plane and clear off the axis and tick marks
subplot(2,1,1);imagesc(FiltOriented);
title(sprintf('%s Series%d, sCorrect%d',nameStr, series_1,sCorrect));

subplot(2,1,2);imagesc(SumOL);
title(sprintf('thickness is %d Pix & %d
micron',vertSumAvg_Pix,vertSumAvg_mum));
```

```
print(sprintf('%s\\Thickness_OrthMAX_iprop2series%d' , ...
   folderLocA,sCorrect),'-dpng');
%% visualize filter changes
%    zp = 35;
%    close all
% figure;
% subplot(3,3,1);imagesc(K(:,:,zp));title('k');
% subplot(3,3,2);imagesc(P(:,:,zp));title('p');
% subplot(3,3,3);imagesc(D(:,:,zp));title('d');
% subplot(3,3,4);imagesc(Km1(:,:,zp));title('km1');
% subplot(3,3,5);imagesc(Pm1(:,:,zp));title('pm1');
% subplot(3,3,6);imagesc(Dm1(:,:,zp));title('dm1');
% subplot(3,3,7);imagesc(Km2(:,:,zp));title('km2');
% subplot(3,3,8);imagesc(Pm2(:,:,zp));title('pm2');
% subplot(3,3,9);imagesc(Dm2(:,:,zp));title('dm2');
%
% figure;
% subplot(3,3,1);imagesc(Km3(:,:,zp));title('km3');
% subplot(3,3,2);imagesc(Pm3(:,:,zp));title('pm3');
% subplot(3,3,3);imagesc(Dm3(:,:,zp));title('dm3');
% subplot(3,3,4);imagesc(KBW(:,:,zp));title('kbw');
% subplot(3,3,5);imagesc(PBW(:,:,zp));title('pbw');
% subplot(3,3,6);imagesc(DBW(:,:,zp));title('dbw');
% subplot(3,3,7);imagesc(KBWc(:,:,zp));title('kclose');
% subplot(3,3,8);imagesc(PBWc(:,:,zp));title('pclose');
% subplot(3,3,9);imagesc(DBWc(:,:,zp));title('close');
%
% figure;
% subplot(3,3,1);imagesc(KBWcO(:,:,zp));title('kbwco');
% subplot(3,3,2);imagesc(PBWcO(:,:,zp));title('pbwco');
% subplot(3,3,3);imagesc(DBWcO(:,:,zp));title('dbwco');
% subplot(3,3,4);imagesc(BWsum(:,:,zp));title('BWsum');
% subplot(3,3,5);imagesc(FiltSum(:,:,zp));title('fs');
%% functions ******************************************************

%% hysteresis3draw
function [tri,hys]=hysteresis3draw(img,t1,t2,conn)
% function [tri,hys]=HYSTERESIS3D(img,t1,t2,conn)
%
% Hysteresis3d is a simple function that performs trinarisation and
% hysteresis for 2D and 3D images. Hysteresis3d was inspired by Peter
% Kovesi's 2D hysteresis function
% (http://www.csse.uwa.edu.au/~pk/research/matlabfns/). This 3D function
% takes advantage of the 3D connectivities of imfill instead of the 2D
% connectivities of bwselect.
%
% Usage:        [tri,hys]=HYSTERESIS3D(img,t1,t2,conn)
%
% Arguments:    img - image for hysteresis (assumed to be non-negative)
%               t1 - lower threshold value (fraction b/w 0-1, e.g.: 0.1)
%               t2 - upper threshold value (fraction b/w 0-1, e.g.: 0.9)
%                   (t1/t2 can be entered in any order, larger one will be
%                   set as the upper threshold)
%               conn - number of connectivities (4 or 8 for 2D)
%                                               (6, 18, or 26 for 3D)
% Returns:
%               tri - the trinarisation image (values are 0, 1, or 2)
%               hys - the hysteresis image (logical mask image)
%
```

```
% Examples:     [tri,hys]=HYSTERESIS3D(img,0.25,0.8,26)
%
% 2012/07/10: written by Luke Xie
% 2013/12/09: defaults added
%
% To see an example of hysteresis used to segment a kidney region, please
% refer to supplement in QSM of Kidney, NMR Biomed, 2013 Dec;26(12):1853-63
% (http://onlinelibrary.wiley.com/doi/10.1002/nbm.3039/abstract).
% Supplemental material is also available on our CIVMspace:
% http://www.civm.duhs.duke.edu/lx201204/

%% arguments
if nargin<3
    disp('function needs at least 3 inputs')
    return;
elseif nargin==3
    disp('inputs=3')
    if numel(size(img))==2;
        disp('img=2D')
        disp('conn set at 4 connectivies (number of neighbors)')
        conn=4;
    end
    if numel(size(img))==3;
        disp('img=3D')
        disp('conn set at 6 connectivies (number of neighbors)')
        conn=6;
    end
end

%% DO NOT scale t1 & t2 based on image intensity range
if t1>t2    % swap values if t1>t2
    tmp=t1;
    t1=t2;
    t2=tmp;
end
t1v=t1;
t2v=t2;

%% trinarisation
tri=zeros(size(img));
tri(img>=t1v)=1;
tri(img>=t2v)=2;

%% hysteresis
abovet1=img>t1v;                                    % points above lower
threshold
seed_indices=sub2ind(size(abovet1),find(img>t2v));   % indices of points above
upper threshold
hys=imfill(~abovet1,seed_indices,conn);              % obtain all connected
regions in abovet1 that include points with values above t2
hys=hys & abovet1;
```

Chapter 4: Vascular quantification scripts and functions

Vascular quantification script

```
%% Vascular quantification script
% Author: Martina M. Sanchez and incorporation of functions from Joshua T.
% Morgan, Peter Kovesi, and Tim Jerman.

%Info: Script written to analyze vascular networks in 3D culture. Works on
%uncleared and cleared structures, but uncleared structures may require
%more filter optimization. This particular analysis works of staining form
%vessels, adipose, and nuclei. The adipose and nuclei stains are used to
%determine planes of noise that interfere with the vascular network. 3D and
%3D renderings are generated to compare computational network formation to
%actual images. Catching vasculature and eliminating noise is a delicate
%balance and this should be optimized through filtering.

%it is advised to begin by running image sets through just the vesselness3D
%filter (line 466). Vesselness 3D by Tim Jerman is a pre-segmentation
%function. It works well by itself but our data sets required more
%de-noising so more filters were added before vesselness3D

%% requires these to run
[fList,pList] =
matlab.codetools.requiredFilesAndProducts('vesselness3D_20x_AVHSEclearedVasc_MMS_publicat
ion.m');
fList = fList';

%-image analysis toolbox
%-parallel computing toolbox

% requires bioformats toolbox
    % https://docs.openmicroscopy.org/bio-formats/6.1.0/index.html


%%
clear all
close all
clc
%% all files
tic
strData = 'D:\Martina\3D HSE_HEE_VHSE analysis\AVHSE 202102 cleared\';
FileList = dir([strData, '*.lif']);

for h = 1:length(FileList)
clearvars -except keepVariables allFiles h strData FileList
close all
clc


%% Filename you want to open
IM_FILE = FileList(h).name;
%% Open File (takes time)
%Using the Bioformats Toolbox, we can extract most life sciences formats
%into a consistant structure
 tic;A = bfopen(IM_FILE);toc;
 fprintf('finished opening file');
%% Save Directory
outdir1 = 'D:\Martina\3D HSE_HEE_VHSE analysis\AVHSE 202102 cleared\Vesselness';

BaseFileName = sprintf('M%s', IM_FILE(1:end-4),'_VascQuant');

outdir2 = BaseFileName;
    if ~isdir(outdir2)
        mkdir(outdir2)
    end

outdir3 = [date 'VascQuant'];
```

```
folderLoc=fullfile(outdir1,outdir2,outdir3);
    %is there a folder? If not, make one
    if ~isfolder(folderLoc)
        mkdir(folderLoc);
    end

%% change per image set if needed
sphere = strel('sphere',10);
isovalue = 0.1;
Overlap = 0.8;
AnalysisDepth = 350;%runs to a z depth of 350 or the whole volume

lowZcatch = 5; %eliminate planes before z plane 5 because of noise from glass
highZcatch = 40; %if plane elimination starts at z plane 40 then re-evaluate

DlowThresh = 18000; %for nuclei
RlowThresh = 8000; %for adipose

SZvolFrac = 2;
StartCushion = 2;

erodeStr = 2;
dilateStr = (2*erodeStr);

preFrangiBWvol = (1.05);
postFrangiBWvol = 1.05;



%% Begin Vesselness Sequence
fprintf('\n BEGIN vesselness sequence \n');

lengthA = length(A(:,1));
for n=3:lengthA-2;
    %^^^change depending on how many tilescan positions you want to analyze
    %or how many series are in the file

sing = tic
    series=n-1
    series_1=n
    strSeries = sprintf('series%d',series_1);

    fprintf(sprintf('\n starting series %d \n',series_1));
%% OME metadata opening using bioformats toolbox functions
reader = bfGetReader(IM_FILE); %the reader variable is a pointer to the file
omeMeta = reader.getMetadataStore(); %pull OME metadata

SX = omeMeta.getPixelsSizeX(series).getValue(); % image width, pixels
SY = omeMeta.getPixelsSizeY(series).getValue(); % image height, pixels
SZ = omeMeta.getPixelsSizeZ(series).getValue(); % number of Z slices
nC = omeMeta.getChannelCount(series); %number of channels
nP = omeMeta.getPlaneCount(series); %number of planes
PX = omeMeta.getPixelsPhysicalSizeX(series).value().doubleValue(); %physical pixel X dim,
um
PY = omeMeta.getPixelsPhysicalSizeY(series).value().doubleValue();%physical pixel Y dim,
um
PZ = omeMeta.getPixelsPhysicalSizeZ(series).value().doubleValue(); %physical pixel Z dim,
um
%% Define channels based on channels present in file
if nC==1
    K = cat(3,A{series_1,1}{1:nC:nP,1});  %1st Channel

elseif nC==2
    K = cat(3,A{series_1,1}{1:nC:nP-1,1});  %1st Channel
    D = cat(3,A{series_1,1}{2:nC:nP,1}); %2nd Channel
```

```
elseif nC==3

    P = cat(3,A{series_1,1}{1:nC:nP-2,1});  %1st Channel
    K = cat(3,A{series_1,1}{2:nC:nP-1,1}); %2nd Channel
    D = cat(3,A{series_1,1}{3:nC:nP, 1}); %3rd Channel

elseif nC==4 %assuming DRAQ7 is on 3rd channel
    P = cat(3,A{series_1,1}{1:nC:nP-3,1});  %1st Channel(Bodipy)
    K = cat(3,A{series_1,1}{2:nC:nP-2,1}); %2nd channel (COlIV)
    D = cat(3,A{series_1,1}{3:nC:nP-1,1}); %third Channel
    R = cat(3,A{series_1,1}{4:nC:nP, 1}); %4th Channel
end

%% begin filtering
fprintf('\n begin filtering \n')

%filter vasculature,median filter
Km1 = medfilt3(K,[5 5 5]);

%filter nuclei: median and tophat
Dm1 = medfilt3(D, [3 3 3]);
Dm2 = imtophat(Dm1,sphere);

%% adjust by volume
Dm3 = imadjustn(Dm2);
Km2 = imadjustn(Km1,[0.002 0.035]);

%tophat filter by plane
for i= 1:SZ
   [Km3(:,:,i)] = imtophat(Km2(:,:,i),strel('disk',20));
end

%Kuwahara filter (edge preservation)
for q = 1: size(Km3,3)
    KmKuw(:,:,q) = KuwaharaFast(Km3(:,:,q),2);
end

%% View initial segmentation success: Vasculature (2nd ch)
% close all
% for i = 1:SZ  %size(G, 3) %z stacks
%     figure(50);image(K(:,:,i), 'CDataMapping', 'scaled'); movegui('southwest');%OG
medfilt image
%     figure(5); image(Km2(:,:,i), 'CDataMapping', 'scaled'); title(['Km2, frame '
num2str(i) '/' num2str(size(K, 3))]); movegui('northeast');
%     figure(6); image(Km3(:,:,i),'CDataMapping', 'scaled'); title(['Km3, frame '
num2str(i) '/' num2str(size(K, 3))]); movegui('southeast');
%     figure(7); image(KmKuw(:,:,i),'CDataMapping', 'scaled'); title(['KmKuw, frame '
num2str(i) '/' num2str(size(K, 3))]); movegui('southeast');
% end
%% medfilt volume
Km6 = medfilt3(KmKuw);
Dm6 = medfilt3(Dm3);

%% Noise comp 3D (phase preserving denoising [Peter Kovesi 1999; adapted for 3D by Joshua
T. Morgan]
SF=PZ/PX;
Km6NC2 = noisecomp3D(Km6,2,7,3,1,SF,false);%changed 0 to 1 before SF
toc;

%% homomorphic filtering (a frequency domain transform function) [Peter Kovesi]
for i = 1:SZ;
[Km6hmp(:,:,i)] = homomorphic(Km6NC2(:,:,i),3,.5,2,80,2); %H  very good
end
%% View initial segmentation success: Vasculature (2nd ch)
% close all
% for i = 1:SZ  %size(G, 3) %z stacks
%
```

```
%     figure(50);image(Km6(:,:,i), 'CDataMapping', 'scaled'); movegui('southwest');%OG
medfilt image
%     figure(5); image(Km6NC2(:,:,i), 'CDataMapping', 'scaled'); title(['Km6NC2 frame '
num2str(i) '/' num2str(size(K, 3))]); movegui('northeast');
%     figure(6); image(Km6hmp(:,:,i),'CDataMapping', 'scaled'); title(['Km6hmp, frame '
num2str(i) '/' num2str(size(K, 3))]); movegui('southeast');
%     figure(7); image(Dm6(:,:,i),'CDataMapping', 'scaled'); title(['Dm6, frame '
num2str(i) '/' num2str(size(K, 3))]); movegui('northwest');
% end

%% imocbr
for i = 1:SZ
[Km7(:,:,i)] = imocbr(Km6hmp(:,:,i),strel('disk',6));
end
%% Threshold using hysteresis
%% remove homomorphic filter artifacts
[Km6Hyst] = hysteresis3draw(Km6,3400,60000);

%%% compare binary images, eliminate objects that 'appear' from homomorphic filtering
Ks = uint8(Km6Hyst)+uint8(Km7);
[Ks1] = hysteresis3draw(Ks,1.9,2.9,26);

%% Use a long rectangle structuring element to enhance 'stripe' noise
Ks2 = imclose(Ks1, strel('rectangle',[3 20]));

%%  Sum row for each Z frame and find where there are more than __objects in one line
% this finds long horizonntal lines and makes their whole row positive
% so that it can increase the area of the object and then can be easily
% removed; this is specific to noise created in these images

for i = 1:SZ
    for j = 1:512
        [tmp(j,i)]=sum(Ks2(j,:,i));
    end
end
[ind1,ind2]= find(tmp>260);

dum= ones(1,512);
for t = 1: length(ind1)
Ks2(ind1(t),:,ind2(t)) = dum;
end
Ks2 = logical(Ks2);

% %% erode in case large objects catch tiny spines of vasc
for t = 1:SZ
Ks2erode(:,:,t) = imerode(Ks2(:,:,t),strel('disk',7));
end
%% Use bwareafilt to remove super large objects in the shape of rectangles
for i = 1:SZ
    [Ks3(:,:,i)] = bwareafilt(Ks2(:,:,i),[1 14500]);% 14500
    [Ks1t(:,:,i)] = bwareaopen((Ks1(:,:,i)),150);
end
%% remove large objects that don't correspond with vasculature
Ks4 = uint8(Ks1)+uint8(Ks1t.*2) +uint8(Ks3)+uint8(Ks2erode);
Ks5 = Ks4>=2;

%% if a few frames of vascular have a gap in the z-direction, this fixes it
Ks6= imclose(Ks5, strel('sphere',4));
%% imclose--try to preserve thin spiny vasculature (could be optimized a lot)
      nhoody1 = strel('line', 10, 45)
      nhoody2 = strel('line', 10, 90)
      nhoody3 = strel('line', 10, 180)
      nhoody4 = strel('line', 10, 225)

for i = 1:SZ
Km8(:,:,i) = imclose(Ks6(:,:,i),strel(nhoody1));
end
```

```
for i = 1:SZ
Km8(:,:,i) = imclose(Km8(:,:,i),strel(nhoody2));
end
for i = 1:SZ
Km8(:,:,i) = imclose(Km8(:,:,i),strel(nhoody3));
end
for i = 1:SZ
Km8(:,:,i) = imclose(Km8(:,:,i),strel(nhoody4));
end
Km7Bin = Km8;
%% adjust by volume & homomorphic filtering

Km9 = Km8.*Km6;
Km9hyst= imadjustn(Km9);

clear Km9hmp
for i = 1:SZ;
[Km9hmp(:,:,i)] = homomorphic(Km9(:,:,i),1,.25,2,1); %H  very good
end

Km9Bin = Km9hmp>0.15;

%% bwareaopen
objVolKmBW = 12;
clear Km7BW
for i = 1:SZ
Km7BW(:,:,i) =  bwareaopen((Km9Bin(:,:,i)),objVolKmBW);
end
%% threshold nuclei/adipose using hystersis
[~,Dm7Bin] = hysteresis3draw(Dm6,DlowThresh,60000,18); %threshold DRAQ7 channel
    Pm3 = imadjustn(P); %bodipy
    Pm4 = medfilt3(Pm3,[5 5 5]);
[~,Pm7Bin] = hysteresis3draw(Pm4, RlowThresh,60000,18);

CommonD = imclose(Dm7Bin,strel('disk',60));
CommonR = imclose(Pm7Bin, strel('disk',60));

for i = 1:SZ
        %count all nonzero elements per z position
        Com_D(i) = nnz((CommonD(:,:,i)==1)); %count all nonzero elements pre z position
        Com_R(i) = nnz((CommonR(:,:,i)==1));
    end
CommyD(1,:) = Com_D./nnz(ones(512,512)); %find ratio of D7 coverage
CommyR(1,:) = Com_R./nnz(ones(512,512)); %find ratio of D7 coverage

%% Use bwareafilt to remove super large objects in the shape of rectangles
%filters out the stripe noise specific to these images
obj = [10 15000];
for i = 1:SZ
    [Km7BW1(:,:,i)] = bwareafilt(Km7BW(:,:,i),obj);
end

% median filter the bwareaopen
KBWmed = medfilt3(Km7BW1, [3 3 3]);

%% Detect & remove Glass/ planes of noise
fprintf('\n Detecting Glass \n')
if nC==3 |nC==4
    fprintf('running on nC = 3 or 4')

    %swell  binary images to find common coverage areas
    CommonK = imclose (KBWmed,strel('disk',60)); %30 works for this data set at 20x

    for i = 1:SZ
        Com_K(i)= nnz((CommonK(:,:,i)==1)); %count all nonzero elements per z position
    end
    %find fractions of coverage
```

```
        ComDiv(1,:) = Com_K./Com_R;
        ComDiv(2,:) = Com_K./Com_D;%%%
        ComDiv(3,:) = Com_D./Com_R;%%%%


else
    %if nC ~=4 or 4
    fprintf('running on fraction of K/D');
    CommonK = imclose (KBWmed,strel('disk',60)); %30 works for this data set at 20x
    CommonD = imclose(Dm7Bin,strel('disk',60));
    for i = 1:SZ
        Com_K(i)= nnz((CommonK(:,:,i)==1)); %count all nonzero elements per z position
        Com_D(i) = nnz((CommonD(:,:,i)==1)); %count all nonzero elements pre z position
    end
    ComDiv(2,:) = Com_K./Com_D;
    ComDiv(3,:) = Com_D./Com_R;
end


SZfrac= round((SZ-1)/SZvolFrac) %%
ComDiv(4,:) = abs(ComDiv(1,:)-ComDiv(3,:));
diff4=diff(ComDiv(4,1:SZfrac));

figure;subplot(2,1,1);picSIZE=[8 6];PS = [6 6];
 set(gcf,'units','inches','position',[1 1 picSIZE],'Color','w',...
    'PaperUnits','inches','PaperSize',PS,'PaperPosition',[0 0 picSIZE]);

plot((ComDiv(4,1:SZfrac)))
hold on
plot(diff4)
legend('difference of k/r and d/r','differentiation of diff')
title('difference between k/r and d/r fractions within SZfrac volume');

subplot(2,1,2);
plot((ComDiv(1,:)))
hold on
plot((ComDiv(2,:)));
plot((ComDiv(3,:)));
legend ('k/r','k/d','d/r');
hold off
ylabel('overlay percent')
xlabel('Z position');
title('fractions');

Sfile=sprintf('%s\\%s_ZregionPlot.fig',folderLoc,strSeries);
Pfile=sprintf('%s\\%s_ZregionPlot',folderLoc,strSeries);

print(Pfile,'-dpng');
savefig(Sfile);
clear Sfile Pfile

foundSim1 = diff4 <0.08;
foundSim2 = diff4>(-0.08); %%%(0.04 is strict)changed from VHSE
        % (more leniancy allowed since binary map of vessels is way better)
foundSimy = foundSim1.*foundSim2;
conseqLOW1 = find(foundSimy ==0);

%setting limits for detection of first z frame
conseqLOW = conseqLOW1(conseqLOW1>8); %knock off planes below
conseqLOW = conseqLOW(conseqLOW<205);

j0 =(diff(conseqLOW))%-1));

[u,ind]= min(j0);
j=conseqLOW(ind);
startingZ =j;
```

```
%%%catch and change really low starting Z's (usually first few zplanes are
%%%noise or glass, or just no signal
    if startingZ <= lowZcatch   %first catch.
        j = conseqLOW(ind+1)
        startingZ = j;
        disp('first catch completed');

        if startingZ<=lowZcatch %2nd catch if necessary
             j = conseqLOW(ind+2)
            startingZ = j;
            disp('Second catch completed');
        end
    end

%%% catch and change really high startingZ's. sometimes algorithm starts too
%%% high in the z-stack, 40 is a good catch because sometimes several
%%% low planes have nothing but noise but we also don't want to miss
%%% vessels that might be there. optimize if needed
    if startingZ >= highZcatch
        startingZ = startingZ-10;
        disp('caught a high starting Z (over 40)') %40 is high for a cleared data set
    end

Depth = round(AnalysisDepth/round(PZ)); %Choose what depth to analyze to (set at top)
endingZ = startingZ+Depth;
if endingZ > SZ
    Zcorrect = endingZ-SZ
    startingZ = startingZ-Zcorrect;
    endingZ = startingZ + Depth;
end
depthRep = 0;

%correct plane corrections so that indexing is not starting at 0 or higher
%than whole z stack
if startingZ < 0
    Zcorrect = abs(startingZ)+1;
    startingZ = startingZ + Zcorrect;
    endingZ = endingZ + Zcorrect;
   if endingZ > SZ
    Zcorrect = endingZ-SZ
    endingZ = endingZ-Zcorrect;
    if endingZ >SZ
    depthRep = 1;
    disp('analysis depth not possible; quantifying whole stack');
    end
   end
end

Zframes= startingZ:endingZ;
fprintf('\n starting Z is %d \n',startingZ);
fprintf('\n ending Z is %d \n',endingZ);
%%
%% View initial segmentation success vascular
for i = Zframes  %size(G, 3) %z stacks
    figure(5); image(KBWmed(:,:,i), 'CDataMapping', 'scaled'); title(['KBWmed, frame '
num2str(i) '/' num2str(size(K, 3))]); movegui('northeast');
    figure(6); image(Km6(:,:,i),'CDataMapping', 'scaled'); title(['Km6, frame '
num2str(i) '/' num2str(size(K, 3))]); movegui('southeast');
% trace boundaries
    figure(7); image(Km6(:,:,i), 'CDataMapping', 'scaled'); title(['Km6 w binary map,
frame ' num2str(i) '/' num2str(size(K, 3))]); movegui('northwest');
       RBound = bwboundaries(KBWmed(:,:,i), 8, 'noholes'); hold on
            for j = 1:length(RBound)
                plot(RBound{j}(:,2), RBound{j}(:,1), 'r', 'LineWidth', 1);
            end
       hold off
                hi = figure(7);
```

```
                frame = getframe(hi);
                im = frame2im(frame);
                [imind,cm] = rgb2ind(im,256);
% Write to the GIF File
                name = sprintf('%s\\%s_VascInitialsegB4frangi.gif',folderLoc, strSeries);
                if i == startingZ
                 imwrite(imind,cm,name,'gif', 'Loopcount',inf);
                else
                 imwrite(imind,cm,name,'gif','WriteMode','append');
                end
end

%% Use KBWmed as a mask onto a non-binary image since frangi works on non-binary images
Kmasked = zeros(size(KBWmed));
Kmasked = (double(KmKuw)).*(double(KBWmed));

%% Frangi filter w. vesselness function [Jerman enhancement filter: hessian based Frangi]
% compute enhancement for two different tau values
V = vesselness3D(Kmasked, 1:4, [1;1;1], 0.5, true);

%%%vesselness itself is a pre-segmentation filter. Can start from here and
%%%see how vesselness works then add more pre-segmentation filters as above

%% Add bwareaopen after vesselness frangi filter
V1 = logical(V); %bc regionprops needs a logical image, V is a double
V2 = V1(:,:,Zframes);
%% remove small objectss again
objVolV=20000;
Vasc =  bwareaopen(V2,objVolV,26);
Vasc = medfilt3(Vasc,[9 9 9]);

%% View Post Frangi & bwareaopen segmentation success
fprintf('\n begin view of post frangi segmentation \n')

for i = 1:size(Vasc,3)
starty = i+startingZ;
if starty>SZ
    starty = SZ;
end
    figure(5); image(Vasc(:,:,i), 'CDataMapping', 'scaled'); title(['Vasc, frame '
num2str(i) '/' num2str(size(Vasc,3))]); movegui('northeast');
    figure(6); image(Km6(:,:,(starty)),'CDataMapping', 'scaled'); title(['Km6, frame '
num2str(i) '/' num2str(size(Vasc,3))]); movegui('southeast');
    figure(7); image(KBWmed(:,:,(starty)),'CDataMapping', 'scaled'); title(['KBWmed,
frame ' num2str(i) '/' num2str(size(KBWmed,3))]); movegui('southwest');

    % trace boundaries
    figure(8); image(Km6(:,:,(starty)), 'CDataMapping', 'scaled'); title(['Km6 w Frangi
Seg Map, frame ' num2str(i) '/' num2str(size(Vasc,3))]); movegui('northwest');
       RBound = bwboundaries(Vasc(:,:,i), 8, 'noholes'); hold on
            for j = 1:length(RBound)
                plot(RBound{j}(:,2), RBound{j}(:,1), 'r', 'LineWidth', 1);
            end
       hold off
                hi = figure(8);
                frame = getframe(hi);
                im = frame2im(frame);
                [imind,cm] = rgb2ind(im,256);
% Write to the GIF File
                name = sprintf('%s\\%s_VascSegPostFrangi.gif',folderLoc, strSeries);
                if i == 1
                 imwrite(imind,cm,name,'gif', 'Loopcount',inf);
                else
                 imwrite(imind,cm,name,'gif','WriteMode','append');
                end

end
```

```
fprintf('\n vascular segmentation post frangi gif saved \n');
close all

%% View 3D rendering after frangi filter & bwareaopen, save fig
tic;
fprintf('begin 3D render \n');

%pad array to account for edge objects
G4 = padarray(Vasc(:,:,1:length(Zframes)), [1 1 1], 0);

%isosurfaces (isosurface takes a long time)
Giso = isosurface(G4, isovalue,'verbose');

Giso.vertices = Giso.vertices*[PX 0 0;0 PY 0;0 0 PZ];

%% Only vasculature-3D rendering
figure
PS = [8 6];
set(gcf,'units','inches','position',[2 2 PS],'Color','w',
'PaperUnits','inches','PaperSize',PS,'PaperPosition',[0 0 PS])
patch(Giso,'facecolor',[0 1 1],'facealpha',0.4,'edgecolor','none'); hold on

set(gca,'Xcolor','k','Ycolor','k','Zcolor','k','linewidth',2)
set(gca,'Fontsize',14,'fontweight','bold')
set(gca,'Xgrid','on','Ygrid','on','Zgrid','on')
set(gca,'Xgrid','on','Ygrid','on','Zgrid','on')
zlabel('Depth, \mum')
text(200,-80,0,'Length
(\mum)','Fontsize',14,'Fontweight','bold','rotation',19.5,'horizontalalignment','center')
;
text(-80,200,0,'Width (\mum)','Fontsize',14,'Fontweight','bold','rotation',-
43,'horizontalalignment','center');

%setting the camera position and angle
view([-31.5000 35.2000])

%setting illumination
camlight

%flatten the Z aspect a little with confocal images
daspect([1 1 1.5])

toc; fprintf('save file');

Sfile=sprintf('%s\\%s_SEG_3Drender.fig',folderLoc,strSeries);
Pfile=sprintf('%s\\%s_SEG_3Drender',folderLoc,strSeries);
print(Pfile,'-dpng');
savefig(Sfile);

%% save variables
fprintf('Vesselness Frangi 3D generation complete');
close all

save([sprintf('%s\\%s_SKELDATA.mat',folderLoc, strSeries)],...
    'startingZ','Overlap','Vasc','Zframes','PY','PX','PZ','SZ','SX','SY','depthRep');

%%  Volume distance transform [adapted from Joshua T. Morgan]

% can shrink volumes if necessary

Stic = tic; fprintf(1,'\n Start volume distance transform...\n')
v2t_dist = bwdistsc(Vasc,[PY PX PZ]); %distance from vessel to tissue location

t2v_dist = bwdistsc(~Vasc,[PY PX PZ]); %distance from tissue to vessel location

Stoc = toc(Stic); fprintf(1,'Volume distance transform took %f seconds.\n',Stoc);
```

```
%% loop over #objects then put into skeletonization one object at a time [adapted from
Joshua T. Morgan]
%find connected components in vessel map
connComps = bwconncomp(t2v_dist,26);
labelCC = labelmatrix(connComps);

%feed objects into skeletonization, a single object at a time
Stic = tic;

SkelPool = parpool(4);
parfor (i = 1:connComps.NumObjects,4) %4 is number of workers
    fprintf(1,'Working on object %d of %d\n',i,connComps.NumObjects)
    Vt = false(size(t2v_dist));
    Vt(connComps.PixelIdxList{i}) = true;
    tic;[Skeleton{i},SkeLength{i}] = skel_fm(Vt,2,true);toc
end

delete(SkelPool);
Stoc = toc(Stic);

fprintf(1,'Skeletonization took %f seconds. \n',Stoc)
save([sprintf('%s\\%s_SKELDATA.mat',folderLoc, strSeries)],...
    'v2t_dist','t2v_dist','connComps','labelCC','Skeleton','SkeLength','-append');


%% skel prep
Sm = false(size(t2v_dist));
for i = 1:length(Skeleton)
    for j = 1:length(Skeleton{i})
        Sm(Skeleton{i}{j}) = true;
end
end
%% Skeleton Revision
fprintf(1,'Revise skeletonization \n');
    Stic = tic;
Skel3D = Skeleton3D(Sm);
    Stoc = toc(Stic);   fprintf(1,'Revision took %f seconds.\n',Stoc)

save([sprintf('%s\\%s_SKELDATA.mat',folderLoc, strSeries)],...
    'Overlap','Zframes','Sm','Skel3D','-append');
fprintf(1,'Skeletonization Done!\n')



%% Make a 3D rendering of the skeleton overlayed onto a map of vessel

sphere = strel('sphere',6);
isovalue = 0.1;
Z= length(Zframes);

%pad array to account for edge objects
tic;
fprintf('\n begin 3D render \n');
G4 = (padarray(Skel3D, [1 1 1], 0));
R4 = (padarray(t2v_dist, [1 1 1], 0));

%isosurfaces
Giso = isosurface(G4, isovalue,'verbose');
Riso = isosurface(R4, 0.5);

Giso.vertices = Giso.vertices*[PX 0 0;0 PY 0;0 0 PZ];
Riso.vertices = Riso.vertices*[PX 0 0;0 PY 0;0 0 PZ];
figure
PS = [8 6];
set(gcf,'units','inches','position',[2 2 PS],'Color','w',
'PaperUnits','inches','PaperSize',PS,'PaperPosition',[0 0 PS])
```

```
patch(Giso,'facecolor',[1 0 1],'facealpha',0.6,'edgecolor','none'); hold on
patch(Riso,'facecolor',[0 1 1],'facealpha',0.3,'edgecolor','none'); hold on

set(gca,'Xcolor','k','Ycolor','k','Zcolor','k','linewidth',2)
set(gca,'Fontsize',14,'fontweight','bold')
set(gca,'Xgrid','on','Ygrid','on','Zgrid','on')

zlabel('Depth, \mum')
text(200,-80,0,'Length
(\mum)','Fontsize',14,'Fontweight','bold','rotation',19.5,'horizontalalignment','center')
;
text(-80,200,0,'Width (\mum)','Fontsize',14,'Fontweight','bold','rotation',-
43,'horizontalalignment','center');

%setting the camera position and angle
view([-31.5000 35.2000])

%setting illumination
camlight

%flatten the Z aspect a little with confocal images
daspect([1 1 1.5])

toc; fprintf('save file');

Sfile=sprintf('%s\\%s_VascSkel_OVERLAY3D.fig',folderLoc,strSeries);
Pfile=sprintf('%s\\%s_VascSkel_OVERLAY3D',folderLoc,strSeries);

print(Pfile,'-dpng');
savefig(Sfile);
close all

%% Begin Analysis of network
Stic = tic;fprintf(1,'\n Beginning analysis, will always overwrite existing data!\n')

[~,node1,link1]= Skel2Graph3D(Skel3D,4); %Grab data from skeletonization

Stoc = toc(Stic); fprintf(1,'\n section took %f seconds.\n',Stoc);
save([sprintf('%s\\%s_SKELDATA.mat',folderLoc, strSeries)],'node1','link1','-append');

%%
Slblb = zeros(size(Skel3D)); %pre-allocate
SP = zeros(1,length(link1)); %pre-allocate
EP = zeros(1,length(link1)); %pre-allocate
SegChord = zeros(1,length(link1)); %pre-allocate
SegLength = zeros(1,length(link1)); %pre-allocate

for i = 1:length(link1)
    SP(i) = link1(i).point(1);
    EP(i) = link1(i).point(end);
    Slblb(link1(i).point) = i;
end

Slbln = zeros(size(Skel3D)); %pre-allocate
for i = 1:length(node1)
    Slbln(node1(i).idx) = i;
end

Slblm = Slblb;
Slblm(Slbln>0) = 0;

%% Segment chord, diameter, length, and tortuosity
SegPool = parpool(4);
Stic = tic;
parfor (i = 1:length(link1),4)
    TEMPs = false(size(Skel3D));
```

```
    TEMPs(link1(i).point) = true;
    TEMPm = bwdistgeodesic(TEMPs,SP(i),'quasi')
    SegLength(i) = TEMPm(EP(i));
    [tempX,tempY,tempZ] = ind2sub(size(Skel3D),link1(i).point([1,end]));
    SegChord(i) = sqrt(range(tempX).^2+range(tempY).^2+range(tempZ).^2);
end;toc(Stic)

s = regionprops(Slblb,t2v_dist,'MeanIntensity');

SegMeanDia = [s.MeanIntensity]; %radius value
SegMeanDia = (SegMeanDia.*2);
SegTort = SegLength./SegChord;
delete(SegPool);

%% volume fraction (does not require skeletonization)
VF = sum(Vasc(:))/numel(Vasc(:));

%% coverage of tissue
KTC = v2t_dist; KTC = KTC(:);
[f,x] = ecdf(KTC);
x = x*PX;

%% connectivity
tic
CC = bwconncomp(Vasc);
L = labelmatrix(CC);

Nvol = regionprops(L,'Area'); %volume of connected network chunks
Nvol = [Nvol.Area]; %reformat of above
Nvoltot = sum(Nvol); %total vol of connected network
Nvol3 = Nvol/Nvoltot; %normalized to largest vol

L = double(L);
for i = 1:length(Nvol3); L(L==i) = Nvol3(i); end %recreate label matrix with connected%
of each chunk
H2 = L(:); H2(H2==0) = []; %create pool of values, weight each by volume
[ConnHistValues,ConnHistEdges] = histcounts(H2,[0:.1:1]);toc
ConnHistValues = ConnHistValues/numel(H2); %normalize

%% assess nodes
node_conn = zeros(length(node1),1);
node_ep = false(length(node1),1);%if node is an endpoint (ep) =1; 0 otherwise
for i = 1:length(node1)
    node_conn(i) = length(node1(i).links);
    node_ep(i) = node1(i).ep;
end

node_conn(node_ep) = [];
node_ep(node_ep) = [];

if ~isfile(sprintf('%s\\%s_OUTPUT.mat',folderLoc, strSeries));
save([sprintf('%s\\%s_OUTPUT.mat',folderLoc,
strSeries)],'v2t_dist','t2v_dist','SegTort','SegMeanDia','SegLength','SegChord',...
    'VF','f','x','ConnHistEdges','ConnHistValues',...
    'node_conn','node_ep');
else
    save([sprintf('%s\\%s_OUTPUT.mat',folderLoc,
strSeries)],'SegTort','SegMeanDia','SegLength','SegChord',...
    'VF','f','x','ConnHistEdges','ConnHistValues',...
    'node_conn','node_ep','-append');
end
fprintf('series complete, outputs saved');
% - conn            List of destinations of links of this node
% - ep              1 if node is endpoint (degree 1), 0 otherwise
%% series time
singSerTime = toc(sing);
fprintf(sprintf('\n time for single series took %s \n',singSerTime));
```

```
save([sprintf('%s\\%s_seriesTime.mat',folderLoc, strSeries)],'singSerTime');
%
%% clear vars
clearvars -except keepVariables h allFiles strData FileList A IM_FILE outdir1...
    BaseFileName outdir2 outdir3...
    folderLoc n lengthA sphere isovalue  Overlap AnalysisDepth ...
    DlowThresh RlowThresh SZvolFrac StartCushion ...
    erodeStr dilateStr strSeries strSeries preFrangiBWvol postFrangiBWvol
end

%% Save generation variables
save([sprintf('%s\\%s_GenerationVars.mat',folderLoc, strSeries)],'DlowThresh',...
    'RlowThresh', 'SZvolFrac', 'StartCushion', 'AnalysisDepth','preFrangiBWvol',
'postFrangiBWvol','erodeStr','dilateStr');
%%
end %end allfile vesselness generation

clearvars -except keepVariables h allFiles strData FileList IM_File
fprintf('\n All files quantified \n');
toc
%%% end vesslness3D_20x...
```

Vascular quantification functions

FillEulerLUT

```
%function FillEulerLUT
function LUT = FillEulerLUT

LUT(1)  =  1;
LUT(3)  = -1;
LUT(5)  = -1;
LUT(7)  =  1;
LUT(9)  = -3;
LUT(11) = -1;
LUT(13) = -1;
LUT(15) =  1;
LUT(17) = -1;
LUT(19) =  1;
LUT(21) =  1;
LUT(23) = -1;
LUT(25) =  3;
LUT(27) =  1;
LUT(29) =  1;
LUT(31) = -1;
LUT(33) = -3;
LUT(35) = -1;
LUT(37) =  3;
LUT(39) =  1;
LUT(41) =  1;
LUT(43) = -1;
LUT(45) =  3;
LUT(47) =  1;
LUT(49) = -1;
LUT(51) =  1;

LUT(53) =  1;
LUT(55) = -1;
LUT(57) =  3;
LUT(59) =  1;
LUT(61) =  1;
LUT(63) = -1;
LUT(65) = -3;
LUT(67) =  3;
LUT(69) = -1;
LUT(71) =  1;
LUT(73) =  1;
```

```
LUT(75) =  3;
LUT(77) = -1;
LUT(79) =  1;
LUT(81) = -1;
LUT(83) =  1;
LUT(85) =  1;
LUT(87) = -1;
LUT(89) =  3;
LUT(91) =  1;
LUT(93) =  1;
LUT(95) = -1;
LUT(97) =  1;
LUT(99) =  3;
LUT(101) =  3;
LUT(103) =  1;

LUT(105) =  5;
LUT(107) =  3;
LUT(109) =  3;
LUT(111) =  1;
LUT(113) = -1;
LUT(115) =  1;
LUT(117) =  1;
LUT(119) = -1;
LUT(121) =  3;
LUT(123) =  1;
LUT(125) =  1;
LUT(127) = -1;
LUT(129) = -7;
LUT(131) = -1;
LUT(133) = -1;
LUT(135) =  1;
LUT(137) = -3;
LUT(139) = -1;
LUT(141) = -1;
LUT(143) =  1;
LUT(145) = -1;
LUT(147) =  1;
LUT(149) =  1;
LUT(151) = -1;
LUT(153) =  3;
LUT(155) =  1;

LUT(157) =  1;
LUT(159) = -1;
LUT(161) = -3;
LUT(163) = -1;
LUT(165) =  3;
LUT(167) =  1;
LUT(169) =  1;
LUT(171) = -1;
LUT(173) =  3;
LUT(175) =  1;
LUT(177) = -1;
LUT(179) =  1;
LUT(181) =  1;
LUT(183) = -1;
LUT(185) =  3;
LUT(187) =  1;
LUT(189) =  1;
LUT(191) = -1;
LUT(193) = -3;
LUT(195) =  3;
LUT(197) = -1;
LUT(199) =  1;
LUT(201) =  1;
LUT(203) =  3;
```

```
LUT(205) = -1;
LUT(207) =  1;

LUT(209) = -1;
LUT(211) =  1;
LUT(213) =  1;
LUT(215) = -1;
LUT(217) =  3;
LUT(219) =  1;
LUT(221) =  1;
LUT(223) = -1;
LUT(225) =  1;
LUT(227) =  3;
LUT(229) =  3;
LUT(231) =  1;
LUT(233) =  5;
LUT(235) =  3;
LUT(237) =  3;
LUT(239) =  1;
LUT(241) = -1;
LUT(243) =  1;
LUT(245) =  1;
LUT(247) = -1;
LUT(249) =  3;
LUT(251) =  1;
LUT(253) =  1;
LUT(255) = -1;
%%end function FillEulerLUT
```

KuwaharaFast

```
function d = KuwaharaFast(image_in, L)
% Kuwahara filter implementation. Smoothing and edge preserving filter
%
%INPUTS:
% image_in->    input data - square array. Must be double or integer precision
% L ->          kernel creation integer =1,2,3,4,5...
%               kernel_size -> k = 4*L +1
%               kuwahara subwindow (regions 1-4) size R = 3,5,7,9....
%               Window size J=K= 2R-1;                J = 5,9,13,17......
%
%OUTPUTS:
% d->           double precision output array the same size as image_in. If image_in
%               is an integer array, it will be converted to the double precision
%
% The Kuwahara filter work as follows:
% The sliding window size [K,K]is divided into 4 overlapping sub-windows size [R,R] such
that
% central pixel in [K,K] is included in every sub-window {R,R] (pixel abcd).
%
%    ( a  a  ab   b  b)
%    ( a  a  ab   b  b)
%    (ac ac abcd bd bd)
%    ( c  c  cd   d  d)
%    ( c  c  cd   d  d)
%
% In each sub-window, the mean and variance are computed. The output value at the
position of
% central pixel set to the mean of the subwindow with the smallest variance.
% Then window [K,K] moved to the next pixel.
%
% References:
% http://www.ph.tn.tudelft.nl/DIPlib/docs/FIP.pdf van Vliet "Fundamentals of Image
% Processing"
% http://www.incx.nec.co.jp/imap-vision/library/wouter/kuwahara.html
```

```
%
% Other m-files required: ARRAY_PADD that can be downloaded from FEX:
%
http://www.mathworks.com/matlabcentral/fileexchange/loadFile.do?objectId=7720&objectType=
FILE

% Subfunctions: none
% MAT-files required: none

%-------------------------------------------------------|
%   Sergei Koptenko, Resonant Medical, Montreal, Qc.|
% ph: 514.985.2442 ext265, www.resonantmedical.com  |
%      sergei.koptenko@resonantmedical.com          |
%---------------Aug/12/2006-------------------------|

if isinteger(image_in), image_in = double(image_in); end

if nargin <2, L =1; end  % Rank of the Kuwahara kernel
R = 2*L+1;      % size of the 1/4 sub-window in Kuwahara kernel
[d, indd] = array_padd(image_in, [L,L], 0, 'both', 'replicate');
% [d, indd] = padarray(image_in, [L,L], 0, 'both', 'replicate');

MeanArray =  colfilt(d,[R,R],'sliding',@mean);
VarArray =  colfilt(d,[R,R],'sliding',@var);

LL1= (indd(3):1:indd(4))-L;
LL2= (indd(3):1:indd(4))+L;
ccol = size(image_in,2);
vccol = 1:1:ccol;

d = zeros(size(d,1),ccol);

for ii = indd(1): 1:indd(2),        % Going through rows
        curr_mean = [MeanArray(ii-L, LL1);  MeanArray(ii-L, LL2);  MeanArray(ii+L, LL2);
MeanArray(ii+L, LL1)];
        curr_std = [VarArray(ii-L, LL1);  VarArray(ii-L, LL2);  VarArray(ii+L, LL2);
VarArray(ii+L, LL1);];
        [tmp, iind] = min(curr_std);
        IND = sub2ind([4,ccol], iind, vccol);
        d(ii,:) = curr_mean(IND);
end
d = d(indd(1): 1:indd(2), :); % recover the original size

end

function [data_out, indd] = array_padd(data_in, padsize, paddvalue, direction, paddmode)

% function to pad data array with various border conditions
% INPUTS:
%   DATA_IN - input data array
%   PADSIZE - same as in padarray.m, [rowpad, colpad] number of samples to
%             pad in row and in column direction
%   PADDVALUE - numerical value used to pad (ignored within some pad modes)
%   DIRECTION - same as in padarray.m {'both' 'post' and 'pre'}
%   PADDMODE  - 'circular', 'replicate' and 'symmetric' are the  same as in
%             padarray.m.  New options are:
%    'barthannwin', 'bartlett', 'blackman','blackmanharris', 'bohmanwin',
%    'flattopwin','gausswin','hamming' ,'hann', 'nuttallwin','parzenwin', 'triang'
%     In it, 'symmetric' padded values are multiplied by the 1/2 of corresponding
%     window to taper off the values to zero. Symmetrical padding option in
%     it can be replaced by 'replicate' by uncommenting line 70 and
%     commenting line 71 in function body. With these windowing options,
%     direction and paddvalue is ignored (but must be present for consistency)
%     and internaly 'symmetric' and  'both' are used
%
%
% OUTPUTS:  DATA_OUT    - output padded data array
```

```
%           INDD        - indeces of padded array used to recover the original array
%
%EXAMPLES:
%       data_in = [1 1 1 1 1; 1 2 3 2 1; 1 2 3 2 1; 1 1 1 1 1]
%       [data_out, indd] = array_padd(data_in, [3, 5])
%       [data_out, indd] = array_padd(data_in, [3, 5], 5)
%       [data_out, indd] = array_padd(data_in, [3, 5], 0, 'both')
%       [data_out, indd] = array_padd(data_in, [3, 5], 0, 'both', 'replicate')
%       [data_out, indd] = array_padd(data_in, [3, 5], 0, 'both', 'symmetric')
%       [data_out, indd] = array_padd(data_in, [3, 5], 0, 'both', 'hamming')
%       imagesc(data_out); colorbar
% original array size and position within padded array can be recovered as
%       data_out = data_out(indd(1):indd(2),indd(3):indd(4));

% Other m-files required: none
% Subfunctions: none
% MAT-files required:
% window.m and padarray.m from Signal and Image Processing Toolboxes

%_____________________________________________
%   Sergei Koptenko, Resonant Medical Inc.,
%           Montreal, Qc., Canada
%   sergei.koptenko@resonantmedical.com
%   Website: http://www.resonantmedical.com
%_____________Feb/30/2005_____________________

if nargin <2,
    disp('Not enough arguments')
    elseif  nargin <3, paddvalue =0; direction = 'both'; paddmode = 'simple';
        elseif  nargin <4, direction = 'both'; paddmode = 'simple';
            elseif nargin <5, paddmode = 'simple';
end

[rrow,ccol] = size(data_in);
%Find indices of the original array within the padded array
switch direction
    case {'both','pre' }
       indd = [padsize(1)+1,(padsize(1)+rrow), padsize(2)+1,(padsize(2)+ccol)];
    case 'post'
        indd = [1,rrow, 1,ccol];
end

% Create the padded array
switch paddmode
    case 'simple'
          data_out = padarray(data_in, padsize, paddvalue, direction);

   case {'circular', 'replicate' , 'symmetric' }
        data_out = padarray(data_in,padsize, paddmode, direction);

    case  {'barthannwin', 'bartlett', 'blackman', 'blackmanharris',...
            'bohmanwin', 'flattopwin','gausswin', 'hann' , 'nuttallwin',...
            'parzenwin' , 'triang','hamming'} % This option forces direction == 'both'
        eval(['rowwind =window(@' paddmode ', ' num2str(2*padsize(1)) ');']);
        eval(['colwind =window(@' paddmode ', ' num2str(2*padsize(2)) ');']);

%       data_out = padarray(data_in, padsize, 'replicate', 'both');
        data_out = padarray(data_in, padsize, 'symmetric', 'both');
        [mrow, mcol] = size(data_out);
%________Create a Column mask_____________
        tc =ones(mrow,1); % single column mask
        tc(1:indd(1)-1) = tc(1:indd(1)-1) .* rowwind(1:padsize(1));  % mask for the row
start
        tc(indd(2)+1:end) = tc(indd(2)+1:end) .* rowwind(padsize(1)+1:end);%mask for the
row end
        mc = repmat(tc, 1, mcol); %column mask array
%________Create a ROW mask_____________
```

```
        tr =ones(1, mcol); % single ROW mask
        tr(1:indd(3)-1) = tr(1:indd(3)-1) .* colwind(1:padsize(2))';    % mask for the
col start
        tr(indd(4)+1:end) = tr(indd(4)+1:end) .* colwind(padsize(2)+1:end)'; % mask for
the col end
        mr = repmat(tr, mrow, 1); %  row mask array
%________Create FULL mask_____________
        data_out = data_out .*  mr .* mc;

   otherwise
      disp('Unknown method.')
end
end
function d = KuwaharaFast(image_in, L)
% Kuwahara filter implementation. Smoothing and edge preserving filter
%
%INPUTS:
% image_in->    input data - square array. Must be double or integer precision
% L ->          kernel creation integer =1,2,3,4,5...
%               kernel_size -> k = 4*L +1
%               kuwahara subwindow (regions 1-4) size R = 3,5,7,9....
%               Window size J=K= 2R-1;               J = 5,9,13,17......
%
%OUTPUTS:
% d->           double precision output array the same size as image_in. If image_in
%               is an integer array, it will be converted to the double precision
%
% The Kuwahara filter work as follows:
% The sliding window size [K,K]is divided into 4 overlapping sub-windows size [R,R] such
that
% central pixel in [K,K] is included in every sub-window {R,R] (pixel abcd).
%
%    ( a  a  ab   b  b)
%    ( a  a  ab   b  b)
%    (ac ac abcd bd bd)
%    ( c  c  cd   d  d)
%    ( c  c  cd   d  d)
%
% In each sub-window, the mean and variance are computed. The output value at the
position of
% central pixel set to the mean of the subwindow with the smallest variance.
% Then window [K,K] moved to the next pixel.
%
% References:
% http://www.ph.tn.tudelft.nl/DIPlib/docs/FIP.pdf van Vliet "Fundamentals of Image
% Processing"
% http://www.incx.nec.co.jp/imap-vision/library/wouter/kuwahara.html
%
% Other m-files required: ARRAY_PADD that can be downloaded from FEX:
%
http://www.mathworks.com/matlabcentral/fileexchange/loadFile.do?objectId=7720&objectType=
FILE

% Subfunctions: none
% MAT-files required: none

%-------------------------------------------------|
%   Sergei Koptenko, Resonant Medical, Montreal, Qc.|
% ph: 514.985.2442 ext265, www.resonantmedical.com  |
%      sergei.koptenko@resonantmedical.com          |
%---------------Aug/12/2006-------------------------|

if isinteger(image_in), image_in = double(image_in); end

if nargin <2, L =1; end  % Rank of the Kuwahara kernel
R = 2*L+1;      % size of the 1/4 sub-window in Kuwahara kernel
[d, indd] = array_padd(image_in, [L,L], 0, 'both', 'replicate');
```

```
% [d, indd] = padarray(image_in, [L,L], 0, 'both', 'replicate');

MeanArray =  colfilt(d,[R,R],'sliding',@mean);
VarArray =  colfilt(d,[R,R],'sliding',@var);

LL1= (indd(3):1:indd(4))-L;
LL2= (indd(3):1:indd(4))+L;
ccol = size(image_in,2);
vccol = 1:1:ccol;

d = zeros(size(d,1),ccol);

for ii = indd(1): 1:indd(2),        % Going through rows
        curr_mean = [MeanArray(ii-L, LL1);  MeanArray(ii-L, LL2);  MeanArray(ii+L, LL2);
MeanArray(ii+L, LL1)];
        curr_std = [VarArray(ii-L, LL1);  VarArray(ii-L, LL2);  VarArray(ii+L, LL2);
VarArray(ii+L, LL1);];
        [tmp, iind] = min(curr_std);
        IND = sub2ind([4,ccol], iind, vccol);
        d(ii,:) = curr_mean(IND);
end
d = d(indd(1): 1:indd(2), :); % recover the original size

end

function [data_out, indd] = array_padd(data_in, padsize, paddvalue, direction, paddmode)

% function to pad data array with various border conditions
% INPUTS:
%   DATA_IN - input data array
%   PADSIZE - same as in padarray.m, [rowpad, colpad] number of samples to
%             pad in row and in column direction
%   PADDVALUE - numerical value used to pad (ignored within some pad modes)
%   DIRECTION - same as in padarray.m {'both' 'post' and 'pre'}
%   PADDMODE  - 'circular', 'replicate' and 'symmetric' are the  same as in
%             padarray.m.  New options are:
%    'barthannwin', 'bartlett', 'blackman','blackmanharris', 'bohmanwin',
%    'flattopwin','gausswin','hamming' ,'hann', 'nuttallwin','parzenwin', 'triang'
%     In it, 'symmetric' padded values are multiplied by the 1/2 of corresponding
%     window to taper off the values to zero. Symmetrical padding option in
%     it can be replaced by 'replicate' by uncommenting line 70 and
%     commenting line 71 in function body. With these windowing options,
%     direction and paddvalue is ignored (but must be present for consistency)
%     and internaly 'symmetric' and  'both' are used
%
%
% OUTPUTS:  DATA_OUT    - output padded data array
%           INDD        - indeces of padded array used to recover the original array
%
%EXAMPLES:
%       data_in = [1 1 1 1 1; 1 2 3 2 1; 1 2 3 2 1; 1 1 1 1 1]
%       [data_out, indd] = array_padd(data_in, [3, 5])
%       [data_out, indd] = array_padd(data_in, [3, 5], 5)
%       [data_out, indd] = array_padd(data_in, [3, 5], 0, 'both')
%       [data_out, indd] = array_padd(data_in, [3, 5], 0, 'both', 'replicate')
%       [data_out, indd] = array_padd(data_in, [3, 5], 0, 'both', 'symmetric')
%       [data_out, indd] = array_padd(data_in, [3, 5], 0, 'both', 'hamming')
%       imagesc(data_out); colorbar
% original array size and position within padded array can be recovered as
%       data_out = data_out(indd(1):indd(2),indd(3):indd(4));

% Other m-files required: none
% Subfunctions: none
% MAT-files required:
% window.m and padarray.m from Signal and Image Processing Toolboxes

%_____________________________________________
```

```
%   Sergei Koptenko, Resonant Medical Inc.,
%            Montreal, Qc., Canada
%   sergei.koptenko@resonantmedical.com
%   Website: http://www.resonantmedical.com
%_____________Feb/30/2005_____________________

if nargin <2,
    disp('Not enough arguments')
    elseif  nargin <3, paddvalue =0; direction = 'both'; paddmode = 'simple';
        elseif  nargin <4, direction = 'both'; paddmode = 'simple';
            elseif nargin <5, paddmode = 'simple';
end

[rrow,ccol] = size(data_in);
%Find indices of the original array within the padded array
switch direction
    case {'both','pre' }
       indd = [padsize(1)+1,(padsize(1)+rrow), padsize(2)+1,(padsize(2)+ccol)];
    case 'post'
        indd = [1,rrow, 1,ccol];
end

% Create the padded array
switch paddmode
    case 'simple'
          data_out = padarray(data_in, padsize, paddvalue, direction);

   case {'circular', 'replicate' , 'symmetric' }
        data_out = padarray(data_in,padsize, paddmode, direction);

    case  {'barthannwin', 'bartlett', 'blackman', 'blackmanharris',...
             'bohmanwin', 'flattopwin','gausswin', 'hann' , 'nuttallwin',...
             'parzenwin' , 'triang','hamming'} % This option forces direction == 'both'
        eval(['rowwind =window(@' paddmode ', ' num2str(2*padsize(1)) ');']);
        eval(['colwind =window(@' paddmode ', ' num2str(2*padsize(2)) ');']);

%       data_out = padarray(data_in, padsize, 'replicate', 'both');
        data_out = padarray(data_in, padsize, 'symmetric', 'both');
        [mrow, mcol] = size(data_out);
%________Create a Column mask_____________
        tc =ones(mrow,1); % single column mask
        tc(1:indd(1)-1) = tc(1:indd(1)-1) .* rowwind(1:padsize(1));  % mask for the row
start
        tc(indd(2)+1:end) = tc(indd(2)+1:end) .* rowwind(padsize(1)+1:end);%mask for the
row end
        mc = repmat(tc, 1, mcol); %column mask array
%________Create a ROW mask_____________
        tr =ones(1, mcol); % single ROW mask
        tr(1:indd(3)-1) = tr(1:indd(3)-1) .* colwind(1:padsize(2))';    % mask for the
col start
        tr(indd(4)+1:end) = tr(indd(4)+1:end) .* colwind(padsize(2)+1:end)'; % mask for
the col end
        mr = repmat(tr, mrow, 1); %  row mask array
%________Create FULL mask_____________
        data_out = data_out .*  mr .* mc;

   otherwise
      disp('Unknown method.')
end
end
%%end KuwaharaFast
```

Skel2Graph3D

```
function [A,node,link] = Skel2Graph3D(skel,THR)
% SKEL2GRAPH3D Calculate the network graph of a 3D voxel skeleton
```

```
%
% [A,node,link] = SKEL2GRAPH3D(skel,THR)
%
% where "skel" is the input 3D binary image, and "THR" is a threshold for
% the minimum length of branches. A is the adjacency matrix, and node/link
% are structures describing node and link properties
%
% Philip Kollmannsberger (philipk@gmx.net)
%
% For more information, see <a
% href="matlab:web('http://uk.mathworks.com/matlabcentral/fileexchange/43527-skel2graph-
3d')">Skel2Graph3D</a> at the MATLAB File Exchange.
% This function converts a 3D binary voxel skeleton into a network graph described by
nodes and edges.
%
% The input is a 3D binary image containing a one-dimensional voxel skeleton, generated
e.g. using the "Skeleton3D" thinning function available on MFEX. The output is the
adjacency matrix of the graph, and the nodes and links of the network as MATLAB
structure.
%
% Usage:
%
% [A,node,link] = Skel2Graph(skel,THR),
%
% where "skel" is the input 3D binary image, and "THR" is a threshold for the minimum
length of branches, to filter out skeletonization artifacts.
%
% A is the adjacency matrix with the length of the links as matrix entries, and node/link
are the structures describing node and link properties.
%
% A node has the following properties:
%
% - idx             List of voxel indices of this node
% - links           List of links connected to this node
% - conn            List of destinations of links of this node
% - comX,comY,comZ  Center of mass of all voxels of this node
% - ep              1 if node is endpoint (degree 1), 0 otherwise
%
% A link has the following properties:
%
% - n1      Node where link starts
% - n2      Node where link ends
% - point   List of voxel indices of this link
%
% A second function, "Graph2Skel3D.m", converts the network graph back into a cleaned-up
voxel skeleton image.
%
% An example of how to use these functions is given in the script "Test_Skel2Graph3D.m",
including a test image. In this example, it is also demonstrated how to iteratively
combine both conversion functions in order to obtain a completely cleaned skeleton graph.
%
% Any comments, corrections or suggestions are highly welcome. If you include this in
your own work, please cite our original publicaton [1].
%
% Philip Kollmannsberger 09/2013, 01/2016
% philipk@gmx.net
%
% [1] Kerschnitzki, Kollmannsberger et al.,
% "Architecture of the osteocyte network correl


% pad volume with zeros
skel=padarray(skel,[1 1 1]);

% image dimensions
w=size(skel,1);
l=size(skel,2);
```

```
h=size(skel,3);

% need this for labeling nodes etc.
skel2 = uint16(skel);

% all foreground voxels
list_canal=find(skel);

% 26-nh of all canal voxels
nh = logical(pk_get_nh(skel,list_canal));

% 26-nh indices of all canal voxels
nhi = pk_get_nh_idx(skel,list_canal);

% # of 26-nb of each skel voxel + 1
sum_nh = sum(logical(nh),2);

% all canal voxels with >2 nb are nodes
nodes = list_canal(sum_nh>3);

% all canal voxels with exactly one nb are end nodes
ep = list_canal(sum_nh==2);

% all canal voxels with exactly 2 nb
cans = list_canal(sum_nh==3);

% Nx3 matrix with the 2 nb of each canal voxel
can_nh_idx = pk_get_nh_idx(skel,cans);
can_nh = pk_get_nh(skel,cans);

% remove center of 3x3 cube
can_nh_idx(:,14)=[];
can_nh(:,14)=[];

% keep only the two existing foreground voxels
can_nb = sort(logical(can_nh).*can_nh_idx,2);

% remove zeros
can_nb(:,1:end-2) = [];

% add neighbours to canalicular voxel list (this might include nodes)
cans = [cans can_nb];

% group clusters of node voxels to nodes
node=[];
link=[];

tmp=false(w,l,h);
tmp(nodes)=1;
cc2=bwconncomp(tmp); % number of unique nodes
num_realnodes = cc2.NumObjects;

% create node structure
for i=1:cc2.NumObjects
    node(i).idx = cc2.PixelIdxList{i};
    node(i).links = [];
    node(i).conn = [];
    [x,y,z]=ind2sub([w l h],node(i).idx);
    node(i).comx = mean(x);
    node(i).comy = mean(y);
    node(i).comz = mean(z);
    node(i).ep = 0;

    % assign index to node voxels
    skel2(node(i).idx) = i+1;
end;
```

```
tmp=false(w,l,h);
tmp(ep)=1;
cc3=bwconncomp(tmp); % number of unique nodes

% create node structure
for i=1:cc3.NumObjects
    ni = num_realnodes+i;
    node(ni).idx = cc3.PixelIdxList{i};
    node(ni).links = [];
    node(ni).conn = [];
    [x,y,z]=ind2sub([w l h],node(ni).idx);
    node(ni).comx = mean(x);
    node(ni).comy = mean(y);
    node(ni).comz = mean(z);
    node(ni).ep = 1;

    % assign index to node voxels
    skel2(node(ni).idx) = ni+1;
end;

l_idx = 1;

c2n=zeros(w*l*h,1);
c2n(cans(:,1))=1:length(cans);

s2n=zeros(w*l*h,1);
s2n(nhi(:,14))=1:length(nhi);

% visit all nodes
for i=1:num_realnodes

    % find all canal vox in nb of all node idx
    link_idx = s2n(node(i).idx);

    for j=1:length(link_idx)
        % visit all voxels of this node

        % all potential unvisited links emanating from this voxel
        link_cands = nhi(link_idx(j),nh(link_idx(j),:)==1);
        link_cands = link_cands(skel2(link_cands)==1);

        for k=1:length(link_cands)
            [vox,n_idx,ep] = pk_follow_link(skel2,node,i,j,link_cands(k),cans,c2n);
            skel2(vox(2:end-1))=0;
            if((ep && length(vox)>THR) || (~ep && i~=n_idx))
                link(l_idx).n1 = i;
                link(l_idx).n2 = n_idx; % node number
                link(l_idx).point = vox;
                node(i).links = [node(i).links, l_idx];
                node(i).conn = [int16(node(i).conn), int16(n_idx)];
                node(n_idx).links = [node(n_idx).links, l_idx];
                node(n_idx).conn = [int16(node(n_idx).conn), int16(i)];
                l_idx = l_idx + 1;
            end;
        end;
    end;

end;

% mark all 1-nodes as end points
ep_idx = find(cellfun('length',{node.links})==1);
for i=1:length(ep_idx)
    node(ep_idx(i)).ep = 1;
end;

% number of nodes
n_nodes = length(node);
```

```
% initialize matrix
A = zeros(n_nodes);

% for all nodes, make according entries into matrix for all its links
for i=1:n_nodes
    idx1=find(node(i).conn>0);
    idx2=find(node(i).links>0);
    idx=intersect(idx1,idx2);
    for j=1:length(idx) % for all its links
        if(i==link(node(i).links(idx(j))).n1) % if we are the starting point

A(i,link(node(i).links(idx(j))).n2)=length(link(node(i).links(idx(j))).point);

A(link(node(i).links(idx(j))).n2,i)=length(link(node(i).links(idx(j))).point);
        end;
        if(i==link(node(i).links(idx(j))).n2) % if we are the end point

A(i,link(node(i).links(idx(j))).n1)=length(link(node(i).links(idx(j))).point);

A(link(node(i).links(idx(j))).n1,i)=length(link(node(i).links(idx(j))).point);
        end;
    end;
end;

% convert to sparse
A = sparse(A);

% transform all voxel and position indices back to non-padded coordinates
for i=1:length(node)
    [x,y,z] = ind2sub([w,l,h],node(i).idx);
    node(i).idx = sub2ind([w-2,l-2,h-2],x-1,y-1,z-1);
    node(i).comx = node(i).comx - 1;
    node(i).comy = node(i).comy - 1;
    node(i).comz = node(i).comz - 1;
end;

% transform all link voxel indices back to non-padded coordinates
for i=1:length(link)
    [x,y,z] = ind2sub([w,l,h],link(i).point);
    link(i).point = sub2ind([w-2,l-2,h-2],x-1,y-1,z-1);
end;
%%%end Skel2Graph3D
```

Skeleton3D

```
function skel = Skeleton3D(img,spare)
% SKELETON3D Calculate the 3D skeleton of an arbitrary binary volume using parallel
medial axis thinning.
%
% skel = SKELETON3D(img) returns the skeleton of the binary volume 'img'
% skel = SKELETON3D(img,mask) preserves foreground voxels in 'mask'
%
% MATLAB vectorized implementation of the algorithm by Lee, Kashyap and Chu
% "Building skeleton models via 3-D medial surface/axis thinning algorithms."
% Computer Vision, Graphics, and Image Processing, 56(6):462-478, 1994.
%
% Inspired by the ITK implementation by Hanno Homann
% http://hdl.handle.net/1926/1292
% and the Fiji/ImageJ plugin by Ignacio Arganda-Carreras
% http://fiji.sc/wiki/index.php/Skeletonize3D
%
% Philip Kollmannsberger (philipk@gmx.net)
%
% For more information, see <a
```

```
% href="matlab:web('http://www.mathworks.com/matlabcentral/fileexchange/43400-
skeleton3d')">Skeleton3D</a> at the MATLAB File Exchange.

% pad volume with zeros to avoid edge effects
skel=padarray(img,[1 1 1]);

if(nargin==2)
    spare=padarray(spare,[1 1 1]);
end;

% fill lookup table
eulerLUT = FillEulerLUT;

width = size(skel,1);
height = size(skel,2);
depth = size(skel,3);

unchangedBorders = 0;

while( unchangedBorders < 6 )  % loop until no change for all six border types
    unchangedBorders = 0;
    for currentBorder=1:6 % loop over all 6 directions
        cands=zeros(width,height,depth);
        switch currentBorder
            case 4,
                x=2:size(skel,1); % identify border voxels as candidates
                cands(x,:,:)=skel(x,:,:) - skel(x-1,:,:);
            case 3,
                x=1:size(skel,1)-1;
                cands(x,:,:)=skel(x,:,:) - skel(x+1,:,:);
            case 1,
                y=2:size(skel,2);
                cands(:,y,:)=skel(:,y,:) - skel(:,y-1,:);
            case 2,
                y=1:size(skel,2)-1;
                cands(:,y,:)=skel(:,y,:) - skel(:,y+1,:);
            case 6,
                z=2:size(skel,3);
                cands(:,:,z)=skel(:,:,z) - skel(:,:,z-1);
            case 5,
                z=1:size(skel,3)-1;
                cands(:,:,z)=skel(:,:,z) - skel(:,:,z+1);
        end;

        % if excluded voxels were passed, remove them from candidates
        if(nargin==2)
            cands = cands.*~spare;
        end;

        % make sure all candidates are indeed foreground voxels
        cands = intersect(find(cands(:)==1),find(skel(:)==1));

        noChange = true;

        if(~isempty(cands))
            % get subscript indices of candidates
            [x,y,z]=ind2sub([width height depth],cands);

            % get 26-neighbourhood of candidates in volume
            nhood = logical(pk_get_nh(skel,cands));

            % remove all endpoints (exactly one nb) from list
            di1 = find(sum(nhood,2)==2);
            nhood(di1,:)=[];
            cands(di1)=[];
            x(di1)=[];
            y(di1)=[];
```

```
            z(di1)=[];

            % remove all non-Euler-invariant points from list
            di2 = find(~p_EulerInv(nhood, eulerLUT'));
            nhood(di2,:)=[];
            cands(di2)=[];
            x(di2)=[];
            y(di2)=[];
            z(di2)=[];

            % remove all non-simple points from list
            di3 = find(~p_is_simple(nhood));
            nhood(di3,:)=[];
            cands(di3)=[];
            x(di3)=[];
            y(di3)=[];
            z(di3)=[];


            % if any candidates left: divide into 8 independent subvolumes
            if(~isempty(x))
                x1 = find(mod(x,2));
                x2 = find(~mod(x,2));
                y1 = find(mod(y,2));
                y2 = find(~mod(y,2));
                z1 = find(mod(z,2));
                z2 = find(~mod(z,2));
                ilst(1).l = intersect(x1,intersect(y1,z1));
                ilst(2).l = intersect(x2,intersect(y1,z1));
                ilst(3).l = intersect(x1,intersect(y2,z1));
                ilst(4).l = intersect(x2,intersect(y2,z1));
                ilst(5).l = intersect(x1,intersect(y1,z2));
                ilst(6).l = intersect(x2,intersect(y1,z2));
                ilst(7).l = intersect(x1,intersect(y2,z2));
                ilst(8).l = intersect(x2,intersect(y2,z2));

                idx = [];

                % do parallel re-checking for all points in each subvolume
                for i = 1:8
                    if(~isempty(ilst(i).l))
                        idx = ilst(i).l;
                        li = sub2ind([width height depth],x(idx),y(idx),z(idx));
                        skel(li)=0; % remove points
                        nh = logical(pk_get_nh(skel,li));
                        di_rc = find(~p_is_simple(nh));
                        if(~isempty(di_rc)) % if topology changed: revert
                            skel(li(di_rc))=1;
                        else
                            noChange = false; % at least one voxel removed
                        end;
                    end;
                end;
            end;
        end;

        if( noChange )
            unchangedBorders = unchangedBorders + 1;
        end;

    end;
end;

% get rid of padded zeros
skel = skel(2:end-1,2:end-1,2:end-1);
%%%end Skeleton3D
```

bwdistsc

```
function D=bwdistsc(bw,aspect)
% D=BWDISTSC(BW,ASPECT)
% BWDISTSC computes Euclidean distance transform of a binary 3D image BW.
% Distance transform assigns to each pixel in BW a number that is the
% distance from that pixel to the nearest nonzero pixel in BW. BWDISTSC
% can accept a regular 2D image, a 3D array, and a cell array of 2D slices.
% ASPECT is a 3-component vector defining the voxel-aspect-ratio for BW.
% If ASPECT is not given, [1 1 1] isotropic aspect ratio is assumed.
%
% BWDISTSC uses fast optimized scan algorithm and cell-arrays to
% represent internal data, and is less demanding to physical memory as
% well as in many cases up to 10 times faster than MATLAB's native bwdist.
%
% Example:
% bw=zeros(100,100,100);
% bw(40:60,40:60,40:60)=1;
% tic;D=bwdist(bw);toc
% tic;D=bwdistsc(bw);toc
%
% BWDISTSC tries to use MATLAB bwdist from image processing toolbox for 2D
% scans if possible, which is faster, otherwise BWDISTSC will use its own
% algorithm to also perform 2D scans. Own algorithm is also used if x- and
% y-anisotropy scales are not equal; therefore, if your data has only one
% axis that is anisotropic, it is always advantageous to feed it to
% BWDISTSC so that the anisotropic axis is z.
%
%(c) Yuriy Mishchenko HHMI JFRC Chklovskii Lab JUL 2007
% Updated Yuriy Mishchenko (Toros University) SEP 2013

% This implementation uses optimized forward-backward scan version of the
% algorithm of the original bwdistsc (2007), which substantially improves
% its speed and simplifies the code. The improvement is described in the
% part on the selection initial point in the SIVP paper below. The original
% implementation is still used in bwdistsc1, since forward-backward scan
% does not allow limiting computation to a fixed distance value MAXVAL.

% This code is free for use or modifications, just please give credit
% where appropriate. And if you modify code or fix bugs, please drop
% me a message at gmyuriy@hotmail.com.

%%%%%%%%%%%%%%%%%%%%%%%%%%%%%%%%%%%%%%%%%%%%%%%%%%%%%%%%%%%%%%%%%%%%%%%%%%%
% Scan algorithms below use following Lema:                              %
% LEMA: let F(X,z) be lower envelope of a family of parabola:            %
% F(X,z)=min_{i} [G_i(X)+(z-k_i)^2];                                     %
% and let H_k(X,z)=A(X)+(z-k)^2 be a parabola.                           %
% Then for H_k(X,z)==F(X,z) at each X there exist at most                %
% two solutions k1<k2 such that H_k12(X,z)=F(X,z), and                   %
% H_k(X,z)<F(X,z) is restricted to at most k1<k2.                        %
% Here X is any-dimensional coordinate.                                  %
%                                                                        %
% Thus, simply scan away from any z such that H_k(X,z)<F(X,z)            %
% in either direction as long as H_k(X,z)<F(X,z) and update              %
% F(X,z). Note that need to properly choose starting point;              %
% starting point is any z such that H_k(X,z)<F(X,z); z==k is             %
% usually, but not always the starting point!!!                          %
% usually, but not always the starting point!                            %
%                                                                        %
% Citation:                                                              %
% Mishchenko Y. (2013) A function for fastcomputation of large           %
% discrete Euclidean distance transforms in three or more                %
% dimensions in Matlab. Signal, Image and Video Processing               %
% DOI: 10.1007/s11760-012-0419-9.                                        %
%%%%%%%%%%%%%%%%%%%%%%%%%%%%%%%%%%%%%%%%%%%%%%%%%%%%%%%%%%%%%%%%%%%%%%%%%%%
```

```
% parse inputs
if(nargin<2 || isempty(aspect)) aspect=[1 1 1]; end

% determine geometry of the data
if(iscell(bw)) shape=[size(bw{1}),length(bw)]; else shape=size(bw); end

% correct this for 2D data
if(length(shape)==2) shape=[shape,1]; end
if(length(aspect)==2) aspect=[aspect,1]; end

% allocate internal memory
D=cell(1,shape(3)); for k=1:shape(3) D{k}=zeros(shape(1:2)); end


%%%%%%%%%%%%% scan along XY %%%%%%%%%%%%%%%%
for k=1:shape(3)
    if(iscell(bw)) bwXY=bw{k}; else bwXY=bw(:,:,k); end

    % initialize arrays
    DXY=zeros(shape(1:2));
    D1=zeros(shape(1:2));

    % if can, use 2D bwdist from image processing toolbox
    if(exist('bwdist') && aspect(1)==aspect(2))
        D1=aspect(1)^2*bwdist(bwXY).^2;
    else    % if not, use full XY-scan
        %%%%%%%%%%%%%%%% X-SCAN %%%%%%%%%%%%%%%%
        % reference for nearest "on"-pixel in bw in x direction down

        %  scan bottow-up (for all y), copy x-reference from previous row
        %  unless there is "on"-pixel in that point in current row, then
        %  that's the nearest pixel now
        xlower=repmat(Inf,shape(1:2));

        xlower(1,find(bwXY(1,:)))=1;    % fill in first row
        for i=2:shape(1)
            xlower(i,:)=xlower(i-1,:);  % copy previous row
            xlower(i,find(bwXY(i,:)))=i;% unless there is pixel
        end

        % reference for nearest "on"-pixel in bw in x direction up
        xupper=repmat(Inf,shape(1:2));

        xupper(end,find(bwXY(end,:)))=shape(1);
        for i=shape(1)-1:-1:1
            xupper(i,:)=xupper(i+1,:);
            xupper(i,find(bwXY(i,:)))=i;
        end

        % build (X,Y) for points for which distance needs to be calculated
        idx=find(~bwXY); [x,y]=ind2sub(shape(1:2),idx);

        % update distances as shortest to "on" pixels up/down in the above
        DXY(idx)= aspect(1)^2*min((x-xlower(idx)).^2,(x-xupper(idx)).^2);

        %%%%%%%%%%%%%%%% Y-SCAN %%%%%%%%%%%%%%%%
        % this will be the envelop of parabolas at different y
        D1=repmat(Inf,shape(1:2));

        p=shape(2);
        for i=1:shape(2)
            % some auxiliary datasets
            d0=DXY(:,i);

            % selecting starting point for x:
            % * if parabolas are incremented in increasing order of y,
            %   then all below-envelop intervals are necessarily right-
```

```
            %   open, which means starting point can always be chosen
            %   at the right end of y-axis
            % * if starting point exists it should be below existing
            %   current envelop at the right end of y-axis
            dtmp=d0+aspect(2)^2*(p-i)^2;
            L=D1(:,p)>dtmp;
            idx=find(L);
            D1(idx,p)=dtmp(L);


            % these will keep track along which X should
            % keep updating distances
            map_lower=L;
            idx_lower=idx;

            % scan from starting points down in increments of 1
            for ii=p-1:-1:1
                % new values for D
                dtmp=d0(idx_lower)+aspect(2)^2*(ii-i)^2;

                % these pixels are to be updated
                L=D1(idx_lower,ii)>dtmp;
                D1(idx_lower(L),ii)=dtmp(L);

                % other pixels are removed from scan
                map_lower(idx_lower)=L;
                idx_lower=idx_lower(L);

                if(isempty(idx_lower)) break; end
            end
        end
    end
    D{k}=D1;
end


%%%%%%%%%%%%% scan along Z %%%%%%%%%%%%%%%%
D1=cell(size(D));
for k=1:shape(3)
  D1{k}=repmat(Inf,shape(1:2));
end

% start building the envelope
p=shape(3);
for k=1:shape(3)
    % if there are no objects in this slice, nothing to do
    if(isinf(D{k}(1,1)))
      continue;
    end

    % selecting starting point for (x,y):
    % * if parabolas are incremented in increasing order of k, then all
    %   intersections are necessarily at the right end of the envelop,
    %   and so the starting point can be always chosen as the right end
    %   of the axis

    % check which points are valid starting points, & update the envelope
    dtmp=D{k}+aspect(3)^2*(p-k)^2;
    L=D1{p}>dtmp;
    D1{p}(L)=dtmp(L);

    % map_lower keeps track of which pixels can be yet updated with the
    % new distance, i.e. all such XY that had been under the envelop for
    % all Deltak up to now, for Deltak<0
    map_lower=L;

    % these are maintained to keep fast track of whether map is empty
```

```
    idx_lower=find(map_lower);

    % scan away from the starting points in increments of -1
    for kk=p-1:-1:1
        % new values for D
        dtmp=D{k}(idx_lower)+aspect(3)^2*(kk-k)^2;

        % these pixels are to be updated
        L=D1{kk}(idx_lower)>dtmp;
        map_lower(idx_lower)=L;
        D1{kk}(idx_lower(L))=dtmp(L);

        % other pixels are removed from scan
        idx_lower=idx_lower(L);

        if(isempty(idx_lower)) break; end
    end
end


% prepare the answer
if(iscell(bw))
    D=cell(size(bw));
    for k=1:shape(3) D{k}=sqrt(D1{k}); end
else
    D=zeros(shape);
    for k=1:shape(3) D(:,:,k)=sqrt(D1{k}); end
end

end
%%%end bwdistsc
```

filtergrid

```
% FILTERGRID Generates grid for constructing frequency domain filters
%
% Usage:  [radius, u1, u2] = filtergrid(rows, cols)
%         [radius, u1, u2] = filtergrid([rows, cols])
%
% Arguments:  rows, cols - Size of image/filter
%
% Returns:        radius - Grid of size [rows cols] containing normalised
%                          radius values from 0 to 0.5.  Grid is quadrant
%                          shifted so that 0 frequency is at radius(1,1)
%                 u1, u2 - Grids containing normalised frequency values
%                          ranging from -0.5 to 0.5 in x and y directions
%                          respectively. u1 and u2 are quadrant shifted.
%
% Used by PHASECONGMONO, PHASECONG3 etc etc
%
% See also: WAVENUMBERGRID

% Copyright (c) 1996-2017 Peter Kovesi
% Centre for Exploration Targeting
% The University of Western Australia
% peter.kovesi at uwa edu au
%
% Permission is hereby granted, free of charge, to any person obtaining a copy
% of this software and associated documentation files (the "Software"), to deal
% in the Software without restriction, subject to the following conditions:
%
% The above copyright notice and this permission notice shall be included in
% all copies or substantial portions of the Software.
%
% The Software is provided "as is", without warranty of any kind.
%
% May 2013
```

```
% September 2017 Correction to setting up matrices of frequency values for
%                odd sized images.

function [radius, u1, u2] = filtergrid(rows, cols)

    % Handle case where rows, cols has been supplied as a 2-vector
    if nargin == 1 & length(rows) == 2
        tmp = rows;
        rows = tmp(1);
        cols = tmp(2);
    end

    % Set up X and Y spatial frequency matrices, u1 and u2 The following code
    % adjusts things appropriately for odd and even values of rows and columns
    % so that the 0 frequency point is placed appropriately.  See
    % https://blogs.uoregon.edu/seis/wiki/unpacking-the-matlab-fft/
    if mod(cols,2)
        u1range = [-(cols-1)/2:(cols-1)/2]/cols;
    else
        u1range = [-cols/2:(cols/2-1)]/cols;
    end

    if mod(rows,2)
        u2range = [-(rows-1)/2:(rows-1)/2]/rows;
    else
        u2range = [-rows/2:(rows/2-1)]/rows;
    end

    [u1,u2] = meshgrid(u1range, u2range);

    % Quadrant shift so that filters are constructed with 0 frequency at
    % the corners
    u1 = ifftshift(u1);
    u2 = ifftshift(u2);

    % Construct spatial frequency values in terms of normalised radius from
    % centre.
    radius = sqrt(u1.^2 + u2.^2);
%%%end filtergrid
```

highboostfilter

```
% HIGHBOOSTFILTER - Constructs a high-boost Butterworth filter.
%
% usage: f = highboostfilter(sze, cutoff, n, boost)
%
% where: sze    is a two element vector specifying the size of filter
%               to construct [rows cols].
%        cutoff is the cutoff frequency of the filter 0 - 0.5.
%        n      is the order of the filter, the higher n is the sharper
%               the transition is. (n must be an integer >= 1).
%        boost  is the ratio that high frequency values are boosted
%               relative to the low frequency values.  If boost is less
%               than one then a 'lowboost' filter is generated
%
%
% The frequency origin of the returned filter is at the corners.
%
% See also: LOWPASSFILTER, HIGHPASSFILTER, BANDPASSFILTER
%

% Copyright (c) 1999-2001 Peter Kovesi
% School of Computer Science & Software Engineering
% The University of Western Australia
% http://www.csse.uwa.edu.au/
%
```

```
% Permission is hereby granted, free of charge, to any person obtaining a copy
% of this software and associated documentation files (the "Software"), to deal
% in the Software without restriction, subject to the following conditions:
%
% The above copyright notice and this permission notice shall be included in
% all copies or substantial portions of the Software.
%
% The Software is provided "as is", without warranty of any kind.

% October 1999
% November 2001 modified so that filter is specified in terms of high to
%               low boost rather than a zero frequency offset.


function f = highboostfilter(sze, cutoff, n, boost)

    if cutoff < 0 | cutoff > 0.5
    error('cutoff frequency must be between 0 and 0.5');
    end

    if rem(n,1) ~= 0 | n < 1
    error('n must be an integer >= 1');
    end

    if boost >= 1     % high-boost filter
    f = (1-1/boost)*highpassfilter(sze, cutoff, n) + 1/boost;
    else              % low-boost filter
    f = (1-boost)*lowpassfilter(sze, cutoff, n) + boost;
    end
%%% end highboostfilter
```

highpassfilter

```
% HIGHPASSFILTER  - Constructs a high-pass butterworth filter.
%
% usage: f = highpassfilter(sze, cutoff, n)
%
% where: sze    is a two element vector specifying the size of filter
%               to construct [rows cols].
%        cutoff is the cutoff frequency of the filter 0 - 0.5
%        n      is the order of the filter, the higher n is the sharper
%               the transition is. (n must be an integer >= 1).
%
% The frequency origin of the returned filter is at the corners.
%
% See also: LOWPASSFILTER, HIGHBOOSTFILTER, BANDPASSFILTER

% Copyright (c) 1999 Peter Kovesi
% www.peterkovesi.com/matlabfns
%
% Permission is hereby granted, free of charge, to any person obtaining a copy
% of this software and associated documentation files (the "Software"), to deal
% in the Software without restriction, subject to the following conditions:
%
% The above copyright notice and this permission notice shall be included in
% all copies or substantial portions of the Software.
%
% The Software is provided "as is", without warranty of any kind.

% October 1999

function f = highpassfilter(sze, cutoff, n)

    if cutoff < 0 | cutoff > 0.5
    error('cutoff frequency must be between 0 and 0.5');
    end
```

```
    if rem(n,1) ~= 0 | n < 1
    error('n must be an integer >= 1');
    end

    f = 1.0 - lowpassfilter(sze, cutoff, n);
    %%%end highpassfilter
```

histtruncate

```
%%function Histtruncate

% HISTTRUNCATE - Truncates ends of an image histogram.
%
% Function truncates a specified percentage of the lower and
% upper ends of an image histogram.
%
% This operation allows grey levels to be distributed across
% the primary part of the histogram.  This solves the problem
% when one has, say, a few very bright values in the image which
% have the overall effect of darkening the rest of the image after
% rescaling.
%
% Usage:
%    [newim, sortv] = histtruncate(im, lHistCut, uHistCut)
%    [newim, sortv] = histtruncate(im, lHistCut, uHistCut, sortv)
%
% Arguments:
%    im          -  Image to be processed
%    lHistCut    -  Percentage of the lower end of the histogram
%                   to saturate.
%    uHistCut    -  Percentage of the upper end of the histogram
%                   to saturate.  If omitted or empty defaults to the value
%                   for lHistCut.
%    sortv       -  Optional array of sorted image pixel values obtained
%                   from a previous call to histtruncate.  Supplying this
%                   data speeds the operation of histtruncate when one is
%                   repeatedly varying lHistCut and uHistCut.
%
% Returns:
%    newim       -  Image with values clipped at the specified histogram
%                   fraction values.  If the input image was colour the
%                   lightness values are clipped and stretched to the range
%                   0-1.  If the input image is greyscale no stretching is
%                   applied. You may want to use NORMAALISE to achieve this
%    sortv       -  Sorted image values for reuse in subsequent calls to
%                   histruncate.
%
% See also: NORMALISE

% Copyright (c) 2001-2014 Peter Kovesi
% Centre for Exploration Targeting
% The University of Western Australia
% http://www.cet.edu.au/
%
% Permission is hereby granted, free of charge, to any person obtaining a copy
% of this software and associated documentation files (the "Software"), to deal
% in the Software without restriction, subject to the following conditions:
%
% The above copyright notice and this permission notice shall be included in
% all copies or substantial portions of the Software.
%
% The Software is provided "as is", without warranty of any kind.

% July      2001 - Original version
% February  2012 - Added handling of NaN values in image
% February  2014 - Code cleanup
```

```
% September 2014 - Default for uHistCut + cleanup

function [newim, sortv] = histtruncate(im, lHistCut, uHistCut, sortv)

    if ~exist('uHistCut', 'var') || isempty(uHistCut), uHistCut = lHistCut; end

    if lHistCut < 0 | lHistCut > 100 | uHistCut < 0 | uHistCut > 100
    error('Histogram truncation values must be between 0 and 100');
    end

    if ~exist('sortv', 'var'), sortv = []; end

    if ndims(im) == 3  % Assume colour image in RGB
    hsv = rgb2hsv(im);      % Convert to HSV
        % Apply histogram truncation just to intensity component
        [hsv(:,:,3), sortv] = Ihisttruncate(hsv(:,:,3), lHistCut, uHistCut, sortv);

        % Stretch intensity component to 0-1
        hsv(:,:,3) = normalise(hsv(:,:,3));
    newim = hsv2rgb(hsv);  % Convert back to RGB

    else
        [newim, sortv] = Ihisttruncate(im, lHistCut, uHistCut, sortv);
    end


%---------------------------------------------------------------------
% Internal function that does the work
%---------------------------------------------------------------------

function [im, sortv] = Ihisttruncate(im, lHistCut, uHistCut, sortv)

    if ndims(im) > 2
    error('HISTTRUNCATE only defined for grey value images');
    end

    % Generate a sorted array of pixel values or use supplied values
    if isempty(sortv)
        sortv = sort(im(:));
    end

    % Any NaN values end up at the end of the sorted list. We need to
    % eliminate these
    sortv = sortv(~isnan(sortv));
    N = length(sortv(:));

    % Compute indicies corresponding to specified upper and lower fractions
    % of the histogram.
    lind = floor(1 + N*lHistCut/100);
    hind =  ceil(N - N*uHistCut/100);

    low_in  = sortv(lind);
    high_in = sortv(hind);

    % Adjust image
    im(im < low_in) = low_in;
    im(im > high_in) = high_in;

    % Normalise?  normalise with NaNs?
    %%%end histtruncate
```

homomorphic

```
%%homomorphic filter
% HOMOMORPHIC - Performs homomorphic filtering on an image.
%
```

```
% Function performs homomorphic filtering on an image. This form of
% filtering sharpens features and flattens lighting variantions in an image.
% It usually is very effective on images which have large variations in
% lighting, for example when a subject appears against strong backlighting.
%
%
% Usage: newim =
% homomorphic(inimage,boost,CutOff,order,lhistogram_cut,uhistogram_cut, hndl)
% homomorphic(inimage,boost,CutOff,order,lhistogram_cut,uhistogram_cut)
% homomorphic(inimage,boost,CutOff,order,hndl)
% homomorphic(inimage,boost,CutOff,order)
%
% Parameters:  (suggested values are in brackets)
%         boost    - The ratio that high frequency values are boosted
%                    relative to the low frequency values (2).
%         CutOff   - Cutoff frequency of the filter (0 - 0.5)
%         order    - Order of the modified Butterworth style filter that
%                    is used, this must be an integer > 1 (2)
%         lhistogram_cut - Percentage of the lower end of the filtered image's
%                          histogram to be truncated, this eliminates extreme
%                          values in the image from distorting the final result. (0)
%         uhistogram_cut - Percentage of upper end of histogram to truncate. (5)
%         hndl           - Optional handle to text box for updating
%                          messages to be sent to a GUI interface.
%
%  If lhistogram_cut and uhistogram_cut are not specified no histogram truncation will be
%  applied.
%
%
% Suggested values: newim = homomorphic(im, 2, .25, 2, 0, 5);
%

% homomorphic called with no arguments invokes GUI interface.
%
% or simply   homomorphic  to invoke the GUI   - GUI version does not work!

% Copyright (c) 1999-2001 Peter Kovesi
% School of Computer Science & Software Engineering
% The University of Western Australia
% http://www.csse.uwa.edu.au/
%
% Permission is hereby granted, free of charge, to any person obtaining a copy
% of this software and associated documentation files (the "Software"), to deal
% in the Software without restriction, subject to the following conditions:
%
% The above copyright notice and this permission notice shall be included in
% all copies or substantial portions of the Software.
%
% The Software is provided "as is", without warranty of any kind.

% June 1999
% December 2001 cleaned up and modified to work with colour images

function him = homomorphic(im, boost, CutOff, order, varargin)


%    if nargin == 0             % invoke GUI if it exists
%   if exist('homomorphicGUI.m');
%       homomorphicGUI;
%       return;
%   else
%       error('homomorphicGUI does not exist');
%   end
%
%    else

    if ndims(im) == 2  % Greyscale image
```

```
        him = Ihomomorphic(im, boost, CutOff, order, varargin);

    else              % Assume colour image in RGB format
        hsv = rgb2hsv(im);   % Convert to HSV and apply homomorphic
                  % filtering to just the intensity component.
            hsv(:,:,3) = Ihomomorphic(hsv(:,:,3), boost, CutOff, order, varargin);
        him = hsv2rgb(hsv);  % Convert back to RGB
    end

%    end

%-----------------------------------------------------------------------
% Internal function that does the real work
%-----------------------------------------------------------------------

function him = Ihomomorphic(im, boost, CutOff, order, varargin)

    % The possible elements in varargin are:
    % {lhistogram_cut, uhistogram_cut, hndl}

    varargin = varargin{:};

    if nargin == 5
    nopparams  = length(varargin);
    end

    if (nopparams == 3)
    dispStatus = 1;
    truncate = 1;
    lhistogram_cut = varargin{1};
    uhistogram_cut = varargin{2};
    hndl = varargin{3};
    elseif (nopparams == 2)
    dispStatus = 0;
    truncate = 1;
    lhistogram_cut = varargin{1};
    uhistogram_cut = varargin{2};
    elseif (nopparams == 1)
    dispStatus = 1;
    truncate = 0;
    hndl = varargin{1};
    elseif (nopparams == 0)
    dispStatus = 0;
    truncate = 0;
    else
    disp('Usage: newim =
homomorphic(inimage,LowGain,HighGain,CutOff,order,lhistogram_cut,uhistogram_cut)');
    error('or    newim = homomorphic(inimage,LowGain,HighGain,CutOff,order)');
    end

    [rows,cols] = size(im);

    im = normalise(im);                       % Rescale values 0-1 (and cast
                          % to `double' if needed).
    FFTlogIm = fft2(log(im+.01));             % Take FFT of log (with offset
                                              % to avoid log of 0).
    h = highboostfilter([rows cols], CutOff, order, boost);
    him = exp(real(ifft2(FFTlogIm.*h)));      % Apply the filter, invert
                          % fft, and invert the log.

    if truncate

    % Problem:
    % The extreme bright values in the image are exaggerated by the filtering.
    % These (now very) bright values have the overall effect of darkening the
    % whole image when we rescale values to 0-255.
    %
```

```
    % Solution:
    % Construct a histogram of the image.  Find the level below which a high
    % percentage of the image lies (say 95%).  Saturate the grey levels in
    % the image to this level.

    %{
    if dispStatus
        set(hndl,'String','Calculating histogram and truncating...');
        drawnow;
    else
        disp('Calculating histogram and truncating...');
    end
    %}

    him = histtruncate(him, lhistogram_cut, uhistogram_cut);

    else
    him = normalise(him);  % No truncation, but fix range 0-1
    end

%end homomorphic
```

hysteresis3draw

```
%%hysteresis3d
function [tri,hys]=hysteresis3draw(img,t1,t2,conn)
% function [tri,hys]=HYSTERESIS3D(img,t1,t2,conn)
%
% Hysteresis3d is a simple function that performs trinarisation and
% hysteresis for 2D and 3D images. Hysteresis3d was inspired by Peter
% Kovesi's 2D hysteresis function
% (http://www.csse.uwa.edu.au/~pk/research/matlabfns/). This 3D function
% takes advantage of the 3D connectivities of imfill instead of the 2D
% connectivities of bwselect.
%
% Usage:        [tri,hys]=HYSTERESIS3D(img,t1,t2,conn)
%
% Arguments:    img - image for hysteresis (assumed to be non-negative)
%               t1 - lower threshold value (fraction b/w 0-1, e.g.: 0.1)
%               t2 - upper threshold value (fraction b/w 0-1, e.g.: 0.9)
%                   (t1/t2 can be entered in any order, larger one will be
%                   set as the upper threshold)
%               conn - number of connectivities (4 or 8 for 2D)
%                                               (6, 18, or 26 for 3D)
% Returns:
%               tri - the trinarisation image (values are 0, 1, or 2)
%               hys - the hysteresis image (logical mask image)
%
% Examples:     [tri,hys]=HYSTERESIS3D(img,0.25,0.8,26)
%
% 2012/07/10: written by Luke Xie
% 2013/12/09: defaults added
%
% To see an example of hysteresis used to segment a kidney region, please
% refer to supplement in QSM of Kidney, NMR Biomed, 2013 Dec;26(12):1853-63
% (http://onlinelibrary.wiley.com/doi/10.1002/nbm.3039/abstract).
% Supplemental material is also available on our CIVMspace:
% http://www.civm.duhs.duke.edu/lx201204/

%% arguments
if nargin<3
    disp('function needs at least 3 inputs')
    return;
elseif nargin==3
    disp('inputs=3')
    if numel(size(img))==2;
```

```
        disp('img=2D')
        disp('conn set at 4 connectivies (number of neighbors)')
        conn=4;
    end
    if numel(size(img))==3;
        disp('img=3D')
        disp('conn set at 6 connectivies (number of neighbors)')
        conn=6;
    end
end

%% DO NOT scale t1 & t2 based on image intensity range
if t1>t2    % swap values if t1>t2
    tmp=t1;
    t1=t2;
    t2=tmp;
end
t1v=t1;
t2v=t2;

%% trinarisation
tri=zeros(size(img));
tri(img>=t1v)=1;
tri(img>=t2v)=2;

%% hysteresis
abovet1=img>t1v;                                        % points above lower threshold
seed_indices=sub2ind(size(abovet1),find(img>t2v));   % indices of points above upper
threshold
hys=imfill(~abovet1,seed_indices,conn);              % obtain all connected regions in
abovet1 that include points with values above t2
hys=hys & abovet1;

%%%end hysteresis3draw
```

imocbr

```
%%imocbr
function [IM2] = imocbr(IM1,se)
%%% author JT Morgan
IM1e = imerode(IM1, se);
IM1o = imreconstruct(IM1e, IM1);
IM1od = imdilate(IM1o, se);
IM2 = imcomplement(imreconstruct(imcomplement(IM1od), imcomplement(IM1o)));
%%%end imocbr
```

lowpassfilter

```
%%lowpassfilter
% LOWPASSFILTER - Constructs a low-pass butterworth filter.
%
% usage: f = lowpassfilter(sze, cutoff, n)
%
% where: sze    is a two element vector specifying the size of filter
%               to construct [rows cols].
%        cutoff is the cutoff frequency of the filter 0 - 0.5
%        n      is the order of the filter, the higher n is the sharper
%               the transition is. (n must be an integer >= 1).
%               Note that n is doubled so that it is always an even integer.
%
%                       1
%      f =    --------------------
```

```
%                              2n
%              1.0 + (w/cutoff)
%
% The frequency origin of the returned filter is at the corners.
%
% See also: HIGHPASSFILTER, HIGHBOOSTFILTER, BANDPASSFILTER, FILTERGRID
%

% Copyright (c) 1999 Peter Kovesi
% School of Computer Science & Software Engineering
% The University of Western Australia
% http://www.csse.uwa.edu.au/
%
% Permission is hereby granted, free of charge, to any person obtaining a copy
% of this software and associated documentation files (the "Software"), to deal
% in the Software without restriction, subject to the following conditions:
%
% The above copyright notice and this permission notice shall be included in
% all copies or substantial portions of the Software.
%
% The Software is provided "as is", without warranty of any kind.

% October 1999
% August  2005 - Fixed up frequency ranges for odd and even sized filters
%                (previous code was a bit approximate)
% September 2017 - Changed to use filtergrid()

function f = lowpassfilter(sze, cutoff, n)

    if cutoff < 0 | cutoff > 0.5
    error('cutoff frequency must be between 0 and 0.5');
    end

    if rem(n,1) ~= 0 | n < 1
    error('n must be an integer >= 1');
    end

    if length(sze) == 1
    rows = sze; cols = sze;
    else
    rows = sze(1); cols = sze(2);
    end

    [radius, u1, u2] = filtergrid(rows,cols);

    f = 1.0 ./ (1.0 + (radius ./ cutoff).^(2*n));   % The filter

%%%end lowpassfilter
```

Lowpassfilter3d

```
%%%lowpassfilter3D
% LOWPASSFILTER - Constructs a low-pass butterworth filter.
%
% usage: f = lowpassfilter(sze, cutoff, n)
%
% where: sze    is a two element vector specifying the size of filter
%               to construct [rows cols].
%        cutoff is the cutoff frequency of the filter 0 - 0.5
%        n      is the order of the filter, the higher n is the sharper
%               the transition is. (n must be an integer >= 1).
%               Note that n is doubled so that it is always an even integer.
%
%                       1
%      f =    --------------------
%                              2n
```

```
%              1.0 + (w/cutoff)
%
% The frequency origin of the returned filter is at the corners.
%
% See also: HIGHPASSFILTER, HIGHBOOSTFILTER, BANDPASSFILTER
%

% Copyright (c) 1999 Peter Kovesi
% School of Computer Science & Software Engineering
% The University of Western Australia
% http://www.csse.uwa.edu.au/
%
% Permission is hereby granted, free of charge, to any person obtaining a copy
% of this software and associated documentation files (the "Software"), to deal
% in the Software without restriction, subject to the following conditions:
%
% The above copyright notice and this permission notice shall be included in
% all copies or substantial portions of the Software.
%
% The Software is provided "as is", without warranty of any kind.

% October 1999
% August  2005 - Fixed up frequency ranges for odd and even sized filters
%                (previous code was a bit approximate)

function f = lowpassfilter3D(sze, cutoff, n, SF)

    if cutoff < 0 | cutoff > 0.5
    error('cutoff frequency must be between 0 and 0.5');
    end

    if rem(n,1) ~= 0 | n < 1
    error('n must be an integer >= 1');
    end

    if length(sze) == 1
    rows = sze; cols = sze; slices = sze;
    else
    rows = sze(1); cols = sze(2);  slices = sze(3);
    end

    % Set up X and Y matrices with ranges normalised to +/- 0.5
    % The following code adjusts things appropriately for odd and even values
    % of rows and columns.

    if mod(cols,2)
        xrange = [-(cols-1)/2:(cols-1)/2]/(cols-1);
    else
        xrange = [-cols/2:(cols/2-1)]/cols;
    end

    if mod(rows,2)
        yrange = [-(rows-1)/2:(rows-1)/2]/(rows-1);
    else
        yrange = [-rows/2:(rows/2-1)]/rows;
    end

    if mod(slices,2)
        zrange = [-(slices-1)/2:(slices-1)/2]/(slices-1);
    else
        zrange = [-slices/2:(slices/2-1)]/slices;
    end

    [x,y,z] = meshgrid(xrange, yrange, zrange);
    radius = sqrt(x.^2 + y.^2 + (z*SF).^2);        % A matrix with every pixel = radius
relative to centre.
    f = ifftshift( 1.0 ./ (1.0 + (radius ./ cutoff).^(2*n)) );   % The filter
```

```
%%%end lowpassfilter3D
```

Noisecomp3d

```
%%% noisecomp3d
% NOISECOMP - Function for denoising an image
%
% function cleanimage = noisecomp(image, k, nscale, mult, norient, softness)
%
% Parameters:
%              k - No of standard deviations of noise to reject 2-3
%              nscale - No of filter scales to use (5-7) - the more scales used
%                       the more low frequencies are covered
%              mult   - multiplying factor between scales  (2.5-3)
%              norient - No of orientations to use (6)
%              softness - degree of soft thresholding (0-hard  1-soft)
%
% The convolutions are done via the FFT.  Many of the parameters relate
% to the specification of the filters in the frequency plane.
% The parameters are set within the file rather than being specified as
% arguments because they rarely need to be changed - nor are they very
% critical.
%
% Reference:
% Peter Kovesi, "Phase Preserving Denoising of Images".
% The Australian Pattern Recognition Society Conference: DICTA'99.
% December 1999. Perth WA. pp 212-217
% http://www.cs.uwa.edu.au/pub/robvis/papers/pk/denoise.ps.gz.
%

% Copyright (c) 1998-2000 Peter Kovesi
% School of Computer Science & Software Engineering
% The University of Western Australia
% http://www.csse.uwa.edu.au/
%
% Permission is hereby granted, free of charge, to any person obtaining a copy
% of this software and associated documentation files (the "Software"), to deal
% in the Software without restriction, subject to the following conditions:
%
% The above copyright notice and this permission notice shall be included in
% all copies or substantial portions of the Software.
%
% The Software is provided "as is", without warranty of any kind.

% September 1998 - original version
% May 1999       -
% May 2000       - modified to allow arbitrary size images


function cleanimage = noisecomp3D(im, k, nscale, mult, softness,SF,Verbose)

%nscale          = 6;    % Number of wavelet scales.
minWaveLength   = 2;     % Wavelength of smallest scale filter.
%mult            = 2;    % Scaling factor between successive filters.
sigmaOnf        = 0.55;  % Ratio of the standard deviation of the Gaussian
                         % describing the log Gabor filter's transfer function
                         % in the frequency domain to the filter center frequency.
epsilon         = .00001;% Used to prevent division by zero.

imagefft = perfft3(im);                % Fourier transform of image
[rows,cols,slices] = size(imagefft);

% Create two matrices, x and y. All elements of x have a value equal to its
% x coordinate relative to the centre, elements of y have values equal to
% their y coordinate relative to the centre.
```

```
if mod(cols,2)
    xrange = [-(cols-1)/2:(cols-1)/2]/(cols-1)*2;
else
    xrange = [-cols/2:(cols/2-1)]/cols*2;
end

if mod(rows,2)
    yrange = [-(rows-1)/2:(rows-1)/2]/(rows-1)*2;
else
    yrange = [-rows/2:(rows/2-1)]/rows*2;
end

if mod(slices,2)
    zrange = [-(slices-1)/2:(slices-1)/2]/(slices-1)*2;
else
    zrange = [-slices/2:(slices/2-1)]/slices*2;
end

[x,y,z] = meshgrid(xrange, yrange, zrange);

x = ifftshift(x);   % Quadrant shift to put 0 frequency at the corners
y = ifftshift(y);
z = ifftshift(z);

radius = sqrt(x.^2 + y.^2 + z.^2);      % Matrix values contain normalised radius from
centre.

% Get rid of the 0 radius value in the middle (at top left corner after
% fftshifting) so that taking the log of the radius, or dividing by the
% radius, will not cause trouble.
radius(1,1,1) = 1;

% Construct the monogenic filters in the frequency domain.  The two
% filters would normally be constructed as follows
%    H1 = i*x./radius;
%    H2 = i*y./radius;
% However the two filters can be packed together as a complex valued
% matrix, one in the real part and one in the imaginary part.  Do this by
% multiplying H2 by i and then adding it to H1 (note the subtraction
% because i*i = -1).  When the convolution is performed via the fft the
% real part of the result will correspond to the convolution with H1 and
% the imaginary part with H2.  This allows the two convolutions to be
% done as one in the frequency domain, saving time and memory.
H1 = i*x./radius;
H2 = i*y./radius;
H3 = i*z./radius;

% The two monogenic filters H1 and H2 are not selective in terms of the
% magnitudes of the frequencies.  The code below generates bandpass
% log-Gabor filters which are point-wise multiplied by IM to produce
% different bandpass versions of the image before being convolved with H1
% and H2

% First construct a low-pass filter that is as large as possible, yet falls
% away to zero at the boundaries.  All filters are multiplied by
% this to ensure no extra frequencies at the 'corners' of the FFT are
% incorporated as this can upset the normalisation process when
% calculating phase congruency
lp = lowpassfilter3D([rows,cols,slices],.45,15,SF);    % Radius .4, 'sharpness' 15

sig = [];
estMeanEn = [];
aMean = [];
aSig = [];

totalEnergy = zeros(rows,cols,slices);              % response at each orientation.
```

```
for s = 1:nscale                % For each scale.

    wavelength = minWaveLength*mult^(s-1);

    fo = 1.0/wavelength;                  % Centre frequency of filter.
    logGabor = exp((-(log(radius/fo)).^2) / (2 * log(sigmaOnf)^2));
    logGabor = logGabor.*lp;              % Apply low-pass filter
    logGabor(1,1) = 0;                    % Set the value at the 0 frequency point of the
    % filter back to zero (undo the radius fudge).

    EOfft = imagefft.*logGabor;    % Bandpassed image in the frequency domain
    EO = ifftn(EOfft);  % Bandpassed image in spatial domain
    aEO = abs(EO);

    h1 = real(ifftn(EOfft.*H1));     % Bandpassed monogenic filtering
    h2 = real(ifftn(EOfft.*H2));     % Bandpassed monogenic filtering
    h3 = real(ifftn(EOfft.*H3));     % Bandpassed monogenic filtering

    An = sqrt(real(EO).^2 + h1.^2 + h2.^2+ h3.^2); % Amplitude of this scale component.

    if s == 1
        % Estimate the mean and variance in the amplitude response of the smallest scale
        % filter pair at this orientation.
        % If the noise is Gaussian the amplitude response will have a Rayleigh
distribution.
        % We calculate the median amplitude response as this is a robust statistic.
        % From this we estimate the mean and variance of the Rayleigh distribution

        medianEn =  median(An(:));
        meanEn = medianEn*.5*sqrt(-pi/log(0.5));

        RayVar = (4-pi)*(meanEn.^2)/pi;
        RayMean = meanEn;

        estMeanEn = [estMeanEn meanEn];
        sig = [sig sqrt(RayVar)];

        %% May want to look at actual distribution on special images
        % hist(reshape(aEO,1,rows*cols),100);
        % pause(1);
    end

    % Now apply soft thresholding
    T = (RayMean + k*sqrt(RayVar))/(mult^(s-1));  % Noise effect inversely proportional
to
    % bandwidth/centre frequency.

    validEO = An > T;                   % Find where magnitude of energy exceeds noise.
    V = softness*T*EO./(An + epsilon);  % Calculate array of noise vectors to subtract.
    V = ~validEO.*EO + validEO.*V;       % Adjust noise vectors so that EO values will
    % not be negated
    EO = EO-V;                           % Subtract noise vector.

    totalEnergy = totalEnergy + EO;
end

if Verbose
    disp('Estimated mean noise in each orientation')
    disp(estMeanEn);
end

cleanimage = real(totalEnergy);

%%% end noisecomp3d
```

Normalize

```
% NORMALISE - Normalises image values to 0-1, or to desired mean and variance
%
% Usage:
%             n = normalise(im)
%
% Offsets and rescales image so that the minimum value is 0
% and the maximum value is 1.  Result is returned in n.  If the image is
% colour the image is converted to HSV and the value/intensity component
% is normalised to 0-1 before being converted back to RGB.
%
%
%             n = normalise(im, reqmean, reqvar)
%
% Arguments:  im      - A grey-level input image.
%             reqmean - The required mean value of the image.
%             reqvar  - The required variance of the image.
%
% Offsets and rescales image so that it has mean reqmean and variance
% reqvar.  Colour images cannot be normalised in this manner.

% Copyright (c) 1996-2005 Peter Kovesi
% School of Computer Science & Software Engineering
% The University of Western Australia
% http://www.csse.uwa.edu.au/
%
% Permission is hereby granted, free of charge, to any person obtaining a copy
% of this software and associated documentation files (the "Software"), to deal
% in the Software without restriction, subject to the following conditions:
%
% The above copyright notice and this permission notice shall be included in
% all copies or substantial portions of the Software.
%
% The Software is provided "as is", without warranty of any kind.

% January 2005 - modified to allow desired mean and variance


function n = normalise(im, reqmean, reqvar)

    if ~(nargin == 1 | nargin == 3)
       error('No of arguments must be 1 or 3');
    end

    if nargin == 1   % Normalise 0 - 1
    if ndims(im) == 3         % Assume colour image
        hsv = rgb2hsv(im);
        v = hsv(:,:,3);
        v = v - min(v(:));    % Just normalise value component
        v = v/max(v(:));
        hsv(:,:,3) = v;
        n = hsv2rgb(hsv);
    else                      % Assume greyscale
        if ~isa(im,'double'), im = double(im); end
        n = im - min(im(:));
        n = n/max(n(:));
    end

    else  % Normalise to desired mean and variance

    if ndims(im) == 3         % colour image?
        error('cannot normalise colour image to desired mean and variance');
    end

    if ~isa(im,'double'), im = double(im); end
```

```
    im = im - mean(im(:));
    im = im/std(im(:));      % Zero mean, unit std dev

    n = reqmean + im*sqrt(reqvar);
    end
    %%%normalise
```

P_EulerInv

```
function EulerInv =  p_EulerInv(img,LUT)

% Calculate Euler characteristic for each octant and sum up
eulerChar = zeros(size(img,1),1);
% Octant SWU
n = ones(size(img,1),1);
n(img(:,25)==1) = bitor(n(img(:,25)==1),128);
n(img(:,26)==1) = bitor(n(img(:,26)==1),64);
n(img(:,16)==1) = bitor(n(img(:,16)==1),32);
n(img(:,17)==1) = bitor(n(img(:,17)==1),16);
n(img(:,22)==1) = bitor(n(img(:,22)==1),8);
n(img(:,23)==1) = bitor(n(img(:,23)==1),4);
n(img(:,13)==1) = bitor(n(img(:,13)==1),2);
eulerChar = eulerChar + LUT(n);
% Octant SEU
n = ones(size(img,1),1);
n(img(:,27)==1) = bitor(n(img(:,27)==1),128);
n(img(:,24)==1) = bitor(n(img(:,24)==1),64);
n(img(:,18)==1) = bitor(n(img(:,18)==1),32);
n(img(:,15)==1) = bitor(n(img(:,15)==1),16);
n(img(:,26)==1) = bitor(n(img(:,26)==1),8);
n(img(:,23)==1) = bitor(n(img(:,23)==1),4);
n(img(:,17)==1) = bitor(n(img(:,17)==1),2);
eulerChar = eulerChar + LUT(n);
% Octant NWU
n = ones(size(img,1),1);
n(img(:,19)==1) = bitor(n(img(:,19)==1),128);
n(img(:,22)==1) = bitor(n(img(:,22)==1),64);
n(img(:,10)==1) = bitor(n(img(:,10)==1),32);
n(img(:,13)==1) = bitor(n(img(:,13)==1),16);
n(img(:,20)==1) = bitor(n(img(:,20)==1),8);
n(img(:,23)==1) = bitor(n(img(:,23)==1),4);
n(img(:,11)==1) = bitor(n(img(:,11)==1),2);
eulerChar = eulerChar + LUT(n);
% Octant NEU
n = ones(size(img,1),1);
n(img(:,21)==1) = bitor(n(img(:,21)==1),128);
n(img(:,24)==1) = bitor(n(img(:,24)==1),64);
n(img(:,20)==1) = bitor(n(img(:,20)==1),32);
n(img(:,23)==1) = bitor(n(img(:,23)==1),16);
n(img(:,12)==1) = bitor(n(img(:,12)==1),8);
n(img(:,15)==1) = bitor(n(img(:,15)==1),4);
n(img(:,11)==1) = bitor(n(img(:,11)==1),2);
eulerChar = eulerChar + LUT(n);
% Octant SWB
n = ones(size(img,1),1);
n(img(:,7)==1) = bitor(n(img(:,7)==1),128);
n(img(:,16)==1) = bitor(n(img(:,16)==1),64);
n(img(:,8)==1) = bitor(n(img(:,8)==1),32);
n(img(:,17)==1) = bitor(n(img(:,17)==1),16);
n(img(:,4)==1) = bitor(n(img(:,4)==1),8);
n(img(:,13)==1) = bitor(n(img(:,13)==1),4);
n(img(:,5)==1) = bitor(n(img(:,5)==1),2);
eulerChar = eulerChar + LUT(n);
% Octant SEB
n = ones(size(img,1),1);
n(img(:,9)==1) = bitor(n(img(:,9)==1),128);
```

```
n(img(:,8)==1) = bitor(n(img(:,8)==1),64);
n(img(:,18)==1) = bitor(n(img(:,18)==1),32);
n(img(:,17)==1) = bitor(n(img(:,17)==1),16);
n(img(:,6)==1) = bitor(n(img(:,6)==1),8);
n(img(:,5)==1) = bitor(n(img(:,5)==1),4);
n(img(:,15)==1) = bitor(n(img(:,15)==1),2);
eulerChar = eulerChar + LUT(n);
% Octant NWB
n = ones(size(img,1),1);
n(img(:,1)==1) = bitor(n(img(:,1)==1),128);
n(img(:,10)==1) = bitor(n(img(:,10)==1),64);
n(img(:,4)==1) = bitor(n(img(:,4)==1),32);
n(img(:,13)==1) = bitor(n(img(:,13)==1),16);
n(img(:,2)==1) = bitor(n(img(:,2)==1),8);
n(img(:,11)==1) = bitor(n(img(:,11)==1),4);
n(img(:,5)==1) = bitor(n(img(:,5)==1),2);
eulerChar = eulerChar + LUT(n);
% Octant NEB
n = ones(size(img,1),1);
n(img(:,3)==1) = bitor(n(img(:,3)==1),128);
n(img(:,2)==1) = bitor(n(img(:,2)==1),64);
n(img(:,12)==1) = bitor(n(img(:,12)==1),32);
n(img(:,11)==1) = bitor(n(img(:,11)==1),16);
n(img(:,6)==1) = bitor(n(img(:,6)==1),8);
n(img(:,5)==1) = bitor(n(img(:,5)==1),4);
n(img(:,15)==1) = bitor(n(img(:,15)==1),2);
eulerChar = eulerChar + LUT(n);

EulerInv(eulerChar==0) = true;
%%% end p_EulerInv
```

P_is_simple

```
function p_is_simple = p_is_simple(N)

% copy neighbors for labeling
n_p = size(N,1);
p_is_simple = ones(1,n_p);

cube = zeros(26,n_p);
cube(1:13,:)=N(:,1:13)';
cube(14:26,:)=N(:,15:27)';

label = 2*ones(1,n_p);

% for all points in the neighborhood
for i=1:26

    idx_1 = find(cube(i,:)==1);
    idx_2 = find(p_is_simple);
    idx = intersect(idx_1,idx_2);

    if(~isempty(idx))

        % start recursion with any octant that contains the point i
        switch( i )

            case {1,2,4,5,10,11,13}
                cube(:,idx) = p_oct_label(1, label, cube(:,idx) );
            case {3,6,12,14}
                cube(:,idx) = p_oct_label(2, label, cube(:,idx) );
            case {7,8,15,16}
                cube(:,idx) = p_oct_label(3, label, cube(:,idx) );
            case {9,17}
                cube(:,idx) = p_oct_label(4, label, cube(:,idx) );
```

```
            case {18,19,21,22}
                cube(:,idx) = p_oct_label(5, label, cube(:,idx) );
            case {20,23}
                cube(:,idx) = p_oct_label(6, label, cube(:,idx) );
            case {24,25}
                cube(:,idx) = p_oct_label(7, label, cube(:,idx) );
            case 26,
                cube(:,idx) = p_oct_label(8, label, cube(:,idx) );
        end;

        label(idx) = label(idx)+1;
        del_idx = find(label>=4);

        if(~isempty(del_idx))
            p_is_simple(del_idx) = 0;
        end;
    end;
end;

%%%end p_is_simple
```

P_oct_label

```
%%p_oct_label
function cube = p_oct_label(octant, label, cube)

% check if there are points in the octant with value 1
if( octant==1 )

    % set points in this octant to current label
    % and recurseive labeling of adjacent octants
    idx_1 = find(cube(1,:) == 1);
    if(~isempty(idx_1))
        cube(1,idx_1) = label(idx_1);
    end;

    idx_2 = find(cube(2,:) == 1);
    if(~isempty(idx_2))
        cube(2,idx_2) = label(idx_2);
        cube(:,idx_2) = p_oct_label(2,label(idx_2),cube(:,idx_2));
    end;

    idx_4 = find(cube(4,:) == 1);
    if(~isempty(idx_4))
        cube(4,idx_4) = label(idx_4);
        cube(:,idx_4) = p_oct_label(3,label(idx_4),cube(:,idx_4));
    end;

    idx_5 = find(cube(5,:) == 1);
    if(~isempty(idx_5))
        cube(5,idx_5) = label(idx_5);
        cube(:,idx_5) = p_oct_label(2,label(idx_5),cube(:,idx_5));
        cube(:,idx_5) = p_oct_label(3,label(idx_5),cube(:,idx_5));
        cube(:,idx_5) = p_oct_label(4,label(idx_5),cube(:,idx_5));
    end;

    idx_10 = find(cube(10,:) == 1);
    if(~isempty(idx_10))
        cube(10,idx_10) = label(idx_10);
        cube(:,idx_10) = p_oct_label(5,label(idx_10),cube(:,idx_10));
    end;

    idx_11 = find(cube(11,:) == 1);
    if(~isempty(idx_11))
        cube(11,idx_11) = label(idx_11);
        cube(:,idx_11) = p_oct_label(2,label(idx_11),cube(:,idx_11));
        cube(:,idx_11) = p_oct_label(5,label(idx_11),cube(:,idx_11));
```

```
        cube(:,idx_11) = p_oct_label(6,label(idx_11),cube(:,idx_11));
    end;

    idx_13 = find(cube(13,:) == 1);
    if(~isempty(idx_13))
        cube(13,idx_13) = label(idx_13);
        cube(:,idx_13) = p_oct_label(3,label(idx_13),cube(:,idx_13));
        cube(:,idx_13) = p_oct_label(5,label(idx_13),cube(:,idx_13));
        cube(:,idx_13) = p_oct_label(7,label(idx_13),cube(:,idx_13));
    end;

end;

if( octant==2 )

    idx_2 = find(cube(2,:) == 1);
    if(~isempty(idx_2))
        cube(2,idx_2) = label(idx_2);
        cube(:,idx_2) = p_oct_label(1,label(idx_2),cube(:,idx_2));
    end;

    idx_5 = find(cube(5,:) == 1);
    if(~isempty(idx_5))
        cube(5,idx_5) = label(idx_5);
        cube(:,idx_5) = p_oct_label(1,label(idx_5),cube(:,idx_5));
        cube(:,idx_5) = p_oct_label(3,label(idx_5),cube(:,idx_5));
        cube(:,idx_5) = p_oct_label(4,label(idx_5),cube(:,idx_5));
    end;

    idx_11 = find(cube(11,:) == 1);
    if(~isempty(idx_11))
        cube(11,idx_11) = label(idx_11);
        cube(:,idx_11) = p_oct_label(1,label(idx_11),cube(:,idx_11));
        cube(:,idx_11) = p_oct_label(5,label(idx_11),cube(:,idx_11));
        cube(:,idx_11) = p_oct_label(6,label(idx_11),cube(:,idx_11));
    end;

    idx_3 = find(cube(3,:) == 1);
    if(~isempty(idx_3))
        cube(3,idx_3) = label(idx_3);
    end;

    idx_6 = find(cube(6,:) == 1);
    if(~isempty(idx_6))
        cube(6,idx_6) = label(idx_6);
        cube(:,idx_6) = p_oct_label(4,label(idx_6),cube(:,idx_6));
    end;

    idx_12 = find(cube(12,:) == 1);
    if(~isempty(idx_12))
        cube(12,idx_12) = label(idx_12);
        cube(:,idx_12) = p_oct_label(6,label(idx_12),cube(:,idx_12));
    end;

    idx_14 = find(cube(14,:) == 1);
    if(~isempty(idx_14))
        cube(14,idx_14) = label(idx_14);
        cube(:,idx_14) = p_oct_label(4,label(idx_14),cube(:,idx_14));
        cube(:,idx_14) = p_oct_label(6,label(idx_14),cube(:,idx_14));
        cube(:,idx_14) = p_oct_label(8,label(idx_14),cube(:,idx_14));
    end;

end;

if( octant==3 )

    idx_4 = find(cube(4,:) == 1);
```

```
    if(~isempty(idx_4))
        cube(4,idx_4) = label(idx_4);
        cube(:,idx_4) = p_oct_label(1,label(idx_4),cube(:,idx_4));
    end;

    idx_5 = find(cube(5,:) == 1);
    if(~isempty(idx_5))
        cube(5,idx_5) = label(idx_5);
        cube(:,idx_5) = p_oct_label(1,label(idx_5),cube(:,idx_5));
        cube(:,idx_5) = p_oct_label(2,label(idx_5),cube(:,idx_5));
        cube(:,idx_5) = p_oct_label(4,label(idx_5),cube(:,idx_5));
    end;

    idx_13 = find(cube(13,:) == 1);
    if(~isempty(idx_13))
        cube(13,idx_13) = label(idx_13);
        cube(:,idx_13) = p_oct_label(1,label(idx_13),cube(:,idx_13));
        cube(:,idx_13) = p_oct_label(5,label(idx_13),cube(:,idx_13));
        cube(:,idx_13) = p_oct_label(7,label(idx_13),cube(:,idx_13));
    end;

    idx_7 = find(cube(7,:) == 1);
    if(~isempty(idx_7))
        cube(7,idx_7) = label(idx_7);
    end;

    idx_8 = find(cube(8,:) == 1);
    if(~isempty(idx_8))
        cube(8,idx_8) = label(idx_8);
        cube(:,idx_8) = p_oct_label(4,label(idx_8),cube(:,idx_8));
    end;

    idx_15 = find(cube(15,:) == 1);
    if(~isempty(idx_15))
        cube(15,idx_15) = label(idx_15);
        cube(:,idx_15) = p_oct_label(7,label(idx_15),cube(:,idx_15));
    end;

    idx_16 = find(cube(16,:) == 1);
    if(~isempty(idx_13))
        cube(16,idx_16) = label(idx_16);
        cube(:,idx_16) = p_oct_label(4,label(idx_16),cube(:,idx_16));
        cube(:,idx_16) = p_oct_label(7,label(idx_16),cube(:,idx_16));
        cube(:,idx_16) = p_oct_label(8,label(idx_16),cube(:,idx_16));
    end;

end;

if( octant==4 )

    idx_5 = find(cube(5,:) == 1);
    if(~isempty(idx_5))
        cube(5,idx_5) = label(idx_5);
        cube(:,idx_5) = p_oct_label(1,label(idx_5),cube(:,idx_5));
        cube(:,idx_5) = p_oct_label(2,label(idx_5),cube(:,idx_5));
        cube(:,idx_5) = p_oct_label(3,label(idx_5),cube(:,idx_5));
    end;

    idx_6 = find(cube(6,:) == 1);
    if(~isempty(idx_6))
        cube(6,idx_6) = label(idx_6);
        cube(:,idx_6) = p_oct_label(2,label(idx_6),cube(:,idx_6));
    end;

    idx_14 = find(cube(14,:) == 1);
    if(~isempty(idx_14))
        cube(14,idx_14) = label(idx_14);
```

```
        cube(:,idx_14) = p_oct_label(2,label(idx_14),cube(:,idx_14));
        cube(:,idx_14) = p_oct_label(6,label(idx_14),cube(:,idx_14));
        cube(:,idx_14) = p_oct_label(8,label(idx_14),cube(:,idx_14));
    end;

    idx_8 = find(cube(8,:) == 1);
    if(~isempty(idx_8))
        cube(8,idx_8) = label(idx_8);
        cube(:,idx_8) = p_oct_label(3,label(idx_8),cube(:,idx_8));
    end;

    idx_16 = find(cube(16,:) == 1);
    if(~isempty(idx_16))
        cube(16,idx_16) = label(idx_16);
        cube(:,idx_16) = p_oct_label(3,label(idx_16),cube(:,idx_16));
        cube(:,idx_16) = p_oct_label(7,label(idx_16),cube(:,idx_16));
        cube(:,idx_16) = p_oct_label(8,label(idx_16),cube(:,idx_16));
    end;

    idx_9 = find(cube(9,:) == 1);
    if(~isempty(idx_9))
        cube(9,idx_9) = label(idx_9);
    end;

    idx_17 = find(cube(17,:) == 1);
    if(~isempty(idx_17))
        cube(17,idx_17) = label(idx_17);
        cube(:,idx_17) = p_oct_label(8,label(idx_17),cube(:,idx_17));
    end;

end;

if( octant==5 )

    idx_10 = find(cube(10,:) == 1);
    if(~isempty(idx_10))
        cube(10,idx_10) = label(idx_10);
        cube(:,idx_10) = p_oct_label(1,label(idx_10),cube(:,idx_10));
    end;

    idx_11 = find(cube(11,:) == 1);
    if(~isempty(idx_11))
        cube(11,idx_11) = label(idx_11);
        cube(:,idx_11) = p_oct_label(1,label(idx_11),cube(:,idx_11));
        cube(:,idx_11) = p_oct_label(2,label(idx_11),cube(:,idx_11));
        cube(:,idx_11) = p_oct_label(6,label(idx_11),cube(:,idx_11));
    end;

    idx_13 = find(cube(13,:) == 1);
    if(~isempty(idx_13))
        cube(13,idx_13) = label(idx_13);
        cube(:,idx_13) = p_oct_label(1,label(idx_13),cube(:,idx_13));
        cube(:,idx_13) = p_oct_label(3,label(idx_13),cube(:,idx_13));
        cube(:,idx_13) = p_oct_label(7,label(idx_13),cube(:,idx_13));
    end;

    idx_18 = find(cube(18,:) == 1);
    if(~isempty(idx_18))
        cube(18,idx_18) = label(idx_18);
    end;

    idx_19 = find(cube(19,:) == 1);
    if(~isempty(idx_19))
        cube(19,idx_19) = label(idx_19);
        cube(:,idx_19) = p_oct_label(6,label(idx_19),cube(:,idx_19));
    end;
```

```
    idx_21 = find(cube(21,:) == 1);
    if(~isempty(idx_21))
        cube(21,idx_21) = label(idx_21);
        cube(:,idx_21) = p_oct_label(7,label(idx_21),cube(:,idx_21));
    end;

    idx_22 = find(cube(22,:) == 1);
    if(~isempty(idx_22))
        cube(22,idx_22) = label(idx_22);
        cube(:,idx_22) = p_oct_label(6,label(idx_22),cube(:,idx_22));
        cube(:,idx_22) = p_oct_label(7,label(idx_22),cube(:,idx_22));
        cube(:,idx_22) = p_oct_label(8,label(idx_22),cube(:,idx_22));
    end;

end;

if( octant==6 )

    idx_11 = find(cube(11,:) == 1);
    if(~isempty(idx_11))
        cube(11,idx_11) = label(idx_11);
        cube(:,idx_11) = p_oct_label(1,label(idx_11),cube(:,idx_11));
        cube(:,idx_11) = p_oct_label(2,label(idx_11),cube(:,idx_11));
        cube(:,idx_11) = p_oct_label(5,label(idx_11),cube(:,idx_11));
    end;

    idx_12 = find(cube(12,:) == 1);
    if(~isempty(idx_12))
        cube(12,idx_12) = label(idx_12);
        cube(:,idx_12) = p_oct_label(2,label(idx_12),cube(:,idx_12));
    end;

    idx_14 = find(cube(14,:) == 1);
    if(~isempty(idx_14))
        cube(14,idx_14) = label(idx_14);
        cube(:,idx_14) = p_oct_label(2,label(idx_14),cube(:,idx_14));
        cube(:,idx_14) = p_oct_label(4,label(idx_14),cube(:,idx_14));
        cube(:,idx_14) = p_oct_label(8,label(idx_14),cube(:,idx_14));
    end;

    idx_19 = find(cube(19,:) == 1);
    if(~isempty(idx_19))
        cube(19,idx_19) = label(idx_19);
        cube(:,idx_19) = p_oct_label(5,label(idx_19),cube(:,idx_19));
    end;


    idx_22 = find(cube(22,:) == 1);
    if(~isempty(idx_22))
        cube(22,idx_22) = label(idx_22);
        cube(:,idx_22) = p_oct_label(5,label(idx_22),cube(:,idx_22));
        cube(:,idx_22) = p_oct_label(7,label(idx_22),cube(:,idx_22));
        cube(:,idx_22) = p_oct_label(8,label(idx_22),cube(:,idx_22));
    end;

    idx_20 = find(cube(20,:) == 1);
    if(~isempty(idx_20))
        cube(20,idx_20) = label(idx_20);
    end;

    idx_23 = find(cube(23,:) == 1);
    if(~isempty(idx_23))
        cube(23,idx_23) = label(idx_23);
        cube(:,idx_23) = p_oct_label(8,label(idx_23),cube(:,idx_23));
    end;

end;
```

```
if( octant==7 )

    idx_13 = find(cube(13,:) == 1);
    if(~isempty(idx_13))
        cube(13,idx_13) = label(idx_13);
        cube(:,idx_13) = p_oct_label(1,label(idx_13),cube(:,idx_13));
        cube(:,idx_13) = p_oct_label(3,label(idx_13),cube(:,idx_13));
        cube(:,idx_13) = p_oct_label(5,label(idx_13),cube(:,idx_13));
    end;

    idx_15 = find(cube(15,:) == 1);
    if(~isempty(idx_15))
        cube(15,idx_15) = label(idx_15);
        cube(:,idx_15) = p_oct_label(3,label(idx_15),cube(:,idx_15));
    end;

    idx_16 = find(cube(16,:) == 1);
    if(~isempty(idx_16))
        cube(16,idx_16) = label(idx_16);
        cube(:,idx_16) = p_oct_label(3,label(idx_16),cube(:,idx_16));
        cube(:,idx_16) = p_oct_label(4,label(idx_16),cube(:,idx_16));
        cube(:,idx_16) = p_oct_label(8,label(idx_16),cube(:,idx_16));
    end;

    idx_21 = find(cube(21,:) == 1);
    if(~isempty(idx_21))
        cube(21,idx_21) = label(idx_21);
        cube(:,idx_21) = p_oct_label(5,label(idx_21),cube(:,idx_21));
    end;

    idx_22 = find(cube(22,:) == 1);
    if(~isempty(idx_22))
        cube(22,idx_22) = label(idx_22);
        cube(:,idx_22) = p_oct_label(5,label(idx_22),cube(:,idx_22));
        cube(:,idx_22) = p_oct_label(6,label(idx_22),cube(:,idx_22));
        cube(:,idx_22) = p_oct_label(8,label(idx_22),cube(:,idx_22));
    end;

    idx_24 = find(cube(24,:) == 1);
    if(~isempty(idx_24))
        cube(24,idx_24) = label(idx_24);
    end;

    idx_25 = find(cube(25,:) == 1);
    if(~isempty(idx_25))
        cube(25,idx_25) = label(idx_25);
        cube(:,idx_25) = p_oct_label(8,label(idx_25),cube(:,idx_25));
    end;
end;

if( octant==8 )

    idx_14 = find(cube(14,:) == 1);
    if(~isempty(idx_14))
        cube(14,idx_14) = label(idx_14);
        cube(:,idx_14) = p_oct_label(2,label(idx_14),cube(:,idx_14));
        cube(:,idx_14) = p_oct_label(4,label(idx_14),cube(:,idx_14));
        cube(:,idx_14) = p_oct_label(6,label(idx_14),cube(:,idx_14));
    end;

    idx_16 = find(cube(16,:) == 1);
    if(~isempty(idx_16))
        cube(16,idx_16) = label(idx_16);
        cube(:,idx_16) = p_oct_label(3,label(idx_16),cube(:,idx_16));
        cube(:,idx_16) = p_oct_label(4,label(idx_16),cube(:,idx_16));
        cube(:,idx_16) = p_oct_label(7,label(idx_16),cube(:,idx_16));
```

```
    end;

    idx_17 = find(cube(17,:) == 1);
    if(~isempty(idx_17))
        cube(17,idx_17) = label(idx_17);
        cube(:,idx_17) = p_oct_label(4,label(idx_17),cube(:,idx_17));
    end;

    idx_22 = find(cube(22,:) == 1);
    if(~isempty(idx_22))
        cube(22,idx_22) = label(idx_22);
        cube(:,idx_22) = p_oct_label(5,label(idx_22),cube(:,idx_22));
        cube(:,idx_22) = p_oct_label(6,label(idx_22),cube(:,idx_22));
        cube(:,idx_22) = p_oct_label(7,label(idx_22),cube(:,idx_22));
    end;

    idx_17 = find(cube(17,:) == 1);
    if(~isempty(idx_17))
        cube(17,idx_17) = label(idx_17);
        cube(:,idx_17) = p_oct_label(4,label(idx_17),cube(:,idx_17));
    end;

    idx_23 = find(cube(23,:) == 1);
    if(~isempty(idx_23))
        cube(23,idx_23) = label(idx_23);
        cube(:,idx_23) = p_oct_label(6,label(idx_23),cube(:,idx_23));
    end;

    idx_25 = find(cube(25,:) == 1);
    if(~isempty(idx_25))
        cube(25,idx_25) = label(idx_25);
        cube(:,idx_25) = p_oct_label(7,label(idx_25),cube(:,idx_25));
    end;

    idx_26 = find(cube(26,:) == 1);
    if(~isempty(idx_26))
        cube(26,idx_26) = label(idx_26);
    end;
end;
%%% end p_oct_label
```

Perfft3

```
% PERFFT2  2D Fourier transform of Moisan's periodic image component
%
% Usage: [P, S, p, s] = perfft2(im)
%
% Argument:  im - Image to be transformed
% Returns:    P - 2D fft of periodic image component
%             S - 2D fft of smooth component
%             p - Periodic component (spatial domain)
%             s - Smooth component (spatial domain)
%
% Moisan's "Periodic plus Smooth Image Decomposition" decomposes an image
% into two components
%       im = p + s
% where s is the 'smooth' component with mean 0 and p is the 'periodic'
% component which has no sharp discontinuities when one moves cyclically across
% the image boundaries.
%
% This wonderful decomposition is very useful when one wants to obtain an FFT of
% an image with minimal artifacts introduced from the boundary discontinuities.
% The image p gathers most of the image information but avoids periodization
% artifacts.
%
% The typical use of this function is to obtain a 'periodic only' fft of an
```

```
% image
%   >>  P = perfft2(im);
%
% Displaying the amplitude spectrum of P will yield a clean spectrum without the
% typical vertical-horizontal 'cross' arising from the image boundaries that you
% would normally see.
%
% Note if you are using the function to perform filtering in the frequency
% domain you may want to retain s (the smooth component in the spatial domain)
% and add it back to the filtered result at the end.
%
% The computational cost of obtaining the 'periodic only' FFT involves taking an
% additional FFT.
%
%
% Reference:
% This code is adapted from Lionel Moisan's Scilab function 'perdecomp.sci'
% "Periodic plus Smooth Image Decomposition" 07/2012 available at
%
%   http://www.mi.parisdescartes.fr/~moisan/p+s
%
% Paper:
% L. Moisan, "Periodic plus Smooth Image Decomposition", Journal of
% Mathematical Imaging and Vision, vol 39:2, pp. 161-179, 2011.

% Peter Kovesi
% Centre for Exploration Targeting
% The University of Western Australia
% peter.kovesi at uwa edu au
% September 2012

function [P, S, p, s] = perfft3(im)

    if ~isa(im, 'double'), im = double(im); end
    [rows,cols,slices] = size(im);

    % Compute the boundary image which is equal to the image discontinuity
    % values across the boundaries at the edges and is 0 elsewhere
    s = zeros(size(im));
    s(1,:,:)   = im(1,:,:) - im(end,:,:);
    s(end,:,:) = -s(1,:,:);
    s(:,1,:)   = s(:,1,:)   + im(:,1,:) - im(:,end,:);
    s(:,end,:) = s(:,end,:) - im(:,1,:) + im(:,end,:);
    s(:,:,1)   = s(:,:,1)   + im(:,:,1) - im(:,:,end);
    s(:,:,end) = s(:,:,end) - im(:,:,1) + im(:,:,end);

    % Generate grid upon which to compute the filter for the boundary image in
    % the frequency domain.  Note that cos() is cyclic hence the grid values can
    % range from 0 .. 2*pi rather than 0 .. pi and then pi .. 0
    [cx, cy, cz] = meshgrid(2*pi*[0:cols-1]/cols, 2*pi*[0:rows-1]/rows, 2*pi*[0:slices-
1]/slices);

    % Generate FFT of smooth component
    S = fftn(s)./(2*(3 - cos(cx) - cos(cy) - cos(cz))); %MAYBE CHANGE 2 TO 3?

    % The (1,1) element of the filter will be 0 so S(1,1) may be Inf or NaN
    S(1,1,1) = 0;          % Enforce 0 mean

    P = fftn(im) - S;    % FFT of periodic component

    if nargout > 2       % Generate spatial domain results
        s = real(ifftn(S));
        p = im - s;
    end
    %%% end perfft3
```

Pk_follow_link

```
%%% pk_follow_link
function [vox,n_idx,ep] = pk_follow_link(skel,node,k,j,idx,cans,c2n)

vox = [];
n_idx = [];
ep = 0;

% assign start node to first voxel
vox(1) = node(k).idx(j);

i=1;
isdone = false;
while(~isdone) % while no node reached
    i=i+1; % next voxel
    next_cand = c2n(idx);
        cand = cans(next_cand,2);
        if(cand==vox(i-1)) % switch direction
            cand = cans(next_cand,3);
        end;
        if(skel(cand)>1) % node found
            vox(i) = idx;
            vox(i+1) = cand; % first node
            n_idx = skel(cand)-1; % node #
            if(node(n_idx).ep)
                ep=1;
            end;
            isdone = 1;
        else % next voxel
            vox(i) = idx;
            idx = cand;
        end;
end;
%%% end pk_follow_link
```

Pk_get_nh

```
%%% pk_get_nh
function nhood = pk_get_nh(img,i)

width = size(img,1);
height = size(img,2);
depth = size(img,3);

[x,y,z]=ind2sub([width height depth],i);

nhood = false(length(i),27);

for xx=1:3
    for yy=1:3
        for zz=1:3
            w=sub2ind([3 3 3],xx,yy,zz);
            idx = sub2ind([width height depth],x+xx-2,y+yy-2,z+zz-2);
            nhood(:,w)=img(idx);
        end;
    end;
end;
%%% end pk_get_nh
```

Pk_get_nh_idx

```
%%% pk_get_nh_idx
function nhood = pk_get_nh_idx(img,i)
```

```
width = size(img,1);
height = size(img,2);
depth = size(img,3);

[x,y,z]=ind2sub([width height depth],i);

nhood = zeros(length(i),27);

for xx=1:3
    for yy=1:3
        for zz=1:3
            w=sub2ind([3 3 3],xx,yy,zz);
            nhood(:,w) = sub2ind([width height depth],x+xx-2,y+yy-2,z+zz-2);
        end;
    end;
end;
%%% end pk_get_nh_idx
```

Skel_fm

```
%%% skel_fm
function [S,SLeng] = skel_fm(I,thrsh,verbose)
% This function Skeleton will calculate an accurate skeleton (centerlines)
% of an object represented by an binary image / volume using the fastmarching
% distance transform.
%
% S=skeleton(I,verbose)
%
% inputs,
%   I : A 2D or 3D binary image
%   verbose : Boolean, set to true (default) for debug information
%   thrsh = default set to 1; lower if missing branches; higher if skeleton starts to
gety 'spiky'

% outputs
%   S : Cell array with the indices of the skeleton branches
% This code has been chopped up by Joshua Morgan based loosely on the code
% of others.

if(nargin<3), verbose=true; end

% Distance to vessel boundary
BoundaryDistance = double(bwdist(~I,'euclidean'));
if(verbose)
    disp('Distance Map Constructed');
end

% Get maximum distance value, which is used as starting point of the
% first skeleton branch
[maxD,SourceInd] = max(BoundaryDistance(:));

%in the case of a 1 voxel thick object, return the object
if maxD==1
    fprintf(1,'Warning, object is already a skeleton!\n')

    TEST = convn(uint8(I),ones(3,3,3),'same');
    TEST(~I) = 0;
    endpts = find(ismember(TEST,[1 2]));
    if isempty(endpts) %occasionally the minima hunt method results in zero endpoints
        fprintf(1,'Warning, no endpoints found...using SourceInd...\n')
        endpts = SourceInd(1);
        GDD = bwdistgeodesic(I,endpts(1),'quasi-euclidean');
        linelength = max(GDD(:))-min(GDD(:));
    else
        GDD = bwdistgeodesic(I,endpts(1),'quasi-euclidean');
```

```
        if numel(endpts) == 2
            linelength = GDD(endpts(2));
        else
            sprintf('Warning, number of endpoints not equal to two, using maxima...\n')
            linelength = max(GDD(:));
        end

    end

    %create outputs
    S = {SourceInd};
    SLeng = {linelength};

    return
end

% Make a fastmarching speed image from the distance image
Cost = (BoundaryDistance./maxD).^-1; Cost(BoundaryDistance==0) = Inf;

% Skeleton segments found by fastmarching
SkeletonSegments=cell(1,1000);
SLeng = cell(1,1000);

% Number of skeleton iterations
itt=0;

while(true)
    Tcycle = tic;
    if(verbose)
        disp(['Find Branches Iterations : ' num2str(itt)]);
    end

    % Create a distance map from the source point
    B = I;
    Y = bwdistgeodesic(B,SourceInd,'quasi-euclidean');
    Y(~I) = 0;
    [~,StartInd] = max(Y(:));

    % Do fast marching using the maximum distance value in the image
    % and the points describing all found branches are sourcepoints.
    GD1 = graydist(Cost,SourceInd,'quasi-euclidean');
    GD2 = graydist(Cost,StartInd,'quasi-euclidean');

    GDm = GD1+GD2;
    S = GDm<(min(GDm(:))+.01);
    ShortestLine = find(S(:));

    % Calculate the length of the new skeleton segment
    % This assumes only 2 endpoints
    % In rare cases of symmetry, this may not be the case
    TEST = convn(uint8(S),ones(3,3,3),'same');
    TEST(~S) = 0;
    endpts = find(ismember(TEST,[1 2]));
    if isempty(endpts) %occasionally the minima hunt method results in zero endpoints
        fprintf(1,'Warning, no endpoints found...using StartInd...\n')
        endpts = StartInd;
    end
    GDD = bwdistgeodesic(I,endpts(1),'quasi-euclidean');
    if numel(endpts) == 2
        linelength = GDD(endpts(2));
    else
        sprintf('Warning, number of endpoints not equal to two, using maxima...\n')
        linelength = max(GDD(:));
    end

    % Stop finding branches, if the length of the new branch is smaller
    % then the diameter of the largest vessel
```

```
    if(linelength<maxD*thrsh), break; end;


    % Store the found branch skeleton
    itt=itt+1;
    SkeletonSegments{itt}=ShortestLine;
    SLeng{itt} = linelength;
    if(verbose)
        fprintf(1,'Branch Length %f of max %f\n',linelength,maxD)
    end
    % Add found branch to the list of fastmarching SourcePoints
    SourceInd=unique([SourceInd;ShortestLine]);
    toc(Tcycle)
end
SkeletonSegments(itt+1:end)=[];
SLeng(itt+1:end)=[];

S = SkeletonSegments;

if(verbose)
    disp(['Skeleton Branches Found : ' num2str(length(S))]);
end
%%% end skel_fm
```

Vesselness3d

```
%%%vesselness3D
function vesselness = vesselness3D(I, sigmas, spacing, tau, brightondark)
% calculates vesselness probability map (local tubularity) of a 3D input
% image
%
% vesselness = vesselness3D(V, sigmas, spacing, tau, brightondark)
%
% inputs,
%   I : 3D image
%   sigmas : vector of scales on which the vesselness is computed
%   spacing : input image spacing resolution - during hessian matrix
%       computation, the gaussian filter kernel size in each dimension can
%       be adjusted to account for different image spacing for different
%       dimensions
%   tau : (between 0.5 and 1) : parameter that controls response uniformity
%       - lower tau -> more intense output response
%   brightondark: (true/false) : are vessels (tubular structures) bright on
%       dark background or dark on bright (default for 3D is true)
%
% outputs,
%   vesselness: maximum vesselness response over scales sigmas
%
% example:
%   V = vesselness3D(I, 1:5, [1;1;1], 1, true);
%
% Function was written by T. Jerman, University of Ljubljana (October 2014)
% Based on code by D. Kroon, University of Twente (May 2009)

verbose = 1;

if nargin<5
    brightondark = true; % default
end

I(~isfinite(I)) = 0;
I = single(I);

for j = 1:length(sigmas)

    if verbose
```

```
        disp(['Current Filter Sigma: ' num2str(sigmas(j)) ]);
    end

    [~, Lambda2, Lambda3] = volumeEigenvalues(I,sigmas(j),spacing,brightondark);
    if brightondark == true
        Lambda2 = -Lambda2;
        Lambda3 = -Lambda3;
    end

    % proposed filter
    Lambda_rho = Lambda3;
    Lambda_rho(Lambda3 > 0 & Lambda3 <= tau .* max(Lambda3(:))) = tau .* max(Lambda3(:));
    Lambda_rho(Lambda3 <= 0) = 0;
    response = Lambda2.*Lambda2.*(Lambda_rho-Lambda2).* 27 ./ (Lambda2 + Lambda_rho).^3;

    response(Lambda2 >= Lambda_rho./2 & Lambda_rho > 0) = 1;
    response(Lambda2 <= 0 | Lambda_rho <= 0) = 0;
    response(~isfinite(response)) = 0;

    %keep max response
    if(j==1)
        vesselness = response;
    else
        vesselness = max(vesselness,response);
    end

    clear response Lambda2 Lambda3 Lambda3M

end

vesselness = vesselness ./ max(vesselness(:));
vesselness(vesselness < 1e-2) = 0;


function [Lambda1, Lambda2, Lambda3] = volumeEigenvalues(V,sigma,spacing,brightondark)
% calculates the three eigenvalues for each voxel in a volume

% Calculate 3D hessian
[Hxx, Hyy, Hzz, Hxy, Hxz, Hyz] = Hessian3D(V,sigma,spacing);

% Correct for scaling
c=sigma.^2;
Hxx = c*Hxx; Hxy = c*Hxy;
Hxz = c*Hxz; Hyy = c*Hyy;
Hyz = c*Hyz; Hzz = c*Hzz;

% reduce computation by computing vesselness only where needed
% S.-F. Yang and C.-H. Cheng, "Fast computation of Hessian-based
% enhancement filters for medical images," Comput. Meth. Prog. Bio., vol.
% 116, no. 3, pp. 215-225, 2014.
B1 = - (Hxx + Hyy + Hzz);
B2 = Hxx .* Hyy + Hxx .* Hzz + Hyy .* Hzz - Hxy .* Hxy - Hxz .* Hxz - Hyz .* Hyz;
B3 = Hxx .* Hyz .* Hyz + Hxy .* Hxy .* Hzz + Hxz .* Hyy .* Hxz - Hxx .* Hyy .* Hzz - Hxy
.* Hyz .* Hxz - Hxz .* Hxy .* Hyz;

T = ones(size(B1));

if brightondark == true
    T(B1<=0) = 0;
    T(B2<=0 & B3 == 0) = 0;
    T(B1>0 & B2>0 & B1 .* B2 < B3) = 0;
else
    T(B1>=0) = 0;
    T(B2>=0 & B3 == 0) = 0;
    T(B1<0 & B2<0 & (-B1) .* (-B2) < (-B3)) = 0;
end
clear B1 B2 B3;
```

```
indeces = find(T==1);

Hxx = Hxx(indeces);
Hyy = Hyy(indeces);
Hzz = Hzz(indeces);
Hxz = Hxz(indeces);
Hyz = Hyz(indeces);
Hxy = Hxy(indeces);

% Calculate eigen values
[Lambda1i,Lambda2i,Lambda3i]=eig3volume(Hxx,Hxy,Hxz,Hyy,Hyz,Hzz);

% Free memory
clear Hxx Hyy Hzz Hxy Hxz Hyz;

Lambda1 = zeros(size(T));
Lambda2 = zeros(size(T));
Lambda3 = zeros(size(T));

Lambda1(indeces) = Lambda1i;
Lambda2(indeces) = Lambda2i;
Lambda3(indeces) = Lambda3i;

% some noise removal
Lambda1(~isfinite(Lambda1)) = 0;
Lambda2(~isfinite(Lambda2)) = 0;
Lambda3(~isfinite(Lambda3)) = 0;

Lambda1(abs(Lambda1) < 1e-4) = 0;
Lambda2(abs(Lambda2) < 1e-4) = 0;
Lambda3(abs(Lambda3) < 1e-4) = 0;


function [Dxx, Dyy, Dzz, Dxy, Dxz, Dyz] = Hessian3D(Volume,Sigma,spacing)
%  This function Hessian3D filters the image with an Gaussian kernel
%  followed by calculation of 2nd order gradients, which aprroximates the
%  2nd order derivatives of the image.
%
% [Dxx, Dyy, Dzz, Dxy, Dxz, Dyz] = Hessian3D(Volume,Sigma,spacing)
%
% inputs,
%   I : The image volume, class preferable double or single
%   Sigma : The sigma of the gaussian kernel used. If sigma is zero
%           no gaussian filtering.
%   spacing : input image spacing
%
% outputs,
%   Dxx, Dyy, Dzz, Dxy, Dxz, Dyz: The 2nd derivatives
%
% Function is written by D.Kroon University of Twente (June 2009)
% defaults
if nargin < 2, Sigma = 1; end

if(Sigma>0)
    %F=imbigaussian(Volume,Sigma,0.5);
    F=imgaussian(Volume,Sigma,spacing);
else
    F=Volume;
end

% Create first and second order diferentiations
Dz=gradient3(F,'z');
Dzz=(gradient3(Dz,'z'));
clear Dz;

Dy=gradient3(F,'y');
```

```
Dyy=(gradient3(Dy,'y'));
Dyz=(gradient3(Dy,'z'));
clear Dy;

Dx=gradient3(F,'x');
Dxx=(gradient3(Dx,'x'));
Dxy=(gradient3(Dx,'y'));
Dxz=(gradient3(Dx,'z'));
clear Dx;

function D = gradient3(F,option)
% This function does the same as the default matlab "gradient" function
% but with one direction at the time, less cpu and less memory usage.
%
% Example:
%
% Fx = gradient3(F,'x');

[k,l,m] = size(F);
D  = zeros(size(F),class(F));

switch lower(option)
case 'x'
    % Take forward differences on left and right edges
    D(1,:,:) = (F(2,:,:) - F(1,:,:));
    D(k,:,:) = (F(k,:,:) - F(k-1,:,:));
    % Take centered differences on interior points
    D(2:k-1,:,:) = (F(3:k,:,:)-F(1:k-2,:,:))/2;
case 'y'
    D(:,1,:) = (F(:,2,:) - F(:,1,:));
    D(:,l,:) = (F(:,l,:) - F(:,l-1,:));
    D(:,2:l-1,:) = (F(:,3:l,:)-F(:,1:l-2,:))/2;
case 'z'
    D(:,:,1) = (F(:,:,2) - F(:,:,1));
    D(:,:,m) = (F(:,:,m) - F(:,:,m-1));
    D(:,:,2:m-1) = (F(:,:,3:m)-F(:,:,1:m-2))/2;
otherwise
    disp('Unknown option')
end

function I=imgaussian(I,sigma,spacing,siz)
% IMGAUSSIAN filters an 1D, 2D color/greyscale or 3D image with an
% Gaussian filter. This function uses for filtering IMFILTER or if
% compiled the fast  mex code imgaussian.c . Instead of using a
% multidimensional gaussian kernel, it uses the fact that a Gaussian
% filter can be separated in 1D gaussian kernels.
%
% J=IMGAUSSIAN(I,SIGMA,SIZE)
%
% inputs,
%   I: The 1D, 2D greyscale/color, or 3D input image with
%            data type Single or Double
%   SIGMA: The sigma used for the Gaussian kernel
%   SIZE: Kernel size (single value) (default: sigma*6)
%
% outputs,
%   J: The gaussian filtered image
%
% note, compile the code with: mex imgaussian.c -v
%
% example,
%   I = im2double(imread('peppers.png'));
%   figure, imshow(imgaussian(I,10));
%
% Function is written by D.Kroon University of Twente (September 2009)

if(~exist('siz','var')), siz=sigma*6; end
```

```
if(sigma>0)

    % Filter each dimension with the 1D Gaussian kernels\
    x=-ceil(siz/spacing(1)/2):ceil(siz/spacing(1)/2);
    H = exp(-(x.^2/(2*(sigma/spacing(1))^2)));
    H = H/sum(H(:));
    Hx=reshape(H,[length(H) 1 1]);

    x=-ceil(siz/spacing(2)/2):ceil(siz/spacing(2)/2);
    H = exp(-(x.^2/(2*(sigma/spacing(2))^2)));
    H = H/sum(H(:));
    Hy=reshape(H,[1 length(H) 1]);

    x=-ceil(siz/spacing(3)/2):ceil(siz/spacing(3)/2);
    H = exp(-(x.^2/(2*(sigma/spacing(3))^2)));
    H = H/sum(H(:));
    Hz=reshape(H,[1 1 length(H)]);

    I=imfilter(imfilter(imfilter(I,Hx, 'same' ,'replicate'),Hy, 'same' ,'replicate'),Hz,
'same' ,'replicate');
end
%%%end vesselness3D
```

eig3volume.c

```
%%eig3volume.c
%from Tim Jerman scripts
#include "mex.h"
#include "math.h"
#ifdef MAX
#undef MAX
#endif
#define MAX(a, b) ((a)>(b)?(a):(b))
#define n 3

/* This function
 *
 *
 *
 */

/* Eigen decomposition code for symmetric 3x3 matrices, copied from the public
 * domain Java Matrix library JAMA. */
static double hypot2(double x, double y) { return sqrt(x*x+y*y); }

__inline double absd(double val){ if(val>0){ return val;} else { return -val;} };

/* Symmetric Householder reduction to tridiagonal form. */
static void tred2(double V[n][n], double d[n], double e[n]) {

/*  This is derived from the Algol procedures tred2 by */
/*  Bowdler, Martin, Reinsch, and Wilkinson, Handbook for */
/*  Auto. Comp., Vol.ii-Linear Algebra, and the corresponding */
/*  Fortran subroutine in EISPACK. */
    int i, j, k;
    double scale;
    double f, g, h;
    double hh;
    for (j = 0; j < n; j++) {d[j] = V[n-1][j]; }

    /* Householder reduction to tridiagonal form. */

    for (i = n-1; i > 0; i--) {
```

```
        /* Scale to avoid under/overflow. */
        scale = 0.0;
        h = 0.0;
        for (k = 0; k < i; k++) { scale = scale + fabs(d[k]); }
        if (scale == 0.0) {
            e[i] = d[i-1];
            for (j = 0; j < i; j++) { d[j] = V[i-1][j]; V[i][j] = 0.0;  V[j][i] = 0.0; }
        } else {

            /* Generate Householder vector. */

            for (k = 0; k < i; k++) { d[k] /= scale; h += d[k] * d[k]; }
            f = d[i-1];
            g = sqrt(h);
            if (f > 0) { g = -g; }
            e[i] = scale * g;
            h = h - f * g;
            d[i-1] = f - g;
            for (j = 0; j < i; j++) { e[j] = 0.0; }

            /* Apply similarity transformation to remaining columns. */

            for (j = 0; j < i; j++) {
                f = d[j];
                V[j][i] = f;
                g = e[j] + V[j][j] * f;
                for (k = j+1; k <= i-1; k++) { g += V[k][j] * d[k]; e[k] += V[k][j] * f;
}
                e[j] = g;
            }
            f = 0.0;
            for (j = 0; j < i; j++) { e[j] /= h; f += e[j] * d[j]; }
            hh = f / (h + h);
            for (j = 0; j < i; j++) { e[j] -= hh * d[j]; }
            for (j = 0; j < i; j++) {
                f = d[j]; g = e[j];
                for (k = j; k <= i-1; k++) { V[k][j] -= (f * e[k] + g * d[k]); }
                d[j] = V[i-1][j];
                V[i][j] = 0.0;
            }
        }
        d[i] = h;
    }

    /* Accumulate transformations. */

    for (i = 0; i < n-1; i++) {
        V[n-1][i] = V[i][i];
        V[i][i] = 1.0;
        h = d[i+1];
        if (h != 0.0) {
            for (k = 0; k <= i; k++) { d[k] = V[k][i+1] / h;}
            for (j = 0; j <= i; j++) {
                g = 0.0;
                for (k = 0; k <= i; k++) { g += V[k][i+1] * V[k][j]; }
                for (k = 0; k <= i; k++) { V[k][j] -= g * d[k]; }
            }
        }
        for (k = 0; k <= i; k++) { V[k][i+1] = 0.0;}
    }
    for (j = 0; j < n; j++) { d[j] = V[n-1][j]; V[n-1][j] = 0.0; }
    V[n-1][n-1] = 1.0;
    e[0] = 0.0;
}

/* Symmetric tridiagonal QL algorithm. */
static void tql2(double V[n][n], double d[n], double e[n]) {
```

```
/*  This is derived from the Algol procedures tql2, by */
/*  Bowdler, Martin, Reinsch, and Wilkinson, Handbook for */
/*  Auto. Comp., Vol.ii-Linear Algebra, and the corresponding */
/*  Fortran subroutine in EISPACK. */

    int i, j, k, l, m;
    double f;
    double tst1;
    double eps;
    int iter;
    double g, p, r;
    double dl1, h, c, c2, c3, el1, s, s2;

    for (i = 1; i < n; i++) { e[i-1] = e[i]; }
    e[n-1] = 0.0;

    f = 0.0;
    tst1 = 0.0;
    eps = pow(2.0, -52.0);
    for (l = 0; l < n; l++) {

        /* Find small subdiagonal element */

        tst1 = MAX(tst1, fabs(d[l]) + fabs(e[l]));
        m = l;
        while (m < n) {
            if (fabs(e[m]) <= eps*tst1) { break; }
            m++;
        }

        /* If m == l, d[l] is an eigenvalue, */
        /* otherwise, iterate. */

        if (m > l) {
            iter = 0;
            do {
                iter = iter + 1;  /* (Could check iteration count here.) */
                /* Compute implicit shift */
                g = d[l];
                p = (d[l+1] - g) / (2.0 * e[l]);
                r = hypot2(p, 1.0);
                if (p < 0) { r = -r; }
                d[l] = e[l] / (p + r);
                d[l+1] = e[l] * (p + r);
                dl1 = d[l+1];
                h = g - d[l];
                for (i = l+2; i < n; i++) { d[i] -= h; }
                f = f + h;
                /* Implicit QL transformation. */
                p = d[m]; c = 1.0; c2 = c; c3 = c;
                el1 = e[l+1]; s = 0.0; s2 = 0.0;
                for (i = m-1; i >= l; i--) {
                    c3 = c2;
                    c2 = c;
                    s2 = s;
                    g = c * e[i];
                    h = c * p;
                    r = hypot2(p, e[i]);
                    e[i+1] = s * r;
                    s = e[i] / r;
                    c = p / r;
                    p = c * d[i] - s * g;
                    d[i+1] = h + s * (c * g + s * d[i]);
                    /* Accumulate transformation. */
                    for (k = 0; k < n; k++) {
                        h = V[k][i+1];
```

```
                        V[k][i+1] = s * V[k][i] + c * h;
                        V[k][i] = c * V[k][i] - s * h;
                    }
                }
                p = -s * s2 * c3 * el1 * e[l] / dl1;
                e[l] = s * p;
                d[l] = c * p;

                /* Check for convergence. */
            } while (fabs(e[l]) > eps*tst1);
        }
        d[l] = d[l] + f;
        e[l] = 0.0;
    }

    /* Sort eigenvalues and corresponding vectors. */
    for (i = 0; i < n-1; i++) {
        k = i;
        p = d[i];
        for (j = i+1; j < n; j++) {
            if (d[j] < p) {
                k = j;
                p = d[j];
            }
        }
        if (k != i) {
            d[k] = d[i];
            d[i] = p;
            for (j = 0; j < n; j++) {
                p = V[j][i];
                V[j][i] = V[j][k];
                V[j][k] = p;
            }
        }
    }
}

void eigen_decomposition(double A[n][n], double V[n][n], double d[n]) {
    double e[n];
    double da[3];
    double dt, dat;
    double vet[3];
    int i, j;
    for (i = 0; i < n; i++) {
        for (j = 0; j < n; j++) {
            V[i][j] = A[i][j];
        }
    }
    tred2(V, d, e);
    tql2(V, d, e);

    /* Sort the eigen values and vectors by abs eigen value */
    da[0]=absd(d[0]); da[1]=absd(d[1]); da[2]=absd(d[2]);
    if((da[0]>=da[1])&&(da[0]>da[2]))
    {
        dt=d[2];   dat=da[2];    vet[0]=V[0][2];    vet[1]=V[1][2];    vet[2]=V[2][2];
        d[2]=d[0]; da[2]=da[0];  V[0][2] = V[0][0]; V[1][2] = V[1][0]; V[2][2] = V[2][0];
        d[0]=dt;   da[0]=dat;    V[0][0] = vet[0];  V[1][0] = vet[1];  V[2][0] = vet[2];
    }
    else if((da[1]>=da[0])&&(da[1]>da[2]))
    {
        dt=d[2];   dat=da[2];    vet[0]=V[0][2];    vet[1]=V[1][2];    vet[2]=V[2][2];
        d[2]=d[1]; da[2]=da[1];  V[0][2] = V[0][1]; V[1][2] = V[1][1]; V[2][2] = V[2][1];
        d[1]=dt;   da[1]=dat;    V[0][1] = vet[0];  V[1][1] = vet[1];  V[2][1] = vet[2];
    }
    if(da[0]>da[1])
    {
```

```
        dt=d[1];   dat=da[1];    vet[0]=V[0][1];    vet[1]=V[1][1];    vet[2]=V[2][1];
        d[1]=d[0]; da[1]=da[0];  V[0][1] = V[0][0]; V[1][1] = V[1][0]; V[2][1] = V[2][0];
        d[0]=dt;   da[0]=dat;    V[0][0] = vet[0];  V[1][0] = vet[1];  V[2][0] = vet[2];
    }


}


void mexFunction( int nlhs, mxArray *plhs[], int nrhs, const mxArray *prhs[] ) {
    double *Dxx, *Dxy, *Dxz, *Dyy, *Dyz, *Dzz;
    double *Dvecx, *Dvecy, *Dvecz, *Deiga, *Deigb, *Deigc;

    float *Dxx_f, *Dxy_f, *Dxz_f, *Dyy_f, *Dyz_f, *Dzz_f;
    float *Dvecx_f, *Dvecy_f, *Dvecz_f, *Deiga_f, *Deigb_f, *Deigc_f;

    mwSize output_dims[2]={1, 3};
    double Ma[3][3];
    double Davec[3][3];
    double Daeig[3];

    /* Loop variable */
    int i;

    /* Size of input */
    const mwSize *idims;
    int nsubs=0;

    /* Number of pixels */
    int npixels=1;

    /* Check for proper number of arguments. */
    if(nrhs!=6) {
        mexErrMsgTxt("Six inputs are required.");
    } else if(nlhs<3) {
        mexErrMsgTxt("Three or Six outputs are required");
    }


    /*  Get the number of dimensions */
    nsubs = mxGetNumberOfDimensions(prhs[0]);
    /* Get the sizes of the inputs */
    idims = mxGetDimensions(prhs[0]);
    for (i=0; i<nsubs; i++) { npixels=npixels*idims[i]; }

    if(mxGetClassID(prhs[0])==mxDOUBLE_CLASS) {
       /* Assign pointers to each input. */
        Dxx = (double *)mxGetPr(prhs[0]);
        Dxy = (double *)mxGetPr(prhs[1]);
        Dxz = (double *)mxGetPr(prhs[2]);
        Dyy = (double *)mxGetPr(prhs[3]);
        Dyz = (double *)mxGetPr(prhs[4]);
        Dzz = (double *)mxGetPr(prhs[5]);

        /* Assign pointers to each output. */
        plhs[0] = mxCreateNumericArray(nsubs, idims, mxDOUBLE_CLASS, mxREAL);
        plhs[1] = mxCreateNumericArray(nsubs, idims, mxDOUBLE_CLASS, mxREAL);
        plhs[2] = mxCreateNumericArray(nsubs, idims, mxDOUBLE_CLASS, mxREAL);
        Deiga = mxGetPr(plhs[0]); Deigb = mxGetPr(plhs[1]); Deigc = mxGetPr(plhs[2]);
        if(nlhs==6) {
            /* Main direction (larged eigenvector) */
            plhs[3] = mxCreateNumericArray(nsubs, idims, mxDOUBLE_CLASS, mxREAL);
            plhs[4] = mxCreateNumericArray(nsubs, idims, mxDOUBLE_CLASS, mxREAL);
            plhs[5] = mxCreateNumericArray(nsubs, idims, mxDOUBLE_CLASS, mxREAL);
            Dvecx = mxGetPr(plhs[3]); Dvecy = mxGetPr(plhs[4]); Dvecz = mxGetPr(plhs[5]);
        }
```

```
        for(i=0; i<npixels; i++) {
            Ma[0][0]=Dxx[i]; Ma[0][1]=Dxy[i]; Ma[0][2]=Dxz[i];
            Ma[1][0]=Dxy[i]; Ma[1][1]=Dyy[i]; Ma[1][2]=Dyz[i];
            Ma[2][0]=Dxz[i]; Ma[2][1]=Dyz[i]; Ma[2][2]=Dzz[i];
            eigen_decomposition(Ma, Davec, Daeig);
            Deiga[i]=Daeig[0]; Deigb[i]=Daeig[1]; Deigc[i]=Daeig[2];
            if(nlhs==6) {
                /* Main direction (smallest eigenvector) */
                Dvecx[i]=Davec[0][0];
                Dvecy[i]=Davec[1][0];
                Dvecz[i]=Davec[2][0];
            }
        }
    }
    else if(mxGetClassID(prhs[0])==mxSINGLE_CLASS) {
       /* Assign pointers to each input. */
        Dxx_f = (float *)mxGetPr(prhs[0]);
        Dxy_f = (float *)mxGetPr(prhs[1]);
        Dxz_f = (float *)mxGetPr(prhs[2]);
        Dyy_f = (float *)mxGetPr(prhs[3]);
        Dyz_f = (float *)mxGetPr(prhs[4]);
        Dzz_f = (float *)mxGetPr(prhs[5]);

        /* Assign pointers to each output. */
        plhs[0] = mxCreateNumericArray(nsubs, idims, mxSINGLE_CLASS, mxREAL);
        plhs[1] = mxCreateNumericArray(nsubs, idims, mxSINGLE_CLASS, mxREAL);
        plhs[2] = mxCreateNumericArray(nsubs, idims, mxSINGLE_CLASS, mxREAL);
        Deiga_f  = (float *)mxGetPr(plhs[0]);
        Deigb_f  = (float *)mxGetPr(plhs[1]);
        Deigc_f  = (float *)mxGetPr(plhs[2]);
        if(nlhs==6) {
            /* Main direction (smallest eigenvector) */
            plhs[3] = mxCreateNumericArray(nsubs, idims, mxSINGLE_CLASS, mxREAL);
            plhs[4] = mxCreateNumericArray(nsubs, idims, mxSINGLE_CLASS, mxREAL);
            plhs[5] = mxCreateNumericArray(nsubs, idims, mxSINGLE_CLASS, mxREAL);
            Dvecx_f  = (float *)mxGetPr(plhs[3]);
            Dvecy_f  = (float *)mxGetPr(plhs[4]);
            Dvecz_f  = (float *)mxGetPr(plhs[5]);
        }


        for(i=0; i<npixels; i++) {
            Ma[0][0]=(double)Dxx_f[i]; Ma[0][1]=(double)Dxy_f[i];
Ma[0][2]=(double)Dxz_f[i];
            Ma[1][0]=(double)Dxy_f[i]; Ma[1][1]=(double)Dyy_f[i];
Ma[1][2]=(double)Dyz_f[i];
            Ma[2][0]=(double)Dxz_f[i]; Ma[2][1]=(double)Dyz_f[i];
Ma[2][2]=(double)Dzz_f[i];
            eigen_decomposition(Ma, Davec, Daeig);
            Deiga_f[i]=(float)Daeig[0];
            Deigb_f[i]=(float)Daeig[1];
            Deigc_f[i]=(float)Daeig[2];
            if(nlhs==6) {
                /* Main direction (smallest eigenvector) */
                Dvecx_f[i]=(float)Davec[0][0];
                Dvecy_f[i]=(float)Davec[1][0];
                Dvecz_f[i]=(float)Davec[2][0];
            }
        }

    }
}

%%end eig3volume.c
```

Chapter 8
References

(1) Mathes, S. H.; Ruffner, H.; Graf-Hausner, U. The Use of Skin Models in Drug Development. *Advanced Drug Delivery Reviews* **2014**, *69–70*, 81–102. https://doi.org/10.1016/j.addr.2013.12.006.

(2) Fenske, N. A.; Lober, C. W. Structural and Functional Changes of Normal Aging Skin. *Journal of the American Academy of Dermatology* **1986**, *15* (4, Part 1), 571–585. https://doi.org/10.1016/S0190-9622(86)70208-9.

(3) Tobin, D. J. Introduction to Skin Aging. *Journal of Tissue Viability* **2017**, *26* (1), 37–46. https://doi.org/10.1016/j.jtv.2016.03.002.

(4) Naylor, E. C.; Watson, R. E. B.; Sherratt, M. J. Molecular Aspects of Skin Ageing. *Maturitas* **2011**, *69* (3), 249–256. https://doi.org/10.1016/j.maturitas.2011.04.011.

(5) MAKRANTONAKI, E.; ZOUBOULIS, C. C. Molecular Mechanisms of Skin Aging. *Annals of the New York Academy of Sciences* **2007**, *1119* (1), 40–50. https://doi.org/10.1196/annals.1404.027.

(6) Han, A.; Chien, A. L.; Kang, S. Photoaging. *Dermatologic Clinics* **2014**, *32* (3), 291–299. https://doi.org/10.1016/j.det.2014.03.015.

(7) Helfrich, Y. R.; Sachs, D. L.; Voorhees, J. J. Overview of Skin Aging and Photoaging. *Dermatology Nursing* **2008**, *20* (3), 177.

(8) Lee, D. H.; Oh, J.-H.; Chung, J. H. Glycosaminoglycan and Proteoglycan in Skin Aging. *Journal of Dermatological Science* **2016**, *83* (3), 174–181. https://doi.org/10.1016/j.jdermsci.2016.05.016.

(9) CHUNG, J. H.; EUN, H. C. Angiogenesis in Skin Aging and Photoaging. *The Journal of Dermatology* **2007**, *34* (9), 593–600. https://doi.org/10.1111/j.1346-8138.2007.00341.x.

(10) Farage, M. A.; Miller, K. W.; Zouboulis, C. C.; Piérard, G. E.; Maibach, H. I. Gender Differences in Skin Aging and the Changing Profile of the Sex Hormones with Age. *J Steroids Horm Sci* **2012**, *3* (2), 109.

(11) Ali, N.; Hosseini, M.; Vainio, S.; Taieb, A.; Cario-André, M.; Rezvani, H. R. Skin Equivalents: Skin from Reconstructions as Models to Study Skin Development and Diseases. *British Journal of Dermatology* **2015**, *173* (2), 391–403.

(12) Li, Y.; Liu, Y.; Xia, W.; Lei, D.; Voorhees, J. J.; Fisher, G. J. Age-Dependent Alterations of Decorin Glycosaminoglycans in Human Skin. *Scientific Reports* **2013**, *3* (1), 2422. https://doi.org/10.1038/srep02422.

(13) Hervé Pageon; Hélène Zucchi; Françoise Rousset; Vincent M. Monnier; Daniel Asselineau. Skin Aging by Glycation: Lessons from the Reconstructed Skin Model. *Clinical Chemistry and Laboratory Medicine (CCLM)* **2014**, *52* (1), 169–174. https://doi.org/10.1515/cclm-2013-0091.

(14) Hervé Pageon; Hilaire Bakala; Vincent M Monnier; Daniel Asselineau. Collagen Glycation Triggers the Formation of Aged Skin in Vitro. *European Journal of Dermatology* **2007**, *17* (1), 12–20. https://doi.org/10.1684/ejd.2007.0102.

(15) Pageon, H. Reaction of Glycation and Human Skin: The Effects on the Skin and Its Components, Reconstructed Skin as a Model. *Pathologie Biologie* **2010**, *58* (3), 226–231. https://doi.org/10.1016/j.patbio.2009.09.009.

(16) Pageon, H.; Técher, M.-P.; Asselineau, D. Reconstructed Skin Modified by Glycation of the Dermal Equivalent as a Model for Skin Aging and Its Potential Use to Evaluate Anti-Glycation Molecules. *Experimental Gerontology* **2008**, *43* (6), 584–588. https://doi.org/10.1016/j.exger.2008.04.004.

(17) Gkogkolou, P.; Böhm, M. Advanced Glycation End Products. *null* **2012**, *4* (3), 259–270. https://doi.org/10.4161/derm.22028.

(18) Bucala, R.; Cerami, A. Advanced Glycosylation: Chemistry, Biology, and Implications for Diabetes and Aging. In *Advances in Pharmacology*; August, J. T., Anders, M. W., Murad, F., Eds.; Academic Press, 1992; Vol. 23, pp 1–34. https://doi.org/10.1016/S1054-3589(08)60961-8.

(19) Angel, P.; Szabowski, A.; Schorpp-Kistner, M. Function and Regulation of AP-1 Subunits in Skin Physiology and Pathology. *Oncogene* **2001**, *20* (19), 2413–2423. https://doi.org/10.1038/sj.onc.1204380.

(20) Dos Santos, M.; Metral, E.; Boher, A.; Rousselle, P.; Thepot, A.; Damour, O. In Vitro 3-D Model Based on Extending Time of Culture for Studying Chronological Epidermis Aging. *Matrix Biology* **2015**, *47*, 85–97. https://doi.org/10.1016/j.matbio.2015.03.009.

(21) Mansouri, P.; Chalangari, R.; Chalangari, K. M.; Saffarian, Z. Skin Aging and Immune System. In *Immunology of Aging*; Massoud, A., Rezaei, N., Eds.; Springer Berlin Heidelberg: Berlin, Heidelberg, 2014; pp 339–368. https://doi.org/10.1007/978-3-642-39495-9_25.

(22) Bennett, M. F.; Robinson, M. K.; Baron, E. D.; Cooper, K. D. Skin Immune Systems and Inflammation: Protector of the Skin or Promoter of Aging? *Journal of Investigative Dermatology Symposium Proceedings* **2008**, *13* (1), 15–19. https://doi.org/10.1038/jidsymp.2008.3.

(23) Janson, D.; Rietveld, M.; Willemze, R.; El Ghalbzouri, A. Effects of Serially Passaged Fibroblasts on Dermal and Epidermal Morphogenesis in Human Skin Equivalents.

Biogerontology **2013**, *14* (2), 131–140. https://doi.org/10.1007/s10522-013-9416-9.

(24) Varani, J.; Dame, M. K.; Rittie, L.; Fligiel, S. E. G.; Kang, S.; Fisher, G. J.; Voorhees, J. J. Decreased Collagen Production in Chronologically Aged Skin: Roles of Age-Dependent Alteration in Fibroblast Function and Defective Mechanical Stimulation. *The American Journal of Pathology* **2006**, *168* (6), 1861–1868. https://doi.org/10.2353/ajpath.2006.051302.

(25) Sandilands, A.; Sutherland, C.; Irvine, A. D.; McLean, W. H. I. Filaggrin in the Frontline: Role in Skin Barrier Function and Disease. *J. Cell Sci.* **2009**, *122* (9), 1285. https://doi.org/10.1242/jcs.033969.

(26) Ponec, M.; Weerheim, A.; Kempenaar, J.; Mulder, A.; Gooris, G. S.; Bouwstra, J.; Mieke Mommaas, A. The Formation of Competent Barrier Lipids in Reconstructed Human Epidermis Requires the Presence of Vitamin C. *Journal of Investigative Dermatology* **1997**, *109* (3), 348–355. https://doi.org/10.1111/1523-1747.ep12336024.

(27) Boyce, S. T.; Williams, M. L. Lipid Supplemented Medium Induces Lamellar Bodies and Precursors of Barrier Lipids in Cultured Analogues of Human Skin. *Journal of Investigative Dermatology* **1993**, *101* (2), 180–184. https://doi.org/10.1111/1523-1747.ep12363678.

(28) Rinnerthaler, M.; Richter, K. The Influence of Calcium on the Skin PH and Epidermal Barrier During Aging. In *Current Problems in Dermatology*; 2018; Vol. 54, pp 79–86. https://doi.org/10.1159/000489521.

(29) Wang, Z.; Man, M.-Q.; Li, T.; Elias, P. M.; Mauro, T. M. Aging-Associated Alterations in Epidermal Function and Their Clinical Significance. *aging* **2020**. https://doi.org/10.18632/aging.102946.

(30) Jungersted, J. M. Stratum Corneum Lipids and Filaggrin. In *Filaggrin: Basic Science, Epidemiology, Clinical Aspects and Management*; Thyssen, J. P., Maibach, H. I., Eds.; Springer Berlin Heidelberg: Berlin, Heidelberg, 2014; pp 23–26. https://doi.org/10.1007/978-3-642-54379-1_3.

(31) Blume-Peytavi, U.; Kottner, J.; Sterry, W.; Hodin, M. W.; Griffiths, T. W.; Watson, R. E. B.; Hay, R. J.; Griffiths, C. E. M. Age-Associated Skin Conditions and Diseases: Current Perspectives and Future Options. *The Gerontologist* **2016**, *56* (Suppl_2), S230–S242. https://doi.org/10.1093/geront/gnw003.

(32) Pageon, H.; Técher, M.-P.; Asselineau, D. Reconstructed Skin Modified by Glycation of the Dermal Equivalent as a Model for Skin Aging and Its Potential Use to Evaluate Anti-Glycation Molecules. *Experimental Gerontology* **2008**, *43* (6), 584–588. https://doi.org/10.1016/j.exger.2008.04.004.

(33) Sonnenberg, A.; Calafat, J.; Janssen, H.; Daams, H.; van der Raaij-Helmer, L. M.; Falcioni, R.; Kennel, S. J.; Aplin, J. D.; Baker, J.; Loizidou, M. Integrin Alpha 6/Beta 4

Complex Is Located in Hemidesmosomes, Suggesting a Major Role in Epidermal Cell-Basement Membrane Adhesion. *Journal of Cell Biology* **1991**, *113* (4), 907–917. https://doi.org/10.1083/jcb.113.4.907.

(34) Kaur, P.; Li, A. Adhesive Properties of Human Basal Epidermal Cells: An Analysis of Keratinocyte Stem Cells, Transit Amplifying Cells, and Postmitotic Differentiating Cells. *Journal of Investigative Dermatology* **2000**, *114* (3), 413–420. https://doi.org/10.1046/j.1523-1747.2000.00884.x.

(35) Shuster, S.; Black, M. M.; McVitie, E. The Influence of Age and Sex on Skin Thickness, Skin Collagen and Density. *British Journal of Dermatology* **1975**, *93* (6), 639–643. https://doi.org/10.1111/j.1365-2133.1975.tb05113.x.

(36) Saville, C. R.; Hardman, M. J. The Role of Estrogen Deficiency in Skin Aging and Wound Healing. In *Skin, Mucosa and Menopause: Management of Clinical Issues*; Farage, M. A., Miller, K. W., Fugate Woods, N., Maibach, H. I., Eds.; Springer Berlin Heidelberg: Berlin, Heidelberg, 2015; pp 71–88. https://doi.org/10.1007/978-3-662-44080-3_6.

(37) Kosmadaki, M. G.; Gilchrest, B. A. The Role of Telomeres in Skin Aging/Photoaging. *Micron* **2004**, *35* (3), 155–159. https://doi.org/10.1016/j.micron.2003.11.002.

(38) Duval, C.; Schmidt, R.; Regnier, M.; Facy, V.; Asselineau, D.; Bernerd, F. The Use of Reconstructed Human Skin to Evaluate UV-Induced Modifications and Sunscreen Efficacy. *Experimental Dermatology* **2003**, *12* (s2), 64–70. https://doi.org/10.1034/j.1600-0625.12.s2.10.x.

(39) Lee, K.-E.; Nho, Y.-H.; Yun, S. K.; Park, S.-M.; Kang, S.; Yeo, H. Caviar Extract and Its Constituent DHA Inhibits UVB-Irradiated Skin Aging by Inducing Adiponectin Production. *International Journal of Molecular Sciences* **2020**, *21* (9), 3383. https://doi.org/10.3390/ijms21093383.

(40) Tanaka, K.; Asamitsu, K.; Uranishi, H.; Iddamalgoda, A.; Ito, K.; Kojima, H.; Okamoto, T. Protecting Skin Photoaging by NF-KappaB Inhibitor. *Current Drug Metabolism* **2010**, *11* (5), 431–435. https://doi.org/10.2174/138920010791526051.

(41) Bernerd, F.; Asselineau, D. UVA Exposure of Human Skin Reconstructed in Vitro Induces Apoptosis of Dermal Fibroblasts: Subsequent Connective Tissue Repair and Implications in Photoaging. *Cell Death & Differentiation* **1998**, *5* (9), 792–802. https://doi.org/10.1038/sj.cdd.4400413.

(42) Bernerd, F.; Asselineau, D. Successive Alteration and Recovery of Epidermal Differentiation and Morphogenesis after Specific UVB-Damages in Skin Reconstructedin Vitro. *Developmental Biology* **1997**, *183* (2), 123–138. https://doi.org/10.1006/dbio.1996.8465.

(43) Bernerd, F.; Vioux, C.; Asselineau, D. Evaluation of the Protective Effect of Sunscreens on In Vitro Reconstructed Human Skin Exposed to UVB or UVA

Irradiation. *Photochemistry and Photobiology* **2000**, *71* (3), 314–320. https://doi.org/10.1562/0031-8655(2000)0710314EOTPEO2.0.CO2.

(44) Amano, S.; Ogura, Y.; Akutsu, N.; Matsunaga, Y.; Kadoya, K.; Adachi, E.; Nishiyama, T. Protective Effect of Matrix Metalloproteinase Inhibitors against Epidermal Basement Membrane Damage: Skin Equivalents Partially Mimic Photoageing Process. *British Journal of Dermatology* **2005**, *153* (s2), 37–46. https://doi.org/10.1111/j.1365-2133.2005.06968.x.

(45) Bell, E.; Ehrlich, H.; Sher, S.; Merrill, C.; Sarber, R.; Hull, B.; Nakatsuji, T.; Church, D.; Buttle, D. Development and Use of a Living Skin Equivalent. *Plastic and reconstructive surgery* **1981**, *67* (3), 386–392. https://doi.org/10.1097/00006534-198103000-00024.

(46) Bell, E.; Sher, S.; Hull, B.; Merrill, C.; Rosen, S.; Chamson, A.; Asselineau, D.; Dubertret, L.; Lapiere, C.; Neveux, Y.; Coulomb, B.; Nusgens, B. The Reconstitution of Living Skin. *Journal of Investigative Dermatology* **1983**, *81* (1, Supplement), S2–S10. https://doi.org/10.1111/1523-1747.ep12539993.

(47) El Ghalbzouri, A.; Commandeur, S.; Rietveld, M. H.; Mulder, A. A.; Willemze, R. Replacement of Animal-Derived Collagen Matrix by Human Fibroblast-Derived Dermal Matrix for Human Skin Equivalent Products. *Biomaterials* **2009**, *30* (1), 71–78. https://doi.org/10.1016/j.biomaterials.2008.09.002.

(48) Sanchez, M. M.; Morgan, J. T. Generation of Self-Assembled Vascularized Human Skin Equivalents. *JoVE* **2021**, No. 168, e62125. https://doi.org/10.3791/62125.

(49) Shevchenko, R. V.; James, S. L.; James, S. E. A Review of Tissue-Engineered Skin Bioconstructs Available for Skin Reconstruction. *Journal of The Royal Society Interface* **2010**, *7* (43), 229–258. https://doi.org/10.1098/rsif.2009.0403.

(50) Goodarzi, P.; Falahzadeh, K.; Nematizadeh, M.; Farazandeh, P.; Payab, M.; Larijani, B.; Tayanloo Beik, A.; Arjmand, B. Tissue Engineered Skin Substitutes. In *Cell Biology and Translational Medicine, Volume 3: Stem Cells, Bio-materials and Tissue Engineering*; Turksen, K., Ed.; Advances in Experimental Medicine and Biology; Springer International Publishing: Cham, 2018; pp 143–188. https://doi.org/10.1007/5584_2018_226.

(51) Hudon, V.; Berthod, F.; Black, A. F.; Damour, O.; Germain, L.; Auger, F. A. A Tissue-Engineered Endothelialized Dermis to Study the Modulation of Angiogenic and Angiostatic Molecules on Capillary-like Tube Formation in Vitro. *British Journal of Dermatology* **2003**, *148* (6), 1094–1104. https://doi.org/10.1046/j.1365-2133.2003.05298.x.

(52) Black, A. F.; Berthod, F.; L'heureux, N.; Germain, L.; Auger, F. A. In Vitro Reconstruction of a Human Capillary-like Network in a Tissue-Engineered Skin Equivalent. *The FASEB Journal* **1998**, *12* (13), 1331–1340. https://doi.org/10.1096/fasebj.12.13.1331.

(53) Martins-Green, M.; Li, Q.-J.; Yao, M. A New Generation Organ Culture Arising from Cross-Talk between Multiple Primary Human Cell Types. *The FASEB Journal* **2004**, *19* (2), 222–224. https://doi.org/10.1096/fj.04-1725fje.

(54) Klar, A. S.; Güven, S.; Biedermann, T.; Luginbühl, J.; Böttcher-Haberzeth, S.; Meuli-Simmen, C.; Meuli, M.; Martin, I.; Scherberich, A.; Reichmann, E. Tissue-Engineered Dermo-Epidermal Skin Grafts Prevascularized with Adipose-Derived Cells. *Biomaterials* **2014**, *35* (19), 5065–5078. https://doi.org/10.1016/j.biomaterials.2014.02.049.

(55) Baltazar, T.; Merola, J.; Catarino, C. M.; Xie, C. B.; Kirkiles-Smith, N.; Lee, V.; Hotta, S. Y. K.; Dai, G.; Xu, X.; Ferreira, F. C.; Saltzman, W. M.; Pober, J. S.; Karande, P. 3D Bioprinting of a Vascularized and Perfusable Skin Graft Using Human Keratinocytes, (...). *Tissue Engineering Part A* **2019**. https://doi.org/10.1089/ten.TEA.2019.0201.

(56) Tremblay, P.-L.; Hudon, V.; Berthod, F.; Germain, L.; Auger, F. A. Inosculation of Tissue-Engineered Capillaries with the Host's Vasculature in a Reconstructed Skin Transplanted on Mice. *American Journal of Transplantation* **2005**, *5* (5), 1002–1010. https://doi.org/10.1111/j.1600-6143.2005.00790.x.

(57) Bergers, L. I. J. C.; Reijnders, C. M. A.; van den Broek, L. J.; Spiekstra, S. W.; de Gruijl, T. D.; Weijers, E. M.; Gibbs, S. Immune-Competent Human Skin Disease Models. *Drug Discovery Today* **2016**, *21* (9), 1479–1488. https://doi.org/10.1016/j.drudis.2016.05.008.

(58) Bechetoille, N.; Dezutter-Dambuyant, C.; Damour, O.; André, V.; Orly, I.; Perrier, E. Effects of Solar Ultraviolet Radiation on Engineered Human Skin Equivalent Containing Both Langerhans Cells and Dermal Dendritic Cells. *Tissue Engineering* **2007**, *13* (11), 2667–2679. https://doi.org/10.1089/ten.2006.0405.

(59) Linde, N.; Gutschalk, C. M.; Hoffmann, C.; Yilmaz, D.; Mueller, M. M. Integrating Macrophages into Organotypic Co-Cultures: A 3D in Vitro Model to Study Tumor-Associated Macrophages. *PLoS One* **2012**, *7* (7), e40058–e40058. https://doi.org/10.1371/journal.pone.0040058.

(60) Dezutter-Dambuyant, C.; Black, A.; Bechetoille, N.; Bouez, C.; Maréchal, S.; Auxenfans, C.; Cenizo, V.; Pascal, P.; Perrier, E.; Damour, O. Evolutive Skin Reconstructions: From the Dermal Collagen–Glycosaminoglycan– Chitosane Substrate to an Immunocompetent Reconstructed Skin. *Bio-Medical Materials and Engineering* **2006**, *16* (4), S85–S94.

(61) Vermette, M.; Trottier, V.; Ménard, V.; Saint-Pierre, L.; Roy, A.; Fradette, J. Production of a New Tissue-Engineered Adipose Substitute from Human Adipose-Derived Stromal Cells. *Biomaterials* **2007**, *28* (18), 2850–2860. https://doi.org/10.1016/j.biomaterials.2007.02.030.

(62) Son, W.-C.; Yun, J.-W.; Kim, B.-H. Adipose-Derived Mesenchymal Stem Cells Reduce MMP-1 Expression in UV-Irradiated Human Dermal Fibroblasts: Therapeutic

Potential in Skin Wrinkling. *null* **2015**, *79* (6), 919–925. https://doi.org/10.1080/09168451.2015.1008972.

(63) Trottier, V.; Marceau-Fortier, G.; Germain, L.; Vincent, C.; Fradette, J. IFATS Collection: Using Human Adipose-Derived Stem/Stromal Cells for the Production of New Skin Substitutes. *STEM CELLS* **2008**, *26* (10), 2713–2723. https://doi.org/10.1634/stemcells.2008-0031.

(64) Topol, B. M.; Haimes, H. B.; Dubertret, L.; Bell, E. Transfer of Melanosomes in a Skin Equivalent Model In Vitro. *Journal of Investigative Dermatology* **1986**, *87* (5), 642–647. https://doi.org/10.1111/1523-1747.ep12456314.

(65) Okazaki, M.; Suzuki, Y.; Yoshimura, K.; Harii, K. Construction of Pigmented Skin Equivalent and Its Application to the Study of Congenital Disorders of Pigmentation. *null* **2005**, *39* (6), 339–343. https://doi.org/10.1080/02844310500300362.

(66) Boyce, S. T.; Medrano, E. E.; Abdel-Malek, Z.; Supp, A. P.; Dodick, J. M.; Nordlund, J. J.; Warden, G. D. Pigmentation and Inhibition of Wound Contraction by Cultured Skin Substitutes with Adult Melanocytes After Transplantation to Athymic Mice. *Journal of Investigative Dermatology* **1993**, *100* (4), 360–365. https://doi.org/10.1111/1523-1747.ep12471822.

(67) Kim, Y.; Park, N.; Rim, Y. A.; Nam, Y.; Jung, H.; Lee, K.; Ju, J. H. Establishment of a Complex Skin Structure via Layered Co-Culture of Keratinocytes and Fibroblasts Derived from Induced Pluripotent Stem Cells. *Stem Cell Research & Therapy* **2018**, *9* (1), 217. https://doi.org/10.1186/s13287-018-0958-2.

(68) Gingras, M.; Paradis, I.; Berthod, F. Nerve Regeneration in a Collagen–Chitosan Tissue-Engineered Skin Transplanted on Nude Mice. *Biomaterials* **2003**, *24* (9), 1653–1661. https://doi.org/10.1016/S0142-9612(02)00572-0.

(69) Barker, C. L.; McHale, M. T.; Gillies, A. K.; Waller, J.; Pearce, D. M.; Osborne, J.; Hutchinson, P. E.; Smith, G. M.; Pringle, J. H. The Development and Characterization of an In Vitro Model of Psoriasis. *Journal of Investigative Dermatology* **2004**, *123* (5), 892–901. https://doi.org/10.1111/j.0022-202X.2004.23435.x.

(70) van den Bogaard, E. H.; Tjabringa, G. S.; Joosten, I.; Vonk-Bergers, M.; van Rijssen, E.; Tijssen, H. J.; Erkens, M.; Schalkwijk, J.; Koenen, H. J. P. M. Crosstalk between Keratinocytes and T Cells in a 3D Microenvironment: A Model to Study Inflammatory Skin Diseases. *Journal of Investigative Dermatology* **2014**, *134* (3), 719–727. https://doi.org/10.1038/jid.2013.417.

(71) Guerrero-Aspizua, S.; García, M.; Murillas, R.; Retamosa, L.; Illera, N.; Duarte, B.; Holguín, A.; Puig, S.; Hernández, M. I.; Meana, A.; Jorcano, J. L.; Larcher, F.; Carretero, M.; Del Río, M. Development of a Bioengineered Skin-Humanized Mouse Model for Psoriasis: Dissecting Epidermal-Lymphocyte Interacting Pathways. *The American Journal of Pathology* **2010**, *177* (6), 3112–3124. https://doi.org/10.2353/ajpath.2010.100078.

(72) Gache, Y.; Baldeschi, C.; Del Rio, M.; Gagnoux-Palacios, L.; larcher, F.; Lacour, J.-P.; Meneguzzi, G. Construction of Skin Equivalents for Gene Therapy of Recessive Dystrophic Epidermolysis Bullosa. *Human Gene Therapy* **2004**, *15* (10), 921–933. https://doi.org/10.1089/hum.2004.15.921.

(73) Di Nunzio, F.; Maruggi, G.; Ferrari, S.; Di Iorio, E.; Poletti, V.; Garcia, M.; Del Rio, M.; De Luca, M.; Larcher, F.; Pellegrini, G.; Mavilio, F. Correction of Laminin-5 Deficiency in Human Epidermal Stem Cells by Transcriptionally Targeted Lentiviral Vectors. *Molecular Therapy* **2008**, *16* (12), 1977–1985. https://doi.org/10.1038/mt.2008.204.

(74) Aufenvenne, K.; Rice, R. H.; Hausser, I.; Oji, V.; Hennies, H. C.; Rio, M. D.; Traupe, H.; Larcher, F. Long-Term Faithful Recapitulation of Transglutaminase 1-Deficient Lamellar Ichthyosis in a Skin-Humanized Mouse Model, and Insights from Proteomic Studies. *J Invest Dermatol* **2012**, *132* (7), 1918–1921. https://doi.org/10.1038/jid.2012.65.

(75) Di, W.-L.; Larcher, F.; Semenova, E.; Talbot, G. E.; Harper, J. I.; Del Rio, M.; Thrasher, A. J.; Qasim, W. Ex-Vivo Gene Therapy Restores LEKTI Activity and Corrects the Architecture of Netherton Syndrome-Derived Skin Grafts. *Molecular Therapy* **2011**, *19* (2), 408–416. https://doi.org/10.1038/mt.2010.201.

(76) García, M.; Larcher, F.; Hickerson, R. P.; Baselga, E.; Leachman, S. A.; Kaspar, R. L.; Del Rio, M. Development of Skin-Humanized Mouse Models of Pachyonychia Congenita. *Journal of Investigative Dermatology* **2011**, *131* (5), 1053–1060. https://doi.org/10.1038/jid.2010.353.

(77) Larcher, F.; Espada, J.; Díaz-Ley, B.; Jaén, P.; Juarranz, A.; Quintanilla, M. New Experimental Models of Skin Homeostasis and Diseases. *Actas Dermo-Sifiliográficas (English Edition)* **2015**, *106* (1), 17–28. https://doi.org/10.1016/j.adengl.2014.11.013.

(78) Varkey, M.; Ding, J.; Tredget, E. E. Fibrotic Remodeling of Tissue-Engineered Skin with Deep Dermal Fibroblasts Is Reduced by Keratinocytes. *Tissue Engineering Part A* **2013**, *20* (3–4), 716–727. https://doi.org/10.1089/ten.tea.2013.0434.

(79) Moulin, V. J. Reconstitution of Skin Fibrosis Development Using a Tissue Engineering Approach. *Methods Mol Biol* **2013**, *961*, 287–303. https://doi.org/10.1007/978-1-62703-227-8_19.

(80) Berthod, F.; Germain, L.; Li, H.; Xu, W.; Damour, O.; Auger, F. A. Collagen Fibril Network and Elastic System Remodeling in a Reconstructed Skin Transplanted on Nude Mice. *Matrix Biology* **2001**, *20* (7), 463–473. https://doi.org/10.1016/S0945-053X(01)00162-7.

(81) Quan, T.; He, T.; Shao, Y.; Lin, L.; Kang, S.; Voorhees, J. J.; Fisher, G. J. Elevated Cysteine-Rich 61 Mediates Aberrant Collagen Homeostasis in Chronologically Aged

and Photoaged Human Skin. *The American Journal of Pathology* **2006**, *169* (2), 482–490. https://doi.org/10.2353/ajpath.2006.060128.

(82) Borg, M.; Brincat, S.; Camilleri, G.; Schembri-Wismayer, P.; Brincat, M.; Calleja-Agius, J. The Role of Cytokines in Skin Aging. *null* **2013**, *16* (5), 514–521. https://doi.org/10.3109/13697137.2013.802303.

(83) Weinmüllner, R.; Zbiral, B.; Becirovic, A.; Stelzer, E. M.; Nagelreiter, F.; Schosserer, M.; Lämmermann, I.; Liendl, L.; Lang, M.; Terlecki-Zaniewicz, L.; Andriotis, O.; Mildner, M.; Golabi, B.; Waidhofer-Söllner, P.; Schedle, K.; Emsenhuber, G.; Thurner, P. J.; Tschachler, E.; Gruber, F.; Grillari, J. Organotypic Human Skin Culture Models Constructed with Senescent Fibroblasts Show Hallmarks of Skin Aging. *npj Aging and Mechanisms of Disease* **2020**, *6* (1), 4. https://doi.org/10.1038/s41514-020-0042-x.

(84) Diekmann, J.; Alili, L.; Scholz, O.; Giesen, M.; Holtkötter, O.; Brenneisen, P. A Three-Dimensional Skin Equivalent Reflecting Some Aspects of in Vivo Aged Skin. *Experimental Dermatology* **2016**, *25* (1), 56–61. https://doi.org/10.1111/exd.12866.

(85) Weinmüllner, R.; Zbiral, B.; Becirovic, A.; Stelzer, E. M.; Nagelreiter, F.; Schosserer, M.; Lämmermann, I.; Liendl, L.; Lang, M.; Terlecki-Zaniewicz, L.; Andriotis, O.; Mildner, M.; Golabi, B.; Waidhofer-Söllner, P.; Schedle, K.; Emsenhuber, G.; Thurner, P. J.; Tschachler, E.; Gruber, F.; Grillari, J. Organotypic Human Skin Culture Models Constructed with Senescent Fibroblasts Show Hallmarks of Skin Aging. *npj Aging and Mechanisms of Disease* **2020**, *6* (1), 4. https://doi.org/10.1038/s41514-020-0042-x.

(86) Youn, S. W.; Kim, D. S.; Cho, H. J.; Jeon, S. E.; Bae, I. H.; Yoon, H. J.; Park, K. C. Cellular Senescence Induced Loss of Stem Cell Proportion in the Skin in Vitro. *Journal of Dermatological Science* **2004**, *35* (2), 113–123. https://doi.org/10.1016/j.jdermsci.2004.04.002.

(87) Adamus, J.; Aho, S.; Meldrum, H.; Bosko, C.; Lee, J.-M. P16INK4A Influences the Aging Phenotype in the Living Skin Equivalent. *J Invest Dermatol* **2014**, *134* (4), 1131–1133. https://doi.org/10.1038/jid.2013.468.

(88) Ressler, S.; Bartkova, J.; Niederegger, H.; Bartek, J.; Scharffetter-Kochanek, K.; Jansen-Dürr, P.; Wlaschek, M. P16INK4A Is a Robust in Vivo Biomarker of Cellular Aging in Human Skin. *Aging Cell* **2006**, *5* (5), 379–389. https://doi.org/10.1111/j.1474-9726.2006.00231.x.

(89) Oh, J.-H.; Kim, Y. K.; Jung, J.-Y.; Shin, J.; Kim, K. H.; Cho, K. H.; Eun, H. C.; Chung, J. H. Intrinsic Aging- and Photoaging-Dependent Level Changes of Glycosaminoglycans and Their Correlation with Water Content in Human Skin. *Journal of Dermatological Science* **2011**, *62* (3), 192–201. https://doi.org/10.1016/j.jdermsci.2011.02.007.

(90) Maquart, F.-X.; Wegrowski, S. B. Y. 11 Proteoglycans in Skin Aging. *Textbook of Aging Skin* **2009**.

(91) Sok, J.; Pineau, N.; Dalko-Csiba, M.; Breton, L.; Bernerd, F. Improvement of the Dermal Epidermal Junction in Human Reconstructed Skin by a New C-Xylopyranoside Derivative. *European Journal of Dermatology* **2008**, *18* (3), 297–302.

(92) Nomura, Y. Structural Change in Decorin with Skin Aging. *null* **2006**, *47* (5), 249–255. https://doi.org/10.1080/03008200600846606.

(93) Danielson, K. G.; Baribault, H.; Holmes, D. F.; Graham, H.; Kadler, K. E.; Iozzo, R. V. Targeted Disruption of Decorin Leads to Abnormal Collagen Fibril Morphology and Skin Fragility. *Journal of Cell Biology* **1997**, *136* (3), 729–743. https://doi.org/10.1083/jcb.136.3.729.

(94) Henriet, E.; Jäger, S.; Tran, C.; Bastien, P.; Michelet, J.-F.; Minondo, A.-M.; Formanek, F.; Dalko-Csiba, M.; Lortat-Jacob, H.; Breton, L.; Vivès, R. R. A Jasmonic Acid Derivative Improves Skin Healing and Induces Changes in Proteoglycan Expression and Glycosaminoglycan Structure. *Biochimica et Biophysica Acta (BBA) - General Subjects* **2017**, *1861* (9), 2250–2260. https://doi.org/10.1016/j.bbagen.2017.06.006.

(95) Vassal-Stermann, E.; Duranton, A.; Black, A. F.; Azadiguian, G.; Demaude, J.; Lortat-Jacob, H.; Breton, L.; Vivès, R. R. A New C-Xyloside Induces Modifications of GAG Expression, Structure and Functional Properties. *PLOS ONE* **2012**, *7* (10), e47933. https://doi.org/10.1371/journal.pone.0047933.

(96) Claire DELOCHE; Anne Marie MINONDO; Bruno A. BERNARD; Françoise BERNERD; Fabien SALAS; Julien GARNIER; Emmanuelle TANCRÈDE. Effect of C-Xyloside on Morphogenesis of the Dermal Epidermal Junction in Aged Female Skin. An Unltrastuctural Pilot Study. *European Journal of Dermatology* **2011**, *21* (2), 191–196. https://doi.org/10.1684/ejd.2010.1225.

(97) Kissa, E. *Fluorinated Surfactants and Repellents*; CRC Press, 2001; Vol. 97.

(98) Patel, R.; Bradner, J. M.; Stout, K. A.; Caudle, W. M. Alteration to Dopaminergic Synapses Following Exposure to Perfluorooctane Sulfonate (PFOS), in Vitro and in Vivo. *Medical Sciences* **2016**, *4* (3), 13. https://doi.org/10.3390/medsci4030013.

(99) Haug, L. S.; Huber, S.; Becher, G.; Thomsen, C. Characterisation of Human Exposure Pathways to Perfluorinated Compounds — Comparing Exposure Estimates with Biomarkers of Exposure. *Environment International* **2011**, *37* (4), 687–693. https://doi.org/10.1016/j.envint.2011.01.011.

(100) United States Environmental Protection Agency. Technical Fact Sheet - Perfluorooctane Sulfonate (PFOS) and Perfluorooctanoic Acid (PFOA). United States Environmental Protection Agency Office of Land and Emergency Management (5106P) November 2017.

(101) Domingo, J. L.; Nadal, M. Human Exposure to Per- and Polyfluoroalkyl Substances (PFAS) through Drinking Water: A Review of the Recent Scientific Literature. *Environmental Research* **2019**, *177*, 108648. https://doi.org/10.1016/j.envres.2019.108648.

(102) Mora Ana María; Oken Emily; Rifas-Shiman Sheryl L.; Webster Thomas F.; Gillman Matthew W.; Calafat Antonia M.; Ye Xiaoyun; Sagiv Sharon K. Prenatal Exposure to Perfluoroalkyl Substances and Adiposity in Early and Mid-Childhood. *Environmental Health Perspectives* **2017**, *125* (3), 467–473. https://doi.org/10.1289/EHP246.

(103) Hartman, K. G.; Bortner, J. D.; Falk, G. W.; Yu, J.; Martín, M. G.; Rustgi, A. K.; Lynch, J. P. Modeling Inflammation and Oxidative Stress in Gastrointestinal Disease Development Using Novel Organotypic Culture Systems. *Stem Cell Research & Therapy* **2013**, *4* (1), S5. https://doi.org/10.1186/scrt366.

(104) Lauritzen, H. B.; Larose, T. L.; Øien, T.; Sandanger, T. M.; Odland, J. Ø.; van de Bor, M.; Jacobsen, G. W. Prenatal Exposure to Persistent Organic Pollutants and Child Overweight/Obesity at 5-Year Follow-up: A Prospective Cohort Study. *Environmental Health* **2018**, *17* (1), 9. https://doi.org/10.1186/s12940-017-0338-x.

(105) Liu, G.; Dhana, K.; Furtado, J. D.; Rood, J.; Zong, G.; Liang, L.; Qi, L.; Bray, G. A.; DeJonge, L.; Coull, B.; Grandjean, P.; Sun, Q. Perfluoroalkyl Substances and Changes in Body Weight and Resting Metabolic Rate in Response to Weight-Loss Diets: A Prospective Study. *PLoS Med* **2018**, *15* (2), e1002502–e1002502. https://doi.org/10.1371/journal.pmed.1002502.

(106) Braun, J. M. Early-Life Exposure to EDCs: Role in Childhood Obesity and Neurodevelopment. *Nature Reviews Endocrinology* **2017**, *13* (3), 161–173. https://doi.org/10.1038/nrendo.2016.186.

(107) Stojic, M.; Lopez, V.; Montero, A.; Quílez, C.; de Aranda Izuzquiza, G.; Vojtova, L.; Jorcano, J. L.; Velasco, D. Skin Tissue Engineering 3. *Biomaterials for Skin Repair and Regeneration* **2019**, 59.

(108) Shevchenko, R. V.; James, S. L.; James, S. E. A Review of Tissue-Engineered Skin Bioconstructs Available for Skin Reconstruction. *Journal of The Royal Society Interface* **2010**, *7* (43), 229–258. https://doi.org/10.1098/rsif.2009.0403.

(109) Kolarsick, P. A. J.; Kolarsick, M. A.; Goodwin, C. Anatomy and Physiology of the Skin. *Journal of the Dermatology Nurses' Association* **2011**, *3* (4).

(110) McGrath, J. A.; Eady, R. A. J.; Pope, F. M. Anatomy and Organization of Human Skin. *Rook's textbook of dermatology* **2004**, *10*, 9781444317633.

(111) Zomer, H. D.; Trentin, A. G. Skin Wound Healing in Humans and Mice: Challenges in Translational Research. *Journal of Dermatological Science* **2018**, *90* (1), 3–12. https://doi.org/10.1016/j.jdermsci.2017.12.009.

(112) Zhang, Z.; Michniak-Kohn, B. B. Tissue Engineered Human Skin Equivalents. *Pharmaceutics* **2012**, *4* (1). https://doi.org/10.3390/pharmaceutics4010026.

(113) Oh, J. W.; Hsi, T.-C.; Guerrero-Juarez, C. F.; Ramos, R.; Plikus, M. V. Organotypic Skin Culture. *The Journal of investigative dermatology* **2013**, *133* (11), 1–4. https://doi.org/10.1038/jid.2013.387.

(114) El-Ghalbzouri, A.; Gibbs, S.; Lamme, E.; Van Blitterswijk, C. A.; Ponec, M. Effect of Fibroblasts on Epidermal Regeneration. *British Journal of Dermatology* **2002**, *147* (2), 230–243. https://doi.org/10.1046/j.1365-2133.2002.04871.x.

(115) Sun, T.; Haycock, J.; MacNeil, S. In Situ Image Analysis of Interactions between Normal Human Keratinocytes and Fibroblasts Cultured in Three-Dimensional Fibrin Gels. *Biomaterials* **2006**, *27* (18), 3459–3465. https://doi.org/10.1016/j.biomaterials.2006.01.058.

(116) Kreimendahl, F.; Marquardt, Y.; Apel, C.; Bartneck, M.; Zwadlo-Klarwasser, G.; Hepp, J.; Jockenhoevel, S.; Baron, J. M. Macrophages Significantly Enhance Wound Healing in a Vascularized Skin Model. *Journal of Biomedical Materials Research Part A* **2019**, *107A*, 1340–1350.

(117) Roger, M.; Fullard, N.; Costello, L.; Bradbury, S.; Markiewicz, E.; O'Reilly, S.; Darling, N.; Ritchie, P.; Määttä, A.; Karakesisoglou, I.; Nelson, G.; Zglinicki, T. von; Dicolandrea, T.; Isfort, R.; Bascom, C.; Przyborski, S. Bioengineering the Microanatomy of Human Skin. *Journal of Anatomy 0* (0). https://doi.org/10.1111/joa.12942.

(118) Carlson, M. W.; Alt-Holland, A.; Egles, C.; Garlick, J. A. Three-Dimensional Tissue Models of Normal and Diseased Skin. *Current Protocols in Cell Biology* **2008**, *41* (1), 19.9.1-19.9.17. https://doi.org/10.1002/0471143030.cb1909s41.

(119) El Ghalbzouri, A.; Jonkman, M. F.; Dijkman, R.; Ponec, M. Basement Membrane Reconstruction in Human Skin Equivalents Is Regulated by Fibroblasts and/or Exogenously Activated Keratinocytes. *Journal of Investigative Dermatology* **2005**, *124* (1), 79–86. https://doi.org/10.1111/j.0022-202X.2004.23549.x.

(120) Pruniéras, M.; Régnier, M.; Woodley, D. Methods for Cultivation of Keratinocytes with an Air-Liquid Interface. *J Invest Dermatol* **1983**, *81* (1 Suppl), 28s–33s. https://doi.org/10.1111/1523-1747.ep12540324.

(121) Mathes, S. H.; Ruffner, H.; Graf-Hausner, U. The Use of Skin Models in Drug Development. *Advanced Drug Delivery Reviews* **2014**, *69–70*, 81–102. https://doi.org/10.1016/j.addr.2013.12.006.

(122) Mieremet, A.; Rietveld, M.; Absalah, S.; van Smeden, J.; Bouwstra, J. A.; El Ghalbzouri, A. Improved Epidermal Barrier Formation in Human Skin Models by Chitosan Modulated Dermal Matrices. *PLOS ONE* **2017**, *12* (3), e0174478. https://doi.org/10.1371/journal.pone.0174478.

(123) Lightfoot Vidal, S. E.; Tamamoto, K. A.; Nguyen, H.; Abbott, R. D.; Cairns, D. M.; Kaplan, D. L. 3D Biomaterial Matrix to Support Long Term, Full Thickness, Immuno-Competent Human Skin Equivalents with Nervous System Components. *Biomaterials* **2019**, *198*, 194–203. https://doi.org/10.1016/j.biomaterials.2018.04.044.

(124) Smits, J. P. H.; Niehues, H.; Rikken, G.; Vlijmen-Willems, I. M. J. J. van; Zande, G. W. H. J. F. van de; Zeeuwen, P. L. J. M.; Schalkwijk, J.; Bogaard, E. H. van den. Immortalized N/TERT Keratinocytes as an Alternative Cell Source in 3D Human Epidermal Models. *Scientific Reports* **2017**, *7* (1), 11838. https://doi.org/10.1038/s41598-017-12041-y.

(125) Lebonvallet, N.; Boulais, N.; Le Gall, C.; Pereira, U.; Gauché, D.; Gobin, E.; Pers, J.-O.; Jeanmaire, C.; Danoux, L.; Pauly, G.; Misery, L. Effects of the Re-Innervation of Organotypic Skin Explants on the Epidermis. *Experimental Dermatology* **2011**, *21* (2), 156–158. https://doi.org/10.1111/j.1600-0625.2011.01421.x.

(126) van Drongelen, V.; Danso, M. O.; Mulder, A.; Mieremet, A.; van Smeden, J.; Bouwstra, J. A.; El Ghalbzouri, A. Barrier Properties of an N/TERT-Based Human Skin Equivalent. *Tissue Engineering Part A* **2014**, *20* (21–22), 3041–3049. https://doi.org/10.1089/ten.tea.2014.0011.

(127) Hensler, S.; Kühlbach, C.; Parente, J. D.; Krüger-Ziolek, S.; Möller, K.; Müller, M. Establishment and Initial Characterization of a Simple 3D Organotypic Wound Healing Model; 2018.

(128) Breslin, S.; O'Driscoll, L. Three-Dimensional Cell Culture: The Missing Link in Drug Discovery. *Drug Discovery Today* **2013**, *18* (5), 240–249. https://doi.org/10.1016/j.drudis.2012.10.003.

(129) Shamir, E. R.; Ewald, A. J. Three-Dimensional Organotypic Culture: Experimental Models of Mammalian Biology and Disease. *Nature Reviews Molecular Cell Biology* **2014**, *15* (10), 647–664. https://doi.org/10.1038/nrm3873.

(130) Amelian, A.; Wasilewska, K.; Megias, D.; Winnicka, K. Application of Standard Cell Cultures and 3D in Vitro Tissue Models as an Effective Tool in Drug Design and Development. *Pharmacological Reports* **2017**, *69* (5), 861–870. https://doi.org/10.1016/j.pharep.2017.03.014.

(131) Lu, W.; Yu, J.; Zhang, Y.; Ji, K.; Zhou, Y.; Li, Y.; Deng, Z.; Jin, Y. Mixture of Fibroblasts and Adipose Tissue-Derived Stem Cells Can Improve Epidermal Morphogenesis of Tissue-Engineered Skin. *Cells Tissues Organs* **2012**, *195* (3), 197–206. https://doi.org/10.1159/000324921.

(132) Marino, D.; Luginbühl, J.; Scola, S.; Meuli, M.; Reichmann, E. Bioengineering Dermo-Epidermal Skin Grafts with Blood and Lymphatic Capillaries. *Science Translational Medicine* **2014**, *6* (221), 221ra14-221ra14. https://doi.org/10.1126/scitranslmed.3006894.

(133) Kim, B. S.; Gao, G.; Kim, J. Y.; Cho, D.-W. 3D Cell Printing of Perfusable Vascularized Human Skin Equivalent Composed of Epidermis, Dermis, and Hypodermis for Better Structural Recapitulation of Native Skin. *Advanced Healthcare Materials* **2019**, *8* (7), 1801019. https://doi.org/10.1002/adhm.201801019.

(134) Klar, A. S.; Güven, S.; Biedermann, T.; Luginbühl, J.; Böttcher-Haberzeth, S.; Meuli-Simmen, C.; Meuli, M.; Martin, I.; Scherberich, A.; Reichmann, E. Tissue-Engineered Dermo-Epidermal Skin Grafts Prevascularized with Adipose-Derived Cells. *Biomaterials* **2014**, *35* (19), 5065–5078. https://doi.org/10.1016/j.biomaterials.2014.02.049.

(135) Grebenyuk, S.; Ranga, A. Engineering Organoid Vascularization. *Front. Bioeng. Biotechnol.* **2019**, *7*. https://doi.org/10.3389/fbioe.2019.00039.

(136) Black, A. F.; Berthod, F.; L'heureux, N.; Germain, L.; Auger, F. A. In Vitro Reconstruction of a Human Capillary-like Network in a Tissue-Engineered Skin Equivalent. *The FASEB Journal* **1998**, *12* (13), 1331–1340. https://doi.org/10.1096/fasebj.12.13.1331.

(137) Huber, B.; Link, A.; Linke, K.; Gehrke, S. A.; Winnefeld, M.; Kluger, P. J. Integration of Mature Adipocytes to Build-Up a Functional Three-Layered Full-Skin Equivalent. *Tissue Engineering Part C: Methods* **2016**, *22* (8), 756–764. https://doi.org/10.1089/ten.tec.2016.0141.

(138) Monfort, A.; Soriano-Navarro, M.; García-Verdugo, J. M.; Izeta, A. Production of Human Tissue-Engineered Skin Trilayer on a Plasma-Based Hypodermis. *Journal of Tissue Engineering and Regenerative Medicine* **2013**, *7* (6), 479–490. https://doi.org/10.1002/term.548.

(139) Shamis, Y.; Hewitt, K. J.; Carlson, M. W.; Margvelashvilli, M.; Dong, S.; Kuo, C. K.; Daheron, L.; Egles, C.; Garlick, J. A. Fibroblasts Derived from Human Embryonic Stem Cells Direct Development and Repair of 3D Human Skin Equivalents. *Stem Cell Research & Therapy* **2011**, *2* (1), 10. https://doi.org/10.1186/scrt51.

(140) Kim, Y.; Park, N.; Rim, Y. A.; Nam, Y.; Jung, H.; Lee, K.; Ju, J. H. Establishment of a Complex Skin Structure via Layered Co-Culture of Keratinocytes and Fibroblasts Derived from Induced Pluripotent Stem Cells. *Stem Cell Research & Therapy* **2018**, *9* (1), 217. https://doi.org/10.1186/s13287-018-0958-2.

(141) Chau, D. Y. S.; Johnson, C.; MacNeil, S.; Haycock, J. W.; Ghaemmaghami, A. M. The Development of a 3D Immunocompetent Model of Human Skin. *Biofabrication* **2013**, *5* (3), 035011. https://doi.org/10.1088/1758-5082/5/3/035011.

(142) Linde, N.; Gutschalk, C. M.; Hoffmann, C.; Yilmaz, D.; Mueller, M. M. Integrating Macrophages into Organotypic Co-Cultures: A 3D In Vitro Model to Study Tumor-Associated Macrophages. *PLOS ONE* **2012**, *7* (7), e40058. https://doi.org/10.1371/journal.pone.0040058.

(143) Ouwehand, K.; Spiekstra, S. W.; Waaijman, T.; Scheper, R. J.; de Gruijl, T. D.; Gibbs, S. Technical Advance: Langerhans Cells Derived from a Human Cell Line in a Full-Thickness Skin Equivalent Undergo Allergen-Induced Maturation and Migration. *Journal of Leukocyte Biology* **2011**, *90* (5), 1027–1033. https://doi.org/10.1189/jlb.0610374.

(144) Morgan, J. T.; Shirazi, J.; Comber, E. M.; Eschenburg, C.; Gleghorn, J. P. Fabrication of Centimeter-Scale and Geometrically Arbitrary Vascular Networks Using in Vitro Self-Assembly. *Biomaterials* **2019**, *189*, 37–47. https://doi.org/10.1016/j.biomaterials.2018.10.021.

(145) Ludovico Silvestri; Irene Costantini; Leonardo Sacconi; Francesco Saverio Pavone. Clearing of Fixed Tissue: A Review from a Microscopist's Perspective. *Journal of Biomedical Optics* **2016**, *21* (8), 1–8. https://doi.org/10.1117/1.JBO.21.8.081205.

(146) Cross, V. L.; Zheng, Y.; Won Choi, N.; Verbridge, S. S.; Sutermaster, B. A.; Bonassar, L. J.; Fischbach, C.; Stroock, A. D. Dense Type I Collagen Matrices That Support Cellular Remodeling and Microfabrication for Studies of Tumor Angiogenesis and Vasculogenesis in Vitro. *Biomaterials* **2010**, *31* (33), 8596–8607. https://doi.org/10.1016/j.biomaterials.2010.07.072.

(147) Rajan, N.; Habermehl, J.; Coté, M.-F.; Doillon, C. J.; Mantovani, D. Preparation of Ready-to-Use, Storable and Reconstituted Type I Collagen from Rat Tail Tendon for Tissue Engineering Applications. *Nature Protocols* **2007**, *1*, 2753.

(148) Bornstein, M. B. Reconstituted Rat-Tail Collagen Used as Substrate for Tissue Cultures on Coverslips in Maximow Slides and Roller Tubes. *Laboratory Investigation* **1958**, *7* (2), 134–137.

(149) Clément, M.-V.; Ramalingam, J.; Long, L. H.; Halliwell, B. The In Vitro Cytotoxicity of Ascorbate Depends on the Culture Medium Used to Perform the Assay and Involves Hydrogen Peroxide. *Antioxidants & Redox Signaling* **2001**, *3* (1), 157–163. https://doi.org/10.1089/152308601750100687.

(150) Tajima, S.; Pinnell, S. R. Ascorbic Acid Preferentially Enhances Type I and III Collagen Gene Transcription in Human Skin Fibroblasts. *Journal of Dermatological Science* **1996**, *11* (3), 250–253. https://doi.org/10.1016/0923-1811(95)00640-0.

(151) Murad, S.; Tajima, S.; Johnson, G. R.; Sivarajah, A.; Pinnell, S. R. Collagen Synthesis in Cultured Human Skin Fibroblasts: Effect of Ascorbic Acid and Its Analogs. *Journal of Investigative Dermatology* **1983**, *81* (2), 158–162. https://doi.org/10.1111/1523-1747.ep12543573.

(152) Villacorta, L.; Azzi, A.; Zingg, J.-M. Regulatory Role of Vitamins E and C on Extracellular Matrix Components of the Vascular System. *Molecular Aspects of Medicine* **2007**, *28* (5), 507–537. https://doi.org/10.1016/j.mam.2007.05.002.

(153) Ashino, H.; Shimamura, M.; Nakajima, H.; Dombou, M.; Kawanaka, S.; Oikawa, T.; Iwaguchi, T.; Kawashima, S. Novel Function of Ascorbic Acid as an Angiostatic Factor. *Angiogenesis* **2003**, *6* (4), 259–269. https://doi.org/10.1023/B:AGEN.0000029390.09354.f8.

(154) Dickson, M. A.; Hahn, W. C.; Ino, Y.; Ronfard, V.; Wu, J. Y.; Weinberg, R. A.; Louis, D. N.; Li, F. P.; Rheinwald, J. G. Human Keratinocytes That Express HTERT and Also Bypass a P16(INK4a)-Enforced Mechanism That Limits Life Span Become Immortal yet Retain Normal Growth and Differentiation Characteristics. *Mol. Cell. Biol.* **2000**, *20* (4), 1436–1447.

(155) Johansen, C. Generation and Culturing of Primary Human Keratinocytes from Adult Skin. *J Vis Exp* **2017**, No. 130, 56863. https://doi.org/10.3791/56863.

(156) Richardson, D. S.; Lichtman, J. W. Clarifying Tissue Clearing. *Cell* **2015**, *162* (2), 246–257. https://doi.org/10.1016/j.cell.2015.06.067.

(157) Ariel, P. A Beginner's Guide to Tissue Clearing. *The International Journal of Biochemistry & Cell Biology* **2017**, *84*, 35–39. https://doi.org/10.1016/j.biocel.2016.12.009.

(158) Friend, J.; Yeo, L. Fabrication of Microfluidic Devices Using Polydimethylsiloxane. *Biomicrofluidics* **2010**, *4* (2), 026502. https://doi.org/10.1063/1.3259624.

(159) Ng, J. M. K.; Gitlin, I.; Stroock, A. D.; Whitesides, G. M. Components for Integrated Poly(Dimethylsiloxane) Microfluidic Systems. *ELECTROPHORESIS* **2002**, *23* (20), 3461–3473. https://doi.org/10.1002/1522-2683(200210)23:20<3461::AID-ELPS3461>3.0.CO;2-8.

(160) Eddings, M. A.; Johnson, M. A.; Gale, B. K. Determining the Optimal PDMS–PDMS Bonding Technique for Microfluidic Devices. *Journal of Micromechanics and Microengineering* **2008**, *18* (6), 067001. https://doi.org/10.1088/0960-1317/18/6/067001.

(161) Markov, D. A.; Lillie, E. M.; Garbett, S. P.; McCawley, L. J. Variation in Diffusion of Gases through PDMS Due to Plasma Surface Treatment and Storage Conditions. *Biomed Microdevices* **2014**, *16* (1), 91–96. https://doi.org/10.1007/s10544-013-9808-2.

(162) Katzenberg, F. Plasma-Bonding of Poly(Dimethylsiloxane) to Glass. *e-Polymers* **2005**, *5* (1). https://doi.org/10.1515/epoly.2005.5.1.638.

(163) El Ghalbzouri, A.; Lamme, E.; Ponec, M. Crucial Role of Fibroblasts in Regulating Epidermal Morphogenesis. *Cell and Tissue Research* **2002**, *310* (2), 189–199. https://doi.org/10.1007/s00441-002-0621-0.

(164) Kanitakis, J. Anatomy, Histology and Immunohistochemistry of Normal Human Skin. *European journal of dermatology: EJD* **2002**, *12* (4), 390–399; quiz 400–401.

(165) Kroon, D.-J. *Hessian Based Frangi Vesselness Filter*; MATLAB Central File Exchange, 2010.

(166) T. Jerman; F. Pernuš; B. Likar; Ž. Špiclin. Enhancement of Vascular Structures in 3D and 2D Angiographic Images. *IEEE Transactions on Medical Imaging* **2016**, *35* (9), 2107–2118. https://doi.org/10.1109/TMI.2016.2550102.

(167) Kovesi, P. Phase Preserving Denoising of Images. *signal* **1999**, *4.1*, 6.

(168) L. Vincent. Morphological Grayscale Reconstruction in Image Analysis: Applications and Efficient Algorithms. *IEEE Transactions on Image Processing* **1993**, *2* (2), 176–201. https://doi.org/10.1109/83.217222.

(169) Xie, L.; Sparks, M. A.; Li, W.; Qi, Y.; Liu, C.; Coffman, T. M.; Johnson, G. A. Quantitative Susceptibility Mapping of Kidney Inflammation and Fibrosis in Type 1 Angiotensin Receptor-Deficient Mice. *NMR in Biomedicine* **2013**, *26* (12), 1853–1863. https://doi.org/10.1002/nbm.3039.

(170) Van Uitert, R.; Bitter, I. Subvoxel Precise Skeletons of Volumetric Data Based on Fast Marching Methods. *Medical Physics* **2007**, *34* (2), 627–638. https://doi.org/10.1118/1.2409238.

(171) Sethian, J. A. A Fast Marching Level Set Method for Monotonically Advancing Fronts. *Proc Natl Acad Sci U S A* **1996**, *93* (4), 1591–1595. https://doi.org/10.1073/pnas.93.4.1591.

(172) Sethian, J. A. Fast Marching Methods. *SIAM Rev.* **1999**, *41* (2), 199–235. https://doi.org/10.1137/S0036144598347059.

(173) Commandeur, S.; Ho, S. H.; de Gruijl, F. R.; Willemze, R.; Tensen, C. P.; El Ghalbzouri, A. Functional Characterization of Cancer-Associated Fibroblasts of Human Cutaneous Squamous Cell Carcinoma. *Experimental Dermatology* **2011**, *20* (9), 737–742. https://doi.org/10.1111/j.1600-0625.2011.01305.x.

(174) Thakoersing, V. S.; Danso, M. O.; Mulder, A.; Gooris, G.; Ghalbzouri, A. E.; Bouwstra, J. A. Nature versus Nurture: Does Human Skin Maintain Its Stratum Corneum Lipid Properties in Vitro? *Experimental Dermatology* **2012**, *21* (11), 865–870. https://doi.org/10.1111/exd.12031.

(175) Thakoersing, V. S.; Gooris, G. S.; Mulder, A.; Rietveld, M.; El Ghalbzouri, A.; Bouwstra, J. A. Unraveling Barrier Properties of Three Different In-House Human Skin Equivalents. *Tissue Eng Part C Methods* **2012**, *18* (1), 1–11. https://doi.org/10.1089/ten.TEC.2011.0175.

(176) Bouwstra, J. A.; Groenink, H. W. W.; Kempenaar, J. A.; Romeijn, S. G.; Ponec, M. Water Distribution and Natural Moisturizer Factor Content in Human Skin Equivalents Are Regulated by Environmental Relative Humidity. *J. Invest. Dermatol.* **2008**, *128* (2), 378–388. https://doi.org/10.1038/sj.jid.5700994.

(177) Thakoersing, V. S.; van Smeden, J.; Mulder, A. A.; Vreeken, R. J.; El Ghalbzouri, A.; Bouwstra, J. A. Increased Presence of Monounsaturated Fatty Acids in the Stratum Corneum of Human Skin Equivalents. *Journal of Investigative Dermatology* **2013**, *133* (1), 59–67. https://doi.org/10.1038/jid.2012.262.

(178) Smola, H.; Thiekötter, G.; Fusenig, N. Mutual Induction of Growth Factor Gene Expression by Epidermal-Dermal Cell Interaction. *J Cell Biol* **1993**, *122* (2), 417. https://doi.org/10.1083/jcb.122.2.417.

(179) Fluck, J.; Querfeld, C.; Cremer, A.; Niland, S.; Krieg, T.; Sollberg, S. Normal Human Primary Fibroblasts Undergo Apoptosis in Three-Dimensional Contractile Collagen Gels. *Journal of Investigative Dermatology* **1998**, *110* (2), 153–157. https://doi.org/10.1046/j.1523-1747.1998.00095.x.

(180) Nakagawa, S.; Pawelek, P.; Grinnell, F. Long-Term Culture of Fibroblasts in Contracted Collagen Gels: Effects on Cell Growth and Biosynthetic Activity. *Journal of Investigative Dermatology* **1989**, *93* (6), 792–798. https://doi.org/10.1111/1523-1747.ep12284425.

(181) Smith, L. E.; Bonesi, M.; Smallwood, R.; Matcher, S. J.; MacNeil, S. Using Swept-Source Optical Coherence Tomography to Monitor the Formation of Neo-Epidermis in Tissue-Engineered Skin. *Journal of Tissue Engineering and Regenerative Medicine* **2010**, *4* (8), 652–658. https://doi.org/10.1002/term.281.

(182) Mark C. Pierce; John Strasswimmer; B. Hyle Park; Barry Cense; Johannes F. de Boer. Birefringence Measurements in Human Skin Using Polarization-Sensitive Optical Coherence Tomography; 2004; Vol. 5312.

(183) Pierce, M. C.; Strasswimmer, J.; Hyle Park, B.; Cense, B.; de Boer, J. F. Advances in Optical Coherence Tomography Imaging for Dermatology. *Journal of Investigative Dermatology* **2004**, *123* (3), 458–463. https://doi.org/10.1111/j.0022-202X.2004.23404.x.

(184) Alvin T. Yeh; Bunsho Kao; Woong Gyu Jung; Zhongping Chen; John Stuart Nelson; Bruce J. Tromberg. Imaging Wound Healing Using Optical Coherence Tomography and Multiphoton Microscopy in an in Vitro Skin-Equivalent Tissue Model. *Journal of Biomedical Optics* **2004**, *9* (2), 9–6.

(185) Derr, K.; Zou, J.; Luo, K.; Song, M. J.; Sittampalam, G. S.; Zhou, C.; Michael, S.; Ferrer, M.; Derr, P. Fully Three-Dimensional Bioprinted Skin Equivalent Constructs with Validated Morphology and Barrier Function. *Tissue Engineering Part C: Methods* **2019**, *25* (6), 334–343. https://doi.org/10.1089/ten.tec.2018.0318.

(186) Park, B. H.; de Boer, J. F. Polarization Sensitive Optical Coherence Tomography. In *Optical Coherence Tomography: Technology and Applications*; Drexler, W., Fujimoto, J. G., Eds.; Springer International Publishing: Cham, 2015; pp 1055–1101. https://doi.org/10.1007/978-3-319-06419-2_34.

(187) Batheja, P.; Song, Y.; Wertz, P.; Michniak-Kohn, B. Effects of Growth Conditions on the Barrier Properties of a Human Skin Equivalent. *Pharmaceutical Research* **2009**, *26* (7), 1689–1700. https://doi.org/10.1007/s11095-009-9879-1.

(188) Braverman, I. M. The Cutaneous Microcirculation. *Journal of Investigative Dermatology Symposium Proceedings* **2000**, *5* (1), 3–9. https://doi.org/10.1046/j.1087-0024.2000.00010.x.

(189) Men, S. J.; Chen, C.-L.; Wei, W.; Lai, T.-Y.; Song, S. Z.; Wang, R. K. Repeatability of Vessel Density Measurement in Human Skin by OCT-Based Microangiography. *Skin Res Technol* **2017**, *23* (4), 607–612. https://doi.org/10.1111/srt.12379.

(190) Auxenfans, Celine; Fradette, Julie; Lequeux, Charlotte; Germain, Lucie; KINIKOGLU, B.; Bechetoille, Nicolas; BRAYE, F.; AUGER, F. A.; DAMOUR, O. Evolution of Three Dimensional Skin Equivalent Models Reconstructed in Vitro by Tissue Engineering. *European journal of dermatology* **2009**, *19* (2), 107–113.

(191) Saxer, C. E.; de Boer, J. F.; Park, B. H.; Zhao, Y.; Chen, Z.; Nelson, J. S. High-Speed Fiber–Based Polarization-Sensitive Optical Coherence Tomography of in Vivo Human Skin. *Opt. Lett.* **2000**, *25* (18), 1355–1357. https://doi.org/10.1364/OL.25.001355.

(192) Strasswimmer, J.; Pierce, M. C.; Park, H.; Neel, V.; de Boer, J. F. Polarization-Sensitive Optical Coherence Tomography of Invasive Basal Cell Carcinoma. *Journal of biomedical optics* **2004**, *9* (2), 292–299.

(193) Carina Trojahn; Gabor Dobos; Claudia Richter; Ulrike Blume-Peytavi; Jan Kottner. Measuring Skin Aging Using Optical Coherence Tomography in Vivo: A Validation Study. *Journal of Biomedical Optics* **2015**, *20* (4), 1–7. https://doi.org/10.1117/1.JBO.20.4.045003.

(194) Gambichler, T.; Matip, R.; Moussa, G.; Altmeyer, P.; Hoffmann, K. In Vivo Data of Epidermal Thickness Evaluated by Optical Coherence Tomography: Effects of Age, Gender, Skin Type, and Anatomic Site. *Journal of Dermatological Science* **2006**, *44* (3), 145–152. https://doi.org/10.1016/j.jdermsci.2006.09.008.

(195) Gladkova, N. D.; Petrova, G. A.; Nikulin, N. K.; Radenska-Lopovok, S. G.; Snopova, L. B.; Chumakov, Yu. P.; Nasonova, V. A.; Gelikonov, V. M.; Gelikonov, G. V.; Kuranov, R. V.; Sergeev, A. M.; Feldchtein, F. I. In Vivo Optical Coherence Tomography Imaging of Human Skin: Norm and Pathology. *Skin Research and Technology* **2000**, *6* (1), 6–16. https://doi.org/10.1034/j.1600-0846.2000.006001006.x.

(196) Chen, C.-H.; Hsu, M.-Y.; Jiang, R.-S.; Wu, S.-H.; Chen, F.-J.; Liu, S.-A. Shrinkage of Head and Neck Cancer Specimens after Formalin Fixation. *Journal of the Chinese Medical Association* **2012**, *75* (3), 109–113. https://doi.org/10.1016/j.jcma.2012.02.006.

(197) Mansouri, P.; Chalangari, R.; Chalangari, K. M.; Saffarian, Z. Skin Aging and Immune System. In *Immunology of Aging*; Massoud, A., Rezaei, N., Eds.; Springer Berlin

Heidelberg: Berlin, Heidelberg, 2014; pp 339–368. https://doi.org/10.1007/978-3-642-39495-9_25.

(198) Berneburg, M.; Plettenberg, H.; Krutmann, J. Photoaging of Human Skin. *Photodermatology, Photoimmunology & Photomedicine* **2000**, *16* (6), 239–244. https://doi.org/10.1034/j.1600-0781.2000.160601.x.

(199) Helfrich, Y. R.; Sachs, D. L.; Voorhees, J. J. Overview of Skin Aging and Photoaging. *Dermatology Nursing* **2008**, *20* (3), 177.

(200) Bernstein, E. F.; Brown, D. B.; Schwartz, M. D.; Kaidbey, K.; Ksenzenko, S. M. The Polyhydroxy Acid Gluconolactone Protects Against Ultraviolet Radiation in an In Vitro Model of Cutaneous Photoaging. *Dermatologic Surgery* **2004**, *30* (2), 189–196. https://doi.org/10.1111/j.1524-4725.2004.30060.x.

(201) Krutmann, J. Ultraviolet A Radiation-Induced Biological Effects in Human Skin: Relevance for Photoaging and Photodermatosis. *Journal of Dermatological Science* **2000**, *23*, S22–S26. https://doi.org/10.1016/S0923-1811(99)00077-8.

(202) Bernerd, F.; Asselineau, D. Successive Alteration and Recovery of Epidermal Differentiation and Morphogenesis after Specific UVB-Damages in Skin Reconstructedin Vitro. *Developmental Biology* **1997**, *183* (2), 123–138. https://doi.org/10.1006/dbio.1996.8465.

(203) Kim, E. J.; Kim, Y. K.; Kim, M.-K.; Kim, S.; Kim, J. Y.; Lee, D. H.; Chung, J. H. UV-Induced Inhibition of Adipokine Production in Subcutaneous Fat Aggravates Dermal Matrix Degradation in Human Skin. *Scientific Reports* **2016**, *6* (1), 25616. https://doi.org/10.1038/srep25616.

(204) Quan, T.; He, T.; Kang, S.; Voorhees, J. J.; Fisher, G. J. Solar Ultraviolet Irradiation Reduces Collagen in Photoaged Human Skin by Blocking Transforming Growth Factor-β Type II Receptor/Smad Signaling. *The American Journal of Pathology* **2004**, *165* (3), 741–751. https://doi.org/10.1016/S0002-9440(10)63337-8.

(205) Kim, W.-S.; Park, B.-S.; Sung, J.-H. Protective Role of Adipose-Derived Stem Cells and Their Soluble Factors in Photoaging. *Archives of Dermatological Research* **2009**, *301* (5), 329–336. https://doi.org/10.1007/s00403-009-0951-9.

(206) Watson, R. E. B.; Griffiths, C. E. M.; Craven, N. M.; Shuttleworth, C. A.; Kielty, C. M. Fibrillin-Rich Microfibrils Are Reduced in Photoaged Skin. Distribution at the Dermal–Epidermal Junction. *Journal of Investigative Dermatology* **1999**, *112* (5), 782–787. https://doi.org/10.1046/j.1523-1747.1999.00562.x.

(207) Bataillon, M.; Lelièvre, D.; Chapuis, A.; Thillou, F.; Autourde, J. B.; Durand, S.; Boyera, N.; Rigaudeau, A.-S.; Besné, I.; Pellevoisin, C. Characterization of a New Reconstructed Full Thickness Skin Model, T-Skin™, and Its Application for Investigations of Anti-Aging Compounds. *International Journal of Molecular Sciences* **2019**, *20* (9), 2240. https://doi.org/10.3390/ijms20092240.

(208) Charles-de-Sá, L.; Gontijo-de-Amorim, N.; Sbarbati, A.; Benati, D.; Bernardi, P.; Borojevic, R.; Carias, R. B. V.; Rigotti, G. Photoaging Skin Therapy with PRP and ADSC: A Comparative Study. *Stem Cells International* **2020**, *2020*, 2032359. https://doi.org/10.1155/2020/2032359.

(209) Taherzadeh, O.; Otto, W. R.; Anand, U.; Nanchahal, J.; Anand, P. Influence of Human Skin Injury on Regeneration of Sensory Neurons. *Cell and Tissue Research* **2003**, *312* (3), 275–280. https://doi.org/10.1007/s00441-003-0724-2.

(210) Braziulis, E.; Diezi, M.; Biedermann, T.; Pontiggia, L.; Schmucki, M.; Hartmann-Fritsch, F.; Luginbühl, J.; Schiestl, C.; Meuli, M.; Reichmann, E. Modified Plastic Compression of Collagen Hydrogels Provides an Ideal Matrix for Clinically Applicable Skin Substitutes. *Tissue Engineering Part C: Methods* **2011**, *18* (6), 464–474. https://doi.org/10.1089/ten.tec.2011.0561.

(211) Fernandez, T. L.; Van Lonkhuyzen, D. R.; Dawson, R. A.; Kimlin, M. G.; Upton, Z. Characterization of a Human Skin Equivalent Model to Study the Effects of Ultraviolet B Radiation on Keratinocytes. *Tissue Engineering Part C: Methods* **2013**, *20* (7), 588–598. https://doi.org/10.1089/ten.tec.2013.0293.

(212) Fleischmajer, R.; Utani, A.; MacDonald, E. D.; Perlish, J. S.; Pan, T. C.; Chu, M. L.; Nomizu, M.; Ninomiya, Y.; Yamada, Y. Initiation of Skin Basement Membrane Formation at the Epidermo-Dermal Interface Involves Assembly of Laminins through Binding to Cell Membrane Receptors. *J. Cell Sci.* **1998**, *111* (14), 1929.

(213) Bacqueville, D.; Mavon, A. Comparative Analysis of Solar Radiation-Induced Cellular Damage between Ex Vivo Porcine Skin Organ Culture and in Vitro Reconstructed Human Epidermis. *International Journal of Cosmetic Science* **2009**, *31* (4), 293–302. https://doi.org/10.1111/j.1468-2494.2009.00506.x.

(214) Gangatirkar, P.; Paquet-Fifield, S.; Li, A.; Rossi, R.; Kaur, P. Establishment of 3D Organotypic Cultures Using Human Neonatal Epidermal Cells. *Nature Protocols* **2007**, *2*, 178.

(215) Chan, R. K.; Zamora, D. O.; Wrice, N. L.; Baer, D. G.; Renz, E. M.; Christy, R. J.; Natesan, S. Development of a Vascularized Skin Construct Using Adipose-Derived Stem Cells from Debrided Burned Skin. *Stem Cells International* **2012**, *2012*, 841203. https://doi.org/10.1155/2012/841203.

(216) Bellas, E.; Seiberg, M.; Garlick, J.; Kaplan, D. L. In Vitro 3D Full-Thickness Skin-Equivalent Tissue Model Using Silk and Collagen Biomaterials. *Macromolecular Bioscience* **2012**, *12* (12), 1627–1636. https://doi.org/10.1002/mabi.201200262.

(217) Kober, J.; Gugerell, A.; Schmid, M.; Kamolz, L.-P.; Keck, M. Generation of a Fibrin Based Three-Layered Skin Substitute. *BioMed Research International* **2015**, *2015*, 170427. https://doi.org/10.1155/2015/170427.

(218) Kon, A.; Takeda, H.; Ito, N.; Hanada, K.; Takagaki, K. Tissue-Specific Downregulation of Type VII Collagen Gene (COL7A1) Transcription in Cultured Epidermal Keratinocytes by Ultraviolet A Radiation (UVA) and UVA-Inducible Cytokines, with Special Reference to Cutaneous Photoaging. *Journal of Dermatological Science Supplement* **2005**, *1* (2), S29–S35. https://doi.org/10.1016/j.descs.2005.06.004.

(219) Qin, H.; Zhang, G.; Zhang, L. GSK126 (EZH2 Inhibitor) Interferes with Ultraviolet A Radiation-induced Photoaging of Human Skin Fibroblast Cells. *Exp Ther Med* **2018**, *15* (4), 3439–3448. https://doi.org/10.3892/etm.2018.5863.

(220) Ades, E. W.; Candal, F. J.; Swerlick, R. A.; George, V. G.; Summers, S.; Bosse, D. C.; Lawley, T. J. HMEC-1: Establishment of an Immortalized Human Microvascular Endothelial Cell Line. *Journal of Investigative Dermatology* **1992**, *99* (6), 683–690.

(221) Wolbank, S.; Stadler, G.; Peterbauer, A.; Gillich, A.; Karbiener, M.; Streubel, B.; Wieser, M.; Katinger, H.; van Griensven, M.; Redl, H.; Gabriel, C.; Grillari, J.; Grillari-Voglauer, R. Telomerase Immortalized Human Amnion- and Adipose-Derived Mesenchymal Stem Cells: Maintenance of Differentiation and Immunomodulatory Characteristics. *Tissue Engineering Part A* **2009**, *15* (7), 1843–1854. https://doi.org/10.1089/ten.tea.2008.0205.

(222) Morgan, J. T.; Wood, J. A.; Walker, N. J.; Raghunathan, V. K.; Borjesson, D. L.; Murphy, C. J.; Russell, P. Human Trabecular Meshwork Cells Exhibit Several Characteristics of, but Are Distinct from, Adipose-Derived Mesenchymal Stem Cells. *Journal of Ocular Pharmacology and Therapeutics* **2014**, *30* (2–3), 254–266. https://doi.org/10.1089/jop.2013.0175.

(223) Yu, G.; Floyd, Z. E.; Wu, X.; Hebert, T.; Halvorsen, Y.-D. C.; Buehrer, B. M.; Gimble, J. M. Adipogenic Differentiation of Adipose-Derived Stem Cells. In *Adipose-Derived Stem Cells: Methods and Protocols*; Gimble, J. M., Bunnell, B. A., Eds.; Humana Press: Totowa, NJ, 2011; pp 193–200. https://doi.org/10.1007/978-1-61737-960-4_14.

(224) Kovesi, P. Phase Preserving Denoising of Images. In *signal*; Perth, WA, 1999; Vol. 4, pp 212–217.

(225) Kovesi, P. Phase Preserving Tone Mapping of Non-Photographic High Dynamic Range Images. In *Digital Image Computing: Techniques and Applications DICTA 2012*; 2012.

(226) Jerman, T. *Jerman Enhancement Filter*; 2021.

(227) Tim Jerman; Franjo Pernuš; Boštjan Likar; Žiga Špiclin. Beyond Frangi: An Improved Multiscale Vesselness Filter; 2015; Vol. 9413.

(228) Kim, E. J.; Kim, Y. K.; Kim, J. E.; Kim, S.; Kim, M.-K.; Park, C.-H.; Chung, J. H. UV Modulation of Subcutaneous Fat Metabolism. *Journal of Investigative Dermatology* **2011**, *131* (8), 1720–1726. https://doi.org/10.1038/jid.2011.106.

(229) Chung, J. H.; Yano, K.; Lee, M. K.; Youn, C. S.; Seo, J. Y.; Kim, K. H.; Cho, K. H.; Eun, H. C.; Detmar, M. Differential Effects of Photoaging vs Intrinsic Aging on the Vascularization of Human Skin. *Archives of Dermatology* **2002**, *138* (11), 1437–1442. https://doi.org/10.1001/archderm.138.11.1437.

(230) Rittié, L.; Fisher, G. J. Natural and Sun-Induced Aging of Human Skin. *Cold Spring Harb Perspect Med* **2015**, *5* (1), a015370. https://doi.org/10.1101/cshperspect.a015370.

(231) ASCHER, B.; COLEMAN, S.; ALSTER, T.; BAUER, U.; BURGESS, C.; BUTTERWICK, K.; DONOFRIO, L.; ENGELHARD, P.; GOLDMAN, M. P.; KATZ, P.; VLEGGAAR, D. Full Scope of Effect of Facial Lipoatrophy: A Framework of Disease Understanding. *Dermatologic Surgery* **2006**, *32* (8), 1058–1069. https://doi.org/10.1111/j.1524-4725.2006.32230.x.

(232) Saely, C. H.; Geiger, K.; Drexel, H. Brown versus White Adipose Tissue: A Mini-Review. *Gerontology* **2012**, *58* (1), 15–23. https://doi.org/10.1159/000321319.

(233) Fiorenza, C. G.; Chou, S. H.; Mantzoros, C. S. Lipodystrophy: Pathophysiology and Advances in Treatment. *Nature Reviews Endocrinology* **2011**, *7* (3), 137–150. https://doi.org/10.1038/nrendo.2010.199.

(234) Reitman, M. L.; Arioglu, E.; Gavrilova, O.; Taylor, S. I. Lipoatrophy Revisited. *Trends in Endocrinology & Metabolism* **2000**, *11* (10), 410–416. https://doi.org/10.1016/S1043-2760(00)00309-X.

(235) Hammel, J. H.; Bellas, E. Endothelial Cell Crosstalk Improves Browning but Hinders White Adipocyte Maturation in 3D Engineered Adipose Tissue. *Integrative Biology* **2020**, *12* (4), 81–89. https://doi.org/10.1093/intbio/zyaa006.

(236) Kang, J. H.; Gimble, J. M.; Kaplan, D. L. In Vitro 3D Model for Human Vascularized Adipose Tissue. *Tissue Engineering Part A* **2009**, *15* (8), 2227–2236. https://doi.org/10.1089/ten.tea.2008.0469.

(237) Mauney, J. R.; Nguyen, T.; Gillen, K.; Kirker-Head, C.; Gimble, J. M.; Kaplan, D. L. Engineering Adipose-like Tissue in Vitro and in Vivo Utilizing Human Bone Marrow and Adipose-Derived Mesenchymal Stem Cells with Silk Fibroin 3D Scaffolds. *Biomaterials* **2007**, *28* (35), 5280–5290. https://doi.org/10.1016/j.biomaterials.2007.08.017.

(238) Trottier, V.; Marceau-Fortier, G.; Germain, L.; Vincent, C.; Fradette, J. IFATS Collection: Using Human Adipose-Derived Stem/Stromal Cells for the Production of New Skin Substitutes. *STEM CELLS* **2008**, *26* (10), 2713–2723. https://doi.org/10.1634/stemcells.2008-0031.

(239) Battie, C.; Jitsukawa, S.; Bernerd, F.; Del Bino, S.; Marionnet, C.; Verschoore, M. New Insights in Photoaging, UVA Induced Damage and Skin Types. *Experimental Dermatology* **2014**, *23* (s1), 7–12. https://doi.org/10.1111/exd.12388.

(240) Agar, N. S.; Halliday, G. M.; Barnetson, R. StC.; Ananthaswamy, H. N.; Wheeler, M.; Jones, A. M. The Basal Layer in Human Squamous Tumors Harbors More UVA than UVB Fingerprint Mutations: A Role for UVA in Human Skin Carcinogenesis. *Proc Natl Acad Sci U S A* **2004**, *101* (14), 4954. https://doi.org/10.1073/pnas.0401141101.

(241) Mertsching, H.; Walles, T.; Hofmann, M.; Schanz, J.; Knapp, W. H. Engineering of a Vascularized Scaffold for Artificial Tissue and Organ Generation. *Biomaterials* **2005**, *26* (33), 6610–6617. https://doi.org/10.1016/j.biomaterials.2005.04.048.

(242) Cao, Y.; Wang, H.; Wang, Q.; Han, X.; Zeng, W. Three-Dimensional Volume Fluorescence-Imaging of Vascular Plasticity in Adipose Tissues. *Molecular Metabolism* **2018**, *14*, 71–81. https://doi.org/10.1016/j.molmet.2018.06.004.

(243) Huber, B.; Volz, A.-C.; Kluger, P. J. Understanding the Effects of Mature Adipocytes and Endothelial Cells on Fatty Acid Metabolism and Vascular Tone in Physiological Fatty Tissue for Vascularized Adipose Tissue Engineering. *Cell and Tissue Research* **2015**, *362* (2), 269–279. https://doi.org/10.1007/s00441-015-2274-9.

(244) Kligman, A. M. Perspectives and Problems in Cutaneous Gerontology. *Journal of Investigative Dermatology* **1979**, *73* (1), 39–46. https://doi.org/10.1111/1523-1747.ep12532758.

(245) Lovett, M.; Lee, K.; Edwards, A.; Kaplan, D. L. Vascularization Strategies for Tissue Engineering. *Tissue Engineering Part B: Reviews* **2009**, *15* (3), 353–370. https://doi.org/10.1089/ten.teb.2009.0085.

(246) Kim, M.-S.; Kim, Y. K.; Eun, H. C.; Cho, K. H.; Chung, J. H. All-Trans Retinoic Acid Antagonizes UV-Induced VEGF Production and Angiogenesis via the Inhibition of ERK Activation in Human Skin Keratinocytes. *Journal of Investigative Dermatology* **2006**, *126* (12), 2697–2706. https://doi.org/10.1038/sj.jid.5700463.

(247) Imanishi, N.; Kishi, K.; Chang, H.; Nakajima, H.; Aiso, S. Three-Dimensional Venous Anatomy of the Dermis Observed Using Stereography. *Journal of Anatomy* **2008**, *212* (5), 669–673. https://doi.org/10.1111/j.1469-7580.2008.00890.x.

(248) Braverman, I. M.; Yen, A. ULTRASTRUCTURE OF THE CAPILLARY LOOPS IN THE DERMAL PAPILLAE OF PSORIASIS. *Journal of Investigative Dermatology* **1977**, *68* (1), 53–60. https://doi.org/10.1111/1523-1747.ep12485169.

(249) Arai, Y.; Takayama, M.; Abe, Y.; Hirose, N. Adipokines and Aging. *Journal of Atherosclerosis and Thrombosis* **2011**, *advpub*, 1105060376–1105060376. https://doi.org/10.5551/jat.7039.

(250) Kadowaki, T.; Yamauchi, T. Adiponectin and Adiponectin Receptors. *Endocrine Reviews* **2005**, *26* (3), 439–451. https://doi.org/10.1210/er.2005-0005.

(251) Schneider, L. A.; Raizner, K.; Wlaschek, M.; Brenneisen, P.; Gethöffer, K.; Scharffetter-Kochanek, K. UVA-1 Exposure in Vivo Leads to an IL-6 Surge within the Skin.

Experimental Dermatology **2017**, *26* (9), 830–832. https://doi.org/10.1111/exd.13286.

(252) Wlaschek, M.; Bolsen, K.; Herrmann, G.; Schwarz, A.; Wilmroth, F.; Heinrich, P. C.; Goerz, G.; Scharffetter-Kochanek, K. UVA-Induced Autocrine Stimulation of Fibroblast-Derived-Collagenase by IL-6: A Possible Mechanism in Dermal Photodamage? *Journal of Investigative Dermatology* **1993**, *101* (2), 164–168. https://doi.org/10.1111/1523-1747.ep12363644.

(253) Vielhaber, G.; Grether-Beck, S.; Koch, O.; Johncock, W.; Krutmann, J. Sunscreens with an Absorption Maximum of ≥360 Nm Provide Optimal Protection against UVA1-Induced Expression of Matrix Metalloproteinase-1, Interleukin-1, and Interleukin-6 in Human Dermal Fibroblasts. *Photochemical & Photobiological Sciences* **2006**, *5* (3), 275–282. https://doi.org/10.1039/B516702G.

(254) Grinnell, F.; Lamke, C. R. Reorganization of Hydrated Collagen Lattices by Human Skin Fibroblasts. *Journal of Cell Science* **1984**, *66* (1), 51–63. https://doi.org/10.1242/jcs.66.1.51.

(255) Zghoul, N.; Fuchs, R.; Lehr, C.-M.; Schaefer, U. F. Reconstructed Skin Equivalents for Assessing Percutaneous Drug Absorption from Pharmaceutical Formulations. *ALTEX-Alternatives to animal experimentation* **2001**, *18* (2), 103–106.

(256) Xie, Y.; Rizzi, S. C.; Dawson, R.; Lynam, E.; Richards, S.; Leavesley, D. I.; Upton, Z. Development of a Three-Dimensional Human Skin Equivalent Wound Model for Investigating Novel Wound Healing Therapies. *Tissue Engineering Part C: Methods* **2010**, *16* (5), 1111–1123.

(257) Rappazzo, K. M.; Coffman, E.; Hines, E. P. Exposure to Perfluorinated Alkyl Substances and Health Outcomes in Children: A Systematic Review of the Epidemiologic Literature. *International Journal of Environmental Research and Public Health* **2017**, *14* (7), 691. https://doi.org/10.3390/ijerph14070691.

(258) Egeghy, P. P.; Lorber, M. An Assessment of the Exposure of Americans to Perfluorooctane Sulfonate: A Comparison of Estimated Intake with Values Inferred from NHANES Data. *Journal of Exposure Science & Environmental Epidemiology* **2011**, *21* (2), 150–168. https://doi.org/10.1038/jes.2009.73.

(259) Nouhi, S.; Ahrens, L.; Campos Pereira, H.; Hughes, A. V.; Campana, M.; Gutfreund, P.; Palsson, G. K.; Vorobiev, A.; Hellsing, M. S. Interactions of Perfluoroalkyl Substances with a Phospholipid Bilayer Studied by Neutron Reflectometry. *Journal of Colloid and Interface Science* **2018**, *511*, 474–481. https://doi.org/10.1016/j.jcis.2017.09.102.

(260) Fitzgerald, N. J. M.; Wargenau, A.; Sorenson, C.; Pedersen, J.; Tufenkji, N.; Novak, P. J.; Simcik, M. F. Partitioning and Accumulation of Perfluoroalkyl Substances in Model Lipid Bilayers and Bacteria. *Environ. Sci. Technol.* **2018**, *52* (18), 10433–10440. https://doi.org/10.1021/acs.est.8b02912.

(261) Sanchez Garcia, D.; Sjödin, M.; Hellstrandh, M.; Norinder, U.; Nikiforova, V.; Lindberg, J.; Wincent, E.; Bergman, Å.; Cotgreave, I.; Munic Kos, V. Cellular Accumulation and Lipid Binding of Perfluorinated Alkylated Substances (PFASs) – A Comparison with Lysosomotropic Drugs. *Chemico-Biological Interactions* **2018**, *281*, 1–10. https://doi.org/10.1016/j.cbi.2017.12.021.

(262) Kato, K.; Wong, L.-Y.; Jia, L. T.; Kuklenyik, Z.; Calafat, A. M. Trends in Exposure to Polyfluoroalkyl Chemicals in the U.S. Population: 1999–2008. *Environ. Sci. Technol.* **2011**, *45* (19), 8037–8045. https://doi.org/10.1021/es1043613.

(263) Franko, J.; Meade, B. J.; Frasch, H. F.; Barbero, A. M.; Anderson, S. E. Dermal Penetration Potential of Perfluorooctanoic Acid (PFOA) in Human and Mouse Skin. *null* **2012**, *75* (1), 50–62. https://doi.org/10.1080/15287394.2011.615108.

(264) Han, J.-S.; Jang, S.; Son, H.-Y.; Kim, Y.-B.; Kim, Y.; Noh, J.-H.; Kim, M.-J.; Lee, B.-S. Subacute Dermal Toxicity of Perfluoroalkyl Carboxylic Acids: Comparison with Different Carbon-Chain Lengths in Human Skin Equivalents and Systemic Effects of Perfluoroheptanoic Acid in Sprague Dawley Rats. *Archives of Toxicology* **2020**, *94* (2), 523–539. https://doi.org/10.1007/s00204-019-02634-z.

(265) Fasano, W. J.; Kennedy, G. L.; Szostek, B.; Farrar, D. G.; Ward, R. J.; Haroun, L.; Hinderliter, P. M. Penetration of Ammonium Perfluorooctanoate Through Rat and Human Skin In Vitro. *null* **2005**, *28* (1), 79–90. https://doi.org/10.1081/DCT-39707.

(266) Jensen, A. A.; Leffers, H. Emerging Endocrine Disrupters: Perfluoroalkylated Substances. *International Journal of Andrology* **2008**, *31* (2), 161–169. https://doi.org/10.1111/j.1365-2605.2008.00870.x.

(267) Lin, P.-I. D.; Cardenas, A.; Hauser, R.; Gold, D. R.; Kleinman, K. P.; Hivert, M.-F.; Fleisch, A. F.; Calafat, A. M.; Webster, T. F.; Horton, E. S.; Oken, E. Per- and Polyfluoroalkyl Substances and Blood Lipid Levels in Pre-Diabetic Adults—Longitudinal Analysis of the Diabetes Prevention Program Outcomes Study. *Environment International* **2019**, *129*, 343–353. https://doi.org/10.1016/j.envint.2019.05.027.

(268) Sakr, C. J.; Kreckmann, K. H.; Green, J. W.; Gillies, P. J.; Reynolds, J. L.; Leonard, R. C. Cross-Sectional Study of Lipids and Liver Enzymes Related to a Serum Biomarker of Exposure (Ammonium Perfluorooctanoate or APFO) as Part of a General Health Survey in a Cohort of Occupationally Exposed Workers. *Journal of Occupational and Environmental Medicine* **2007**, *49* (10).

(269) Hu, W.; Jones, P. D.; Upham, B. L.; Trosko, J. E.; Lau, C.; Giesy, J. P. Inhibition of Gap Junctional Intercellular Communication by Perfluorinated Compounds in Rat Liver and Dolphin Kidney Epithelial Cell Lines in Vitro and Sprague-Dawley Rats in Vivo. *Toxicological Sciences* **2002**, *68* (2), 429–436. https://doi.org/10.1093/toxsci/68.2.429.

(270) Liu, Q. S.; Hao, F.; Sun, Z.; Long, Y.; Zhou, Q.; Jiang, G. Perfluorohexadecanoic Acid Increases Paracellular Permeability in Endothelial Cells through the Activation of Plasma Kallikrein-Kinin System. *Chemosphere* **2018**, *190*, 191–200. https://doi.org/10.1016/j.chemosphere.2017.10.002.

(271) Gao, Y.; Chen, H.; Xiao, X.; Lui, W.; Lee, W. M.; Mruk, D. D.; Cheng, C. Y. Perfluorooctanesulfonate (PFOS)-Induced Sertoli Cell Injury through a Disruption of F-Actin and Microtubule Organization Is Mediated by Akt1/2. *Scientific Reports* **2017**, *7* (1), 1110. https://doi.org/10.1038/s41598-017-01016-8.

(272) Wang, X.; Li, B.; Zhao, W.-D.; Liu, Y.-J.; Shang, D.-S.; Fang, W.-G.; Chen, Y.-H. Perfluorooctane Sulfonate Triggers Tight Junction "Opening" in Brain Endothelial Cells via Phosphatidylinositol 3-Kinase. *Biochemical and Biophysical Research Communications* **2011**, *410* (2), 258–263. https://doi.org/10.1016/j.bbrc.2011.05.128.

(273) Qian, Y.; Ducatman, A.; Ward, R.; Leonard, S.; Bukowski, V.; Lan Guo, N.; Shi, X.; Vallyathan, V.; Castranova, V. Perfluorooctane Sulfonate (PFOS) Induces Reactive Oxygen Species (ROS) Production in Human Microvascular Endothelial Cells: Role in Endothelial Permeability. *null* **2010**, *73* (12), 819–836. https://doi.org/10.1080/15287391003689317.

(274) Tsai, M.-S.; Lin, C.-Y.; Lin, C.-C.; Chen, M.-H.; Hsu, S. H. J.; Chien, K.-L.; Sung, F.-C.; Chen, P.-C.; Su, T.-C. Association between Perfluoroalkyl Substances and Reproductive Hormones in Adolescents and Young Adults. *International Journal of Hygiene and Environmental Health* **2015**, *218* (5), 437–443. https://doi.org/10.1016/j.ijheh.2015.03.008.

(275) Blake, B. E.; Pinney, S. M.; Hines, E. P.; Fenton, S. E.; Ferguson, K. K. Associations between Longitudinal Serum Perfluoroalkyl Substance (PFAS) Levels and Measures of Thyroid Hormone, Kidney Function, and Body Mass Index in the Fernald Community Cohort. *Environmental Pollution* **2018**, *242*, 894–904. https://doi.org/10.1016/j.envpol.2018.07.042.

(276) Domazet, S. L.; Grøntved, A.; Timmermann, A. G.; Nielsen, F.; Jensen, T. K. Longitudinal Associations of Exposure to Perfluoroalkylated Substances in Childhood and Adolescence and Indicators of Adiposity and Glucose Metabolism 6 and 12 Years Later: The European Youth Heart Study. *Diabetes Care* **2016**, *39* (10), 1745. https://doi.org/10.2337/dc16-0269.

(277) Karlsen, M.; Grandjean, P.; Weihe, P.; Steuerwald, U.; Oulhote, Y.; Valvi, D. Early-Life Exposures to Persistent Organic Pollutants in Relation to Overweight in Preschool Children. *Reproductive Toxicology* **2017**, *68*, 145–153. https://doi.org/10.1016/j.reprotox.2016.08.002.

(278) Cerf, M. E. Beta Cell Dysfunction and Insulin Resistance. *Front Endocrinol (Lausanne)* **2013**, *4*, 37–37. https://doi.org/10.3389/fendo.2013.00037.

(279) Fei Chunyuan; McLaughlin Joseph K.; Tarone Robert E.; Olsen Jørn. Perfluorinated Chemicals and Fetal Growth: A Study within the Danish National Birth Cohort. *Environmental Health Perspectives* **2007**, *115* (11), 1677–1682. https://doi.org/10.1289/ehp.10506.

(280) Bach, C. C.; Bech, B. H.; Brix, N.; Nohr, E. A.; Bonde, J. P. E.; Henriksen, T. B. Perfluoroalkyl and Polyfluoroalkyl Substances and Human Fetal Growth: A Systematic Review. *Critical Reviews in Toxicology* **2015**, *45* (1), 53–67. https://doi.org/10.3109/10408444.2014.952400.

(281) Gao, K.; Zhuang, T.; Liu, X.; Fu, J.; Zhang, J.; Fu, J.; Wang, L.; Zhang, A.; Liang, Y.; Song, M.; Jiang, G. Prenatal Exposure to Per- and Polyfluoroalkyl Substances (PFASs) and Association between the Placental Transfer Efficiencies and Dissociation Constant of Serum Proteins–PFAS Complexes. *Environ. Sci. Technol.* **2019**, *53* (11), 6529–6538. https://doi.org/10.1021/acs.est.9b00715.

(282) Mamsen, L. S.; Björvang, R. D.; Mucs, D.; Vinnars, M.-T.; Papadogiannakis, N.; Lindh, C. H.; Andersen, C. Y.; Damdimopoulou, P. Concentrations of Perfluoroalkyl Substances (PFASs) in Human Embryonic and Fetal Organs from First, Second, and Third Trimester Pregnancies. *Environment International* **2019**, *124*, 482–492. https://doi.org/10.1016/j.envint.2019.01.010.

(283) Starling Anne P.; Adgate John L.; Hamman Richard F.; Kechris Katerina; Calafat Antonia M.; Ye Xiaoyun; Dabelea Dana. Perfluoroalkyl Substances during Pregnancy and Offspring Weight and Adiposity at Birth: Examining Mediation by Maternal Fasting Glucose in the Healthy Start Study. *Environmental Health Perspectives* **2017**, *125* (6). https://doi.org/10.1289/EHP641.

(284) Starling, A. P.; Adgate, J. L.; Hamman, R. F.; Kechris, K.; Calafat, A. M.; Dabelea, D. Prenatal Exposure to Per- and Polyfluoroalkyl Substances and Infant Growth and Adiposity: The Healthy Start Study. *Environment International* **2019**, *131*, 104983. https://doi.org/10.1016/j.envint.2019.104983.

(285) Hartman, T. J.; Calafat, A. M.; Holmes, A. K.; Marcus, M.; Northstone, K.; Flanders, W. D.; Kato, K.; Taylor, E. V. Prenatal Exposure to Perfluoroalkyl Substances and Body Fatness in Girls. *Childhood Obesity* **2017**, *13* (3), 222–230. https://doi.org/10.1089/chi.2016.0126.

(286) Liu, P.; Yang, F.; Wang, Y.; Yuan, Z. Perfluorooctanoic Acid (PFOA) Exposure in Early Life Increases Risk of Childhood Adiposity: A Meta-Analysis of Prospective Cohort Studies. *International Journal of Environmental Research and Public Health* **2018**, *15* (10), 2070. https://doi.org/10.3390/ijerph15102070.

(287) Mora, A. M.; Fleisch, A. F.; Rifas-Shiman, S. L.; Woo Baidal, J. A.; Pardo, L.; Webster, T. F.; Calafat, A. M.; Ye, X.; Oken, E.; Sagiv, S. K. Early Life Exposure to Per- and Polyfluoroalkyl Substances and Mid-Childhood Lipid and Alanine Aminotransferase Levels. *Environment International* **2018**, *111*, 1–13. https://doi.org/10.1016/j.envint.2017.11.008.

(288) Bjerregaard-Olesen, C.; Ghisari, M.; Bonefeld-Jørgensen, E. C. Activation of the Estrogen Receptor by Human Serum Extracts Containing Mixtures of Perfluorinated Alkyl Acids from Pregnant Women. *Environmental Research* **2016**, *151*, 71–79. https://doi.org/10.1016/j.envres.2016.07.001.

(289) Lind, D. V.; Priskorn, L.; Lassen, T. H.; Nielsen, F.; Kyhl, H. B.; Kristensen, D. M.; Christesen, H. T.; Jørgensen, J. S.; Grandjean, P.; Jensen, T. K. Prenatal Exposure to Perfluoroalkyl Substances and Anogenital Distance at 3 Months of Age in a Danish Mother-Child Cohort. *Reproductive Toxicology* **2017**, *68*, 200–206. https://doi.org/10.1016/j.reprotox.2016.08.019.

(290) Kirkley, A. G.; Sargis, R. M. Environmental Endocrine Disruption of Energy Metabolism and Cardiovascular Risk. *Curr Diab Rep* **2014**, *14* (6), 494–494. https://doi.org/10.1007/s11892-014-0494-0.

(291) Chang, S.-C.; Thibodeaux, J. R.; Eastvold, M. L.; Ehresman, D. J.; Bjork, J. A.; Froehlich, J. W.; Lau, C.; Singh, R. J.; Wallace, K. B.; Butenhoff, J. L. Thyroid Hormone Status and Pituitary Function in Adult Rats given Oral Doses of Perfluorooctanesulfonate (PFOS). *Toxicology* **2008**, *243* (3), 330–339. https://doi.org/10.1016/j.tox.2007.10.014.

(292) Yu, W.-G.; Liu, W.; Jin, Y.-H. Effects of Perfluorooctane Sulfonate on Rat Thyroid Hormone Biosynthesis and Metabolism. *Environmental Toxicology and Chemistry* **2009**, *28* (5), 990–996. https://doi.org/10.1897/08-345.1.

(293) Lau, C.; Anitole, K.; Hodes, C.; Lai, D.; Pfahles-Hutchens, A.; Seed, J. Perfluoroalkyl Acids: A Review of Monitoring and Toxicological Findings. *Toxicological Sciences* **2007**, *99* (2), 366–394. https://doi.org/10.1093/toxsci/kfm128.

(294) Rosen, M. B.; Lee, J. S.; Ren, H.; Vallanat, B.; Liu, J.; Waalkes, M. P.; Abbott, B. D.; Lau, C.; Corton, J. C. Toxicogenomic Dissection of the Perfluorooctanoic Acid Transcript Profile in Mouse Liver: Evidence for the Involvement of Nuclear Receptors PPARα and CAR. *Toxicological Sciences* **2008**, *103* (1), 46–56. https://doi.org/10.1093/toxsci/kfn025.

(295) Vanden Heuvel, J. P.; Thompson, J. T.; Frame, S. R.; Gillies, P. J. Differential Activation of Nuclear Receptors by Perfluorinated Fatty Acid Analogs and Natural Fatty Acids: A Comparison of Human, Mouse, and Rat Peroxisome Proliferator-Activated Receptor-α, -β, and -γ, Liver X Receptor-β, and Retinoid X Receptor-α. *Toxicological Sciences* **2006**, *92* (2), 476–489. https://doi.org/10.1093/toxsci/kfl014.

(296) Taxvig, C.; Dreisig, K.; Boberg, J.; Nellemann, C.; Schelde, A. B.; Pedersen, D.; Boergesen, M.; Mandrup, S.; Vinggaard, A. M. Differential Effects of Environmental Chemicals and Food Contaminants on Adipogenesis, Biomarker Release and PPARγ Activation. *Molecular and Cellular Endocrinology* **2012**, *361* (1), 106–115. https://doi.org/10.1016/j.mce.2012.03.021.

(297) Li, A. C.; Glass, C. K. PPAR- and LXR-Dependent Pathways Controlling Lipid Metabolism and the Development of Atherosclerosis. *Journal of Lipid Research* **2004**, *45* (12), 2161–2173. https://doi.org/10.1194/jlr.R400010-JLR200.

(298) Djiane, J.; Attig, L. Role of Leptin during Perinatal Metabolic Programming and Obesity. *J Physiol Pharmacol* **2008**, *59* (Suppl 1), 55–63.

(299) Vickers, M. H. Developmental Programming and Adult Obesity: The Role of Leptin. *Current Opinion in Endocrinology, Diabetes and Obesity* **2007**, *14* (1).

(300) Lam Juleen; Koustas Erica; Sutton Patrice; Johnson Paula I.; Atchley Dylan S.; Sen Saunak; Robinson Karen A.; Axelrad Daniel A.; Woodruff Tracey J. The Navigation Guide—Evidence-Based Medicine Meets Environmental Health: Integration of Animal and Human Evidence for PFOA Effects on Fetal Growth. *Environmental Health Perspectives* **2014**, *122* (10), 1040–1051. https://doi.org/10.1289/ehp.1307923.

(301) Hill, C. E.; Myers, J. P.; Vandenberg, L. N. Nonmonotonic Dose-Response Curves Occur in Dose Ranges That Are Relevant to Regulatory Decision-Making. *Dose Response* **2018**, *16* (3), 1559325818798282–1559325818798282. https://doi.org/10.1177/1559325818798282.

(302) Vandenberg, L. N.; Colborn, T.; Hayes, T. B.; Heindel, J. J.; Jacobs, D. R., Jr.; Lee, D.-H.; Shioda, T.; Soto, A. M.; vom Saal, F. S.; Welshons, W. V.; Zoeller, R. T.; Myers, J. P. Hormones and Endocrine-Disrupting Chemicals: Low-Dose Effects and Nonmonotonic Dose Responses. *Endocrine Reviews* **2012**, *33* (3), 378–455. https://doi.org/10.1210/er.2011-1050.

(303) Butenhoff, J. L.; Kennedy, G. L.; Frame, S. R.; O'Connor, J. C.; York, R. G. The Reproductive Toxicology of Ammonium Perfluorooctanoate (APFO) in the Rat. *Toxicology* **2004**, *196* (1), 95–116. https://doi.org/10.1016/j.tox.2003.11.005.

(304) Pizzurro, D. M.; Seeley, M.; Kerper, L. E.; Beck, B. D. Interspecies Differences in Perfluoroalkyl Substances (PFAS) Toxicokinetics and Application to Health-Based Criteria. *Regulatory Toxicology and Pharmacology* **2019**, *106*, 239–250. https://doi.org/10.1016/j.yrtph.2019.05.008.

(305) Château-Degat, M.-L.; Pereg, D.; Dallaire, R.; Ayotte, P.; Dery, S.; Dewailly, É. Effects of Perfluorooctanesulfonate Exposure on Plasma Lipid Levels in the Inuit Population of Nunavik (Northern Quebec). *Environmental Research* **2010**, *110* (7), 710–717. https://doi.org/10.1016/j.envres.2010.07.003.

(306) Costa, G.; Sartori, S.; Consonni, D. Thirty Years of Medical Surveillance in Perfluorooctanoic Acid Production Workers. *Journal of Occupational and Environmental Medicine* **2009**, *51* (3).

(307) Eriksen, K. T.; Raaschou-Nielsen, O.; McLaughlin, J. K.; Lipworth, L.; Tjønneland, A.; Overvad, K.; Sørensen, M. Association between Plasma PFOA and PFOS Levels and

Total Cholesterol in a Middle-Aged Danish Population. *PLOS ONE* **2013**, *8* (2), e56969. https://doi.org/10.1371/journal.pone.0056969.

(308) Fisher, M.; Arbuckle, T. E.; Wade, M.; Haines, D. A. Do Perfluoroalkyl Substances Affect Metabolic Function and Plasma Lipids?—Analysis of the 2007–2009, Canadian Health Measures Survey (CHMS) Cycle 1. *Environmental Research* **2013**, *121*, 95–103. https://doi.org/10.1016/j.envres.2012.11.006.

(309) Fitz-Simon, N.; Fletcher, T.; Luster, M. I.; Steenland, K.; Calafat, A. M.; Kato, K.; Armstrong, B. Reductions in Serum Lipids with a 4-Year Decline in Serum Perfluorooctanoic Acid and Perfluorooctanesulfonic Acid. *Epidemiology* **2013**, *24* (4).

(310) Kirk, M.; Smurthwaite, K.; Bräunig, J.; Trevenar, S.; D'Este, C.; Lucas, R.; Lal, A.; Korda, R.; Clements, A.; Mueller, J. The PFAS Health Study: Systematic Literature Review. *Canberra: The Australian National University* **2018**.

(311) Nelson Jessica W.; Hatch Elizabeth E.; Webster Thomas F. Exposure to Polyfluoroalkyl Chemicals and Cholesterol, Body Weight, and Insulin Resistance in the General U.S. Population. *Environmental Health Perspectives* **2010**, *118* (2), 197–202. https://doi.org/10.1289/ehp.0901165.

(312) Skuladottir, M.; Ramel, A.; Rytter, D.; Haug, L. S.; Sabaredzovic, A.; Bech, B. H.; Henriksen, T. B.; Olsen, S. F.; Halldorsson, T. I. Examining Confounding by Diet in the Association between Perfluoroalkyl Acids and Serum Cholesterol in Pregnancy. *Environmental Research* **2015**, *143*, 33–38. https://doi.org/10.1016/j.envres.2015.09.001.

(313) Starling, A. P.; Engel, S. M.; Whitworth, K. W.; Richardson, D. B.; Stuebe, A. M.; Daniels, J. L.; Haug, L. S.; Eggesbø, M.; Becher, G.; Sabaredzovic, A.; Thomsen, C.; Wilson, R. E.; Travlos, G. S.; Hoppin, J. A.; Baird, D. D.; Longnecker, M. P. Perfluoroalkyl Substances and Lipid Concentrations in Plasma during Pregnancy among Women in the Norwegian Mother and Child Cohort Study. *Environment International* **2014**, *62*, 104–112. https://doi.org/10.1016/j.envint.2013.10.004.

(314) Steenland, K.; Tinker, S.; Frisbee, S.; Ducatman, A.; Vaccarino, V. Association of Perfluorooctanoic Acid and Perfluorooctane Sulfonate With Serum Lipids Among Adults Living Near a Chemical Plant. *American Journal of Epidemiology* **2009**, *170* (10), 1268–1278. https://doi.org/10.1093/aje/kwp279.

(315) Olsen, G. W.; Zobel, L. R. Assessment of Lipid, Hepatic, and Thyroid Parameters with Serum Perfluorooctanoate (PFOA) Concentrations in Fluorochemical Production Workers. *International Archives of Occupational and Environmental Health* **2007**, *81* (2), 231–246. https://doi.org/10.1007/s00420-007-0213-0.

(316) Liu, H.-S.; Wen, L.-L.; Chu, P.-L.; Lin, C.-Y. Association among Total Serum Isomers of Perfluorinated Chemicals, Glucose Homeostasis, Lipid Profiles, Serum Protein and

Metabolic Syndrome in Adults: NHANES, 2013–2014. *Environmental Pollution* **2018**, *232*, 73–79. https://doi.org/10.1016/j.envpol.2017.09.019.

(317) Butenhoff, J. L.; Bjork, J. A.; Chang, S.-C.; Ehresman, D. J.; Parker, G. A.; Das, K.; Lau, C.; Lieder, P. H.; van Otterdijk, F. M.; Wallace, K. B. Toxicological Evaluation of Ammonium Perfluorobutyrate in Rats: Twenty-Eight-Day and Ninety-Day Oral Gavage Studies. *Reproductive Toxicology* **2012**, *33* (4), 513–530. https://doi.org/10.1016/j.reprotox.2011.08.004.

(318) Fu, V.; Plouffe, S. W.; Guan, K.-L. The Hippo Pathway in Organ Development, Homeostasis, and Regeneration. *Current Opinion in Cell Biology* **2017**, *49*, 99–107. https://doi.org/10.1016/j.ceb.2017.12.012.

(319) Varelas, X. The Hippo Pathway Effectors TAZ and YAP in Development, Homeostasis and Disease. *Development* **2014**, *141* (8), 1614. https://doi.org/10.1242/dev.102376.

(320) Boopathy, G. T. K.; Hong, W. Role of Hippo Pathway-YAP/TAZ Signaling in Angiogenesis. *Frontiers in Cell and Developmental Biology* **2019**, *7*, 49. https://doi.org/10.3389/fcell.2019.00049.

(321) Maugeri-Saccà, M.; De Maria, R. The Hippo Pathway in Normal Development and Cancer. *Pharmacology & Therapeutics* **2018**, *186*, 60–72. https://doi.org/10.1016/j.pharmthera.2017.12.011.

(322) Patel, S. H.; Camargo, F. D.; Yimlamai, D. Hippo Signaling in the Liver Regulates Organ Size, Cell Fate, and Carcinogenesis. *Gastroenterology* **2017**, *152* (3), 533–545. https://doi.org/10.1053/j.gastro.2016.10.047.

(323) Yu, F.-X.; Zhao, B.; Guan, K.-L. Hippo Pathway in Organ Size Control, Tissue Homeostasis, and Cancer. *Cell* **2015**, *163* (4), 811–828. https://doi.org/10.1016/j.cell.2015.10.044.

(324) Gao, T.; Zhou, D.; Yang, C.; Singh, T.; Penzo–Méndez, A.; Maddipati, R.; Tzatsos, A.; Bardeesy, N.; Avruch, J.; Stanger, B. Z. Hippo Signaling Regulates Differentiation and Maintenance in the Exocrine Pancreas. *Gastroenterology* **2013**, *144* (7), 1543-1553.e1. https://doi.org/10.1053/j.gastro.2013.02.037.

(325) Pan, F. C.; Wright, C. Pancreas Organogenesis: From Bud to Plexus to Gland. *Developmental Dynamics* **2011**, *240* (3), 530–565. https://doi.org/10.1002/dvdy.22584.

(326) Zhao, B.; Li, L.; Guan, K.-L. Hippo Signaling at a Glance. *J. Cell Sci.* **2010**, *123* (23), 4001. https://doi.org/10.1242/jcs.069070.

(327) Meng, Z.; Moroishi, T.; Guan, K.-L. Mechanisms of Hippo Pathway Regulation. *Genes Dev* **2016**, *30* (1), 1–17. https://doi.org/10.1101/gad.274027.115.

(328) Zhao, B.; Li, L.; Lei, Q.; Guan, K.-L. The Hippo–YAP Pathway in Organ Size Control and Tumorigenesis: An Updated Version. *Genes Dev.* **2010**, *24* (9), 862–874. https://doi.org/10.1101/gad.1909210.

(329) Piccolo, S.; Dupont, S.; Cordenonsi, M. The Biology of YAP/TAZ: Hippo Signaling and Beyond. *Physiological Reviews* **2014**, *94* (4), 1287–1312. https://doi.org/10.1152/physrev.00005.2014.

(330) Reginensi, A.; Scott, R. P.; Gregorieff, A.; Bagherie-Lachidan, M.; Chung, C.; Lim, D.-S.; Pawson, T.; Wrana, J.; McNeill, H. Yap- and Cdc42-Dependent Nephrogenesis and Morphogenesis during Mouse Kidney Development. *PLOS Genetics* **2013**, *9* (3), e1003380. https://doi.org/10.1371/journal.pgen.1003380.

(331) Pan, J.-X.; Xiong, L.; Zhao, K.; Zeng, P.; Wang, B.; Tang, F.-L.; Sun, D.; Guo, H.; Yang, X.; Cui, S.; Xia, W.-F.; Mei, L.; Xiong, W.-C. YAP Promotes Osteogenesis and Suppresses Adipogenic Differentiation by Regulating β-Catenin Signaling. *Bone Research* **2018**, *6* (1), 18. https://doi.org/10.1038/s41413-018-0018-7.

(332) Hong, A. W.; Meng, Z.; Guan, K.-L. The Hippo Pathway in Intestinal Regeneration and Disease. *Nature Reviews Gastroenterology & Hepatology* **2016**, *13* (6), 324–337. https://doi.org/10.1038/nrgastro.2016.59.

(333) Yi, J.; Lu, L.; Yanger, K.; Wang, W.; Sohn, B. H.; Stanger, B. Z.; Zhang, M.; Martin, J. F.; Ajani, J. A.; Chen, J.; Lee, J.-S.; Song, S.; Johnson, R. L. Large Tumor Suppressor Homologs 1 and 2 Regulate Mouse Liver Progenitor Cell Proliferation and Maturation through Antagonism of the Coactivators YAP and TAZ. *Hepatology* **2016**, *64* (5), 1757–1772. https://doi.org/10.1002/hep.28768.

(334) Nardone, G.; Oliver-De La Cruz, J.; Vrbsky, J.; Martini, C.; Pribyl, J.; Skládal, P.; Pešl, M.; Caluori, G.; Pagliari, S.; Martino, F.; Maceckova, Z.; Hajduch, M.; Sanz-Garcia, A.; Pugno, N. M.; Stokin, G. B.; Forte, G. YAP Regulates Cell Mechanics by Controlling Focal Adhesion Assembly. *Nature Communications* **2017**, *8* (1), 15321. https://doi.org/10.1038/ncomms15321.

(335) Pan, H.; Xie, Y.; Zhang, Z.; Li, K.; Hu, D.; Zheng, X.; Fan, Q.; Tang, T. YAP-Mediated Mechanotransduction Regulates Osteogenic and Adipogenic Differentiation of BMSCs on Hierarchical Structure. *Colloids and Surfaces B: Biointerfaces* **2017**, *152*, 344–353. https://doi.org/10.1016/j.colsurfb.2017.01.039.

(336) Oliver-De La Cruz, J.; Nardone, G.; Vrbsky, J.; Pompeiano, A.; Perestrelo, A. R.; Capradossi, F.; Melajová, K.; Filipensky, P.; Forte, G. Substrate Mechanics Controls Adipogenesis through YAP Phosphorylation by Dictating Cell Spreading. *Biomaterials* **2019**, *205*, 64–80. https://doi.org/10.1016/j.biomaterials.2019.03.009.

(337) Xiao, X.; Mruk, D. D.; Tang, E. I.; Wong, C. K. C.; Lee, W. M.; John, C. M.; Turek, P. J.; Silvestrini, B.; Cheng, C. Y. Environmental Toxicants Perturb Human Sertoli Cell Adhesive Function via Changes in F-Actin Organization Mediated by Actin

Regulatory Proteins. *Human Reproduction* **2014**, *29* (6), 1279–1291. https://doi.org/10.1093/humrep/deu011.

(338) Wan, H.-T.; Mruk, D. D.; Wong, C. K. C.; Cheng, C. Y. Perfluorooctanesulfonate (PFOS) Perturbs Male Rat Sertoli Cell Blood-Testis Barrier Function by Affecting F-Actin Organization via p-FAK-Tyr407: An in Vitro Study. *Endocrinology* **2014**, *155* (1), 249–262. https://doi.org/10.1210/en.2013-1657.

(339) Mostowy, S.; Cossart, P. Septins: The Fourth Component of the Cytoskeleton. *Nature Reviews Molecular Cell Biology* **2012**, *13* (3), 183–194. https://doi.org/10.1038/nrm3284.

(340) Moreno-Castellanos, N.; Rodríguez, A.; Rabanal-Ruiz, Y.; Fernández-Vega, A.; López-Miranda, J.; Vázquez-Martínez, R.; Frühbeck, G.; Malagón, M. M. The Cytoskeletal Protein Septin 11 Is Associated with Human Obesity and Is Involved in Adipocyte Lipid Storage and Metabolism. *Diabetologia* **2017**, *60* (2), 324–335. https://doi.org/10.1007/s00125-016-4155-5.

(341) Palanivel, R.; Ganguly, R.; Turdi, S.; Xu, A.; Sweeney, G. Adiponectin Stimulates Rho-Mediated Actin Cytoskeleton Remodeling and Glucose Uptake via APPL1 in Primary Cardiomyocytes. *Metabolism* **2014**, *63* (10), 1363–1373. https://doi.org/10.1016/j.metabol.2014.07.005.

(342) Mitsuyama, S.; Abe, F.; Kimura, M.; Yoshida, M.; Higuchi, T. Association between Leptin Gene Expression in Subcutaneous Adipose Tissue and Circulating Leptin Levels in Obese Patients with Psoriasis. *Archives of Dermatological Research* **2015**, *307* (6), 539–544. https://doi.org/10.1007/s00403-015-1581-z.

(343) Dopytalska, K.; Baranowska-Bik, A.; Roszkiewicz, M.; Bik, W.; Walecka, I. The Role of Leptin in Selected Skin Diseases. *Lipids Health Dis* **2020**, *19* (1), 215–215. https://doi.org/10.1186/s12944-020-01391-8.

(344) Rheinwald, J. G.; Hahn, W. C.; Ramsey, M. R.; Wu, J. Y.; Guo, Z.; Tsao, H.; De Luca, M.; Catricalà, C.; O'Toole, K. M. A Two-Stage, $P16^{INK4A}$- and P53-Dependent Keratinocyte Senescence Mechanism That Limits Replicative Potential Independent of Telomere Status. *Mol. Cell. Biol.* **2002**, *22* (14), 5157. https://doi.org/10.1128/MCB.22.14.5157-5172.2002.

(345) Kraus, N. A.; Ehebauer, F.; Zapp, B.; Rudolphi, B.; Kraus, B. J.; Kraus, D. Quantitative Assessment of Adipocyte Differentiation in Cell Culture. *Adipocyte* **2016**, *5* (4), 351–358. https://doi.org/10.1080/21623945.2016.1240137.

(346) Gorrochategui, E.; Lacorte, S.; Tauler, R.; Martin, F. L. Perfluoroalkylated Substance Effects in Xenopus Laevis A6 Kidney Epithelial Cells Determined by ATR-FTIR Spectroscopy and Chemometric Analysis. *Chem. Res. Toxicol.* **2016**, *29* (5), 924–932. https://doi.org/10.1021/acs.chemrestox.6b00076.

(347) Kennedy, G. L.; Butenhoff, J. L.; Olsen, G. W.; O'Connor, J. C.; Seacat, A. M.; Perkins, R. G.; Biegel, L. B.; Murphy, S. R.; Farrar, D. G. The Toxicology of Perfluorooctanoate. *null* **2004**, *34* (4), 351–384. https://doi.org/10.1080/10408440490464705.

(348) Cordner, A.; De La Rosa, V. Y.; Schaider, L. A.; Rudel, R. A.; Richter, L.; Brown, P. Guideline Levels for PFOA and PFOS in Drinking Water: The Role of Scientific Uncertainty, Risk Assessment Decisions, and Social Factors. *Journal of Exposure Science & Environmental Epidemiology* **2019**, *29* (2), 157–171. https://doi.org/10.1038/s41370-018-0099-9.

(349) Dykema, L. D. *Measuring Perfluorinated Compunds in Michigan Surface Waters and Fish.*; Michigan Department of Community Health, 2015; pp 1–54.

(350) Qiu, L.; Zhang, X.; Zhang, X.; Zhang, Y.; Gu, J.; Chen, M.; Zhang, Z.; Wang, X.; Wang, S.-L. Sertoli Cell Is a Potential Target for Perfluorooctane Sulfonate–Induced Reproductive Dysfunction in Male Mice. *Toxicological Sciences* **2013**, *135* (1), 229–240. https://doi.org/10.1093/toxsci/kft129.

(351) Palazzo, A.; Ackerman, B.; Gundersen, G. G. Tubulin Acetylation and Cell Motility. *Nature* **2003**, *421* (6920), 230–230. https://doi.org/10.1038/421230a.

(352) Nekooki-Machida, Y.; Hagiwara, H. Role of Tubulin Acetylation in Cellular Functions and Diseases. *Medical Molecular Morphology* **2020**, *53* (4), 191–197. https://doi.org/10.1007/s00795-020-00260-8.

(353) Hammond, J. W.; Cai, D.; Verhey, K. J. Tubulin Modifications and Their Cellular Functions. *Current Opinion in Cell Biology* **2008**, *20* (1), 71–76. https://doi.org/10.1016/j.ceb.2007.11.010.

(354) Mahoney, J. E.; Mori, M.; Szymaniak, A. D.; Varelas, X.; Cardoso, W. V. The Hippo Pathway Effector Yap Controls Patterning and Differentiation of Airway Epithelial Progenitors. *Developmental Cell* **2014**, *30* (2), 137–150. https://doi.org/10.1016/j.devcel.2014.06.003.

(355) Makita, R.; Uchijima, Y.; Nishiyama, K.; Amano, T.; Chen, Q.; Takeuchi, T.; Mitani, A.; Nagase, T.; Yatomi, Y.; Aburatani, H.; Nakagawa, O.; Small, E. V.; Cobo-Stark, P.; Igarashi, P.; Murakami, M.; Tominaga, J.; Sato, T.; Asano, T.; Kurihara, Y.; Kurihara, H. Multiple Renal Cysts, Urinary Concentration Defects, and Pulmonary Emphysematous Changes in Mice Lacking TAZ. *American Journal of Physiology-Renal Physiology* **2008**, *294* (3), F542–F553. https://doi.org/10.1152/ajprenal.00201.2007.

(356) Yimlamai, D.; Fowl, B. H.; Camargo, F. D. Emerging Evidence on the Role of the Hippo/YAP Pathway in Liver Physiology and Cancer. *Journal of Hepatology* **2015**, *63* (6), 1491–1501. https://doi.org/10.1016/j.jhep.2015.07.008.

(357) Li, L.; Dong, L.; Wang, Y.; Zhang, X.; Yan, J. Lats1/2-Mediated Alteration of Hippo Signaling Pathway Regulates the Fate of Bone Marrow-Derived Mesenchymal Stem

Cells https://www.hindawi.com/journals/bmri/2018/4387932/ (accessed 2020 -03 -25). https://doi.org/10.1155/2018/4387932.

(358) Hu, J. L.; Todhunter, M. E.; LaBarge, M. A.; Gartner, Z. J. Opportunities for Organoids as New Models of Aging. *Journal of Cell Biology* **2017**, *217* (1), 39–50. https://doi.org/10.1083/jcb.201709054.